AD-A178 629 DUAL CYLINDRICAL WAVE LASER-DOPPLER METHOD FOR MEASUREMENT OF SKIN FRICTI..(U) STANFORD UNIV CA DEPT OF MECHANICAL ENGINEERING A A NAQWI ET AL. JAN 87 1/3

UNCLASSIFIED ARO-19976.3-EG DAAG29-83-K-0056 F/G 20/4 NL

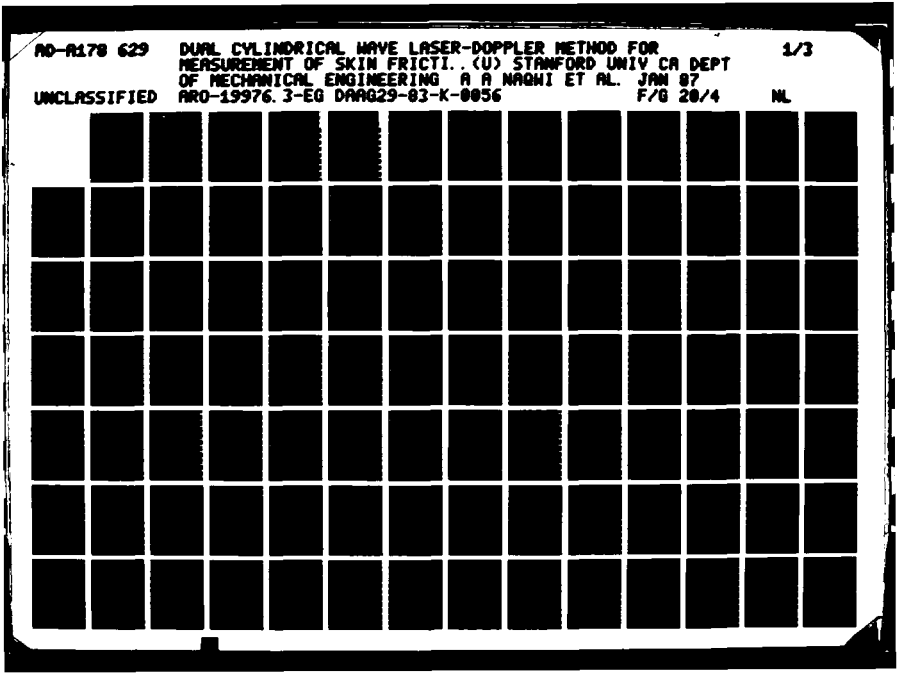

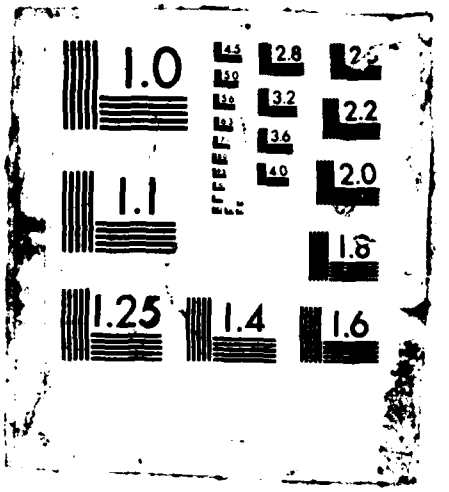
1.0
1.1
1.25
1.4
1.6
2.8
3.2
3.6
4.0
2.2
2.0
1.8

DUAL CYLINDRICAL WAVE LASER–DOPPLER METHOD FOR MEASUREMENT OF SKIN FRICTION IN FLUID FLOW

by

Amir A. Naqwi

William C. Reynolds

Prepared under the joint support of

Army Research Office

Aeromechanics Laboratory, RTL (AVRADCOM)

NASA-Ames Research Center

Report No. TF-28

Thermosciences Division

Department of Mechanical Engineering

Stanford University

Stanford, California 94305

January, 1987

UNCLASSIFIED MASTER COPY - FOR REPRODUCTION PURPOSES

CURITY CLASSIFICATION OF THIS PAGE

REPORT DOCUMENTATION PAGE

1. REPORT SECURITY CLASSIFICATION: Unclassified	1b. RESTRICTIVE MARKINGS
2a. SECURITY CLASSIFICATION AUTHORITY	3. DISTRIBUTION/AVAILABILITY OF REPORT: Approved for public release; distribution unlimited.
2b. DECLASSIFICATION/DOWNGRADING SCHEDULE	
4. PERFORMING ORGANIZATION REPORT NUMBER(S)	5. MONITORING ORGANIZATION REPORT NUMBER(S): ARO 19976.3-EG
6a. NAME OF PERFORMING ORGANIZATION: Stanford University; 6b. OFFICE SYMBOL (If applicable)	7a. NAME OF MONITORING ORGANIZATION: U. S. Army Research Office
6c. ADDRESS (City, State, and ZIP Code): Standord, CA 94305	7b. ADDRESS (City, State, and ZIP Code): P. O. Box 12211, Research Triangle Park, NC 27709-2211
8a. NAME OF FUNDING/SPONSORING ORGANIZATION: U. S. Army Research Office; 8b. OFFICE SYMBOL (If applicable)	9. PROCUREMENT INSTRUMENT IDENTIFICATION NUMBER: DAAG29-83-K-0056
8c. ADDRESS (City, State, and ZIP Code): P. O. Box 12211, Research Triangle Park, NC 27709-2211	10. SOURCE OF FUNDING NUMBERS: PROGRAM ELEMENT NO. / PROJECT NO. / TASK NO. / WORK UNIT ACCESSION NO.

11. TITLE (Include Security Classification)
Dual Cylindrical Wave Laser-Doppler Method for Measurement of Skin Friction in Fluid Flow

12. PERSONAL AUTHOR(S)
Amir A. Naqwi and William C. Reynolds

13a. TYPE OF REPORT	13b. TIME COVERED FROM ____ TO ____	14. DATE OF REPORT (Year, Month, Day)	15. PAGE COUNT
		Jan 87	261

16. SUPPLEMENTARY NOTATION
The view, opinions and/or findings contained in this report are those of the author(s) and should not be construed as an official Department of the Army position, policy, or decision, unless so designated by other documentation.

17. COSATI CODES		
FIELD	GROUP	SUB-GROUP

18. SUBJECT TERMS (Continue on reverse if necessary and identify by block number)
Skin Friction; Fluid Flow; Lasers; Boundary Layers; Doppler Method; Wall Shear Stress; Laser Beams; Cylindrical Waves

19. ABSTRACT (Continue on reverse if necessary and identify by block number)

The objective of the present work is to overcome the inadequacies of conventional skin friction measuring methods in terms of temporal and spatial resolution.

An instrument has been developed for measurement of the instantaneous velocity gradient in a boundary layer at a solid surface, from which the instantaneous wall shear stress can be deduced. The principle of the device is akin to that of dual beam Laser Doppler Anemometer. In-

20. DISTRIBUTION/AVAILABILITY OF ABSTRACT	21. ABSTRACT SECURITY CLASSIFICATION
☐ UNCLASSIFIED/UNLIMITED ☐ SAME AS RPT. ☐ DTIC USERS	Unclassified
22a NAME OF RESPONSIBLE INDIVIDUAL	22b. TELEPHONE (Include Area Code) / 22c OFFICE SYMBOL

D FORM 1473, 84 MAR 83 APR edition may be used until exhausted. All other editions are obsolete

SECURITY CLASSIFICATION OF THIS PAGE
UNCLASSIFIED

20. ABSTRACT CONTINUED

stead of crossing two laser beams to produce the measuring volume, the present technique uses interference between two closely spaced cylindrical waves emanating from the solid surface. The interference fringes which constitute the measuring volume appear to be radiating from a point on the surface. Keywords: 2 half page

DUAL CYLINDRICAL WAVE LASER-DOPPLER METHOD FOR MEASUREMENT OF SKIN FRICTION IN FLUID FLOW

by

Amir A. Naqwi
William C. Reynolds

Prepared under the joint support of

Army Research Office
Aeromechanics Laboratory, RTL (AVRADCOM)
NASA-Ames Research Center

Technical Report Number TF-28

Thermosciences Division
Department of Mechanical Engineering
Stanford University
Stanford, California 94305

January, 1987

Acknowledgments

Acknowledgments are due to:

- Dr. Rangarajan Jayaraman, who performed the preliminary analysis of this work.
- The U. S. Army Research Office, which provided the main financial support for this work under Contract DAAG 29-83-K-0056.
- The NASA-Ames Research Center, which financed parts of this project.
- Members of the Integrated Circuit Laboratory and the Center for Materials Research at Stanford, who produced the final samples of the parts that required applications of microfabrication technology.
- The administrative staff of HTTM, Mechanical Engineering Department, and Research Coordination, who have been helpful and cooperative during the course of this work.
- Professor Ronald J. Adrian of the University of Michigan, Ann Arbor, who provided the necessary information for developing the computer codes for analysis of the signal quality.
- Mr. Robin Birch and Mr. Lakhbir Johal, whose craftsmanship in fabrication of various parts has been indispensible in the successful completion of this work.
- Mr. Michael Castellano and Mr. Roy Niegel, who provided efficient services and expert advice on auxiliary instruments.
- Ms. Ruth Korb, who did an excellent job of typing and editing the manuscript.

Abstract

The objective of the present work is to overcome the inadequacies of conventional skin friction measuring methods in terms of temporal and spatial resolution.

An instrument has been developed for measurement of the instantaneous velocity gradient in a boundary layer at a solid surface, from which the instantaneous wall shear stress can be deduced. The principle of the device is akin to that of dual beam Laser Doppler Anemometer. Instead of crossing two laser beams to produce the measuring volume, the present technique uses interference between two closely spaced cylindrical waves emanating from the solid surface. The interference fringes which constitute the measuring volume appear to be radiating from a point on the surface.

Laser light is focused on a pair of optical slits in the wall to produce the cylindrical waves. The slits are etched on a chromium coating (~ 0.1 micron thick) deposited on a glass window. The window is mounted in the wall with the coated side facing the fluid and flush with the surface. In the present arrangement, the slits are 1 μm wide, 400 microns long and 10 microns apart.

Seed particles in the fluid scatter light while crossing the measuring volume. The scattered light is collected and analysed in a conventional manner. In the present arrangement, the velocity and the fringe spacing increase proportionally with distance from the wall. This is true as long as measurement is made within the linear region of the velocity profile. It is possible to apply this method conveniently to boundary layers with a linear region as small as 0.1 millimeter. For a given value of velocity gradient, the frequency of modulation of scattered light is invariant throughout the linear region. This single frequency is a direct measure of the instantaneous wall velocity gradient.

This device has been tested in plane Poiseuille flow as well as in flat plate turbulent boundary layer. Water has been used as the flow medium for all the experiments. The results from the laminar flow are

in agreement with theory within the uncertainty limits of the experiment. The data for turbulent flow include measurement of mean skin friction, wall turbulence intensity, skewness and flatness factors of near-wall turbulence and the probability density function of the skin friction. These parameters are also reported for spanwise fluctuations. All the data were obtained from a flat-plate boundary layer having a Reynolds number of ~ 3700 based on momentum thickness. The mean skin friction coefficient was found to be 0.0032 with a standard deviation of 38%. The probability density function has a positive skewness; the flatness and skewness factors being 4.0 and 0.78, respectively. For spanwise velocity gradient, the standard deviation is 11% of the streamwise mean value, and the flatness factor is 4.6. Since the spanwise velocity profile appears to be nonlinear even within five wall units, it is not certain that the measurements truly represent the value of the spanwise velocity gradient at the wall. In the absence of truly definitive measurements or computational results for comparison, it is difficult to establish the accuracy of these data with a high precision. The author believes that the search for an exact knowledge of turbulent skin friction is a continuing process advanced by progress in computational methods as well as experimental techniques. The present work may be considered a significant contribution to this process.

Table of Contents

Nomenclature

a	Width of the optical slit.
$\hat{a} \equiv ka/2$	Normalized slit width.
a_o	Amplitude of free-stream periodic velocity as a ratio of mean free-stream velocity.
A_o	Normalized amplitude of the periodic velocity; Eqn. (3.31).
A_{C_1}, A_{C_2}	Components of the propagation vector, $\vec{s}$; Eqn. (4.13).
A_{s_1}, A_{s_2}	Parameters of scattering coefficients, $\vec{C}_{s_1}$ and $\vec{C}_{s_2}$; Eqns. (A.68) through (A.80).
$B \equiv B(x,y;u,v)$	Transfer function of the instrument; Eqn. (2.10).
$\mathcal{B} \equiv B\lambda/S$	Normalized transfer function.
B_{s_1}, B_{s_2}	Parameters of scattering coefficients, $\vec{C}_{s_1}$ and $\vec{C}_{s_2}$; Eqns. (A.68) through (A.80).
c	Constant in universal logarithmic velocity profile; Eqn. (9.1).
c_s	Speed of sound in acousto-optic modulator.
C_f	Skin friction coefficient.
$\vec{C}_{s_1}$, $\vec{C}_{s_2}$	Scattering coefficients from the two slits.
d_f	Fringe spacing.
d_m	Distance between the mirrors in the beam generator.
d_p	Particle diameter.
D_c, D_s	Real and imaginary components of $2(\vec{C}^*_{s_1} \cdot \vec{C}_{s_2})$, respectively.
$\overline{D}_c$, $\overline{D}_s$	Integrated D_c and D_s over solid angle of the receiving aperture.
e	Complex diffracted field, normalized by field strength at the slit center.
e	Charge of an electron
$\vec{e}_{\theta_1}$, $\vec{e}_{\phi_1}$	Unit vectors in polar coordinates for the electromagnetic wave from the downstream slit.
$\vec{e}_{\theta_2}$, $\vec{e}_{\phi_2}$	Unit vectors in polar coordinates for the electromagnetic wave from the upstream slit.
$\vec{E}_s$	Combined scattered field from both the slits.
$\vec{E}_{i_1}$, $\vec{E}_{i_2}$	Strengths of fields from the downstream and upstream slits, respectively.

f_1	Frequency of laser light on the downstream slit.
f_1'	Doppler-shifted frequency from the downstream slit after scattering from a particle.
f_2	Frequency of laser light on the upstream slit.
f_2'	Doppler-shifted frequency from the upstream slit.
f_c	Focal length of the cylindrical lens.
f_d	Frequency of the signal detected.
f_{dm}	Down-mix frequency.
f_m	Anisotropic scattering shift in the detected signal; Eqn. (4.22).
f_s	Frequency of sound waves in an acousto-optic modulator.
$F(\ )$	Fresnel integral.
$F_c(\ ), F_s(\ )$	Real and imaginary parts of Fresnel integral, respectively.
$g = g(t)$	Wall velocity gradient, instantaneous.
g_c	Acceleration due to gravity.
g_{max}, g_{min}	The upper and lower limits for the velocity gradient being measured.
$G = \dfrac{\int_o^\delta \left(\dfrac{\bar{U}-\bar{u}}{u_\tau}\right)^2 dy}{\int_o^\delta \left(\dfrac{\bar{U}-\bar{u}}{u_\tau}\right) dy}$	Clauser shape factor of a turbulent boundary layer.
h	Planck's constant.
$H = \delta_1/\delta_2$	Shape factor of turbulent boundary layer.
H	Height of the laminar channel.
I_{i_1}, I_{i_2}	Intensity of light waves incident on a scattering particle.
i_n	Root-mean-square noise current from the photomultiplier tube.
i_s	Signal current from the photomultiplier tube.
$\vec{i}$, $\vec{j}$, $\vec{k}$	Unit vectors along x, y, and z, respectively.

k	Wavenumber, $2\pi/\lambda$.
k_1	Ratio of fringe spacing to particle diameter.
k_2	Ratio of the peak negative turbulent velocity to the mean velocity.
$K_1 \ldots K_4$	Parameters in the scattering theory; Eqns. (4.23) through (4.26).
ℓ	Length of the slits.
$\hat{\ell} \equiv k\ell/2$	Normalized slit length.
ℓ_{am}	Length of the acousto-optic modulator.
L	$1/e^2$ length of cross section of the laser-sheet in the slit-plane.
$\hat{L} \equiv kL/2$	Normalized length of the laser-sheet cross-section in the slit plane.
L_m	Migration length of a particle.
N	Number of cycles in a Doppler burst.
N_o	Number of cycles in a Doppler burst without frequency shifting.
$\vec{n}$	Difference of unit vectors along the local direction of propagation of two light waves, Fig. 2.1.
$\vec{p}$	Polarization vector of a diffracted field.
$\tilde{p}$	Periodic component of pressure.
P	Laser power transmitted through the slits.
P_o	Laser power incident on the slits.
P_1, P_2	Amplitude of scattering coefficients, $\vec{C}_{s_1}$ and $\vec{C}_{s_2}$, respectively.
$\overline{P}_1$, $\overline{P}_2$	Integrated P_1 and P_2 over solid angle of the receiving aperture.
P_s	Power in the scattered light, instantaneous.
$q \equiv \frac{\hat{z}-\hat{z}_o}{\hat{r}_o}$	Normalized $\hat{z}$ for stationary phase simplification.
r	Distance from the scattering particle center; Fig. A.7.

$\hat{r}$	Unit vector in the direction of observation of scattered light, in the boundary-layer coordinates.
$\hat{r}_a$	Unit vector for observation of the scattered light, in the aperture coordinates.
$\hat{r}_o$	Projection onto $\hat{x}_o\hat{y}_o$ plane of the line connecting (x,z) to (x_o, y_o, z_o).
Re_H	Reynolds number for laminar channel flow, based on the channel height and the mean velocity.
Re_{δ_1}	Reynolds number of a turbulent boundary layer, based on the displacement thickness and the free-stream velocity.
Re_{δ_2}	Reynolds number of a turbulent boundary layer, based on the momentum thickness and the free-stream velocity.
$\hat{s}$	Propagation vector of a diffracted field.
s_1	Spacing between the intra-cavity laser waist and the cylindrical lens.
S	Slit spacing.
$S = S/2y$	Normalized slit spacing.
SNR	Local signal-to-noise ratio.
$\overline{SNR}$	Average SNR over the receiving aperture.
t	Time.
U	Free-stream velocity, instantaneous.
$\overline{U}$	Mean free-stream velocity.
$U^+ = \overline{U}/u_\tau$	Normalized mean free-stream velocity.
$\tilde{U}$	Periodic free-stream velocity.
u	Streamwise velocity.
$\overline{u}$	Mean streamwise velocity.
$\tilde{u}$	Periodic component of streamwise velocity.
u'	Turbulent component of streamwise velocity.
u_τ	Friction velocity.
u^*	Apparent friction velocity from Coles' fit to a turbulent velocity profile.

$u^+ = \bar{u}/u_\tau$	Mean streamwise velocity normalized with the inner variables.
u'^+	Root-mean-square u' normalized with u_τ.
$\hat{u}_1$, $\hat{u}_2$	Unit vectors along the two light waves; Fig. 2.1.
u_ℓ	Linear term in the near-wall velocity, Eqn. (2.9).
$u_{n\ell}$	Higher-order term in the near-wall velocity profile; Eqn. (2.8).
$u_{n\ell} = u_{n\ell}/u_\ell$	Normalized higher-order term in the near-wall velocity.
v	Normal velocity.
v'^+	Root-mean-square fluctuation in the normal velocity normalized with u_τ.
v	Normalized normal velocity.
v_c	Linear speed of the laser chopper.
v_{mn}	Migration velocity of a neutrally buoyant particle.
v_{ms}	Velocity of particle migration due to sedimentation.
$\hat{V}$	Velocity vector in the measuring volume, instantaneous.
V	Local signal visibility.
$\bar{V}$	Signal visibility averaged over the receiving aperture.
w	Spanwise velocity.
w'	Root-mean-square fluctuation in spanwise velocity.
w	Half-width of $1/e^2$ intensity profile of a laser beam.
w_o	Half-width of the waist of a laser beam for $1/e^2$ intensity.
w_{01}	Half-width of the intra-cavity waist.
W	$1/e^2$ width of a laser sheet incident on a slit.
$\hat{W} = kW/2$	Normalized laser width in the slit plane.
x	Streamwise distance.
$x = x/y$	Normalized streamwise distance across the fan.
x_m	Half streamwise extent of the measuring volume.

$x_m = x_m/y$	Normalized half streamwise extent of the measuring volume.
$\hat{x} = kx$	Normalized distance along the slit-width in incident field coordinates, Fig. A.3.
x_o	Distance along the slit-width in diffracted field coordinates, Fig. A.3.
$\hat{x}_o = kx_o$	Normalized x_o.
y	Distance from the wall.
$y^+ = yu_\tau/\nu$	Distance y normalized with the inner variables.
y_{max}, y_{min}	Upper and lower bounds of the measuring volume in y.
y_s	Distance y normalized with Stokes length scale; Eqn. (3.25).
y_o	Distance normal to the slit plane.
$\hat{y}_o = ky_o$	Normalized y.
z	Distance (spanwise).
$z^+ = zu_\tau/\nu$	Spanwise distance normalized with the inner variables.
$\hat{z} = kz$	Normalized distance along the slit-length in the incident field coordinates, Fig. A.3.
z_o	Distance along the slit length in the diffracted field.
$\hat{z}_o = kz_o$	Normalized z_o.
$z_R = \pi w_o^2/\lambda$	Rayleigh range of the laser beam at the slits.
$z_{R_1} = \pi w_{o1}^2/\lambda$	Rayleigh range at the intra-cavity waist.

Greek Symbols

α — Half spreading angle of the cylindrical wave produced by a slit.

α_a — Half receiving-cone angle.

α_b — Angle between laser beams approaching the cylindrical lens.

β — Phase angle of the diffracted field e.

γ_n, γ_s — Normal and streamwise angles for description of the scattered field.

δ — Turbulent boundary-layer thickness from Coles' scheme.

$\delta_1 \equiv \int_o^\delta \left(1 - \frac{\overline{u}}{\overline{U}}\right) dy$ — Displacement thickness of a turbulent boundary layer.

$\delta_2 = \int_o^\delta \frac{\overline{u}}{\overline{U}} \left(1 - \frac{\overline{u}}{\overline{U}}\right) dy$ — Momentum thickness of turbulent boundary layer.

$\delta_3 = \int_o^\delta \frac{\overline{u}^2}{\overline{U}^2} \left(1 - \frac{\overline{u}}{\overline{U}}\right) dy$ — Energy thickness of turbulent boundary layer.

$\delta^+ = \delta u^*/\nu$ — Normalized boundary-layer thickness.

Δf_{down} — Effective frequency shift: $f_{dm} < |f_1 - f_2|$.

Δf_s — Frequency bandwidth of the signal processor.

Δf_{up} — Effective frequency shift: $f_{dm} > |f_1 - f_2|$.

$\Delta\tilde{u}$ — Nonlinear part of $\tilde{u}$.

Δy — y-extent of the measuring volume.

$\Delta\Psi$ — Change in Ψ over time Δt.

η_q — Quantum efficiency of photomultiplier tube.

θ — Altitude angle in polar coordinates for scattering theory; Fig. A.7.

θ_a — Altitude angle in the aperture coordinate system.

θ_c	Altitude angle of the center of the receiving aperture; Fig. 4.8.
θ_m	Angle of mirror tile in beam generator.
κ	Constant in universal logarithmic velocity profile; Eqn. (9.1).
λ	Wavelength of light in the fluid.
Λ	Wavelength of sound in acousto-optic modulator.
ν	Kinematic viscosity of the fluid.
ν_o	Frequency of light in vacuum.
Π	Coefficient of wake function in Coles' profile.
ρ	Density of the fluid.
ρ_p	Particle density.
τ	Wall shear stress.
$\overline{\tau}$	Time-averaged wall shear stress.
τ'	Root-mean-square fluctuation in wall shear stress.
τ^*	Normalized wall shear stress in laminar flow; Eqn. (8.1).
ϕ	Azimuth angle in polar coordinates for scattering theory; Fig. A.7.
ϕ_a	Azimuth angle in the aperture coordinate system.
ϕ_c	Azimuth angle of the center of the receiving aperture; Fig. 4.8.
χ_1, χ_2	Phases of A_{s_1} and A_{s_2}, respectively.
ψ_1, ψ_2	Phases of B_{s_1} and B_{s_2}, respectively.
Ψ	Phase angle caused by local anisotropic scattering shift.
$\overline{\Psi}$	Phase angle caused by average anisotropic scattering shift over receiving aperture.
ω	Frequency of free-stream unsteadiness; radians/sec.
Ω	Solid angle of the receiving optics.

Chapter 1

INTRODUCTION

1.1 Objectives

Knowledge of the viscous drag caused by a fluid flowing past a solid surface is of prime importance in fluid mechanics; however, quantitative measurement of skin friction, even in steady flow, is a difficult task. A variety of techniques has been developed and employed for measurement of skin friction over the past few decades. The purpose of this work was to develop a new optical method for measurement of skin friction in unsteady flow, to be used in a water-flow facility for study of turbulent boundary layers.

1.2 Previous Works

1.2.1 Conventional Methods

Laufer (1975) has identified periods of distinct trends in experimental research on turbulence. Eddy-viscosity models based on mean quantities were the main tools for studying turbulence during the 1920's and 30's. Measurement of mean skin friction (averaged over time and surface area) was considered adequate during this period. The earliest attempts to localize the measurement of skin friction along the flow direction were made by Ludwieg and Tillmann (1949) in the late 40's. Nevertheless, the hypothesis that a steady laminar sublayer existed within a turbulent boundary layer had been widely accepted until visual studies beginning in the 50's revealed that the wall velocity gradient in a turbulent boundary layer is actually time-dependent; see Kline et al. (1967). It was further discovered that the flow in a nominally two-dimensional boundary layer consists of spanwise streaks of fast and slow-moving fluid. These discoveries have led to the necessity of measuring temporally- and spatially-resolved skin friction, in order to obtain detailed information about the fluid behavior next to the wall. However, there exists a variety of methods which were originally developed prior to the realization of this particular need. These methods shall hereafter be referred to as "conventional" methods.

Winter (1977) reviewed the conventional techniques for measurement of skin friction. These methods can be classified as follows.

1. Force measurement (floating-element devices);

2. Velocity profile methods (Clauser plot etc.);

3. Pressure measurement (surface Pitot tube and obstacles);

4. Analogies: Heat transfer, mass transfer, surface oil flow.

The conventional methods are either indirect (and dependent on the validity of certain assumptions and analogies) or direct and intrusive. One of the least intrusive of these instruments is the floating-element device, which continues to offer difficulties in the presence of pressure gradients, as noted by Acharya and Escudier (1983). Furthermore, as pointed out earlier, these devices measure shear stress averaged over a certain time interval and surface area which is frequently inadequate for exploring the correlation between skin friction and the nature of near-wall turbulence. A typical floating-element is larger than 5 mm in diameter and hence not capable of resolving spanwise streaks or streamwise structures under typical experimental conditions, and at best measures the time-averaged stress.

1.2.2 Current Developments

An experimental evaluation of time-dependent shear stress is valuable not only for the classical case of a flat-plate turbulent boundary layer but also for other flow models of practical significance. These flow models include boundary layer separation and reattachment and unsteady turbulent flow on a flat surface. The cases of a curved surface and an imposed pressure gradient are also of interest. An experimental data set of time-dependent shear stress is also understood to be indispensable for evaluation of computational models of near-wall turbulence.

The earliest efforts to measure the fluctuating shear stress were made using a hot-film surface gauge (Bellhouse and Schultz, 1968). This device is based on the analogy between local skin friction and surface heat transfer. Ludwieg (1949) proposed this device, recognizing that heat flow from a surface element is proportional to the one-third power of the wall shearing stress, provided that the thermal layer lies within

the linear velocity region of the boundary layer. The hot-film element is normally small in physical dimensions (e.g., DISA 55R45 is 0.75 mm along the spanwise and 0.2 mm along the streamwise direction) and has adequate spatial resolution. The frequency response of these devices is also believed to be sufficiently high for typical laboratory use. However, this feature is not very well understood. The hot-film gauge is usually maintained at a fixed temperature using electrical heating during its operation. Fluctuations in voltage resulting from variation in heat transfer rate from the film are recorded. The sixth power of the instantaneous voltage is proportional to the instantaneous shear stress, making the instrument inherently weak in sensitivity. For instance, a 100% increase in the shear stress causes only 12% increase in the voltage. It should also be noted that the one-third-power law is based on the assumptions of quasi-steady flow and heat transfer as well as unidirectional flow, neither of which may apply in unsteady flow.

Calibration of a hot-film gauge in a fluctuating flow is a difficult task. Sandborn (1979) and Ramaprian & Tu (1983) have addressed this issue in different manners and have suggested procedures for calibration of such devices in turbulent flow. Cook and Giddings (1984) have evaluated such gauges in unsteady laminar flow. Their results indicate large errors in the phase information deduced from hot-film measurements.

The thermal tuft developed at Stanford University by Westphal, et al. (1981), is a recent advance in instrumentation for measurement of skin friction. The thermal tuft is a modified pulsed-wire anemometer probe used to measure very near-wall velocity, from which the velocity gradient and shear stress can be deduced. This method uses a time-of-flight measurement of a tracer of heated fluid. It has been proven valuable in a study of turbulent separation and reattachment in air flow. This device involves a very short duration to produce a tracer. The time of flight is typically of the order of a millisecond, which signifies a high temporal resolution; however, it loses resolution at low speeds which makes it virtually ineffective for application to a typical water channel. The physical dimensions of the current version of the probe are larger than those considered appropriate for obtaining desirable spatial resolution.

Laser methods appear potentially powerful, especially for a non-intrusive measurement. Monson and Higuchi (1980) have suggested an interferometric laser method for evaluation of skin friction by measurement of the thickness of an oil film on the solid surface. This method is applicable to gas flow only. Furthermore, it is not yet developed to the level of being used for local instantaneous measurements. The complexity of the oil flow is apparently the main limitation.

As compared to the above-mentioned method, laser Doppler Anemometry (LDA) is a more developed technique. The transfer function of LDA is simple and well-established in comparison to the complex relationships between output and measurand encountered frequently in other devices. Mazumder et al. (1981) and several other researchers have attempted to employ the conventional LDA directly for measuring very near-wall velocities for the purpose of deducing shear stress. Such efforts, however, have not yielded reliable results for the following reasons:

1) Distortion of fringes and additional noise due to interference of beams with the wall as the distance between the measuring volume and wall becomes small.

2) Uncertainty in the knowledge of the location of the measuring volume, causing large errors in the estimates of wall velocity gradient.

3) Substantial change in velocity across the finite size of the measuring volume, prohibiting interpretation of an individual burst generated by a seed particle, since location within the measuring volume cannot be accurately established. This effect is illustrated in Figure 1.1; particles at different y-locations within the measuring volume are shown to be producing signals of different frequencies for the same velocity gradient. Under such conditions, only time-averaged data can be meaningful, and correlation of skin friction with any other instantaneous measurement is not possible.

Goldstein and Adrian (1971) have suggested a method which uses the spectrum of the LDA signals measured over a large time interval to deduce the velocity gradient. However, this method is applicable only to steady state flows.

A number of exotic concepts besides those mentioned above have been employed by researchers in order to improve resolution of the measurement and to eliminate disturbance to the flow. Mention of the electrochemical probe of Mitchell and Hanratty (1966) and the method of speckle motion suggested by Keveloh and Staude (1983) is appropriate in this context. However, these methods are not yet developed to the stage of being used with confidence for extensive research on turbulence.

1.3 The Motivation for the Present Work

As the above review of the previous work may have revealed, a powerful method for measurement of skin friction could be developed by modifying an LDA system to eliminate the peculiar difficulties of near-wall measurements. The present work has been aimed at practical implementation of a variant of the LDA concept which seeks to circumvent the above-mentioned problems.

The new system will be used to measure skin friction in an existing water-flow facility which has been built to study steady and unsteady boundary layers. Jayaraman et al. (1982) have described this apparatus in detail. In this facility, the turbulent boundary layer is about 50 mm thick with a viscous sublayer (up to $y^+ = 5$) of thickness 150 microns. The layer may be perturbed by changing the free-stream velocity abruptly or sinusoidally. Further details about relevant parameters of the boundary layer are provided in Table 3.1.

1.4 The Present Technique

The essence of the present method can be explained in terms of a simple fringe model. Suppose one could create a " fan-like " fringe pattern in the region where at any instant, the fluid velocity parallel to the wall varies linearly with distance from the wall (Fig. 1.2). Since the fringe spacing would also vary linearly with distance from the wall, the Doppler signal from particles passing through this region will have the same frequency for all the particles, and this frequency would be proportional to the instantaneous velocity gradient. Such a device could therefore be used to measure instantaneous wall shear stress. If the fringes could be made to rotate about the fan vertex, the device could be used for flows reversing in direction.

A fringe pattern with the above mentioned properties can be produced by interference of laser light diffracted from a pair of slits. Rotation of the fringes can be accomplished by shifting the frequency of light from one of the slits.

A mathematical treatment of this model involves expressions for velocity and fringe-spacing as functions of distance from the wall. The velocity profile can be expressed as follows:

$$u = gy \tag{1.1}$$

The fringe-spacing in the far-field of diffraction from a pair of slits is available in standard texts on physical optics (e.g., Jenkins and White, 1957).

$$d_f = \frac{\lambda y}{S} \tag{1.2}$$

This expression adequately describes the case of stationary fringes. The frequency of the scattered signal is given by

$$f_d = \frac{u}{d_f} = \frac{Sg}{\lambda} \tag{1.3}$$

Since the expression for the Doppler frequency is independent of particle location, it is a direct measure of the velocity gradient, g.

Equation (1.3) is valid over a sizeable region next to the wall. Signals are collected from a portion of this region called the measuring volume, which is illustrated schematically in Fig. 1.2. In the present system, the slits are 1 micron wide, 400 micron long and 10 microns apart. They are etched in a 0.1-micron-thick layer of chromium, using integrated circuit technology. A special optical arrangement is used to focus laser light properly on each slit.

The present technique circumvents the problems associated with the conventional dual beam LDA (listed in the previous section) in the following manner:

1) Laser beams originate from slits in the wall--this eliminates the problems with the beams grazing the wall;

2) Since the fringe pattern originates from the slits in the wall, its location relative to the wall is fixed and known, helping to reduce the uncertainty about the location of the measuring volume;

3) Since, within the limits of linear velocity profile and linear fringe spacing, the frequency of the Doppler signal is independent of the location from which it originates, the uncertainty about the particle location does not affect the accuracy of the measurement.

This instrument, like conventional LDA, has high temporal resolution. It can be made small enough to resolve spanwise variations in the flow and is essentially non-intrusive. The current version of this system requires delicate alignments and cannot be transported very quickly from one measuring location to the other.

This technique is also prone to errors in the measurement resulting from the non-representative motion of seed particles in the presence of large and unsteady velocity gradients. However, it is estimated that particles of diameter 2-8 microns are likely to follow the fluid closely and produce a discernible signal for the conditions under which this device is usable. This assessment is validated experimentally in a water channel with a high-skin-friction laminar flow.

Because of the small size of the slits and the need to collect scattered light in almost side-scatter, the signals have been weak and the signal rate meager (1-2 Hz). Later in this report, some suggestions are made to improve the signal rate for future experiments.

1.5 Organization of the Report

The above description of the technique is simplified and inadequate for practical implementation. A more comprehensive model of the device, based on the electromagnetic theory of light, is outlined in the next chapter. In Chapter 3, based on the formulation of Chapter 2 and considerations of boundary-layer parameters, criteria have been developed for evaluation of slit geometry. Both steady and unsteady layers are discussed. The design criteria are generalized and may be used for

building the instrument for a variety of flow conditions. Chapter 4 deals with a detailed analysis of the signal quality and the secondary effects associated with diffraction of light from the slits. The optical arrangement used to illuminate the slits is explained in Chapter 5. In order to achieve accurate alignment, the optical setup allows adjustment of the positions of various components. However, a large number of degrees of freedom make it impossible to align the system by trial and error. A systematic procedure for alignment of the device is presented in Chapter 6. Motion of scattering particles in the vicinity of the wall is considered in Chapter 7, which has led to the concept of "wall seeding" for obtaining high signal rates. Chapter 8 describes evaluation of the instrument in a laminar flow channel. The first application of the technique to a turbulent boundary layer is discussed in Chapter 9. In the last chapter, some conclusions are drawn about the technique and the results of turbulent measurements.

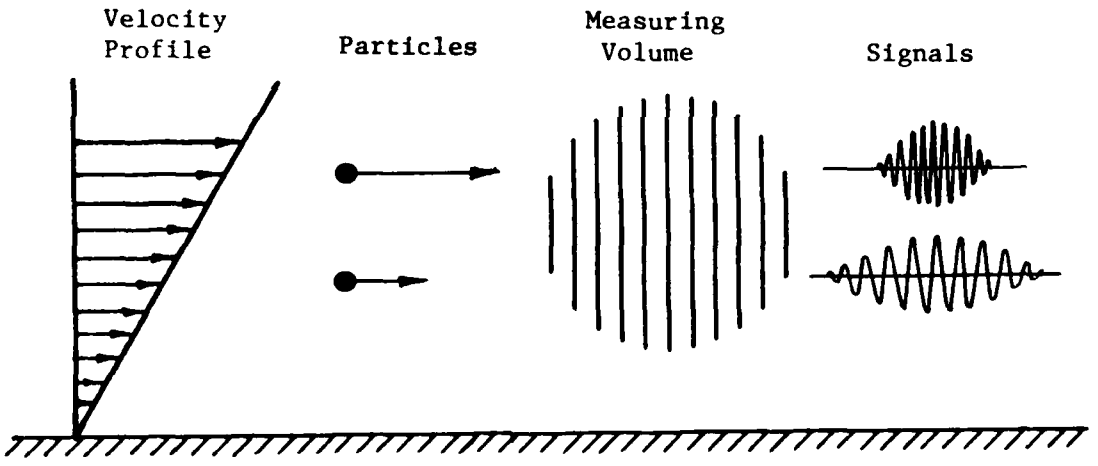

Fig. 1.1. Conventional LDA: Uncertainty due to finite size of the measuring volume.

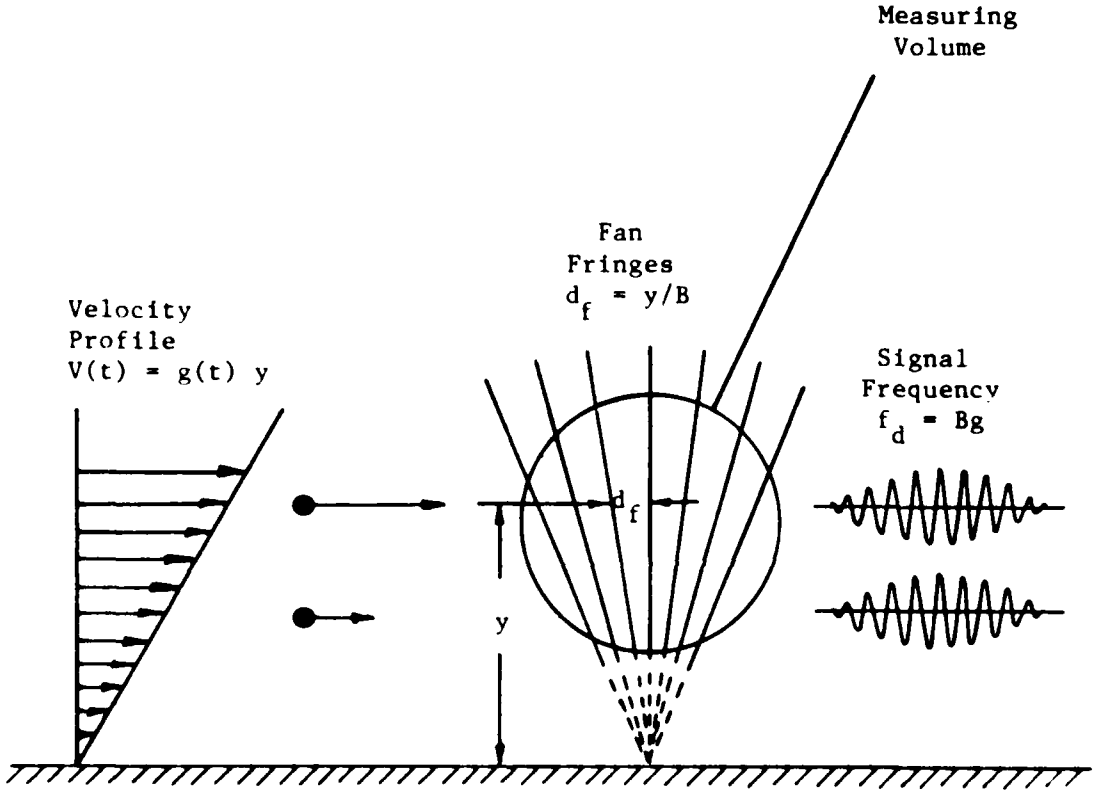

Fig. 1.2. Fringe model of the system.

Chapter 2

PRINCIPLE OF THE INSTRUMENT

2.1 Optical Considerations

The working principle of the device was explained in terms of fringes in the previous chapter. Fringes describe the spatial distribution of time-averaged power intensity associated with the interference of light waves. Such a treatment is conceptually simple and practically adequate for evaluation of the signal frequency but it does not encompass all the important aspects of the phenomenon. Additional information is needed for a detailed description of the diffraction of light from the slits and its subsequent scattering by moving particles. A more rigorous treatment of the phenomenon can be accomplished by considering the laser light as an electromagnetic wave and employing the principle of the Doppler effect to ascertain the frequency shift caused by the motion of the scattering particles. In this model, propagation of the electromagnetic wave is governed by a set of differential equations, known as Maxwell's equations. Standard solutions of Maxwell's equations are utilized in this work to explore various aspects of the phenomenon under consideration. The discussion in this context can be divided into the following topics:

i. Propagation of laser light from the laser head to the slits through various optical elements.

This part of the analysis can be conveniently treated with a solution of Maxwell's equations, describing propagation of laser beams through homogeneous, isotropic and nonconducting media. Based on the existing solutions for plain media and lenses, Self (1983) has documented standardized procedures for application in optical design. A consideration of the present system in this respect is postponed to the chapter on the optical arrangement.

ii. Diffraction of laser light from the slits.

The nature of diffracted light depends upon several parameters such as the orientation of the polarization axis relative to the slits and the electrical conductivity of the coating in which slits are etched. A

description of the diffracted light may consist of the extent of the near-field region, the shape of the wavefronts and the intensity distribution along the wavefronts. These aspects are considered in Chapters 3 and 4 (Design of Slits and Signal Simulation) and in Appendix B. The starting point for the current discussion is the deduction that the wave-front issuing from each slit is almost circularly cylindrical in the far-field of diffraction; hence the scheme is now designated as the Dual Cylindrical Wave (DCW) method. This result is used in the next section to demonstrate that the difference in Doppler-shifted frequencies from the two cylindrical waves can be related linearly to the wall velocity gradient under fairly general conditions.

iii. Scattering of light by moving particles.

The shift in the frequency of scattered light can be determined from the Doppler effect. A knowledge of the intensity and polarization of the scattered light in various directions is also important. An exact solution of Maxwell's equations for scattering of a plane wave from a homogeneous spherical particle, known as Mie scattering theory, can be used for this purpose. Adrian and Early (1976) have used this theory to develop procedures for evaluation of LDA systems.

Since Maxwell's equations are the main tools for the analysis and design of this system, these are documented and discussed in Appendix A. This appendix contains various simplifications and solutions of Maxwell's equations for the sake of immediate reference.

2.2 Frequency of the Heterodyne Signal

As mentioned earlier, the frequency of the signal can be considered as the heterodyne (of beat) frequency between two waves scattered by a moving particle as it crosses the cylindrical waves of laser light diffracted from the two slits.

In general, when two coherent waves are incident upon a moving particle of a size sufficiently smaller than the radii of curvature of the waves, the scattered light exhibits a heterodyne frequency due to the Doppler effect. An expression for this frequency can be deduced from a generalized expression given by Durst (1982).

$$f_d = \left| f_1 - f_2 + \frac{\vec{V}\cdot\vec{n}}{\lambda} \right| \tag{2.1}$$

This expression is applicable to two wavefronts of any shape with slightly different frequencies. Nomenclature for this expression is explained in Figure 2.1. In a typical LDA application, either f_1 and f_2 are the same or different by 40 MHz. The 40 MHz frequency shift is incorporated by an acousto-optic modulator (explained in Sec. 5.3).

The vector $\vec{n}$ can be expressed as the difference of unit vectors along the local direction of propagation of the two waves.

$$\vec{n} = \vec{u}_2 - \vec{u}_1 \tag{2.2}$$

Following the convention of Fig. 2.2, the two unit vectors $\vec{u}_1$ and $\vec{u}_2$ can be expressed in terms of the slit spacing S and coordinates x and y;

$$\vec{u}_1 = \frac{(x-S/2)\,\vec{i} + y\vec{j}}{\sqrt{(x-S/2)^2 + y^2}} \tag{2.3}$$

and

$$\vec{u}_2 = \frac{(x+S/2)\vec{i} + y\vec{j}}{\sqrt{(x+S/2)^2 + y^2}} \tag{2.4}$$

The term $\vec{V}\cdot\vec{n}/\lambda$ in Eqn. (2.1) can be evaluated by combining Eqns. (2.2) through (2.4) with the expression for velocity in Cartesian coordinates; i.e.,

$$\vec{V} = u\vec{i} + v\vec{j} + w\vec{k} \quad . \tag{2.5}$$

The following expression is thus obtained for $\vec{V}\cdot\vec{n}/\lambda$.

$$\frac{\vec{V}\cdot\vec{n}}{\lambda} = \frac{1}{\lambda}\left\{ \frac{[(x+S/2)u + yv]}{[(x+S/2)^2 + y^2]^{1/2}} - \frac{[(x-S/2)u + yv]}{[(x-S/2)^2 + y^2]^{1/2}} \right\} \tag{2.6}$$

2.3 Transfer Function

For the present system it is appropriate to relate the velocity gradient to the signal frequency by a transfer function,

$$B = B(x,y;u,v),$$

such that,

$$\frac{\vec{V}\cdot\vec{n}}{\lambda} \equiv B(x,y;u,v)\ g(t) \quad . \tag{2.7}$$

Notice that the terms involving the velocity component w would drop out, because the cylindrical waves are assumed to be two-dimensional. This assumption is examined in detail in Chapter 4. In order to obtain a linear relationship between the signal frequency f_d and the instantaneous wall velocity gradient $g(t)$, the function B should be reasonably constant over the measuring volume defined in terms of the coordinates x and y. It should also be insensitive to the range of velocity components u and v encountered in the measuring volume. The nature of the velocity distribution in the viscous sublayer is discussed in the following section. Current knowledge of the behavior of the velocity components u and v in the viscous sublayer is used later for estimating expected variations in the parameter B.

It is convenient to express the streamwise velocity component u as the sum of a linear and a higher-order term. i.e.,

$$u = u_\ell + u_{n\ell} \tag{2.8}$$

where,

$$u_\ell = g(t)\ y \tag{2.9}$$

Substituting the above relations into (2.6) and invoking the definition of B as given by Eqn. (2.7),

$$B(x,y;u,v) = \frac{y}{\lambda}\left\{\frac{(x+S/2)(1+u_{n\ell}/u_\ell) + yv/u_\ell}{[(x+S/2)^2 + y^2]^{1/2}} - \frac{(x-S/2)(1+u_{n\ell}/u_\ell) + yv/u_\ell}{[(x-S/2)^2 + y^2]^{1/2}}\right\} \tag{2.10}$$

The above expression can be non-dimensionalized by introducing the following definitions:

$$\begin{aligned} \mathbf{B} &= B\lambda/S \\ \mathbf{x} &= x/y \\ \mathbf{S} &= S/2y \\ \mathbf{u}_{n\ell} &= u_{n\ell}/u_\ell \\ \mathbf{v} &= v/u_\ell \end{aligned} \tag{2.11}$$

The following expression is obtained as a result of nondimensionalization.

$$\mathbf{B} = \frac{1}{2\mathbf{S}}\left\{\frac{(\mathbf{x}+\mathbf{S})(1+\mathbf{u}_{n\ell})+\mathbf{v}}{[(\mathbf{x}+\mathbf{S})^2+1]^{1/2}} - \frac{(\mathbf{x}-\mathbf{S})(1+\mathbf{u}_{n\ell})+\mathbf{v}}{[(\mathbf{x}-\mathbf{S})^2+1]^{1/2}}\right\} \tag{2.12}$$

Since $\mathbf{B}$ has been normalized with the nominal value of the transfer function obtained from the fringe model (Eqn. (1.3)), it is expected that the value of $\mathbf{B}$ should be close to unity. It is in fact apparent from Eqn. (2.12) that $\mathbf{B}$ approaches unity if

$$\mathbf{u}_{n\ell} = \mathbf{v} = 0 \quad \text{and} \quad |\mathbf{x} \pm \mathbf{S}| \ll 1 \quad .$$

2.4 Instantaneous Velocity Distribution in the Viscous Sublayer

Estimation of the normal velocity v and the nonlinear term $u_{n\ell}$ in the streamwise velocity is needed for examining invariance of the transfer function. Using results of experimental studies and numerical simulations of steady turbulent boundary layer, such an evaluation is taken up in this section. Effects of free-stream unsteadiness are considered in the later parts of this report.

Coles (1978) has compiled experimental data of near-wall turbulence from various authors. These data indicate that in general the r.m.s. fluctuation u'^+ is found to increase linearly with y^+ up to $y^+ = 5$. This is particularly true of the relatively more reliable data. It is also known from similar studies, such as that of Klebanoff (1954), that

the average velocity u^+ is also linear up to $y^+ = 5$. It may be conjectured, from these two pieces of information, that the instantaneous velocity profile is also linear for $y^+ < 5$. Though the available information does not necessarily imply linearity of the instantaneous velocity profile, the opposite is not likely from a consideration of viscous flow. Coles' model of the viscous sublayer based on Taylor-Görtler instability also suggests a linear increase in u'^+ up to $y^+ = 5$. A numerical simulation of the viscous sublayer by Chapman and Kuhn (1985) has led to similar results regarding the profiles of u^+ and u'^+.

Kim et al. (1971) have reported direct measurement of instantaneous velocity profiles in a turbulent boundary layer using hydrogen bubbles to track the flow. This technique is not accurate for quantitative evaluation; nevertheless it does not show a significant deviation from linearity in the instantaneous profile over the near-wall region, where the mean profile is linear.

In view of the above discussion, it may be assumed that the higher-order term $u_{n\ell}$ in the profile of streamwise velocity component can be kept well within 5% of the linear term u_ℓ by confining the measuring volume to $y^+ \leq 5$.

According to the data compiled by Coles, the r.m.s. normal component of velocity, v'^+, is significantly smaller than the streamwise velocity u^+; e.g., measurements of Laufer (1953) indicate that $v'^+ = 0.2$ at $y^+ = 5$, which implies that the standard deviation in v is only 0.04. This result is in agreement with the simulation of Chapman and Kuhn (1985). Hence, $\pm$ 0.1 are chosen as the extreme values of v for further evaluation.

Measurements of Klebanoff also exhibit that the root-mean-square value of u' is about 0.3 times the mean velocity in the near-wall region of a flat plate turbulent boundary layer. The study of Laufer for pipe flow shows a ratio of rms turbulent velocity to mean velocity of 0.25, in the viscous sublayer. Hot-film measurements of shear stress in channel flow by Blinco and Simons (1974) and Eckelmann (1979) are in agreement with the above-mentioned data. They have also demonstrated that the probability density function of the fluctuating

component is highly skewed towards positive values. It diminishes near twice-the-rms-value on the negative side. Hence it is appropriate to consider $-0.5\,\bar{u}$ as an extreme negative value for u'. This deduction is further substantiated by the experimental results of Sandborn (1979) and Westphal et al. (1981).

2.5 Invariance of the Transfer Function

It is desirable to have a transfer function that is independent of the particle position and velocity. The present device, however, involves minor variations in the multiplier B which converts the output of the device to the measurand. These variations arise from the optical arrangement as well as the flow condition. The variations associated with the optical setup are those pertaining to the relative location and the exact shape of the cylindrical waves. These are predictable to some degree; hence a correction can be applied to minimize uncertainties resulting from such variations. The variations associated with the flow characteristics, on the contrary, are less predictable and prone to cause larger uncertainties in the measurement.

The optics-related variations are illustrated in Figure 2.3. B is plotted for a range of x from -0.3 to $+0.3$ which corresponds to a full vertex angle of 33° for the fan. A variation of 10% occurs in B over this range. In terms of the fringe model, it may be interpreted as an increase in fringe-spacing from the center to the edges of the fan. This variation can be reduced to 5% if measurement is made between $x = -0.2$ and $x = +0.2$.

An increase in slit-spacing (for fixed y) lowers the value of B, as shown in Figure 2.3. It also makes it less sensitive to x. However, it may not be a good choice for practical implementation. If the slits are too far apart, it may not be possible to achieve adequate interference between diffracted light from the two slits. Actually, the slit-spacing should be significantly smaller than thickness of the region in which the velocity profile is expected to be linear. The plot corresponding to $S/y = 0.8$ may also be considered as the case of a very near-wall signal. Despite a weak overlap between the two diffracted waves, the near-wall signal from the central portion of the fan represents the velocity gradient reasonably well. This characteristic of the

signal from the very near-wall region is used for developing a method for alignment of the receiving optics (see Chapter 6).

It should be noted that individual signals correspond to unknown values of x and y within a limited range. This translates into an uncertainty in the knowledge of B for a given signal and hence an uncertainty in the measurement. To minimize this kind of uncertainty, an optimum value of B is evaluated in Appendix C. An estimate of uncertainty associated with the optimum value of B is also given in this appendix.

The flow-related variations in the transfer function are illustrated in Figs. 2.4 through 2.6. The values of v and $u_{n\ell}$ suggested in the previous section are used to evaluate variations in B. As shown in Figure 2.4, the effect of v is small and self-compensating. Decrease in B from the left half of the measuring volume is balanced by increase in the right half (or vice versa). This effect may be explained in terms of the fringe model. As shown in Figure 2.5, a particle with a small positive v-component crosses fringes faster than a particle with zero vertical component in the first half of the fan. The opposite is true for the second half. Hence the average measured frequency roughly corresponds to the u-component without any motion normal to the wall. Since displacement of the particle normal to the wall is small compared to the actual distance of the particle from the wall, it has been ignored in the present discussion.

The variation in B due to $u_{n\ell}$ is shown in Figure 2.6. It is of the same order as $u_{n\ell}$ i.e., $\pm$ 5% in this case. It may be remarked at this point that nonlinearity of the velocity profile in the measuring volume, if present, is perhaps the largest source of uncertainty in the measurement.

The above examination of the concept of the DCW system illustrates that a device can be built on this principle to facilitate a direct measurement of instantaneous wall velocity gradient with a close tolerance of a few percent.

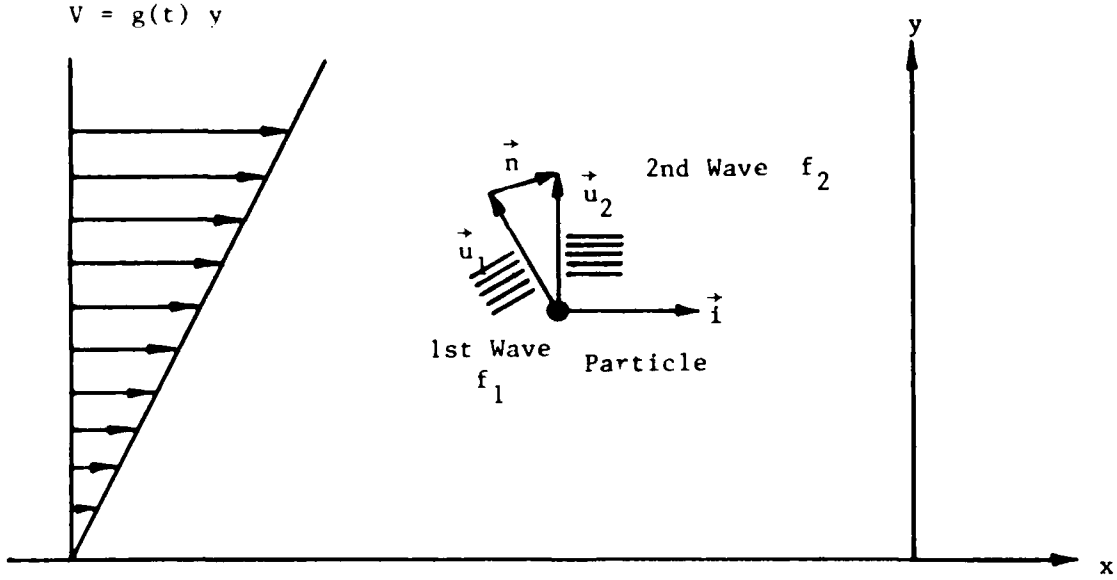

Fig. 2.1. Doppler frequency and linear region of velocity profile.

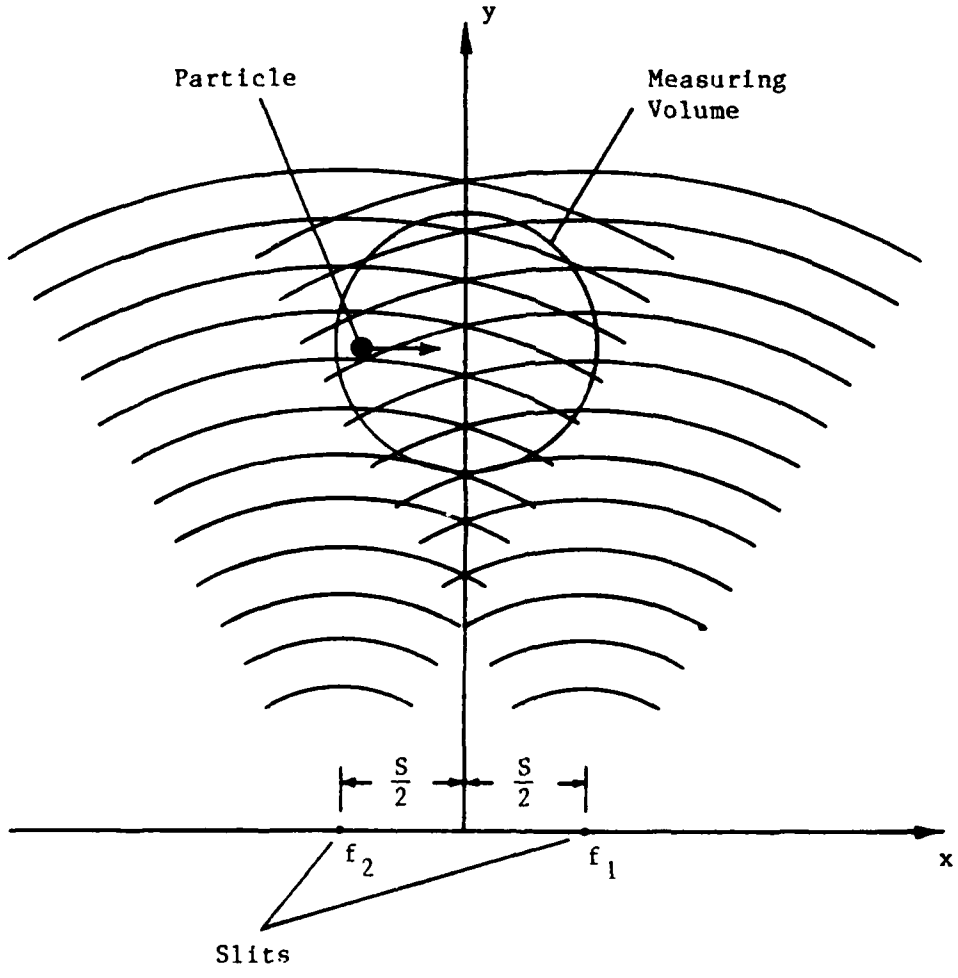

Fig. 2.2. Dual Cylindrical Wave system.

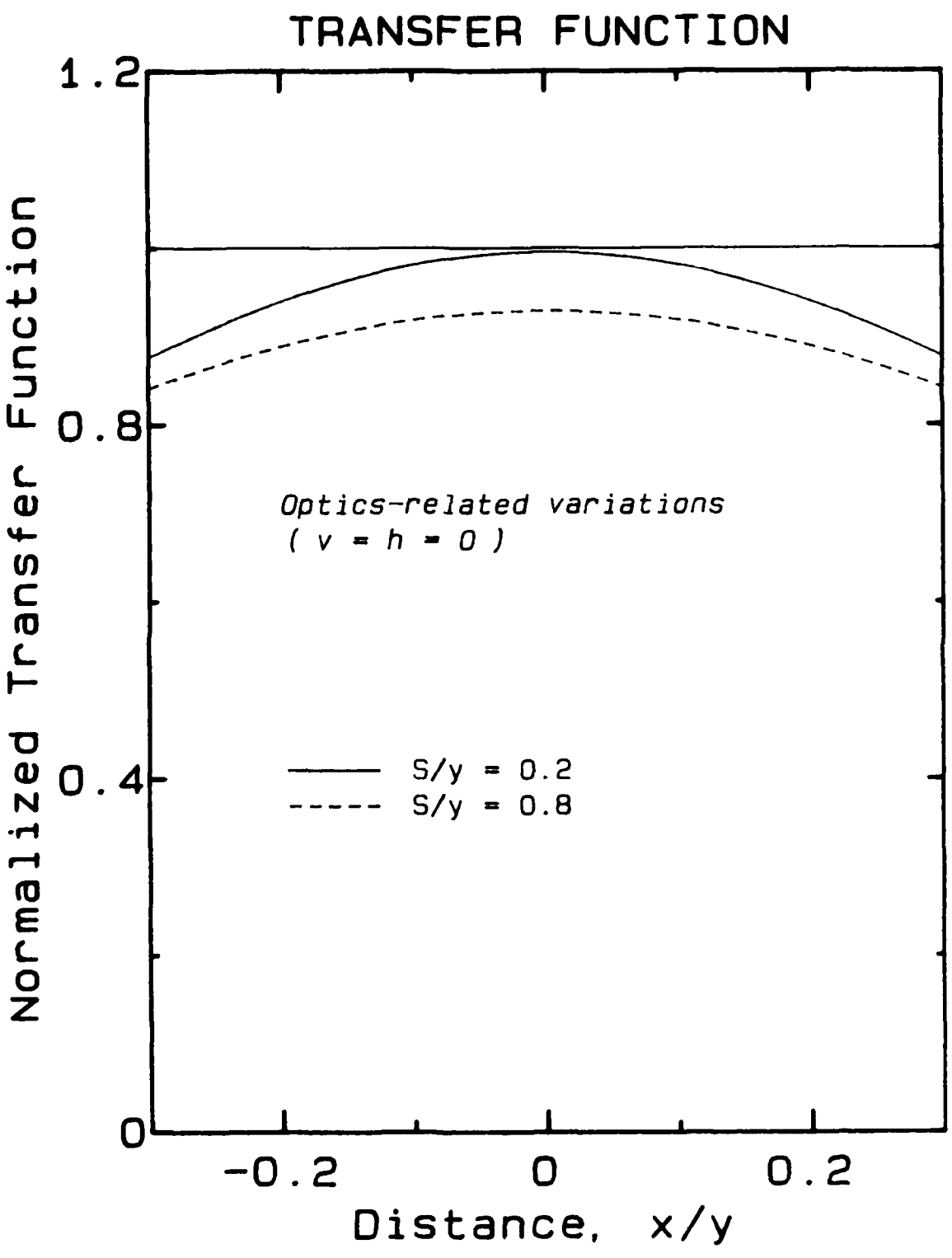

Fig. 2.3. Optics-related variations in the transfer function.

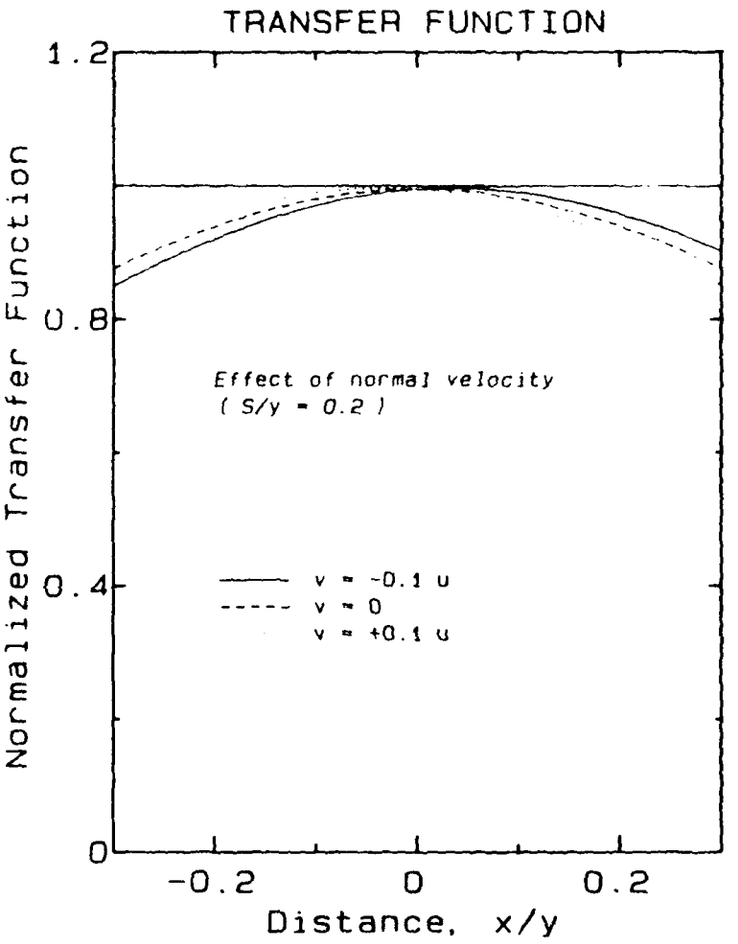

Fig. 2.4. Effect of normal velocity on the transfer function.

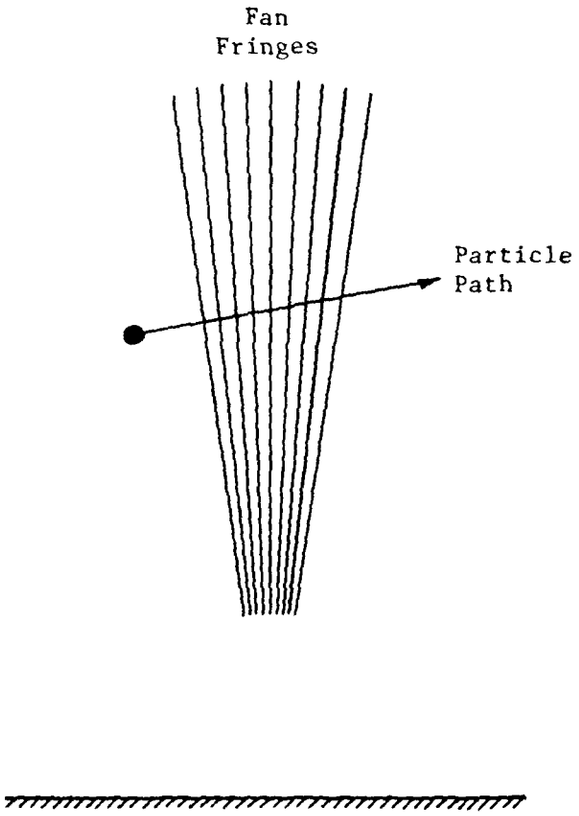

Fig. 2.5. Scattering particles with a normal velocity.

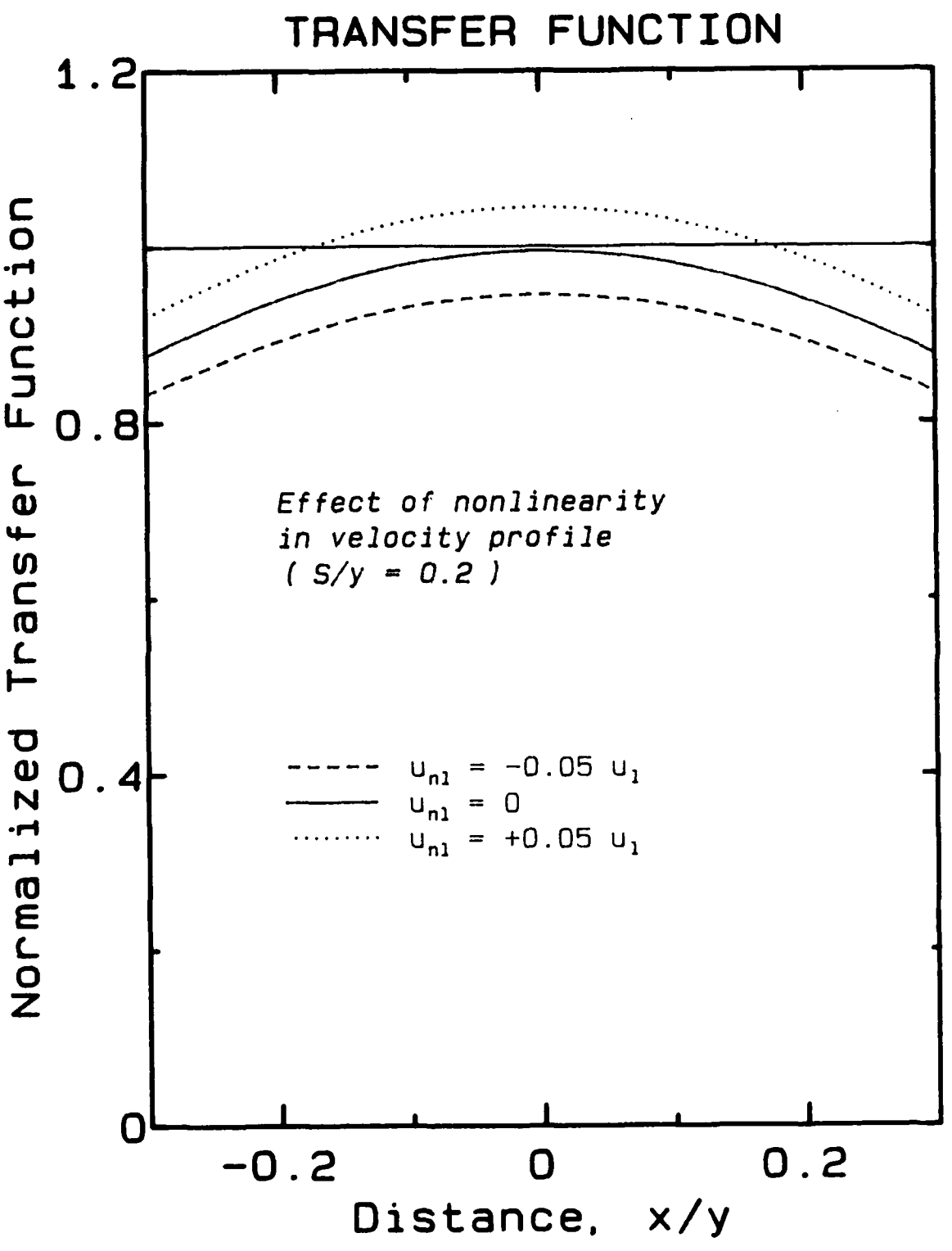

Fig. 2.6. Transfer function for a nonlinear velocity profile.

Chapter 3

THE DESIGN OF THE SLITS

3.1 Overview of Design Considerations

This chapter deals with the choice of the width and length of each slit and the spacing between them. The design in this respect must satisfy certain restrictions imposed by the characteristics of the flow and the properties of light diffracted from the slits. The constraints pertaining to the nature of the flow can be expressed in terms of a Reynolds number based on the upper bound of the measuring volume in y as the characteristic length. The limiting value of this parameter depends upon the friction coefficient, C_f, which has been taken as 0.004 for the present design. This value of C_f is large enough to yield a safe design for the turbulent boundary layer under consideration. Once the upper bound of the measuring volume has been established, it is possible to evaluate the limiting frequency of imposed fluctuations in the free-stream velocity, without exceeding a certain margin of error in the measurement. The limiting frequency is a function of the amplitude of the imposed fluctuating velocity. The lower bound of the measuring volume is calculated by taking 100 microns as the extent of the measuring volume in y, which is comparable with the measuring-volume size for a typical LDV system. Signal quality at the lower bound is used as a criterion for determining the slit spacing.

In order to localize the measurement, the length of the slits is confined to one-fifth of the spacing between spanwise streaks (see Sec. 1.2.1 for a description of streaks).

Other constraints on sizing of the slits pertain to the quality and strength of the signal. The results of this design exercise for the present system are summarized in Table 3.1, which contains the slit dimensions and restrictions on the frequency of imposed unsteadiness for the cases of high and low amplitude of the imposed free-stream fluctuation. In addition to the above, it contains the necessary information about the research facility and certain auxiliary data chosen to complete the input data set required for the design.

3.2 Slit Spacing

The choice of slit spacing influences several parameters. It may be demonstrated that, by increasing the slit spacing,

1. The region of interference between the cylindrical waves is reduced (see Fig. 3.1).
2. The fringe spacing becomes smaller (see Eqn. (1.2)), thus reducing signal visibility.
3. The number of fringes increases, improving the accuracy with which Doppler frequency can be determined.
4. There is a larger spacing between the laser sheets used to illuminate the slits; hence, less chance of cross-talk due to overlap between the two sheets.

It is obvious that the last two effects are favorable, whereas the first two are undesirable. The purpose of this section is to set a criterion for determining the best compromise between the positive and the adverse effects. Subsequently, this criterion is applied to the present system and the optimum slit spacing is evaluated.

3.2.1 Signal Visibility

The signal visibility is defined as the ratio of modulation to the peak value in a Doppler burst. Visibility is a complex function of many parameters including particle size, particle shape, refractive index, collection angle and location of the receiving optics. However, according to Adrian (1978) the first order effect in many situations can be described in terms of the fringe model. The particle size should be smaller than the fringe spacing for a reliably visible signal. The fringe spacing for double-slit geometry has been given in Chapter 1.

Though a high signal visibility does not necessarily imply a high signal-to-noise ratio, it is appropriate to maintain a high visibility for at least the smallest scattering particles. This may be achieved by using a fringe spacing at least k_1 times the particle diameter, then

$$d_f > k_1 d_p$$

Substituting the above in Eqn. (1.2),

$$y_{min} = \frac{k_1 d_p S}{\lambda} \tag{3.1}$$

y_{min} provides a lower bound for the location of the measuring volume.

3.2.2 Linear Region in a Flat Plate Boundary Layer

The thickness of the viscous sublayer can safely be taken to correspond to $y^+ = 5$, on the basis of data compiled by Coles (1957). Hence the value of y at $y^+ = 5$ determines the upper bound for the measuring volume, i.e,

$$\frac{y_{max} u_\tau}{\nu} < 5$$

Since

$$C_f = 2\left(\frac{u_\tau}{\bar{U}}\right)^2 ,$$

$$\frac{\bar{U} y_{max}}{\nu} < 5 \left(\frac{2}{C_f}\right)^{1/2} \tag{3.2}$$

The above equation shows a relationship between the nondimensionalized size of the measuring volume and the coefficient of skin friction.

3.2.3 A Criterion for Evaluating Slit Spacing

The optimum slit spacing is directly dependent upon the size of the measuring volume which must be restricted to the near-wall linear region of the velocity profile. This condition translates into a restriction on the relevant Reynolds number which has been expressed by Eqn. (3.2) and may be used to estimate y_{max}. If this value is exceedingly small (e.g., 20 microns or so), then the proposed method is not feasible.

The allowable value of y_{min} can be worked out as follows:

$$y_{min} = y_{max} - \Delta y \tag{3.3}$$

where Δy is the extent of the measuring volume normal to the wall.

Using the value of y_{min} from (3.3), the value of maximum allowable S can be determined from (3.1).

The smallest possible value of S is dictated by the smallest width of waist of a laser sheet which can be produced and by the need to avoid cross-talk between the separate beams illuminating separate slits. The following criterion is suggested:

$$S > 2W \tag{3.4}$$

where W is the $1/e^2$ width of the waist. A waist of 5 microns can be produced without requiring any extraordinary lens system design. Hence a slit spacing of 10 microns or larger is acceptable.

A variety of important flow models can be studied without violating the restrictions discussed above. For the present system, a mean free stream velocity of 0.73 m/s suggests a y_{max} of 150 microns based on $C_f = 0.004$. We allow 100 microns in y for the measuring volume. Using a particle diameter of 2 microns and $k_1 = 1$, the value of S is found to be 10 microns. This estimate is based on a laser wavelength of 0.3868 micron in water (0.5145 micron in air, i.e, argon-ion green line). Though the present design is based on a particle diameter of 2 microns, it would produce discernible signals for a range of particle diameters as shown in Chapter 4.

The measuring volume is 100 microns in its y-extent and is centered at a distance of 100 microns from the wall. The method for locating the measuring volume in close proximity to the design location is described in Chapter 6.

It is appropriate at this point to comment on the constancy of the transfer function produced by this design. The case of $S = 0.1$ discussed in Chapter 2 corresponds to $y = y_{min}$; the associated variations in B are illustrated in Fig. 2.2. For other locations in the measuring volume, the variation in B is smaller. Further discussion on this topic is postponed till the extreme values of x are deduced from a consideration of slit width.

3.3 Width of Slits

The light diffracted from a slit develops into a cylindrical wave after travelling a certain distance from the wall. This distance becomes smaller with decreasing slit width. Furthermore, thinner slits cause diffracted waves to spread out to larger angles from the normal to the slit. This produces a larger measuring volume and a larger number of cycles in the signal. A very thin slit, however, does not transmit a large amount of power; hence the signal is weak and the signal-to-noise ratio is smaller. A design criterion, taking into account these factors has been developed in the following sections.

3.3.1 Fresnel Approximation

Fresnel approximation of scalar diffraction (explained in App. A) is used for estimating the smallest desirable distance from the slits as well as the spreading angle of the diffracted wave. This approximation is valid if the diffracted light is concentrated in the vicinity of the normal to the aperture. Since the present system allows diffracted light to spread out to fairly large angles, some caution must be exercised in using this approximation. However, for the present system, a detailed solution of the problem (see Section 4.4) validates this approximation.

3.3.2 Far-field Condition

An expression for the distance over which light diffracted by a slit is well represented as a cylindrical wave is referred to as the "far-field condition" and is given in Optics texts (e.g. Goodman (1968)) as,

$$y \gg \frac{\pi a^2}{4\lambda} \tag{3.5}$$

This distance decreases with decreasing slit width, and should be made considerably smaller than y_{min}. This requirement can also be expressed as,

$$a \ll (4k_1 d_p S/\pi)^{1/2} \tag{3.6}$$

3.3.3 Number of Cycles in a Doppler Burst

The number of cycles in an unshifted Doppler burst ($f_1 = f_2$ in Eq. (2.1)) depends upon streamwise extent $2x_m$ of the measuring volume, which in turn depends on the width of the slits. The number of cycles in general is given by

$$N = f_d \left| \frac{2x_m}{u} \right| \tag{3.7}$$

In the case of zero frequency shift,

$$f_d = Bg$$

Hence,

$$N_o = 2B \frac{x_m}{y} = 2Bx_m \tag{3.8}$$

(using the normalization convention of Eqn. (2.11)), where

$$x_m = y \tan \alpha - \frac{S}{2} \tag{3.9}$$

as shown in Fig. 3.1. The half spreading angle, α, of each wave is given in standard texts on Physical Optics (e.g., Jenkins and White (1957)) as follows:

$$a \sin \alpha = \lambda \tag{3.10}$$

The limiting value of a required for producing at least N_o cycles can be derived from Eqns. (3.8), (3.9) and (3.10). Using $y = y_{min}$ from Eq. (3.1) and $B = S/\lambda$, one obtains the following expression.

$$a \leq \left[\lambda^2 + \left(\frac{2k_1 d_p S}{N_o k_1 d_p + S} \right)^2 \right]^{1/2} \tag{3.11}$$

The corresponding expression for the streamwise extent of the measuring volume is as follows:

$$x_m = \frac{\lambda}{\sqrt{a^2 - \lambda^2}} - S \tag{3.12}$$

The above equation is obtained from Eqns. (3.9) and (3.10) after normalizing according to (2.11).

Finally, it may be pointed out that the number of cycles in a shifted Doppler burst is a more complex function of several parameters, including the velocity gradient itself. However, if the range of g being measured is known, it is possible to maintain the number of cycles, N, above N_o. The corresponding conditions are derived in Sec. 3.4.

3.3.4 Power Transmission Through a Slit

Finally, it should be noted that a thinner slit would transmit a smaller fraction of the incident sheet of laser light and hence would require a larger laser power to produce a discernible signal. The ratio of incident to transmitted power on a slit can be expressed as:

$$\frac{P}{P_o} = \text{erf}\left(\frac{\sqrt{2}\,a}{W}\right) \tag{3.15}$$

This expression is based on the assumption that the power incident upon the exposed area of the slit is transmitted through it. This assumption is not valid for very narrow slits (see Keller, 1961). For the present system, the narrow slit effect is small and may be ignored.

3.3.5 A Criterion for Evaluating Slit Width

The requirement of having a certain number of cycles in a burst would usually be more critical than other conditions. It is recommended that this condition be used for the first estimate of a, which may be used to check if other conditions have been satisfied.

Using $N_o = 10$ and other variables as specified earlier, Eqn. (3.11) yields

$$a < 1.39 \text{ micron} \quad .$$

We use a = 1 micron, which transforms the far-field condition of Eqn. (3.5) into the following expression:

$$y \gg 2 \text{ microns.}$$

Since y varies from 50 microns to 150 microns in the measuring volume, this condition is satisfactorily observed.

For a laser-sheet of waist 5 microns, the current setup, according to Eqn. (3.15), allows 30% power transmission which is acceptable for a normal application using 1 Watt power. The details of transmission through the slits and the strength of the resulting signal are discussed in Chapters 4 and 5.

3.4 Restrictions on Downmixing

In the case of a shifted Doppler burst, the number of cycles depend not only upon the streamwise extent of the measuring volume but also upon the velocity gradient and the effective frequency shift at the processor input. As mentioned earlier, the shift frequency $(f_1 - f_2)$ is typically +40 MHz or -40 MHz. For the present applications, the Doppler shift (B g) is less than 100 kHz. Hence, frequencies of the optical signals lie in the range of 40 MHz ± 0.1 MHz. After the optical signal has been converted into an electrical signal, it is convenient to subtract a fixed frequency (e.g., 39.9 MHz) from the signal frequency. This process is called "downmixing" and the amount of the frequency deducted is referred to as "downmix frequency". After downmixing, the effective shift frequency may be expressed as follows:

$$\Delta f_{down} = f_1 - f_2 - f_{dm} \quad , \quad \text{for} \quad f_1 > f_2$$

Or

$$\Delta f_{down} = f_2 - f_1 - f_{dm} \quad , \quad \text{for} \quad f_1 < f_2 \qquad (3.16)$$

Similarly, if f_{dm} is larger than 40 MHz, the effective upshifting may be expressed as below:

$$\Delta f_{up} = f_{dm} - (f_1 - f_2) \quad , \quad \text{for} \quad f_1 > f_2$$

$$\Delta f_{up} = f_{dm} - (f_2 - f_1) \quad , \quad \text{for} \quad f_1 < f_2 \qquad (3.17)$$

Since the effective frequency shift is only of the order of the Doppler shift, the signal processor need not be responsive to very high frequencies.

Six different cases of measurements with frequency shifting may be identified. The classification is based on whether,

- The laser frequency at the downstream slit is higher than that at the upstream slit ($f_1 > f_2$) or vice versa;
- The effective shift is positive or negative (i.e., the signal frequency increases or decreases with increasing g);
- Flow reversal takes place, i.e., $g_{min} < 0$ (notice that the positive flow direction is so chosen that g_{max} is always positive).

For each of these cases, Table 3.2 gives the condition for obtaining at least as many cycles in the shifted burst as in the unshifted one. The derivation of these conditions may be illustrated by considering the first two cases in detail. If the downstream slit is illuminated with the higher frequency, then according to Eqs. (2.1) and (2.7), the signal frequency at the photomultiplier is given by

$$f_1 - f_2 + Bg$$

For positive shift, using Eq. (3.16), the detected frequency is expressed as,

$$f_d = \Delta f_{down} + Bg \tag{3.18}$$

In order to obtain unambiguous signals, the following condition must be satisfied:

$$\Delta f_{down} \geq - Bg_{min}$$

In practice, a more restrictive condition is imposed on Δf_{down}, so that very low frequency signals are prevented. The condition for $N > N_o$ may be deduced from the following expressions for the number of cycles in a burst:

$$\begin{aligned} N &= \frac{f_d}{Bg} N_o \quad , \quad \text{for } g > 0 \\ N &= -\frac{f_d}{Bg} N_o \quad , \quad \text{for } g < 0 \end{aligned} \tag{3.19}$$

The above expressions may be derived from Eqs. (3.7) and (3.8). For the case under consideration, if there is no flow reversal, then

$$N = \left(\frac{\Delta f_{down}}{Bg} + 1 \right) N_o \qquad (3.20)$$

Hence the condition

$$\Delta f_{down} > 0$$

would ensure that $N > N_o$. However, if flow reversal occurs, then for the negative values of g,

$$N = \left(\frac{\Delta f_{down}}{-Bg} - 1 \right) N_o \qquad (3.21)$$

Eqs. (3.20) and (3.21) imply that N would be larger than N_o for all the values of g, if the following condition is satisfied:

$$\Delta f_{down} > -2Bg_{min} \quad .$$

The other cases in Table 3.2 may be analyzed in a similar manner.

3.5 Restrictions on Imposed Unsteadiness

There are not many data available on turbulent boundary layers with imposed unsteadiness. However, a study by Jayaraman et al. (1982) elucidates important aspects of such flows. It has been found convenient to decompose the flow variables into three components; namely, a time-averaged component, a periodic component due to imposed unsteadiness and a turbulent fluctuation. Hence streamwise velocity can be represented as follows:

$$u(x,y,z,t) = \overline{u}(x,y,z) + \tilde{u}(x,y,z,t) + u'(x,y,z,t) \qquad (3.22)$$

Averaging of u for a fixed phase, over a number of ensembles, yields $\overline{u} + \tilde{u}$, whereas $\overline{u}$ can be separated by time-averaging the data.

The continuity and momentum equations for the individual components can be isolated from Navier-Stokes equations by averaging in the above-mentioned manner. The governing equations for the periodic components

of velocity are complex and generally coupled with the velocity of mean flow field as well as the turbulent field. However, an analytical solution is possible under the boundary layer approximation for the case of a large Strouhal number, i.e.,

$$\frac{\omega L}{U} \gg 1$$

where ω is the frequency of imposed unsteadiness in radians/sec and L is a typical length scale along the mean flow. The governing equation for this case is as follows,

$$\frac{\partial \tilde{u}}{\partial t} = -\frac{1}{\rho}\frac{\partial \tilde{p}}{\partial x} + \nu \frac{\partial^2 \tilde{u}}{\partial y^2}$$

In the free-stream, $\tilde{u}$ ceases to change with respect to y. Hence,

$$-\frac{1}{\rho}\frac{\partial \tilde{p}}{\partial x} = \frac{\partial \tilde{U}}{\partial t}$$

This simplifies the governing equation to the standard Stokes equation:

$$\frac{\partial(\tilde{u} - \tilde{U})}{\partial t} = \nu \frac{\partial^2(\tilde{u} - \tilde{U})}{\partial y^2} \tag{3.23}$$

The boundary conditions are as follows:

$$\tilde{u} - \tilde{U} = 0 \quad , \quad y \to \infty \quad ,$$

$$\tilde{u} - \tilde{U} = -\tilde{U} \quad , \quad y = 0 \quad .$$

For a sinusoidal imposed unsteadiness,

$$\tilde{U} = a_o \bar{U} \cos \omega t \quad .$$

The solution to this problem is available in classical literature on heat conduction or fluid mechanics. It can be expressed as follows:

$$\tilde{u} - \tilde{U} = -a_o \bar{U} \exp(-y_s) \cos(\omega t - y_s) \tag{3.24}$$

where,

$$y_s = \sqrt{\frac{\omega}{2\nu}}\, y \tag{3.25}$$

A linear approximation to this profile would be given as,

$$\frac{\tilde{u}}{a_o \bar{U}} = \frac{y}{a_o \bar{U}} \left.\frac{\partial \tilde{u}}{\partial y}\right)_{y=o} = y_s[\cos(\omega t) + \sin(\omega t)]$$
$$= \sqrt{2} y_s \cos(\omega t - \pi/4) \tag{3.26}$$

An expression for deviation from linearity follows from (3.24) and (3.26):

$$\Delta\tilde{u} = a_o \bar{U} \{[1 - y_s - \exp(-y_s) \cos(y_s)] \cos(\omega t)$$
$$+ [\exp(-y_s) \sin(y_s) - y_s] \sin(\omega t)\} \tag{3.27}$$

This parameter may be compared with the total velocity in order to estimate the linearity of the instantaneous velocity profile. Various components of the instantaneous velocity are estimated below.

Mean velocity may be expressed as

$$\bar{u} = \frac{C_f \bar{U}^2}{\sqrt{2\omega\nu}} y_s \tag{3.28}$$

This expression has been deduced from the relation, $u^+ = y^+$, which is valid inside the measuring volume and is believed to be unaltered by the imposed unsteadiness. The above form is obtained by using definitions of y^+ and C_f along with Eqn. (3.25).

The deviation from linearity would be maximum for the largest negative value of u', which may be expressed as a fraction of mean velocity.

$$u' = -k_2 \bar{u}$$
$$= -\frac{k_2 C_f \bar{U}^2}{\sqrt{2\omega\nu}} y_s \tag{3.29}$$

An estimate of k_2 is given later.

The following expression for instantaneous velocity is obtained by substituting (3.26), (3.28) and (3.29) into (3.22).

$$u = \left[\frac{(1-k_2)\, C_f \bar{U}^2}{\sqrt{2\omega\nu}} + \sqrt{2}\, a_o \bar{U} \cos\left(\omega t - \frac{\pi}{4}\right) \right] y_s \qquad (3.30)$$

The deviation from linearity can be expressed as the ratio of (3.27) to (3.30).

$$\frac{\tilde{\Delta u}}{u} = \frac{A_o\{[1-y_s-\exp(-y_s)\cos(y_s)]\cos\omega t + [\exp(-y_s)\sin(y_s) - y_s]\sin\omega t\}}{[1 + \sqrt{2}\, A_o \cos(\omega t - \pi/4)]\, y_s}$$

where normalized amplitude

$$A_o = \frac{\sqrt{2\omega\nu}\, a_o}{(1-k_2)\, C_f \bar{U}} \qquad (3.31)$$

In the near-wall region of interest, Eqn. (3.31) shows a monotonic increase in deviation from linearity with distance y. It also goes through cyclic changes in time as shown in Fig. 3.2. Peak values occur at certain phase angles. The positive peak is somewhat larger in magnitude than the negative one. The phase angle for these peaks can be deduced from the following expressions:

$$\cos(\omega t+\gamma) = \frac{A_o\{1 - \exp(-y_s)[\cos(y_s) + \sin(y_s)]\}}{\{[1-y_s-\exp(-y_s)\cos(y_s)]^2 + [\exp(-y_s)\sin(y_s) - y_s]^2\}^{1/2}} \qquad (3.32)$$

where

$$\sin\gamma \sim [1-y_s - \exp(-y_s)\cos(y_s)]$$

$$\cos\gamma \sim [\exp(-y_s)\sin(y_s) - y_s]$$

The peak error in the measurement would occur at the upper bound of the measuring volume at a phase angle defined by (3.32), provided the peak negative value of turbulent fluctuation coincides with this phase angle. By confining this error to a certain value the allowable amplitude for a given frequency of imposed oscillations can be computed from (3.31) in conjuntion with (3.32) and (3.25).

This computation requires the following inputs:

1) Flow parameters; namely, skin friction, kinematic viscosity and mean free-stream velocity.

2) Upper bound of the measuring volume, y_{max}, as evaluated from a consideration of steady turbulent boundary layer.

3) The ratio of peak negative turbulent velocity to the mean velocity, k_2.

4) Allowable peak error in the signal.

The following remarks are relevant to the value of the peak error in the signal:

1) It would occur only in the case of very high Strouhal numbers approaching Stokes' idealization. In an actual unsteady layer the error would be smaller because effects of imposed unsteadiness, as shown by Jayaraman et al. (1982), tend to be confined to higher values of y than allowed by Stokes solution.

2) It would be experienced only at the upper bound of the measuring volume. Signals from the other parts of the measuring volume would have less error.

3) It would be encountered at a particular phase angle; at other phase angles the error would be smaller.

4) It would occur only if the peak negative turbulent velocity would coincide with the phase angle of maximum error. The probability of such a coincidence is fairly low, hence most of the signals would involve smaller error.

Considering the fact that the specified peak error has a low probability of occurence, it is recommended that a value of 5 to 10% for this parameter would be adequately small to ensure overall accuracy of meaurement.

Figure 3.3 contains results of computation of allowable amplitude for a range of frequencies from 0.1 to 2 Hz. Calculations are done for a distance of 150 microns from the wall and flow parameters of the present system listed in Table 3.1. The value of k_2 (0.5) is based on

the data discussed in Section 2.4. The results for peak errors of 5% and 10% are shown in the figure. Over the range of frequencies considered, the allowable amplitude varies from a large fraction to a few percent of the mean velocity.

Experiments with unsteady flow have been conducted in the present facility for a high amplitude of 33 % and a low amplitude of 5%. Frequencies up to 2 Hz were covered for simple velocity measurements. According to Fig. 3.3, shear stress can be measured accurately for frequencies up to 0.2 Hz for high amplitude and up to 2 Hz for low amplitude.

3.6 The Behavior of the Transfer Function

Nominal value of the transfer function (i.e, S/λ) for the current system is 25.85, implying that signal frequency in Hz would be 25.85 times the velocity gradient in s^{-1}. For a typical velocity gradient of 1000 s^{-1}, the signal frequency would be 25.85 kHz, which is an acceptable value for common LDV signal processing hardware.

In Chapter 2, four parameters influencing invariance of the transfer function were identified. Two of these parameters ($u_{n\ell}$ and v) are fluid-related and have been discussed in detail in the previous chapter. The optics-related parameters (S and x) can now be specified quatitatively. S (i.e, $S/2y$) varies from 0.033 to 0.1 in the measuring volume. We may examine the case of $S = 0.05$ and 0.1, which correspond to the center and the lower bound of the measuring volume respectively. The extreme value of x as given by Eqn. (3.12) for these two cases would be 0.37 and 0.32 in the afore-mentioned order. The corresponding number of cycles, N_o are 17 and 19. Since the cycles near the edges of the burst are weak and probably misrepresented as a result of a relatively high noise, it is appropriate to choose a smaller number of cycles from the middle of the burst for signal detection. If eight cycles are used for registering the signal, the corresponding x would vary from -0.15 to +0.15. In the absence of fluid-related sources of uncertainty, the maximum deviation in the transfer function as found from Eqn. (2.12) is 3.4% at the center of the measuring volume and 3.7% at the lower bound in y_{min}. The curve for S

= 0.1 in Fig. 2.2, over the range of $x = -0.15$ to $+0.15$, represents the behavior of transfer function at $y = y_{min}$. Appendix C deals with evaluation of a correction factor for the transfer function which takes into account the above mentioned variations. Uncertainty in measurement after applying this factor has also been estimated.

3.7 Length of Slits

Longer slits are favorable for ensuring cylindrical shape of light waves and obtaining a large signal rate by creating a large measuring volume. However, there is a limit to the length of the slits, imposed by three dimensionality of the structure of turbulent boundary layer. Spanwise streaks are known to be present in turbulent boundary layer. Kline et al. (1967) have reported a spacing of $100\ \nu/u_\tau$ between the streaks for a flat plate turbulent boundary layer. A recent work by Blackwelder and Eckelmann (1979) also suggests the existence of spanwise structures of spacing $100\ \nu/u_\tau$ in a turbulent boundary layer; the space between two streaks being occupied by a pair of counter-rotating vortices. We propose that the slit length be kept smaller than $20\ \nu/u_\tau$, in order to resolve the streaks. This leads to the following expression for length of the slits:

$$\frac{\bar{U}\ell}{\nu} < 20\sqrt{\frac{2}{C_f}} \qquad (3.33)$$

The current setup uses a slit length of 400 μm, which corresponds to $z^+ = 13$ for the proposed values of $\bar{U}$, ν, and C_f. The slit length for the present system is significantly smaller than the length of the laser sheet (~ 1.4 mm) to be focused on it. Hence, the entire length of the slit is fully illuminated. Some distortion of the diffracted wave occurs near the ends of the finite slits. However, this does not have a significant influence on the measurement, as shown in Chapter 4.

3.8 Fabrication of Slits

The physical dimensions of the slits and the measuring volume are shown in Fig. 3.4. The slits are too narrow to be produced conveniently with a photographic method. Electron-beam technology has been used to etch the slits on a chromium coating of 0.1 micron on optically flat glass. The chromium coating is deposited with 0.1 micron thick layer of quartz (SiO) to protect the slits. The glass plate in the present arrangement is cut into a circular disc of diameter 19 mm. The glass disc is cemented to a lucite plug which fits into a port in the wall such that the etched surface faces the fluid and is flush with the wall within ± 13 microns. This arrangement is shown in Fig. 3.5. The plug provides for mounting a focusing lens close to the glass disc, the datails of which are discussed in Chapter 5.

Table 3.1

Summary of Slit Design

Available Data	
Mean Free-Stream Velocity, $\bar{U}$	0.73 m/s
Maximum Friction Coefficient, C_f	0.004
Amplitude of Imposed Unsteadiness:	
High Amplitude, a_o	0.33
Low Amplitude, a_o	0.05
Kinematic Viscosity (water), ν	1.1×10^{-6} m^2/s
Wavelength of Laser in Fluid, λ	0.3868 micron (0.5145 μm in air)
Auxiliary Data	
Number of Cycles in a Doppler Burst, N_o	~ 10
Ratio of Minimum Fringe Spacing to Particle Diameter, k_1	1.0
Ratio of Peak Negative Turbulent Velocity to Mean Velocity, k_2	0.5
Extent of Measuring Volume in y, Δy	100 microns
Acceptable Peak Error in Unsteady Measurement	5-10%
Design Specifications	
Slit Spacing, S	10 microns
Slit Width, a	1 micron
Slit Length, ℓ	400 microns
Location of Measuring Volume Center in y	100 microns
Allowable Frequency of Imposed Unsteadiness:	
High Amplitude	0.2 Hz
Low Amplitude	2.0 Hz

Table 3.2

Downmixer Setting for $N > N_o$

Frequency at the Downstream Slit	Type of Shift	Flow Reversal	Downmixer Setting
High	Positive	No	$\Delta f_{down} > 0$
High	Positive	Yes	$\Delta f_{down} > -2Bg_{min}$
High	Negative	N.A.	$\Delta f_{up} > 2Bg_{max}$
Low	Negative	N.A.	$\Delta f_{down} > 2Bg_{max}$
Low	Positive	No	$\Delta f_{up} > 0$
Low	Positive	Yes	$\Delta f_{up} > -2Bg_{min}$

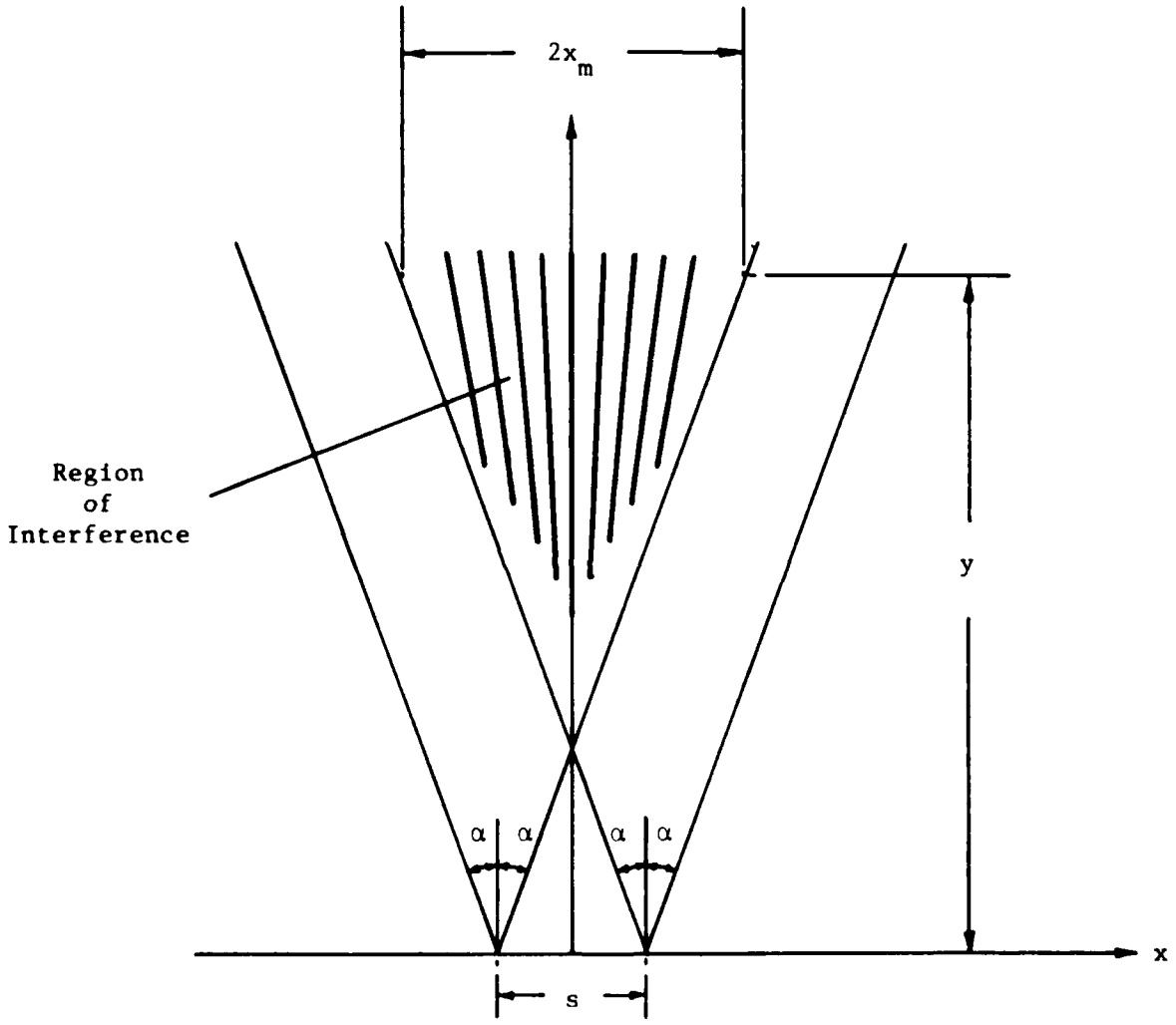

Fig. 3.1. Streamwise extent of the measuring volume.

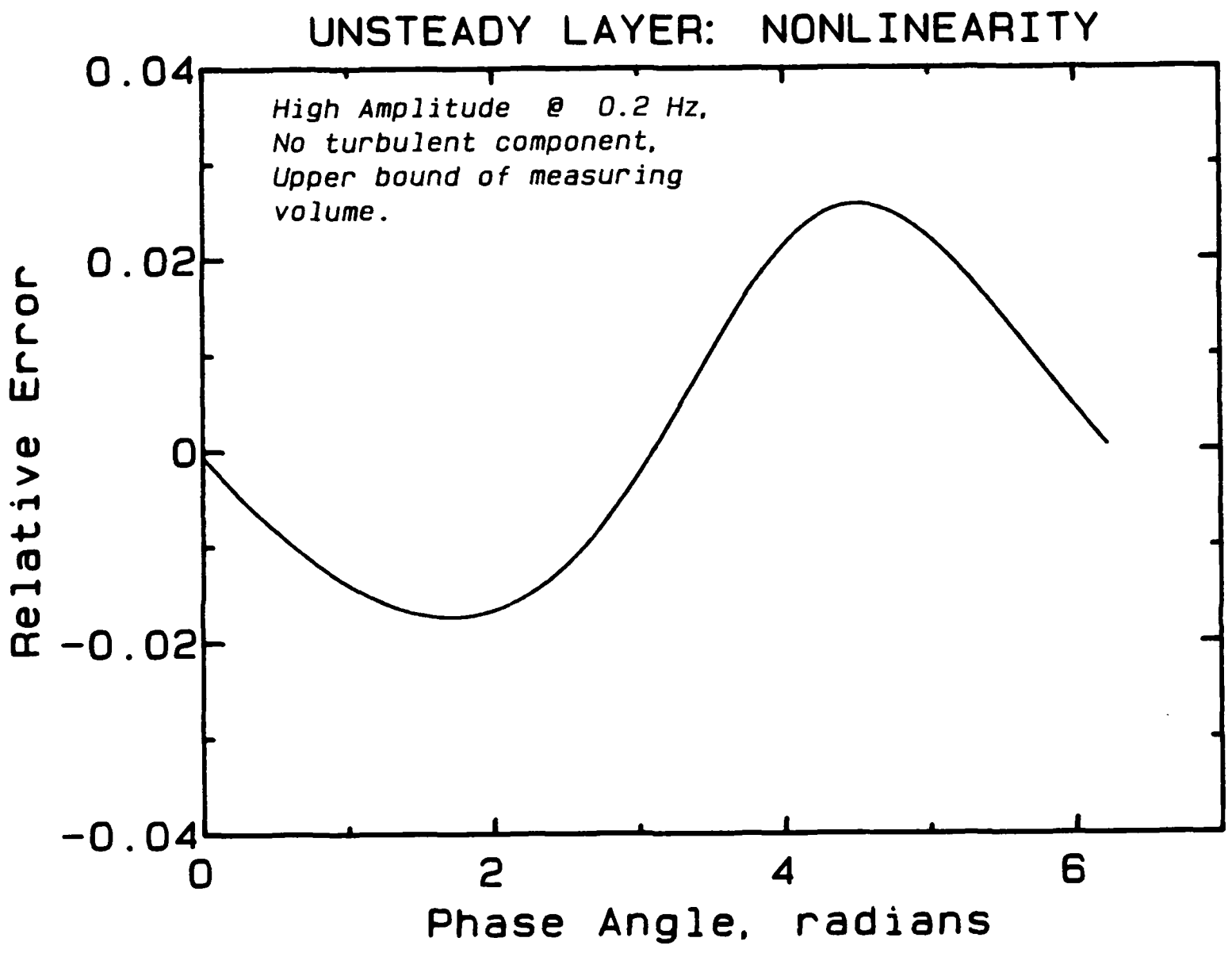

Fig. 3.2. Deviation from linear velocity profile, caused by imposed unsteadiness.

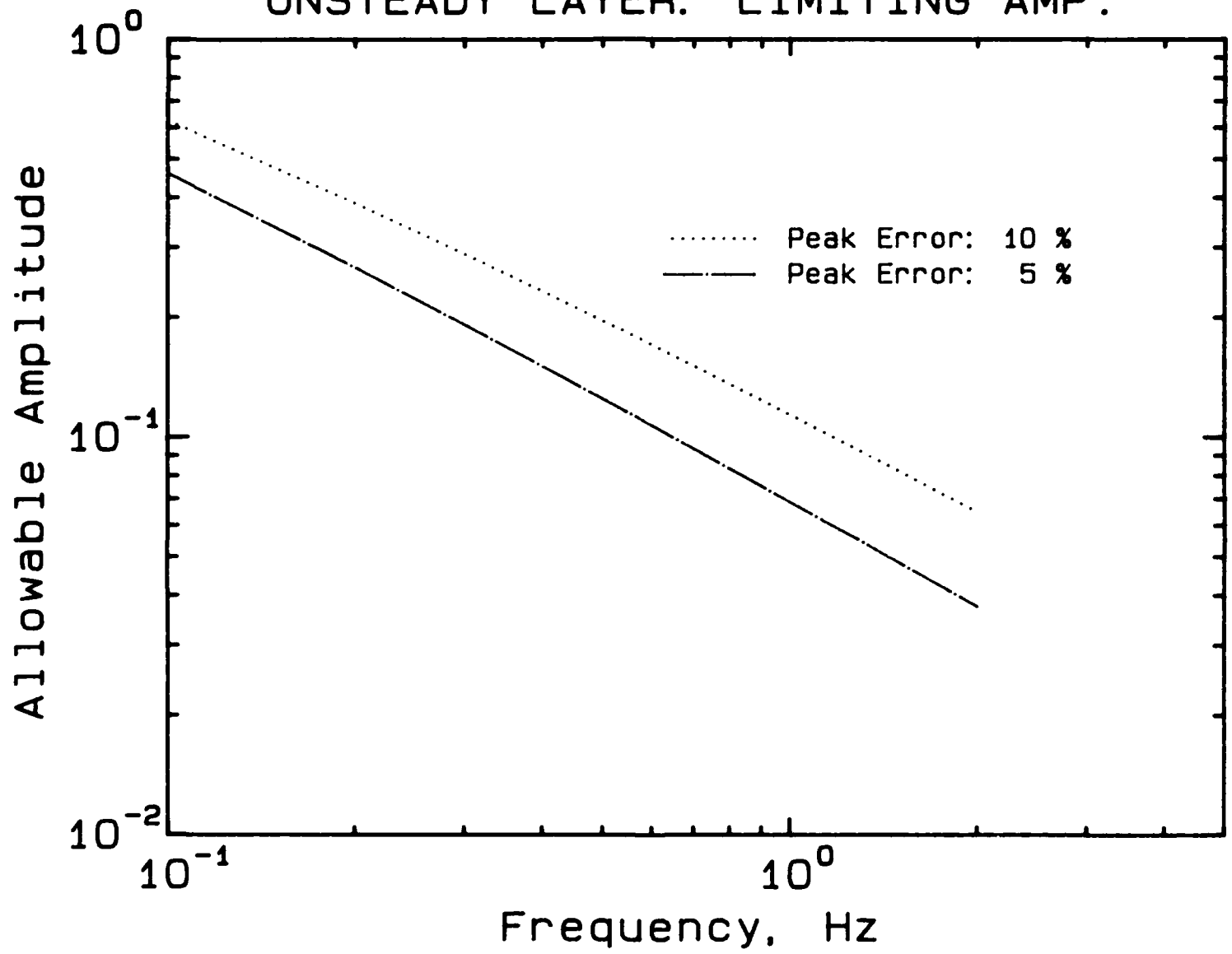

Fig. 3.3. Limiting amplitude of imposed unsteadiness for effective application of the instrument vs. frequency of oscillation.

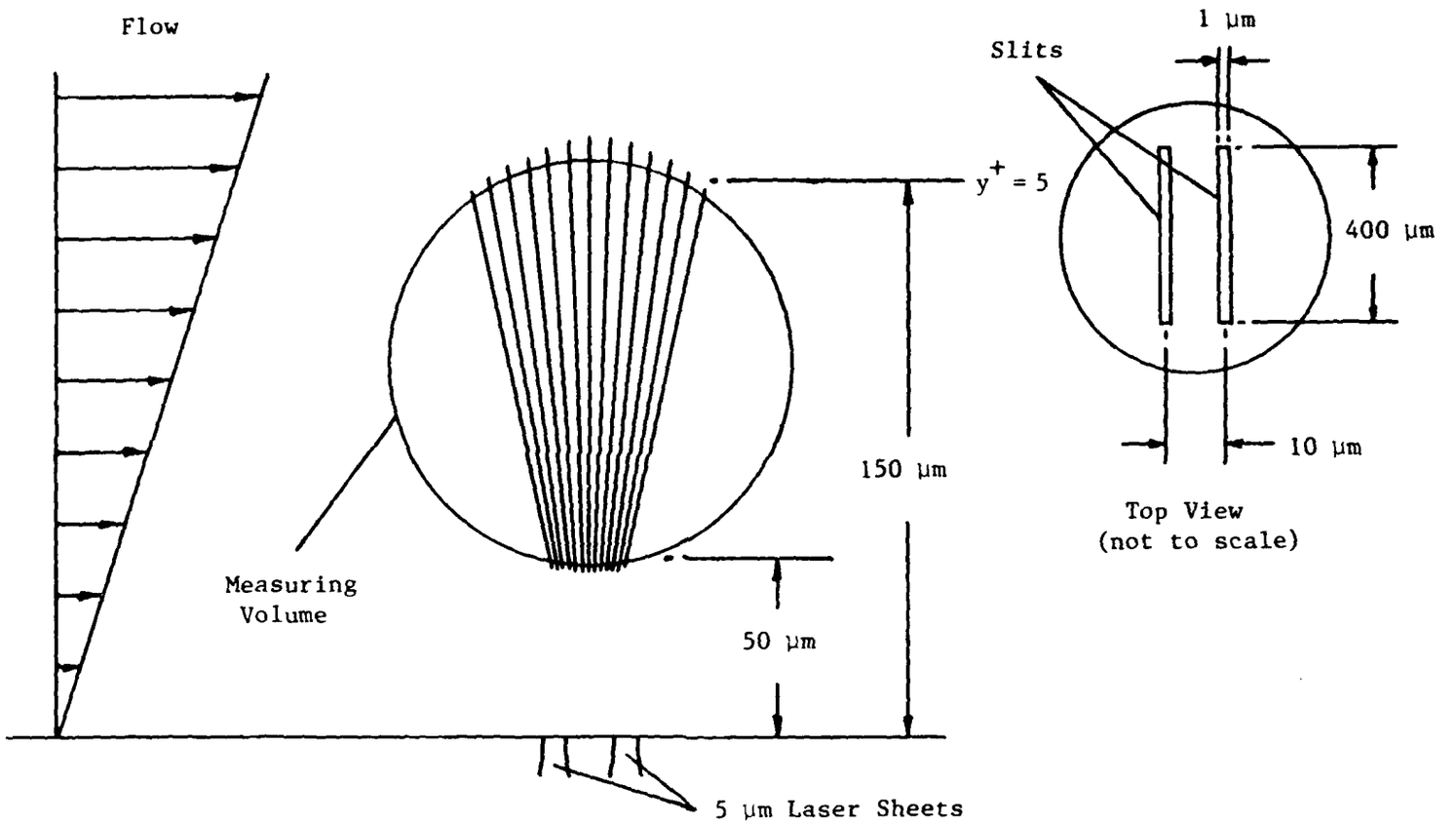

Fig. 3.4. Physical dimensions of the measuring volume and the slits.

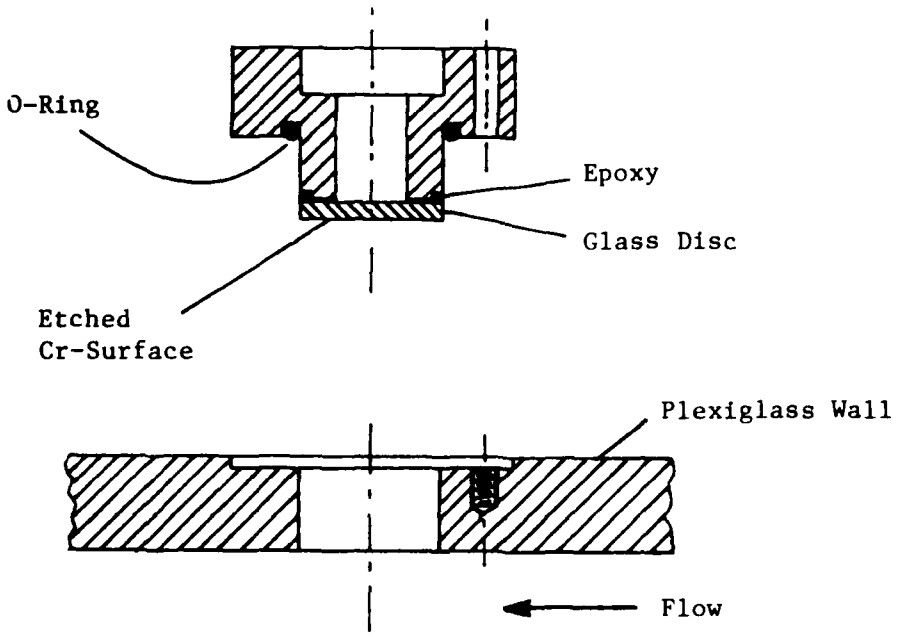

Scale: Full

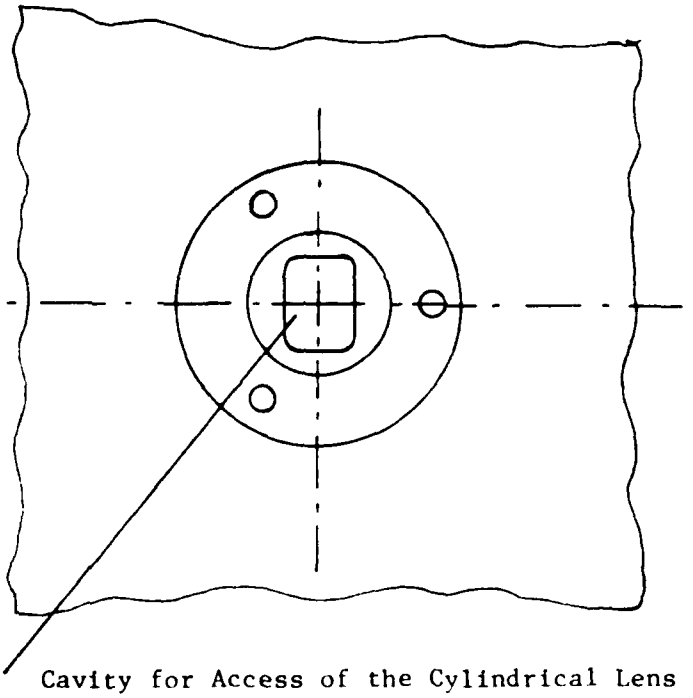

Fig. 3.5. Plug-port arrangement for mounting slits in the wall.

Chapter 4

SIGNAL SIMULATION

4.1 Overview of the Analysis

This chapter presents a detailed mathematical model of the laser light diffracted from the slits. This model extends the cylindrical wave formulation discussed in the previous chapters. The present model provides estimates of all the important properties of diffracted light prior to scattering by the particles. A knowledge of these properties is essential for computing the intensity and other significant characteristics of the scattered light using Mie scattering theory. Such mathematical representation enables us to simulate the signal at the output of the photomultiplier tube. Signal simulation is accomplished through the following steps:

i. Specification of particle location as a function of time;

ii. Calculation of the properties of diffracted light at the particle location;

iii. Computation of scattered light properties at the receiving aperture using local properties of diffracted light as those of plane waves incident on the particle in a Mie formulation;

iv. Evaluation of signal current and noise current generated by the photomultiplier tube.

Signal simulation has been found useful in optimizing the location of the receiving optics and selecting appropriate seed particles. Signal-to-noise ratio has been used as the criterion for such judgments.

Displacement of fringes (a phenomenon introduced in Section A.8.2 of Appendix A) due to finite particle diameter has also been estimated. Displacements up to 1% are noticed in the current simulations.

The diffracted waves are found to be two-dimensional and cylindrical over most of the slit length. Three-dimensional effects near the edges are weak and confined to very small regions; hence the probability of signal distortion due to this effect is very low.

4.2 Diffracted Field of a Finite Slit

In Section A.7.5 of Appendix A, a set of integral equations has been proposed for evaluating the diffracted field generated by an aperture of arbitrary shape. These equations may be applied to a finite slit by specifying the appropriate limits of integration. An expression for field distribution in the plane of the slits is also needed for a numerical evaluation.

4.2.1 Limits of Integration and the Incident Field

As shown in Fig. 4.1, the limits of integration are $-\hat{a}$ to $+\hat{a}$ for $\hat{x}$ and $-\hat{\ell}$ to $+\hat{\ell}$ for $\hat{z}$. The coordinates have been normalized by multiplying distance with the wave number in order to be compatible with the convention of Section A.7.5. In the normalized coordinates, $\hat{a}$ is the half-width and $\hat{\ell}$ is the half-length of the slit.

The illuminating laser sheet has an elliptic cross-section and exhibits the strongest field in the center. The field follows a Gaussian profile and diminishes to $1/e$ times the center value on an ellipse with axes $\hat{W}$ and $\hat{L}$; intensity of light drops to $1/e^2$ of the peak value on this ellipse. The field strength as a ratio of the center-value is given by the following expression:

$$\exp\left\{-\left[\left(\frac{\hat{x}}{\hat{W}}\right)^2+\left(\frac{\hat{z}}{\hat{L}}\right)^2\right]\right\}$$

In the normalized coordinates, $\hat{W}$ and $\hat{L}$ represent half-width and half-length of the laser sheet, respectively.

4.2.2 Simplifications for a Long Slit

The equation of the diffracted field for a finite slit illuminated by a Gaussian laser sheet can now be expressed as follows:

$$e=\frac{\hat{y}_o}{2\pi i}\int_{-\hat{a}}^{\hat{a}}\exp\left[-\left(\frac{\hat{x}}{\hat{W}}\right)^2\right]\int_{-\hat{\ell}}^{\hat{\ell}}\exp\left[-\left(\frac{\hat{z}}{\hat{L}}\right)^2\right]\frac{\exp\left(i\sqrt{\hat{y}_o^2+(\hat{x}_o-\hat{x})^2+(\hat{z}_c-\hat{z})^2}\right)}{\hat{y}_o^2+(\hat{x}_o-\hat{x})^2+(\hat{z}_o-\hat{z})^2}\,d\hat{z}\,d\hat{x} \qquad (4.1)$$

In the above equation, the diffracted field has been normalized by the field strength at the slit-center.

Direct computation of integrals in Eqn. (4.1) is very time-consuming. It is worthwhile to seek an approximate expression for the inner integral using the method of stationary phase (see Nayfeh (1973) for a detailed discussion of this topic). In order to accomplish such a simplification, the inner integral may be written in the following form.

$$\frac{\exp\left[-\left(\frac{\hat{z}_o}{\hat{L}}\right)^2\right]}{\hat{r}_o} \int_{q_1}^{q_2} \frac{\exp\left\{-\left[2\left(\frac{\hat{z}_o}{\hat{L}}\right)\left(\frac{\hat{r}_o}{\hat{L}}\right) q + \left(\frac{\hat{r}_o}{\hat{L}}\right)^2 q^2\right]\right\}}{1 + q^2}$$

$$\times \exp\left[i\hat{r}_o\sqrt{1 + q^2}\right] dq \qquad (4.2)$$

where

$$q = \frac{\hat{z} - \hat{z}_o}{\hat{r}_o} \; ; \quad q_1 = \frac{-\hat{\ell} - \hat{z}_o}{\hat{r}_o} \; ; \quad q_2 = \frac{\hat{\ell} - \hat{z}_o}{\hat{r}_o}$$

and

$$\hat{r}_o = \sqrt{\hat{y}_o^2 + (\hat{x}_o - \hat{x})^2} \; .$$

The phase function, $\hat{r}_o\sqrt{1 + q^2}$ goes through large changes with variations in q, causing rapid oscillations in the integrand. Over most of the range of integration, such oscillations result in approximately equal contributions to the integral from the positive and the negative parts of the integrand. The non-zero contribution to the integral comes from the vicinity of $q = 0$, where the derivative of the phase function with respect to q is zero and hence it varies slowly. Since the non-zero contribution to the integral corresponds to small values of q, it is appropriate to expand the amplitude and the phase functions into respective Taylor series in q and retain only the first few terms. Keeping the first power of q in amplitude and the second power in phase, expression (4.2) transforms to the following form:

$$\frac{\exp\left[-\left(\frac{\hat{z}_o}{\hat{L}}\right)^2\right]\exp(i\hat{r}_o)}{\hat{r}_o}\int_o^{\frac{\hat{\ell}-\hat{z}_o}{\hat{r}_o}} - \int_o^{\frac{-\hat{\ell}-\hat{z}_o}{\hat{r}_o}}\left[1 - 2\left(\frac{\hat{z}_o}{\hat{L}}\right)\left(\frac{\hat{r}_o}{\hat{L}}\right)q\right]\exp\left(\frac{i\hat{r}_o q^2}{2}\right)dq$$

This expression can be written in terms of complex Fresnel integrals as follows:

$$\frac{\sqrt{\pi}\,\exp\left[-\left(\frac{\hat{z}_o}{\hat{L}}\right)^2\right]\exp(i\hat{r}_o)}{\hat{r}_o^{3/2}}\left\{F\left(\frac{\hat{\ell}-\hat{z}_o}{\sqrt{\pi\hat{r}_o}}\right) + F\left(\frac{\hat{\ell}+\hat{z}_o}{\sqrt{\pi\hat{r}_o}}\right)\right.$$

$$\left. + i\,\frac{2\hat{z}_o}{\hat{L}^2}\sqrt{\frac{\hat{r}_o}{\pi}}\left[\exp\left(i\,\frac{(\hat{\ell}-\hat{z}_o)^2}{2\hat{r}_o}\right) - \exp\left(i\,\frac{(\hat{\ell}+\hat{z}_o)^2}{2\hat{r}_o}\right)\right]\right\} \qquad (4.3)$$

where the Fresnel integral $F(z)$ is defined as below.

$$F(z) = \int_o^z \exp\left(i\,\frac{\pi}{2}\,t^2\right)dt$$

Elementary properties of Fresnel integrals relevant to the present application are available in a handbook by Abramowitz and Stegun (1970). The Fresnel integrals may be computed efficiently using appropriate series expansions. Hershey (1962) has proposed one such algorithm.

4.2.3 Simplification for Slow Variation in Illuminating Intensity

The last two terms in the parentheses in (4.3) represent the effect of variation in intensity of the illuminating laser sheet along the slit length. These terms would not be significant unless L is small. For the present case an estimate of these terms can be made using the following data.

$$z = 200 \text{ microns}\,, \qquad L = 1400 \text{ microns}\,,$$

$$r_o = 100 \text{ microns}\,, \qquad \lambda = 0.3868 \text{ micron}\,.$$

The numerical value of the factor preceding the terms under consideration is given below.

$$\frac{2\hat{z}_o}{\hat{L}^2}\sqrt{\frac{\hat{r}_o}{\pi}} \sim 10^{-3}$$

Hence, in general, these terms would be three orders of magnitude smaller than the Fresnel integrals and may be ignored without causing a serious error. Thus the inner integral may be replaced by

$$\frac{\sqrt{\pi}\,\exp\left[-\left(\frac{\hat{z}_o}{\hat{L}}\right)^2\right]\exp(i\hat{r}_o)\left[F\left(\frac{\hat{\ell}-\hat{z}_o}{\sqrt{\pi\hat{r}_o}}\right)+F\left(\frac{\hat{\ell}+\hat{z}_o}{\sqrt{\pi\hat{r}_o}}\right)\right]}{\hat{r}_o^{3/2}} \qquad (4.4)$$

According to the above expression, variation in the illuminating intensity along the slit-length would not affect the phase of the diffracted field. In other words, the shape of the wavefronts is not likely to change unless the illuminating intensity undergoes sharp changes. However, intensity distribution along the diffracted wavefronts would follow the pattern of the illuminating field as represented by the factor $\exp\left[-(\hat{z}_o/\hat{L})^2\right]$ in (4.4).

4.2.4 The Simplified Equation

A comparison of (4.2) and (4.4) has been made in Figs. 4.2 and 4.3. The approximate solution contains all the essential features of the exact one. However, it reduces the computing time enormously.

Replacing the inner integral in (4.1) by expression (4.4),

$$e = \frac{\hat{y}_o\,\exp\left[-\left(\frac{\hat{z}_o}{\hat{L}}\right)^2\right]}{2\sqrt{\pi}\,i}\int_{-\hat{a}}^{\hat{a}} \frac{\exp\left[-\left(\frac{\hat{x}}{\hat{W}}\right)^2\right]\left\{F\left(\frac{\hat{\ell}-\hat{z}_o}{\sqrt{\pi\hat{r}_o}}\right)+F\left(\frac{\hat{\ell}+\hat{z}_o}{\sqrt{\pi\hat{r}_o}}\right)\right\}\exp(i\hat{r}_o)}{\hat{r}_o^{3/2}}\,d\hat{x} \qquad (4.5)$$

Since the range of integration for $\hat{x}$ is very small, the concept of stationary phase cannot be used to any advantage for evaluating the remaining integral in (4.5).

4.2.5 Distinct Zones in the Diffracted Field

The Fresnel integral approaches a constant value $(1+i)/2$ for large arguments. In the case of Fresnel integrals in Eqn. (4.5), the argument would be large enough for the asymptotic approximation to be accurate, except in small regions near the edges, i.e., $\hat{z}_o \approx \pm \hat{\ell}$. These regions may be referred to as "edge boundary layers". This concept may be further illustrated by evaluating thickness of the boundary layer for 5% variation in F from the asymptotic value. According to this definition, the boundary layer would correspond to a range of arguments from -13 to $+13$; i.e.,

$$\frac{\hat{\ell} - \hat{z}_o}{\sqrt{\pi \hat{r}_o}} = \pm 13 \quad , \quad \text{and} \quad \frac{\hat{\ell} + \hat{z}_o}{\sqrt{\pi \hat{r}_o}} = \pm 13 \quad .$$

For the present system, these regions are drawn to scale in Fig. 4.4. A substantial part of the measuring volume over the slits, lies outside the edge boundary layers. The diffracted field over this part may be simplified as follows.

$$e = \frac{\hat{y}_o \exp\left[-\left(\frac{\hat{z}_o}{\hat{L}}\right)^2\right] \exp(-i\,\frac{\pi}{4})}{\sqrt{2\pi}} \int_{-\hat{a}}^{\hat{a}} \frac{\exp\left[-\left(\frac{\hat{x}}{\hat{W}}\right)^2\right] \exp(i\hat{r}_o)}{\hat{r}_o^{3/2}}\, d\hat{x} \qquad (4.6)$$

Notice that the phase of (4.6) is independent of $\hat{z}_o$. Hence the shape of the wavefronts does not change with $\hat{z}_o$; i.e., the wavefronts are two-dimensional in the region governed by the above equation. It is shown later that the wavefronts remain fairly two-dimensional even within the edge boundary layers, except in the close vicinity of the edges. However, amplitude of the field shows significant fluctuations throughout the edge boundary layers.

Further evaluation is done for two cases; namely the global solution given by Eqn. (4.6) and the edge boundary layer near $\hat{z}_o = \hat{\ell}$, which is governed by Eqn. (4.5) with

$$F\left(\frac{\hat{\ell} + \hat{z}_o}{\sqrt{\pi \hat{r}_o}}\right)$$

replaced by the asymptotic value.

4.3 Characteristics of the Diffracted Light in the Edge Boundary Layers

Following the procedure outlined in Section A.7.5, the direction of propagation and that of polarization of the diffracted field may be deduced from an expression for the complex field. This information, along with the local intensity of the field, completes the data set needed for simulation of the light incident on the scattering particles. It also provides an understanding of the geometrical shape of the wavefronts and its effect on the signal.

4.3.1 The Direction of Propagation

A general equation for the wavefronts is needed for determining the direction of propagation of light. For the present case of a finite slit, the equation of a wavefront near the edge $\left(\hat{z}_o = \hat{\ell}\right)$ as deduced from Eqn. (4.5), is given below.

$$\int_{-\hat{a}}^{\hat{a}} \frac{\exp\left[-\left(\frac{\hat{x}}{\hat{W}}\right)^2\right]\left\{\left[\frac{1}{2} + F_c\left(\frac{\hat{\ell}-\hat{z}_o}{\sqrt{\pi\hat{r}_o}}\right)\right]\cos(\hat{r}_o-\beta) - \left[\frac{1}{2} + F_s\left(\frac{\hat{\ell}-\hat{z}_o}{\sqrt{\pi\hat{r}_o}}\right)\right]\sin(\hat{r}_o-\beta)\right\}}{\hat{r}_o^{3/2}} d\hat{x} = 0 \tag{4.7}$$

As in Eqn. (A.59), the direction of propagation may be specified by the cross product of two vectors tangential to the wavefront. Functions A_1, A_2, and A_3 needed for specifying these vectors may be deduced from Eqn. (4.7) by differentiation with respect to $\hat{x}_o$ and $\hat{z}_o$. These functions are as follows.

$$A_1 = \hat{y}_o \int_{-\hat{a}}^{\hat{a}} A \, d\hat{x} \tag{4.8}$$

$$A_2 = -\int_{-\hat{a}}^{\hat{a}} A(\hat{x}_o - \hat{x}) \, d\hat{x} \tag{4.9}$$

$$A_3 = \frac{1}{\sqrt{\pi}} \int_{-\hat{a}}^{\hat{a}} \frac{\exp\left[-\left(\frac{\hat{x}}{\hat{W}}\right)^2\right]\cos\left[\frac{(\hat{\ell}-\hat{z}_o)^2}{2\hat{r}_o} + \hat{r}_o - \beta\right]}{\hat{r}_o^2} d\hat{x} \tag{4.10}$$

where

$$A = \hat{r}_o^{-7/2} \exp\left[-\left(\frac{\hat{x}}{\hat{w}}\right)^2\right]\left\{-\left[\frac{1}{2} + F_c\left(\frac{\hat{\ell}-\hat{z}_o}{\sqrt{\pi\hat{r}_o}}\right)\right]\left[\frac{3}{2}\cos(\hat{r}_o-\beta) + \hat{r}_o \sin(\hat{r}_o-\beta)\right]\right.$$

$$+\left[\frac{1}{2} + F_s\left(\frac{\hat{\ell}-\hat{z}_o}{\sqrt{\pi\hat{r}_o}}\right)\right]\left[\frac{3}{2}\sin(\hat{r}_o-\beta) - \hat{r}_o\cos(\hat{r}_o-\beta)\right] - \frac{(\hat{\ell}-\hat{z}_o)}{2\sqrt{\pi\hat{r}_o}}$$

$$\left.\times \cos\left[\frac{(\hat{\ell}-\hat{z}_o)^2}{2\hat{r}_o} + \hat{r}_o - \beta\right]\right\} \qquad (4.11)$$

The ratio of A_3 to A_1 determines the slope of a wavefront in a plane parallel to the $y_o - z_o$ plane. The wavefronts are truly two-dimensional if A_3 is consistently zero. However, function A_3 would vanish only if the phase of its integrand would undergo a large number of cycles over the range of integration. In the present system, for r_o = 100 microns, at least 1 cm long slit is needed to obtain 10 cycles over the range of integration. Since the actual slits are much shorter, the wavefronts are expected to be slightly corrugated along the entire length of the slits. An estimate of such corrugations is given later.

4.3.2 The Polarization Axis

A vector along the polarization axis of the diffracted field may be determined using Eqn. (A.60) of Appendix A. The local propagation vector as well as the polarization in the slit-plane is needed for this purpose. It may be recalled that Eqn. (A.60) is valid only under the dipole approximation. In order to test the validity of this approximation for the present system, Eqn. (A.44) has been used. This equation yields the tilt of a dipole which could replace two electric dipoles located in the diffracting aperture. If this tilt is generally small, then the dipole approximation may be used. Figure 4.5 shows variation in the tilt of an equivalent dipole which replaces a reference dipole held in one corner of a slit and a test dipole moved along the opposite long side of the slit. The tilt has been calculated for reconstructing the diffracted field at a

point 50 microns above the reference dipole. Maximum tilt for the point under consideration is only 2% of the other significant angle, namely the angle between the propagation vectors of the two diffracted waves. Similar results are obtained for other locations in the diffracted field suggesting validity of the dipole approximation for the present system of finite slits.

4.3.3 Wavefront Corrugations

Figures 4.6(a) and (b) represent the computed diffracted field near the edge which has been calculated along a line defined by $x_o = 0$ and $y_o = 100$ microns (see Fig. 4.1 for a description of the coordinates). The slope of the wavefront is plotted in Fig. 4.6(a). Positive slope at a location indicates that the wavefronts are curving up, whereas the negative slope is indicative of a downward curvature. Beyond the edge of the slit, the curvature is consistently downward. Wavefronts are fairly two-dimensional above the slit exhibiting slight corrugations with a slope upto $\pm$ 0.5 degrees. According to the earlier discussion, such corrugations are expected to be present not only in the edge boundary layers but also in the central portion of the diffracted field. These corrugations would impair the signal by measuring a fraction of the spanwise velocity in addition to the streamwise gradient. However, error in the signal due to this effect would be less than 1% of the instantaneous spanwise velocity.

4.3.4 Near-edge Signal Distortion

Figure 4.6(b) shows variations of intensity near the edge. The intensity has been evaluated from expression (A.48) and normalized with the maximum value in the slit plane. Near the slit-edge, intensity experiences fluctuations as large as 30% of the mean value. It drops sharply beyond the edge. Within 2 microns from the edge, the intensity diminishes to one-tenth of its mean value over the slit. This point may be considered as the cut-off for the measuring volume. The slope of the wavefront is about $-1.5°$ at this location, contributing less than 3% of the spanwise velocity to the measurement. According to the experimental works of Klebanoff (1954) and Laufer (1953), the spanwise velocity in the viscous

sublayer is generally less than one-tenth of the streamwise velocity. Therefore, error due to the edge effect would be only a fraction of a percent. Similar results are obtained from other locations in the measuring volume. Hence no significant signal distortion is expected due to the finite slit length.

4.4 General Properties of Diffracted Light

Properties of the diffracted light near a slit-edge have been examined in the previous section. Wavefronts are found to be corrugated over the entire diffracted field; nevertheless, the corrugations are small and may be neglected in the central portion of the slit. Some general characteristics of diffracted light may be studied conveniently by developing a simple two-dimensional model based on Eqn. (4.6). The simplified equation of a wavefront is given below.

$$\int_{-\hat{a}}^{\hat{a}} \frac{\exp\left[-\left(\frac{\hat{x}}{\hat{w}}\right)^2\right]\left[\cos(\hat{r}_o-\beta) - \sin(\hat{r}_o-\beta)\right]}{\hat{r}_o^{3/2}} d\hat{x} = 0 \qquad (4.12)$$

The direction of propagation would be normal to a tangential vector parallel to the $x_o y_o$ plane. Equation (A.56) simplifies as follows:

$$\vec{s} = -A_{C_2}\vec{i} + A_{C_1}\vec{j} \qquad (4.13)$$

In the above equation, functions A_1 and A_2 of Appendix A have been replaced by A_{C_1} and A_{C_2}, respectively. These functions may be obtained by differentiating (4.12) with respect to x_o. The resulting expressions are as follows:

$$A_{C_1} = \hat{y}_o \int_{-\hat{a}}^{\hat{a}} A_C d\hat{x} \qquad (4.14)$$

and

$$A_{C_2} = -\int_{-\hat{a}}^{\hat{a}} A_C(\hat{x}_o-\hat{x})\, d\hat{x} \qquad (4.15)$$

where

$$A_C = \hat{r}_o^{-7/2} \exp\left[-\left(\frac{\hat{x}}{\hat{w}}\right)^2\right]\left\{-\left[\frac{3}{2}\cos(\hat{r}_o-\beta) + \hat{r}_o \sin(\hat{r}_o-\beta)\right]\right. \quad (4.16)$$
$$\left. + \left[\frac{3}{2}\sin(\hat{r}_o-\beta) - \hat{r}_o \cos(\hat{r}_o-\beta)\right]\right\}$$

Equation (4.13) must be multiplied by the sign of A_{C_1} to ensure that $\hat{s}$ points outward.

Using dipole approximation, the polarization axis would be parallel to the z_o axis at all the locations in the region under consideration.

Figure 4.7(a) represents slope of $\hat{s}$ from the y -axis plotted against x_o/y_o. For a pure cylindrical wave, the slope would be same as x_o/y_o. According to the present computations for $|x_o/y_o| \leq 0.2$, the slope lies within 0.1% of the cylindrical wave approximation. Hence, the cylindrical wave model for design of the slits is validated.

Figure 4.7(b) shows a decrease in intensity with x_o. However, it appears large enough between $x_o/y_o = -0.2$ and $+0.2$ to produce a reasonable signal. This issue is further explored through signal simulation. It may be noticed that the estimate of spreading angle α (Eqn. (3.10)) based on Fresnel approximation agrees well with the present calculation.

4.5 The Scattered Light Model

In the previous sections of this chapter, criteria have been set for evaluating the intensity, direction of propagation and the polarization axis of light diffracted from each slit. These three quatities are essential and adequate for calculation of light scattered by a solid particle. A set of equations (based on Mie scattering theory) has been proposed in Section A.8 of Appendix A for computing the properties of scattered light using this information. In this section, expressions for evaluating intensity and phase of the scattered waves have been developed. The intensity is integrated over the aperture of the receiving lens to obtain the time-dependent power reaching the photomultiplier tube. This quantity consists of a low-frequency pedestal and a high-frequency oscillating component. The r.m.s. shot noise is primarily determined by the pedestal.

Local signal properties are defined in a manner that in the absence of variation over a given aperture size, the local properties would be same as the integrated properties. Local properties are useful in exploring a wide range of receiver location for an optimal signal.

4.5.1 Local Properties of Scattered Field

Scattered fields from the two cylindrical waves may be added as follows.

$$\vec{E}_s(\theta,\phi,t) = \left[E_{i_1} \vec{C}_{s_1} \exp\left(2\pi i \int_o^t f_1' dt\right) + E_{i_2} \vec{C}_{s_2} \exp\left(2\pi i \int_o^t f_2' dt\right)\right] \frac{e^{-ikr}}{kr} \tag{4.17}$$

In the above equation, E_{i_1} and E_{i_2} are the strengths of the two incident fields and f_1' and f_2' are the respective Doppler-shifted frequencies. The use of Doppler-shifted frequencies takes a full account of the particle motion.

The scattering coefficients $\vec{C}_{s_1}$ and $\vec{C}_{s_2}$ correspond to the two incident waves. It may be recalled that the scattering coefficients are functions of θ and ϕ, which define direction of observation relative to propagation and polarization axes of the incident light.

The intensity of the scattered light may be expressed as the scalar product of $\vec{E}_s$ with its complex conjugate $\vec{E}_s^*$.

$$\vec{E}_s \cdot \vec{E}_s^* = k^{-2} r^{-2} \left\{ I_{i_1} P_1 + I_{i_2} P_2 + \sqrt{I_{i_1} I_{i_2}} (D_s^2 + D_c^2) \cos\left[\Psi(t) + 2\pi \int_o^t f_d dt\right]\right\} \tag{4.18}$$

Amplitudes of the scattering coefficients are denoted by P_1 and P_2 in the above equation. For ℓ^{th} wave this quantity may be deduced from the following expression.

$$P_\ell = \vec{C}_{s_\ell} \cdot \vec{C}_{s_\ell}^* = \left|A_{s_\ell}\right|^2 \sin^2\phi_\ell + \left|B_{s_\ell}\right|^2 \cos^2\phi_\ell \tag{4.19}$$

This expression follows from Eqn. (A.68) with A_ℓ and B_ℓ replaced by A_{s_ℓ} and B_{s_ℓ}. The quantities denoted by D_c and D_s are the real and the imaginary components of $2(\vec{C}_{s_1}^* \cdot \vec{C}_{s_2})$, respectively.

$$D_c = 2\text{Real}(\vec{C}^*_{s_1} \cdot \vec{C}_{s_2}) = 2\left[K_1\cos(\psi_1-\psi_2) + K_2\cos(\psi_1-\chi_2) + K_3\cos(\chi_1-\psi_2) + K_4\cos(\chi_1-\chi_2)\right] \quad (4.20)$$

$$D_s = -2\text{Imag}(\vec{C}^*_{s_1} \cdot \vec{C}_{s_2}) = -2\left[K_1\sin(\psi_1-\psi_2) + K_2\sin(\psi_1-\chi_2) + K_3\sin(\chi_1-\psi_2) + K_4\sin(\chi_1-\chi_2)\right] \quad (4.21)$$

The phase of $\vec{C}^*_{s_1} \cdot \vec{C}_{s_2}$ is obtained from the following equation:

$$\Psi(t) = \Psi(o) + 2\pi\int_o^t f_m dt = \tan^{-1}\left(\frac{D_s}{D_c}\right) \quad (4.22)$$

where χ and ψ are phases of A_s and B_s, respectively. Coefficients K_1 through K_4 are defined as below.

$$K_1 = \left|B_{s_1}\right|\left|B_{s_1}\right| \cos\phi_1 \cos\phi_2 \, \hat{e}_{\theta_1}\cdot\hat{e}_{\theta_2} \quad (4.23)$$

$$K_2 = \left|A_{s_2}\right|\left|B_{s_1}\right| \cos\phi_1 \sin\phi_2 \, \hat{e}_{\theta_1}\cdot\hat{e}_{\phi_2} \quad (4.24)$$

$$K_3 = \left|A_{s_1}\right|\left|B_{s_2}\right| \sin\phi_1 \cos\phi_2 \, \hat{e}_{\phi_1}\cdot\hat{e}_{\theta_2} \quad (4.25)$$

$$K_4 = \left|A_{s_1}\right|\left|A_{s_2}\right| \sin\phi_1 \sin\phi_2 \, \hat{e}_{\phi_1}\cdot\hat{e}_{\phi_2} \quad (4.26)$$

$f_d = f_1' - f_2'$ is the heterodyne frequency of Doppler shift as defined by (2.4). An explicit expression for the frequency of anisotropic scattering shift (see Sec. A.8.2) may be obtained by differentiating (4.22) with respect to time. Such an expression would involve time derivatives of θ_1, θ_2, ϕ_1, and ϕ_2. These angles would evidently vary during a burst because of displacement of the particle and cylindrical shape of the incident waves. Hence f_m would normally be non-zero. In the present study, an explicit expression for this frequency shift is not sought. Instead, f_m has been estimated from computation of the phase angle at various locations using Eqn. (4.22).

4.5.2 Integrated Signal Properties

Equation (4.18) may be integrated over the area of the receiving aperture to obtain the power influx to the photomultiplier tube.

$$P_s = k^{-2}\left\{ I_{i_1}\bar{P}_1 + I_{i_2}\bar{P}_2 + \sqrt{I_{i_1} I_{i_2}}\left[\bar{D}_c \cos 2\pi \int_o^t f_d dt + \bar{D}_s \sin 2\pi \int_o^t f_d dt\right]\right\} \tag{4.27}$$

The intensities of the two incident waves are denoted by I_{i_1} and I_{i_2}. These may be obtained by a calculation of the diffracted field produced by the slits. The averaged quantities in (4.27) are defined below.

$$\bar{P}_1 = \int_\Omega P_1 d\Omega \tag{4.28}$$

$$\bar{P}_2 = \int_\Omega P_2 d\Omega \tag{4.29}$$

$$\bar{D}_c = \int_\Omega D_c d\Omega \tag{4.30}$$

$$\bar{D}_s = \int_\Omega D_s d\Omega \tag{4.31}$$

Integration is performed over the solid angle Ω subtended by the aperture on the particle. The first two terms in (4.27) represent the pedestal of the signal at the photomultiplier input which is used to evaluate the shot noise. Following Adrian and Earley (1976), the signal current and the mean-square noise current may be expressed as follows.

$$i_s = \frac{\eta_q e}{h\nu_o k^2}\sqrt{I_{i_1} I_{i_2}}\left[\bar{D}_c \cos\left(2\pi \int_o^t f_d dt\right) + \bar{D}_s \sin\left(2\pi \int_o^t f_d dt\right)\right] \tag{4.32}$$

$$i_n^2 = \frac{2e^2 \Delta f_s \eta_q}{h\nu_o k^2}\left[I_{i_1}\bar{P}_1 + I_{i_2}\bar{P}_2\right] \tag{4.33}$$

The signal-to-noise ratio may be defined as the ratio of mean-square signal current to mean-square noise current.

$$\overline{SNR} = \frac{\eta_q}{4h\nu_o \Delta f_s k^2} \left[\frac{I_{i_1} I_{i_2} (\overline{D}_c^2 + \overline{D}_s^2)}{I_{i_1} \overline{P}_1 + I_{i_2} \overline{P}_2} \right] \tag{4.34}$$

Signal visibility is defined as the ratio of signal amplitude to pedestal. It may be deduced from above relations as follows.

$$\overline{V} = \frac{\sqrt{I_{i_1} I_{i_2} (\overline{D}_c^2 + \overline{D}_s^2)}}{I_{i_1} \overline{P}_1 + I_{i_2} \overline{P}_2} \tag{4.35}$$

The average phase angle for computation of anisotropic scattering shift may be deduced from (4.26).

$$\overline{\Psi} = \tan^{-1}(\overline{D}_s / \overline{D}_c) \tag{4.36}$$

4.5.3 Local Signal Properties

Local signal properties are obtained by evaluating scattering coefficients at a particular location and assuming them to be fixed over a solid angle same as that of the aperture under consideration. This procedure leads to the following expressions for the local properties.

Signal-to-noise ratio:

$$SNR = \frac{\eta_q \Omega}{4h\nu_o \Delta f_s k^2} \left[\frac{I_{i_1} I_{i_2} (D_c^2 + D_s^2)}{I_{i_1} P_1 + I_{i_2} P_2} \right] \tag{4.37}$$

Visibility:

$$V = \frac{\sqrt{I_{i_1} I_{i_2} (D_c^2 + D_s^2)}}{I_{i_1} P_1 + I_{i_2} P_2} \tag{4.38}$$

Phase of anisotropic scattering shift:

$$\Psi = \tan^{-1}(D_s/D_c) \tag{4.39}$$

Maps of these properties over a wide range of possible locations of the receiving optics are presented later. These maps are used for selecting a good location for the receiving lens.

4.6 Computation of the Scattered Light

Computation of the scattering functions begins with specification of a unit vector $\vec{r}$ along the direction of observation. The propagation and polarization vectors ($\vec{s}$ and $\vec{p}$, respectively) for each incident wave are also specified in the same coordinate system as $\vec{r}$. The conventional boundary-layer coordinates illustrated in Fig. 4.8 are used for this purpose. According to the procedure of Secs. 4.3 and 4.4, vectors $\vec{s}$ and $\vec{p}$ for light from each slit are specified in the respective diffracted field coordinates (x_o, y_o, z_o). Since these coordinates are aligned with the boundary-layer coordinates, $\vec{s}$ and $\vec{p}$ do not require further transformation. Knowing $\vec{r}$, $\vec{s}$, and $\vec{p}$, one can evaluate the properties of each scattered wave from a set of equations given in Sec. A.8.1. Subsequently, using the correlations of the previous section, the scattering properties are further simplified to obtain the characteristics of the dual wave system.

For evaluation of the integrated properties, the description of the circular aperture is simplified by defining the aperture coordinate system. The vector $\vec{r}$ is first defined in the aperture coordinates and then transformed to the boundary layer coordinates for evaluation of the scattering functions.

4.6.1 Computation of the Integrated Properties

As shown in Fig. 4.8, a system of spherical polar coordinates is defined in the boundary layer. The center of a circular receiving aperture is specified in terms of the altitude angle, θ_c and the azimuth angle, ϕ_c. The azimuth angle is positive for the upstream locations.

In order to define the aperture coordinate system, the boundary layer coordinates are first rotated through an angle ϕ_c about the z-axis and then through θ_c about the x-axis. These rotations require that each vector in the boundary layer coordinates be multiplied by the matrices

$$\begin{bmatrix} \cos\phi_c & \sin\phi_c & 0 \\ -\sin\phi_c & \cos\phi_c & 0 \\ 0 & 0 & 1 \end{bmatrix} \quad \text{and} \quad \begin{bmatrix} 1 & 0 & 0 \\ 0 & \cos\theta_c & -\sin\theta_c \\ 0 & \sin\theta_c & \cos\theta_c \end{bmatrix} \tag{4.40}$$

In the new coordinate system, z-axis points towards the center of the circular aperture, as shown in Fig. 4.9. The half receiving cone angle of the aperture is denoted by α_a. A unit sphere around the origin is used to evaluate the differential solid angle $d\Omega$.

$$d\Omega = \sin\theta_a d\theta_a d\phi_a \tag{4.41}$$

In the aperture coordinates, the orientation of the solid angle element is given by the following vector:

$$\vec{r}_a = -\sin\phi_a \sin\theta_a \vec{i} + \cos\phi_a \sin\theta_a \vec{j} + \cos\theta_a \vec{k} \tag{4.42}$$

In order to evaluate the scattering functions along this vector, it must be transformed to the boundary layer coordinates. This is accomplished by applying, in the reverse order, the inverse of the rotations expressed by (4.40); i.e.,

$$\begin{bmatrix} \cos\phi_c & -\sin\phi_c\cos\theta_c & -\sin\phi_c\sin\theta_c \\ \sin\phi_c & \cos\phi_c\cos\theta_c & \cos\phi_c\sin\theta_c \\ 0 & -\sin\theta_c & \cos\theta_c \end{bmatrix} \tag{4.43}$$

Now, Eq. (4.41) may be used to simplify Eq. (4.28) as follows:

$$\bar{P}_l = \int_{\theta_a=o}^{\alpha_a} \sin\theta_a \int_{\theta_a=o}^{2\pi} P_l d\phi_a d\theta_a \tag{4.44}$$

In this form, each pair of angles (θ_a, ϕ_a) corresponds to a unit vector $\vec{r}_a$ which is transformed to the boundary layer coordinates and used to

evaluate the corresponding value of P_l. Intergration is performed numerically using Simpson quadrature. The grid increment is chosen to be 1/20th of the nominal lobe angle (λ/d_p).

Finally, it may be mentioned that the distance of the particle from the origin of the coordinates has been ignored in the present formulation. It is justifiable because this distance is extremely small as compared to the distance between the particle and the receiving aperture.

4.6.2 Computation of the Local Properties

The local properties are calculated over an approximately rectangular region on a spherical surface surrounding the scattering particle. As illustrated in Fig. 4.10, streamwise and normal angles are used to specify points on the computational zone which covers the prospective receiving orientations in the side-scatter. For a pair of streamwise and normal angles (γ_s and γ_n, respectively), the unit vector $\hat{r}$ is defined along the line of intersection of the two planes shown in Fig. 4.10. Plane 1 passes through the x-axis and makes an angle γ_n with the xz-plane, whereas plane 2 passes through the y-axis and makes an angle γ_s with the yz plane. These planes may be defined by the following set of equations:

$$\frac{y}{\sin \gamma_n} = \frac{z}{\cos \gamma_n} \quad \text{and} \quad \frac{x}{\sin \gamma_s} = \frac{z}{\cos \gamma_s}$$

Hence, the line of intersection is represented by

$$\frac{x}{\cos \gamma_n \sin \gamma_s} = \frac{y}{\cos \gamma_s \sin \gamma_n} = \frac{z}{\cos \gamma_n \cos \gamma_s}$$

Consequently, the observation vector is expressed as follows:

$$\hat{r} = \frac{\cos \gamma_n \sin \gamma_s \hat{i} + \cos \gamma_s \sin \gamma_n \hat{j} + \cos \gamma_n \cos \gamma_s \hat{k}}{\sqrt{1 - \sin^2 \gamma_n \sin^2 \gamma_s}} \quad (4.44)$$

Knowing the observation vector in the boundary layer coordinates, the scattering functions are evaluated as explained earlier.

For evaluation of the local properties, Eqn. 4.37 requires the value of solid angle of the receiving aperture which is related to the half receiving cone angle by the following equation.

$$\Omega = 2\pi(1 - \cos \alpha_a) \tag{4.45}$$

4.7 Simulation of Local Properties

As mentioned in the previous section, local signal properties have been studied by performing computation over a patch of a sphere surrounding the scattering particle. The results of computation are presented in Figs. 4.11 and 4.12. The input parameters for simulation are specified in Table 4.1. Calculations are done for three choices of particle diameters, i.e., 1, 2, and 5 microns. Typical optical properties of dust particles are obtained from the experimental data presented by Driscoll and Vaughan (1978). The refractive index and extinction coefficient for dust are specified as 1.53 and 0.008, respectively. The response of a 5 micron polysterene latex particle has also been studied which is known to have a refracive index of 1.6 and a negligible extinction coefficient. Signal properties are computed for a particle location specified by $x_o = 20$, $y_o = 100$, and $z_o = 0$. This location corresponds to small and unequal intensities of the incident waves and hence yields conservative estimates for the signal properties.

High signal visibility is observed for 1 micron and 2 micron particles. Significant deterioration in visibility occurs for 5 micron particles. Higher refractive index seems to result in poorer performance in pure side-scatter. However, visibility for a particle with higher refractive index improves at larger normal angles. Polystyrene latex particle appears to have higher visibility near a normal angle of 30°. Since the present system is designed to operate in the vicinity of side-scatter, there is no advantage in using a particularly high refractive index.

Despite a high visibility, smaller particles do not scatter enough light to exhibit a high signal-to-noise ratio. Among the cases studied, only 2 and 5 micron particles appear to have large enough SNR to produce accurate signals. A value of 100 for SNR is considered reasonable for

Table 4.1

Input Data for Numerical Simulation of the Signal Properties

General

Wavelength of laser in air	0.5145 micron
Refractive index of the fluid	1.33
Width of each slit	1 micron
Length of each slit	400 microns
Spacing between the slits	10 microns
Power in each laser sheet	200 mW
Quantum efficiency of the photomultiplier tube	0.22
Bandwidth of the electronic filters	100 kHz

Dimensions of each laser sheet in the slit plane (see fig. 4.1):

$1/e^2$ minor axis	6.5 microns
$1/e^2$ major axis	1400 microns

Optical properties of the scattering media:

	Dust	Polystyrene Latex
Refractive index	1.53	1.60
Extinction coefficient	0.008	0.0

For Local Signal Properties:

Particle location (x_o, y_o, z_o)	20, 100, 0 microns
Particle diameter	1, 2, 5 microns
Grid increment	0.5°
Particle material	Dust, Polystyrene Latex
Region Covered:	
Streamwise angles	-15° to + 15°
Normal angles	0° to 30°
Half receiving-cone angle	3°

For Integrated Signal Properties:

Location of the receiving aperture center:	
Azimuth angle	0° for main results 15° for examining intensity lobes
Altitude angle	20°
Half receiving-cone angle	3° for main results 0.2° for examining intensity lobes
Frequency shift	0
Velocity gradient	1000 s^{-1}
Number of cycles computed	10
Particle material/diameter	Dust/5 microns

Note: See plots of simulated signals for further information about particle location and velocity, and polarization of the incident light.

the current application. The effect of increase in refractive index on SNR is similar to that on visibility. Signal quality for polysterene latex particles is poor in the side-scatter but improves significantly at larger normal angles.

4.8 Simulation of Integrated Properties

Signal properties have been integrated over an aperture with a 6° cone angle. Signal current and noise current have been calculated for near-wall signals as well as signals from the center of the measuring volume. A complete description of the input parameters for simulation of the integrated properties is given in Table 4.1.

An understanding of the near-wall signal is important for locating the measuring volume properly. Figure 4.13 shows near-wall signals with pedestal for distances of 7.5, 15 and 30 microns from the wall. At 7.5 microns, two peaks are distinct and modulation is strongly supressed. At 15 microns, the peaks begin to merge but modulation becomes prominent. Finally, there are no distinct peaks at 30 microns. Hence a signal with seperate peaks may be attributed roughly to a 10 micron thick layer near the wall, whereas one with merging peaks may be expected from a region 10 to 20 microns away from the surface. Modulation in the later case may be used to estimate velocity gradient, whereas velocity can be deduced from time interval between the peaks. A knowledge of both the velocity and the gradient would allow one to specify the location of the particle and use it to properly align the receiving optics. A typical measured signal from the near-wall region has also been included in Fig. 4.13. This signal has distinct peaks peculiar to a signal from a distance of 0 to 10 microns from the wall. As opposed to the simulated signal, the measured one shows a high level of noise which may be a result of multiple reflections from the chromium-coated wall. The phenomenon of mutiple reflections is not included in the simulation model. Peaks in the measured signal are unequal which perhaps is an indication of slight misalignment of laser sheets over the slits.

Transfer function for simulated near-wall signals shows strong deviations from the nominal value. According to Fig. 4.14, the portion of the signal between two peaks appears to be the most reliable for

deducing signal frequency and hence the velocity gradient. It may be noticed that the transfer function is consistently lower than the nominal value. Hence an appropriate multiplication factor must be used with the nominal value. In the central portion, this factor is approximately 0.75, 0.9 and 0.95 for distances of 7.5, 15 and 30 microns from the wall.

Figure 4.15 shows simulated signals (without pedestal) from the center of the measuring volume. The peak-to-peak noise represents ± 3 times the value of r.m.s noise current. The noise level appears to be tolerable over 10 cycles plotted in the figure. The signal is only slightly expanded for a normal velocity which is one-tenth of the streamwise velocity. The near-edge signal with a spanwise component appears to be weak and may be ignored by proper setting of gain in the signal processor. Nevertheless, it does not show a significant departure in its frequency from a normal signal. The measured signal has approximately the same number of cycles as the simulated ones and exhibits a similar variation in intensity across the burst. Transfer functions for the simulated signals are presented in Fig. 4.16. The anisotropic scattering shift has been taken into account in computation of the simulated transfer function. Variation of transfer function in Fig. 4.16 is almost identical with Fig. 2.5 which is based on a simple cylindrical wave model. Hence it substantiates the use of this model for evaluation of the transfer function. In the case of a near-edge particle with a spanwise component, the transfer function does not vary significantly as shown in Fig. 4.16.

4.9 The Frequency Shift and Intensity Modulation Due to Anisotropic Scattering

As discussed in Sec. A.8.2, the scattered light may have an intensity modulation in addition to the intensity variation of the illuminating light along the particle path. In Fig. 4.17(a), this phenomenon is illustrated schematically for the present system. According to this illustration, the receiving aperture is exposed to intensity lobe 1 in the begining of the Doppler burst. As the particle moves across the measuring volume, the intensity lobes sweep across the receiver. Near

the end of the burst, lobe 3 is exposed to the receiver. Hence the signal exhibits a variation in the intensity which is a superposition of the variation in the illuminating intensity and the modulation due to sweeping intensity lobes. The difference between the intensity variation of isotropic and anisotropic scattering is illustrated in Fig. 4.17(b).

Furthermore, as explained in Sec. A.8.2, the phase of the scattered light varies from one lobe to the other. The variation of phase with time causes a frequency shift in the signal. The phase angle for anisotropic scattering shift is expressed by Eqns. (4.36) and (4.39).

The local value of anisotropic scattering shift is plotted in Fig. 4.18. It has been calculated using the following relations.

Anisotropic scattering shift:

$$2\pi f_m = \frac{\Delta\Psi}{\Delta t} = \frac{\Delta\Psi}{\Delta x_o} g y_o \tag{4.46}$$

Doppler shift:

$$2\pi f_d = 2\pi B g \tag{4.47}$$

The anisotropic scattering shift as the ratio of Doppler shift:

$$\frac{f_m}{f_d} = \left(\frac{\Delta\Psi}{2\pi}\right) \frac{y_o}{\Delta x_o B} \tag{4.48}$$

In Eqn. (4.48), phase angle Ψ is a local value at a given altitude and azimuth angle. Calculations have shown that Ψ varies fairly linearly with x_o; hence, the time-averaged value would be close to instantaneous values. For data in Fig. 4.18, x_o is varied from -20 to +20 microns, while y_o is maintained at 100 microns. A range of altitude angle has been examined for a value of zero for the azimuth angle. For a particle diameter of 5 microns, spikes of anisotropic scattering shift appear at intervals of approximately 4°, with peak value reaching 2% at 20° of altitude angle. The actual shift in the signal would be the spatial average over the aperture area. In the laminar flow channel, collection of scattered light takes place in a cone of 6° included angle. Calculations suggest that the average shift is less than 1% for the parameters specified above.

The intensity modulation due to anisotropic scattering is significant only if the receiving aperture is smaller than the angular extent of a typical intensity lobe. According to Figs. 4.11 and 4.12, anisotropy is strong for particles of diameter 5 μm or larger. Also, variations in the scattering properties are slow along the streamwise direction which is the main direction of particle motion. However, this is true only if the electric vector is aligned with the slits. For the case of magnetic polarization (i.e., the magnetic vector being parallel to the long edge of the slits), stronger variations in the scattering properties are expected along the streamwise direction.

Simulated signals for a small receiving aperture are shown in Fig. 4.19. A circular aperture with a receiving-cone angle of 0.4° is located at an azimuth angle of 15°. As expected, the scattering-related intensity modulation is stronger for the case of magnetic polarization. Simulated signals for receiving apertures with a 6° vertex angle are also presented in Fig. 4.19. It is obvious that in either case of polarization, the effects of anisotropic scattering are averaged out for larger apertures.

4.10 Summary of the Results

The main results of the detailed analysis may be summarized as follows:

i) Variation in the intensity of the illuminating sheet does not affect the cylidrical shape of the wavefronts.

ii) Due to the finite length of the slits, the wavefronts are slightly corrugated all along. However, it does not have a significant effect on the transfer function.

iii) Near the edges, the intensity of the diffracted light diminishes before any significant distortion in the shape of the wavefronts occurs. Hence, nonrepresentative signals are not likely to be detectable.

iv) The relationship between the refractive index of the particle and the signal strength is complex at the measuring location. A higher refractive index does not necessarily ensure a stronger signal.

v) For the parameters listed in Table 4.1, particles of diameter larger than 2 μm produce good quality signals.

vi) The anisotropic scattering shift is less than 1% in the measuring volume.

vii) Intensity modulation due to anisotropic scattering is significant only for very small receiving apertures. For a receiving-cone angle of 6°, the scattering-related intensity modulation is strongly suppressed.

viii) Near-wall signals, between 0 and 20 microns from the wall, are very distinct and may be used to locate the measuring volume.

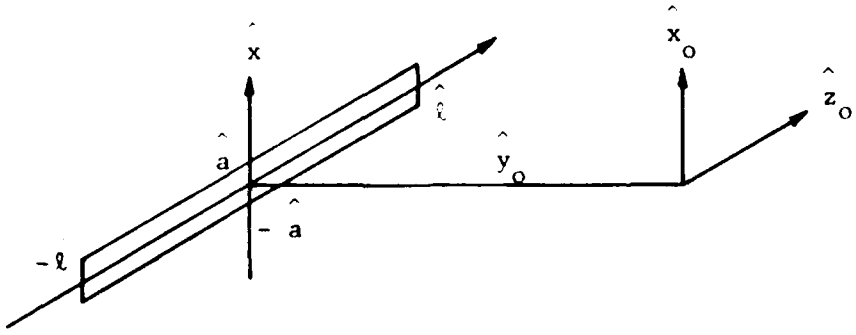

4.1(a). Frames of reference for incident and diffracted fields.

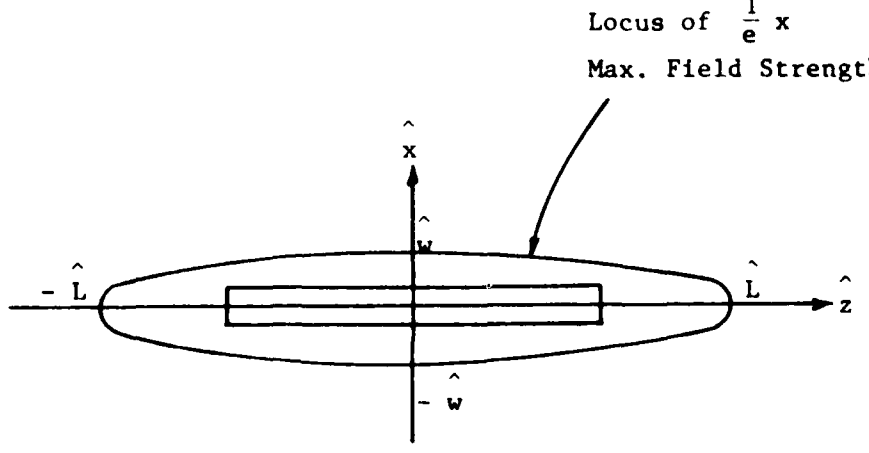

Fig. 4.1(b). Cross-section of laser sheet in the slit plane.

Fig. 4.1. Specification of a slit and the illuminating laser sheet in the appropriate coordinates.

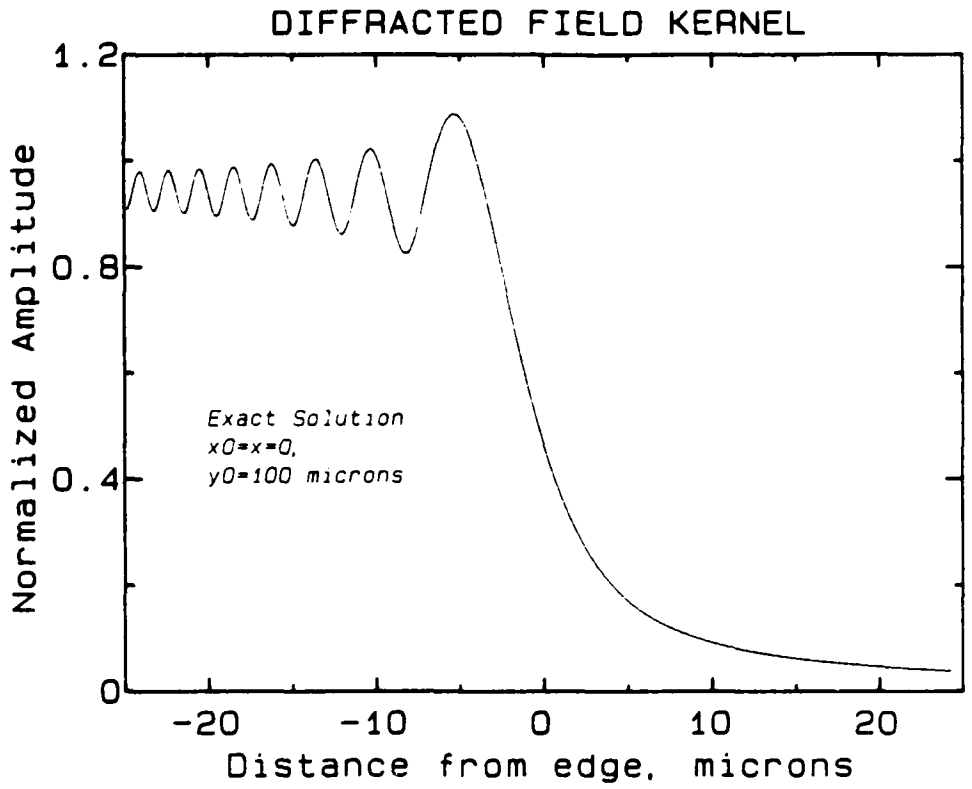

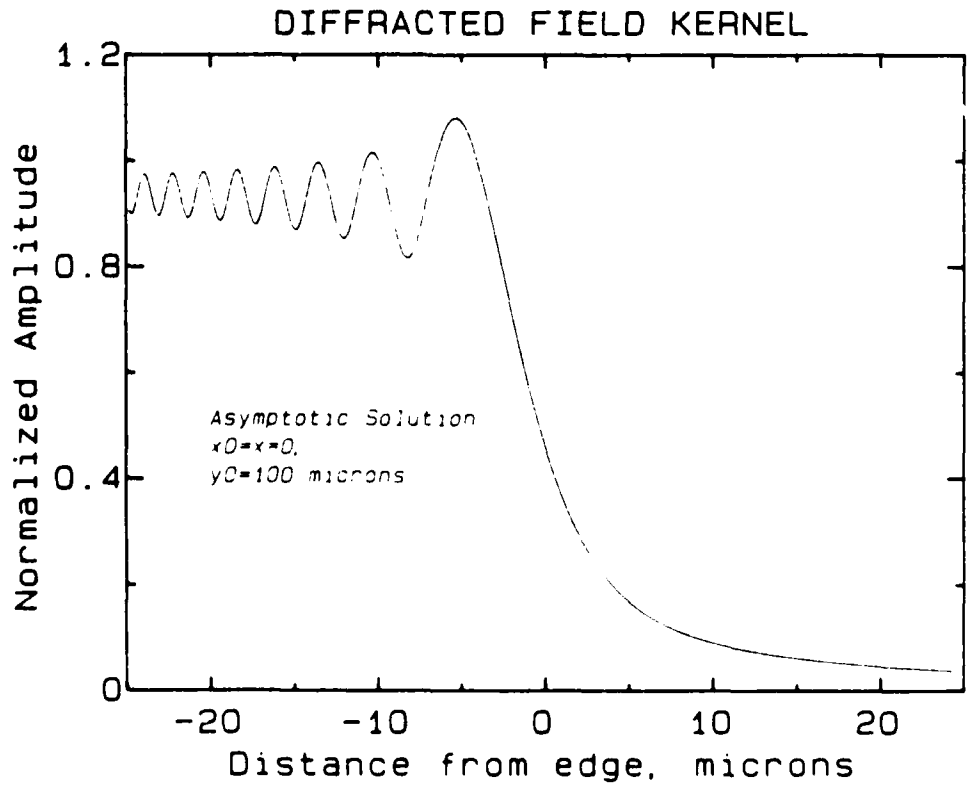

Fig. 4.2. Comparison of exact solution with asymptotic expansion for amplitude of diffracted field kernel (inner integral).

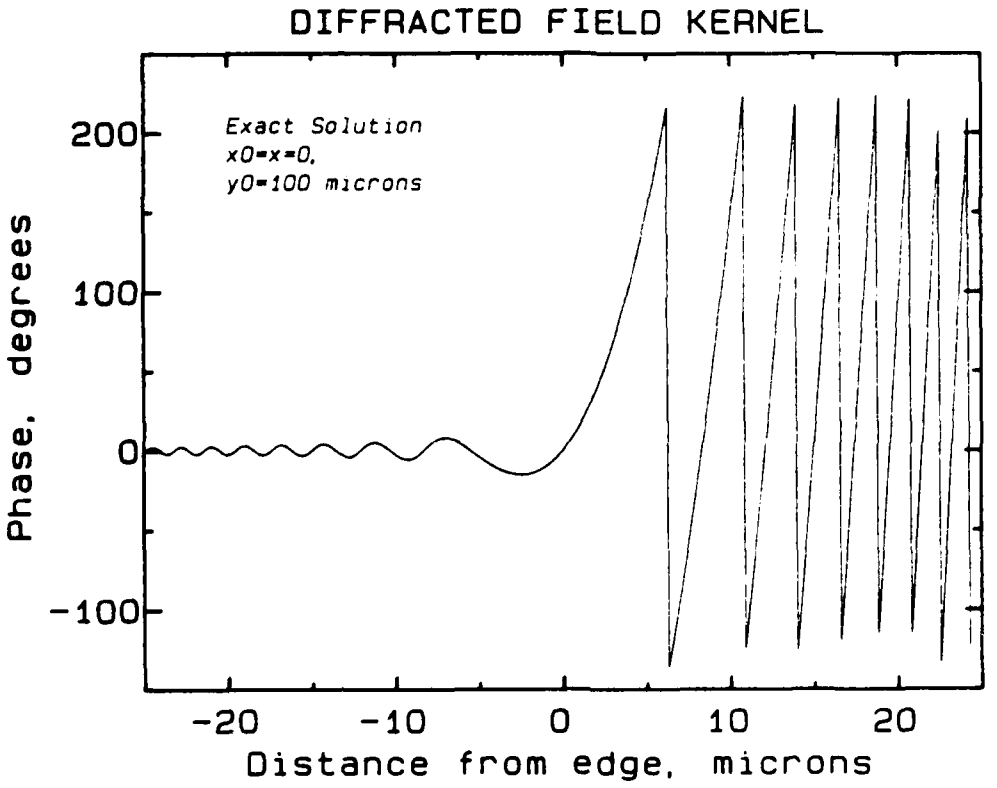

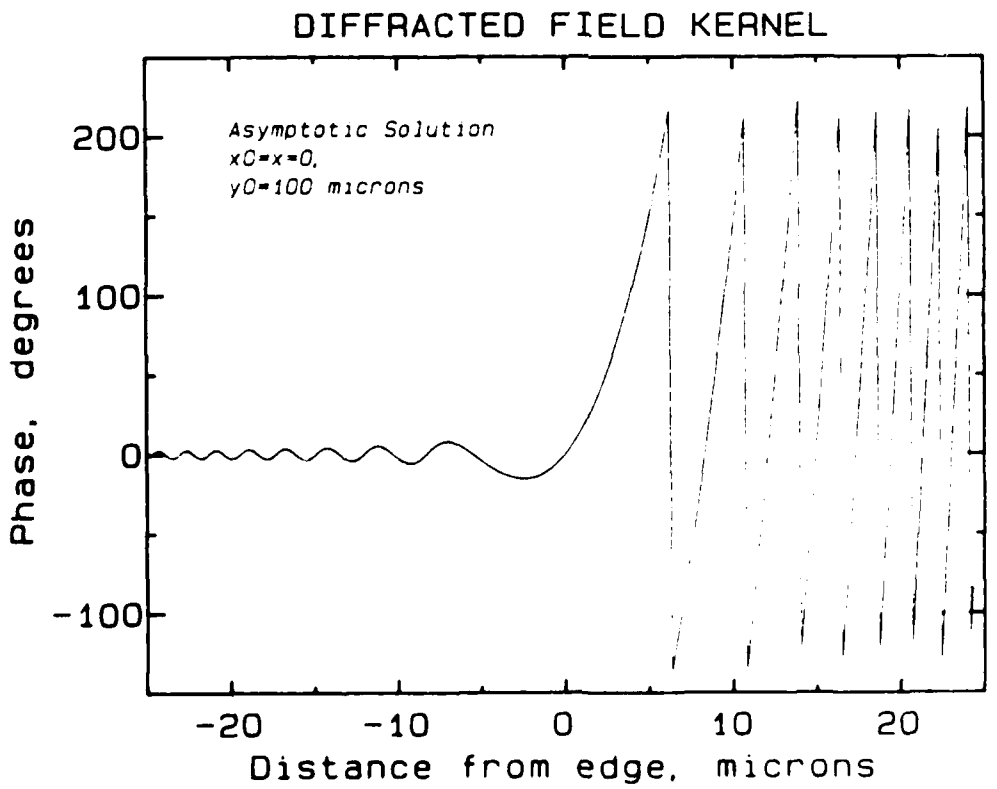

Fig. 4.3. Comparison of exact solution with asymptotic expansion for phase of diffracted field kernel (inner integral).

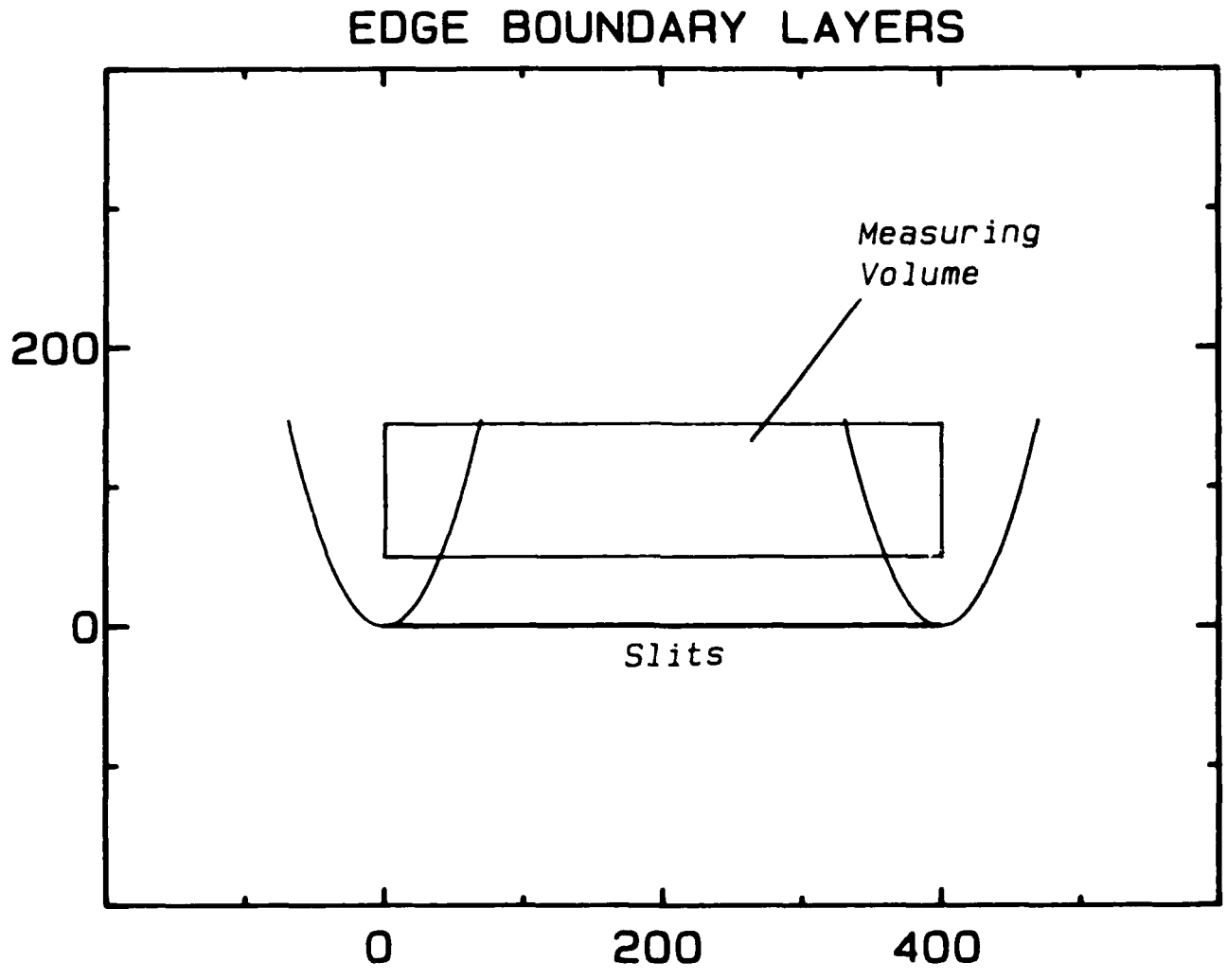

Fig. 4.4. Edge boundary layers in the measuring volume.

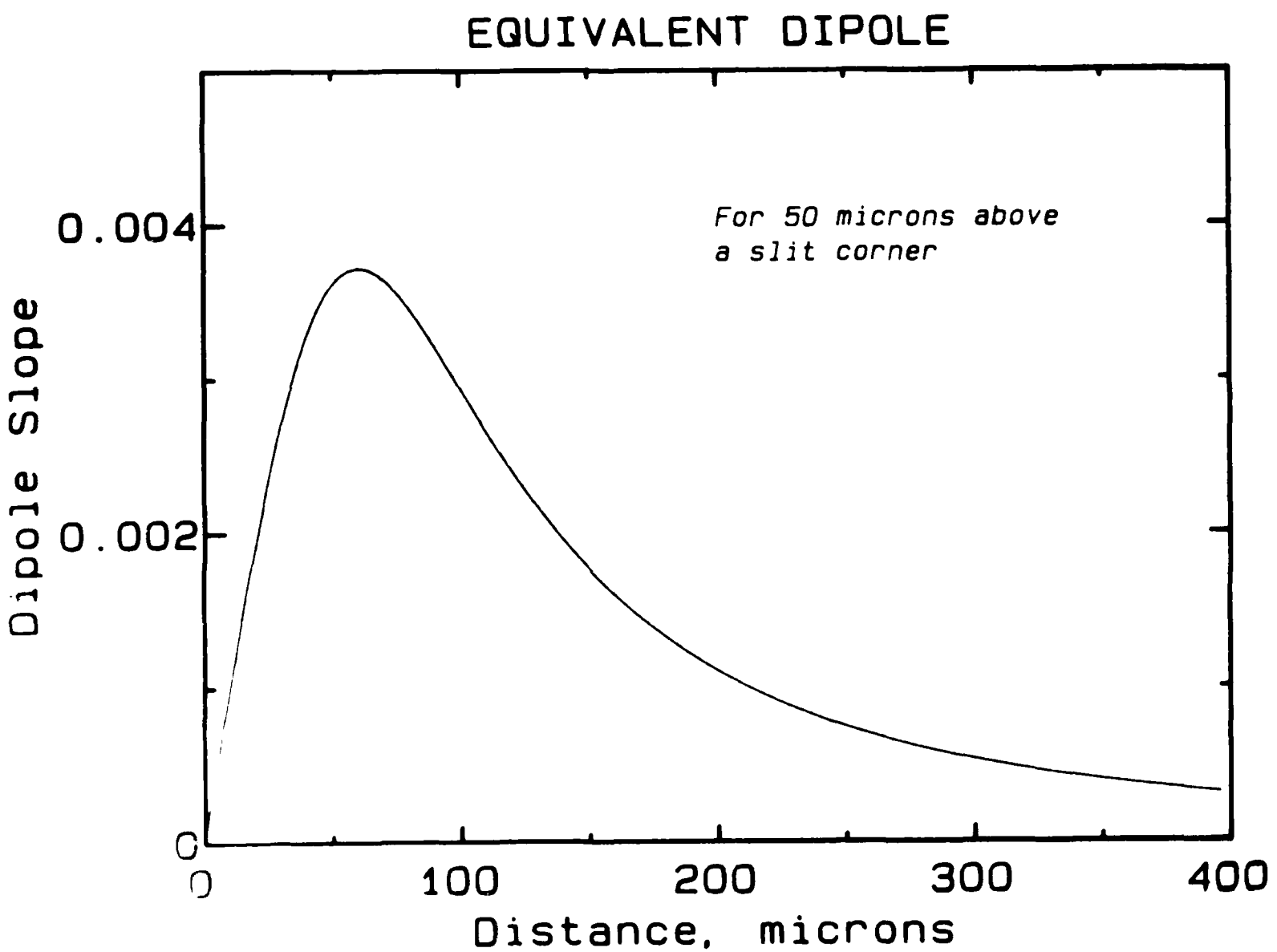

an equivalent dipole which replaces two dipoles in
minating field.

AD-A178 629 DUAL CYLINDRICAL WAVE LASER-DOPPLER METHOD FOR MEASUREMENT OF SKIN FRICTI..(U) STANFORD UNIV CA DEPT OF MECHANICAL ENGINEERING A A NAQWI ET AL. JAN 87 2/3

UNCLASSIFIED ARO-19976.3-EG DAAG29-83-K-0056 F/G 20/4 NL

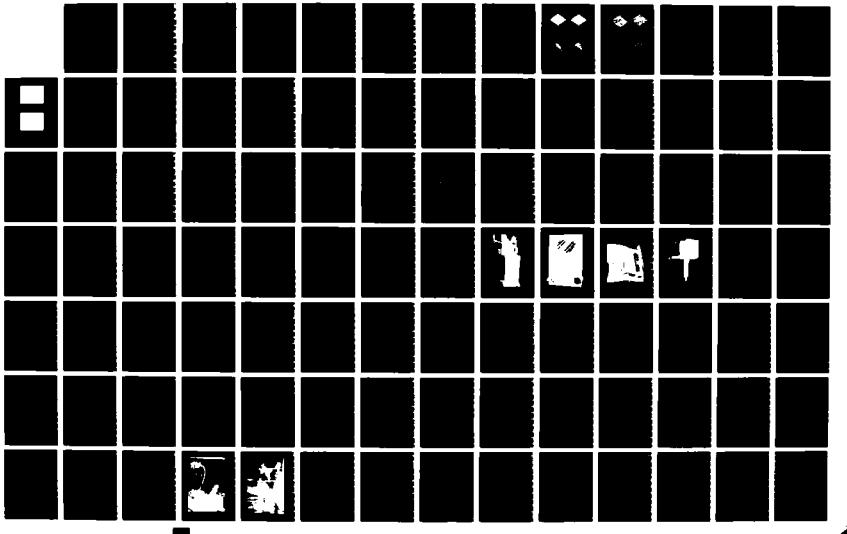

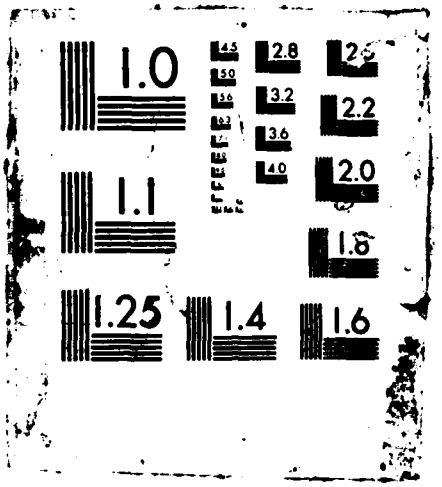
1.0
1.1
1.25
1.4
1.6
2.8
3.2
3.6
4.0
2.2
2.0
1.8

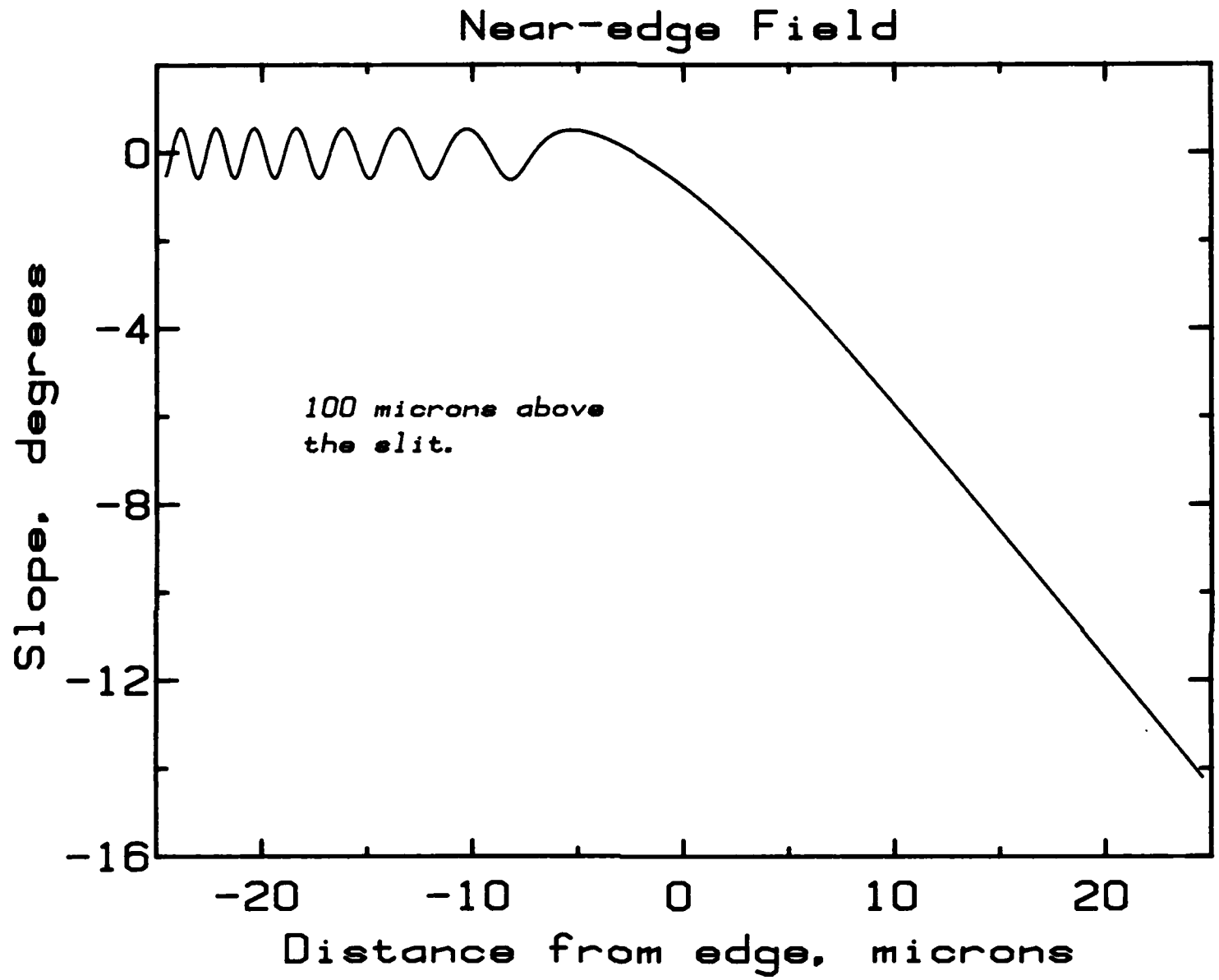

Fig. 4.6(a). Slope of the diffracted field near the edge.

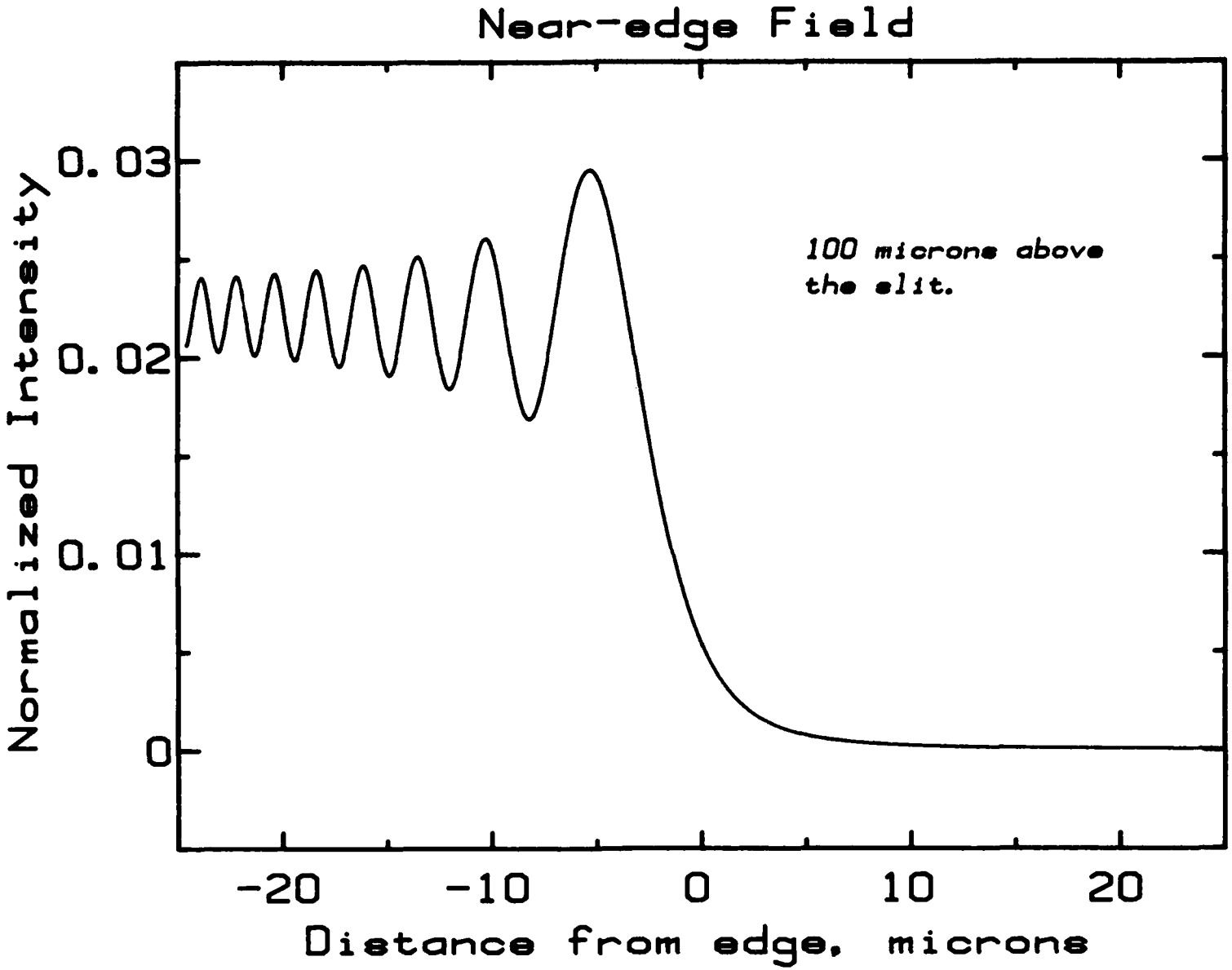

Fig. 4.6(b). Intensity of the diffracted field near the edge.

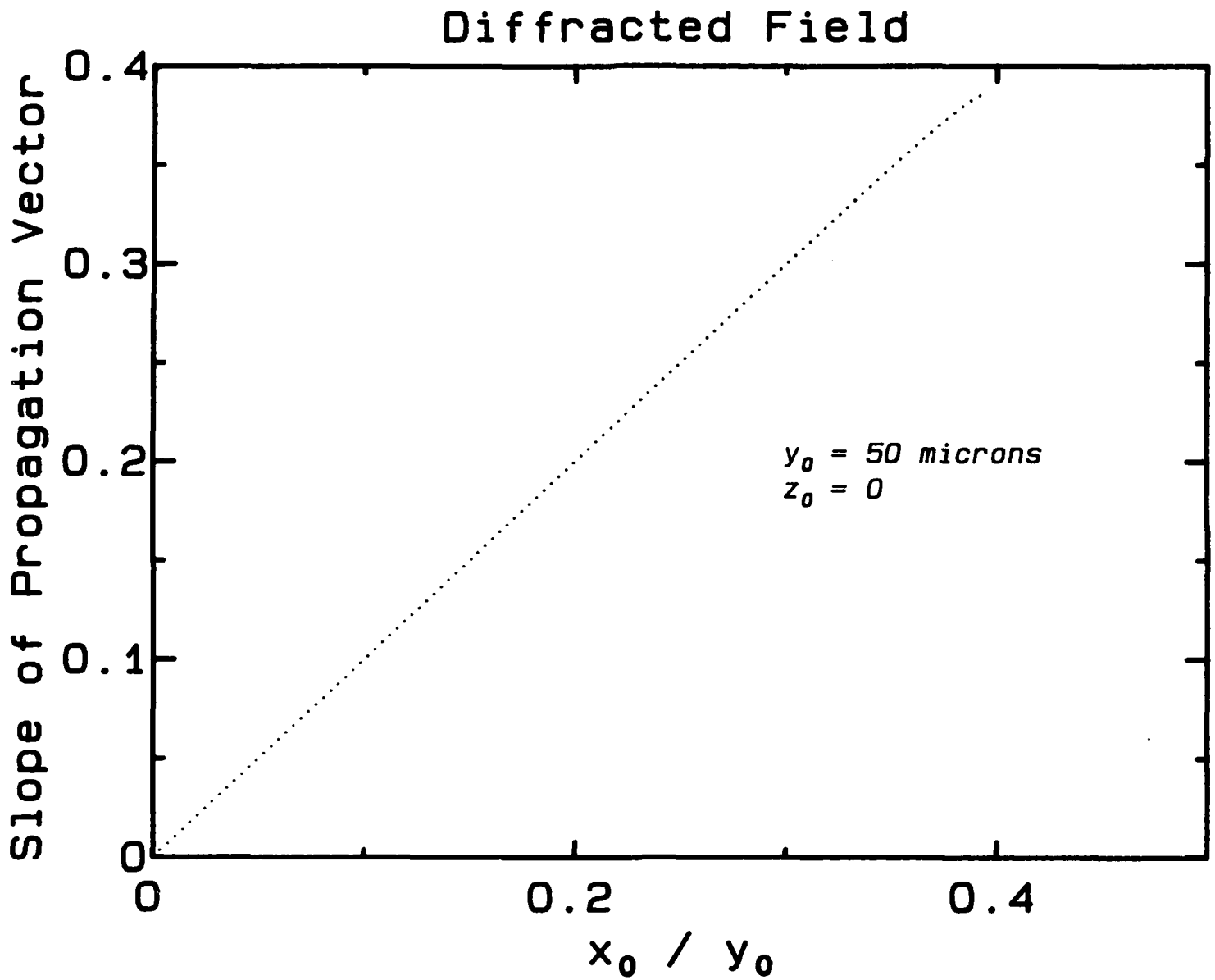

Fig. 4.7(a). Slope of diffracted field showing cylindrical shape of wave fronts.

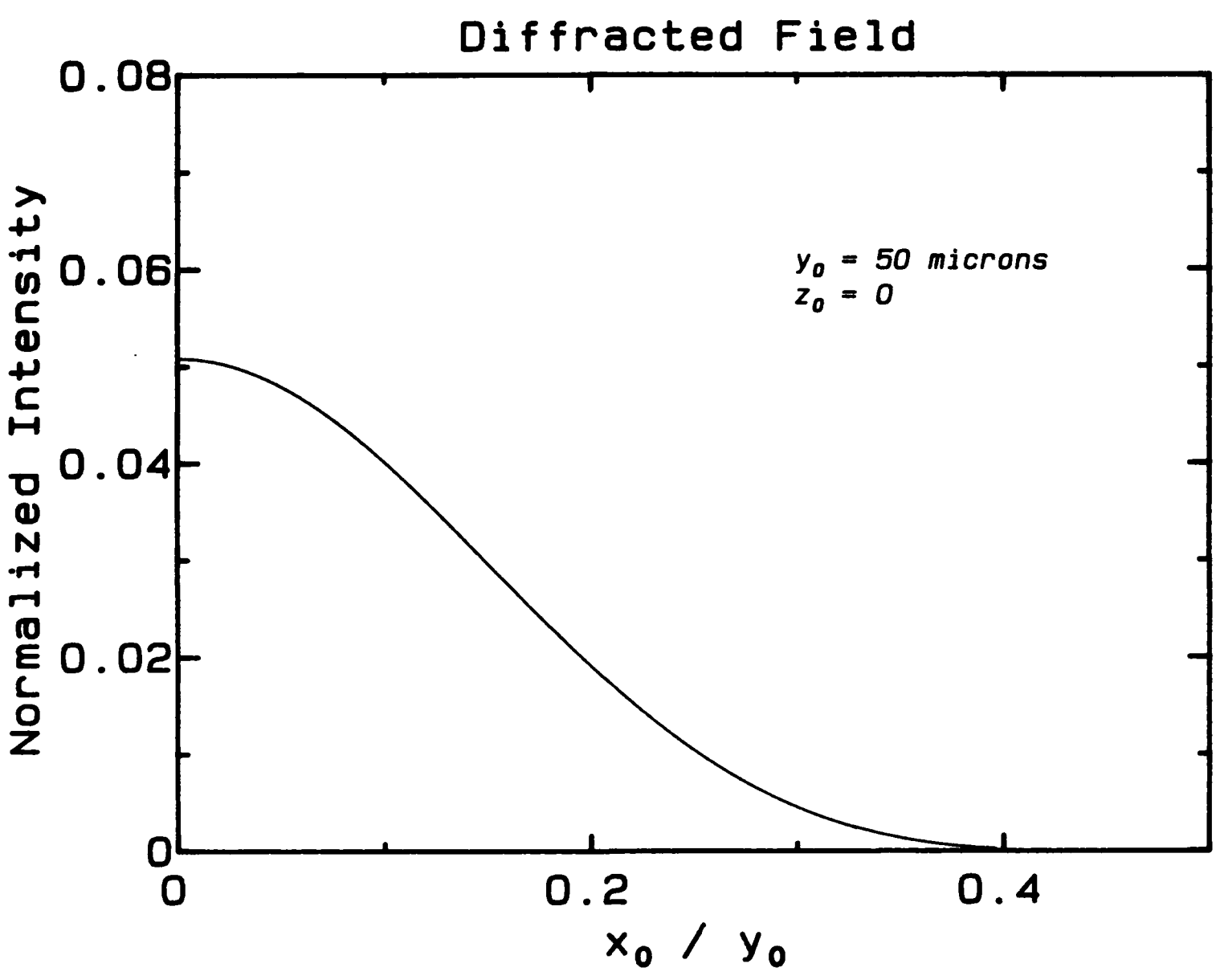

Fig. 4.7(b). Intensity of the diffracted field.

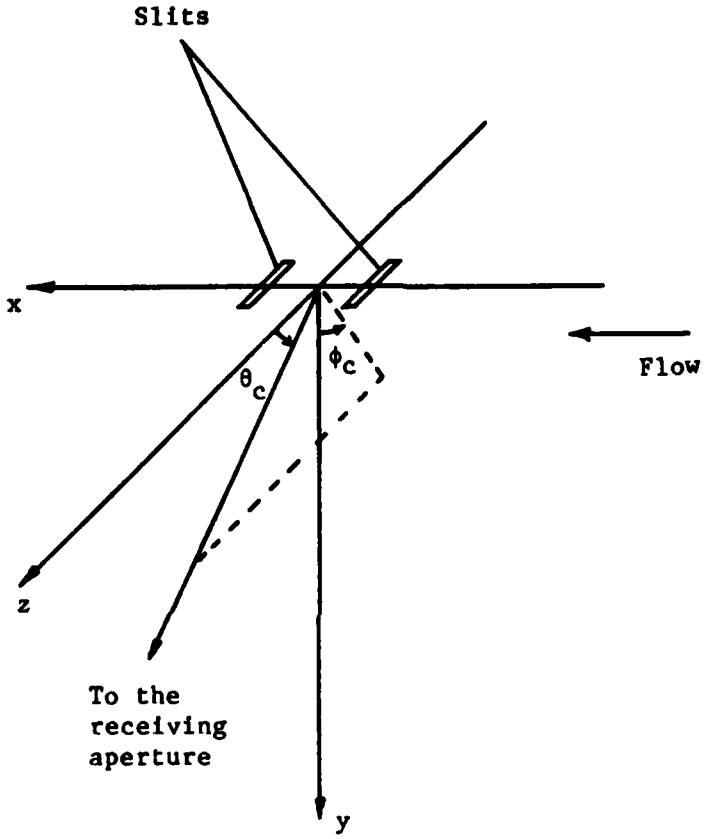

Fig. 4.8. The boundary layer coordinate system and the location of the receiving aperture.

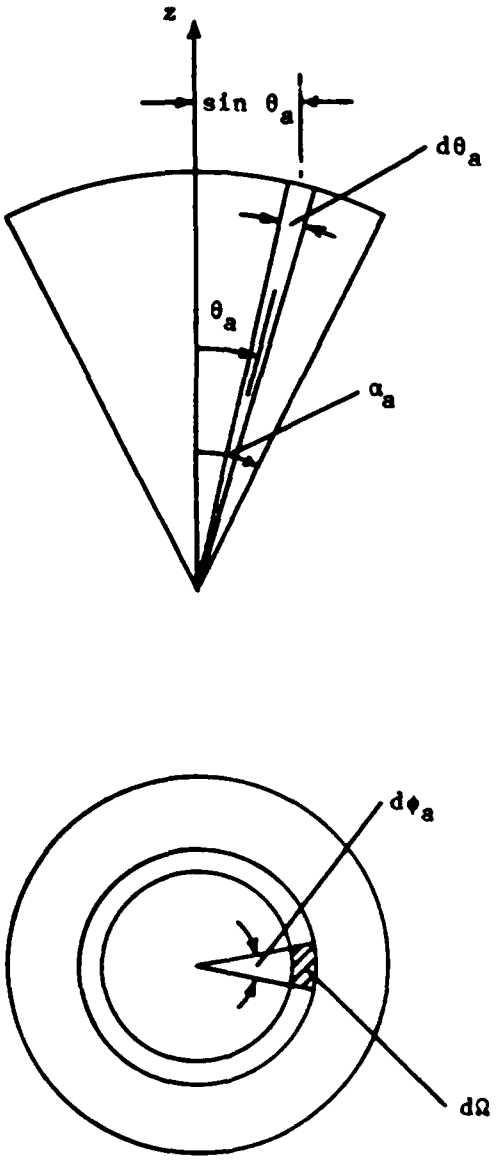

Fig. 4.9. Definition of a solid angle element in the aperture coordinate system.

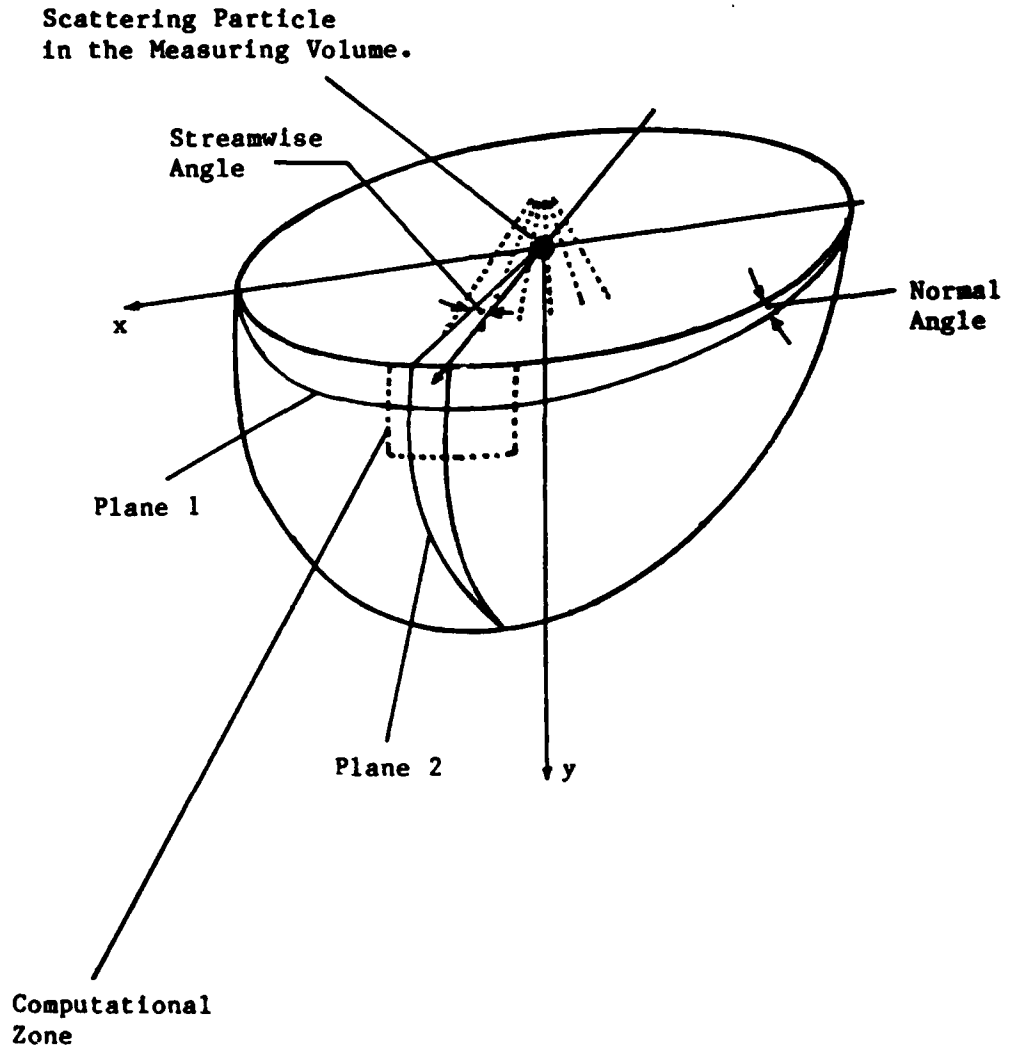

Fig. 4.10 Computational zone for studying the local signal properties.

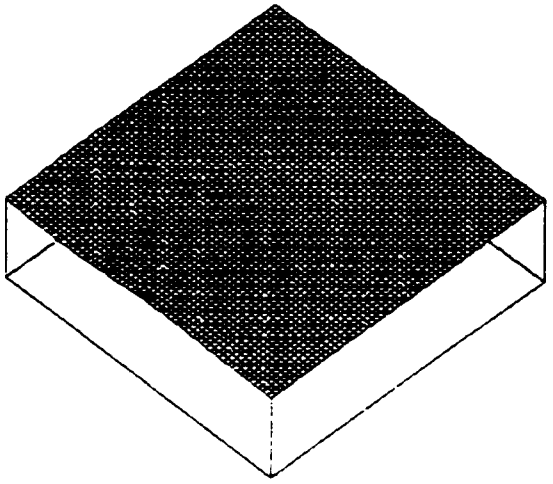

(a) Dust-particle diameter: 1 μm

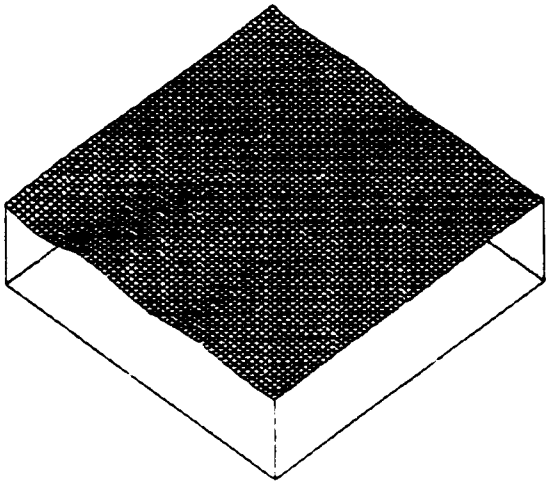

(b) Dust-particle diameter: 2 μm

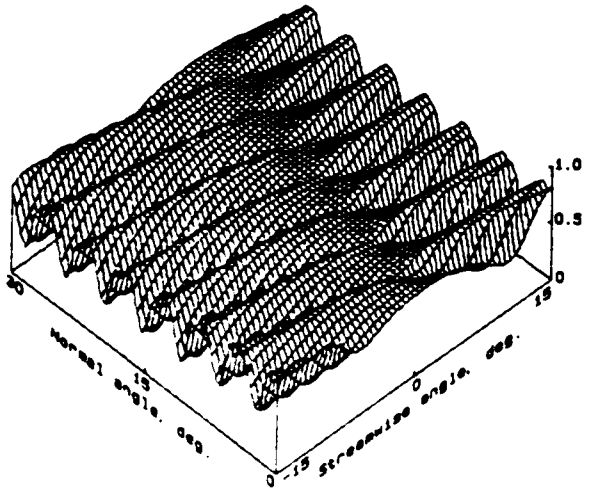

(c) Dust-particle diameter: 5 μm

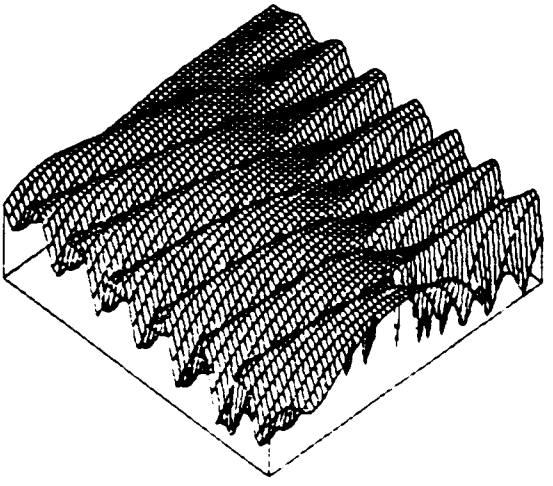

(d) Polystyrene latex particle diameter: 5 μm

Fig. 4.11. Local signal visibility:
Particle at x_o = 20 μm, y_o = 100 μm.

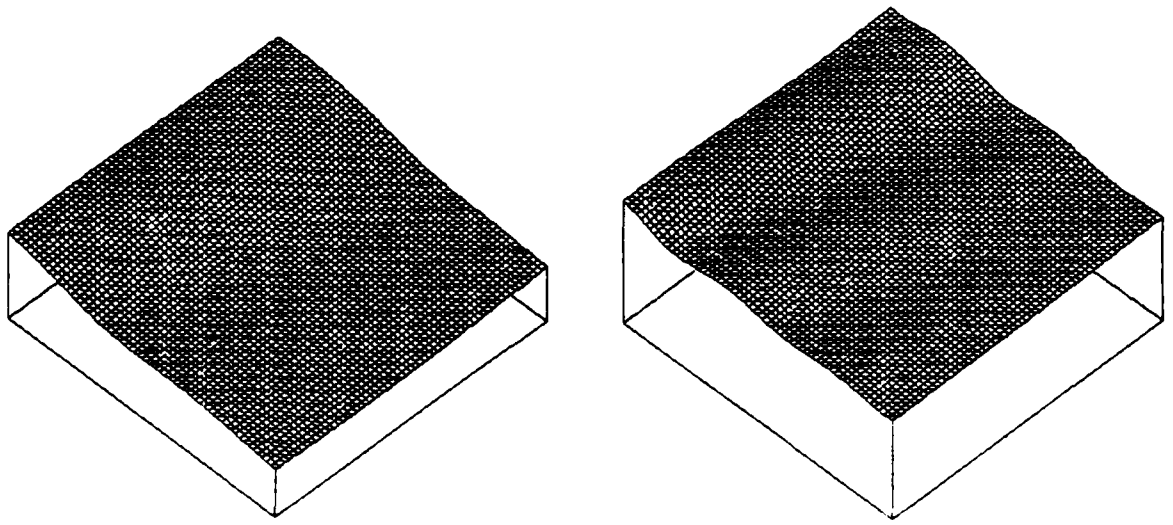

(a) Dust-particle diameter: 1 μm

(b) Dust-particle diameter: 2 μm

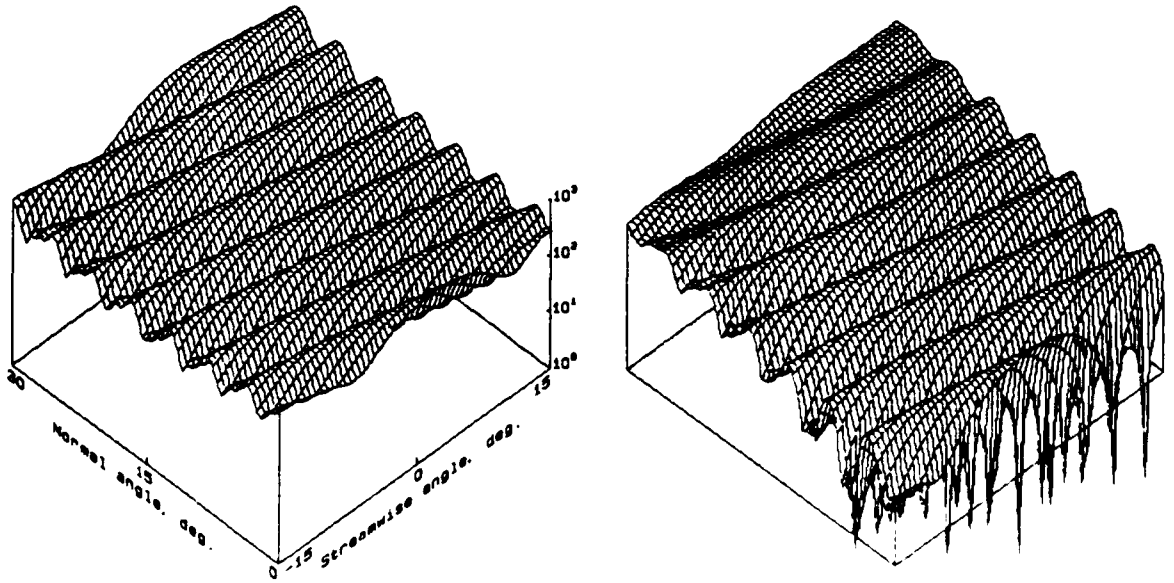

(c) Dust-particle diameter: 5 μm

(d) Polystyrene latex particle diameter: 5 μm

Fig. 4.12. Local SNR: Particle at x_o = 20 μm, y_o = 100 μm.

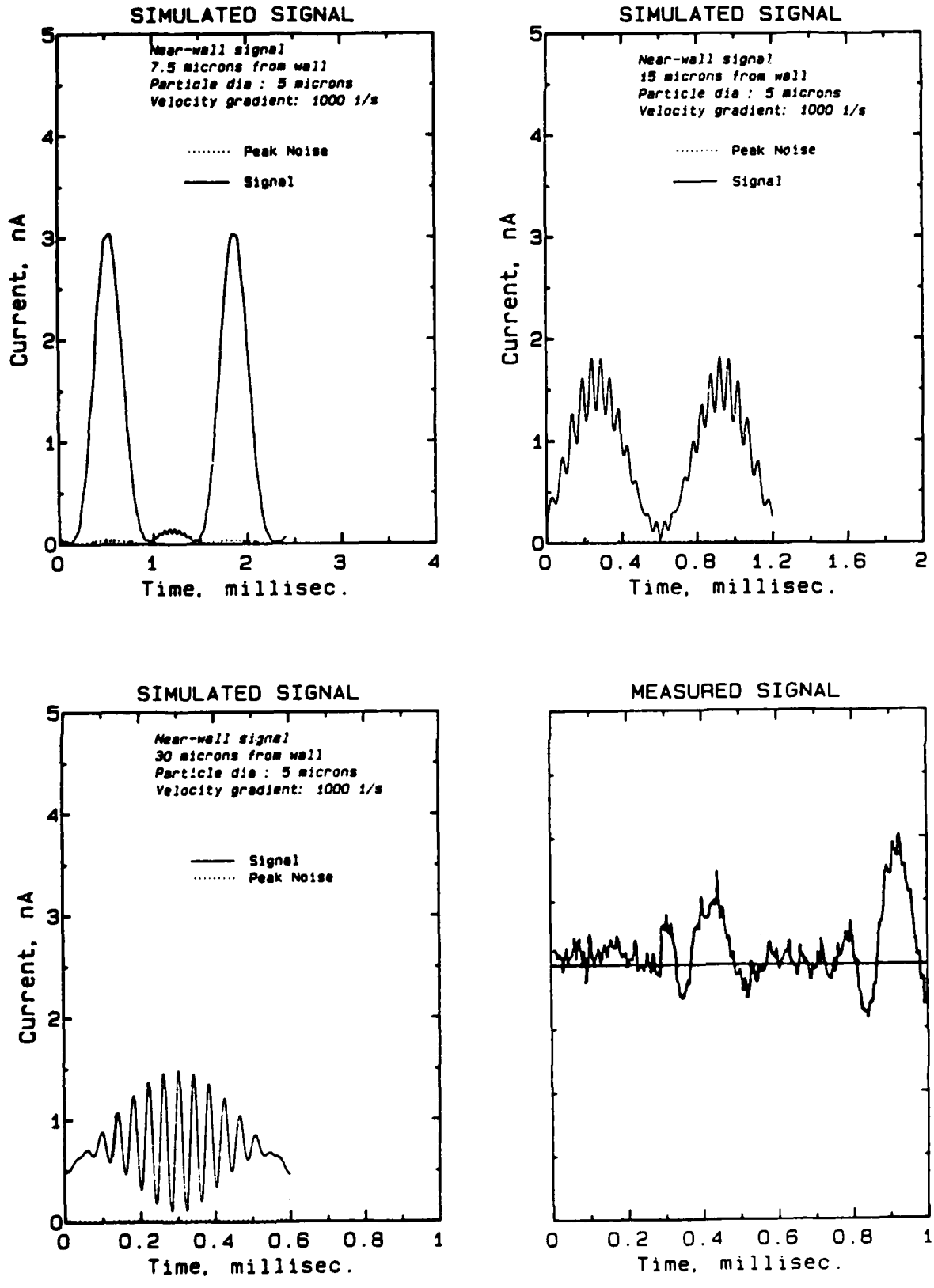

Fig. 4.13. Comparison of a measured near-wall signal with the simulated signals.

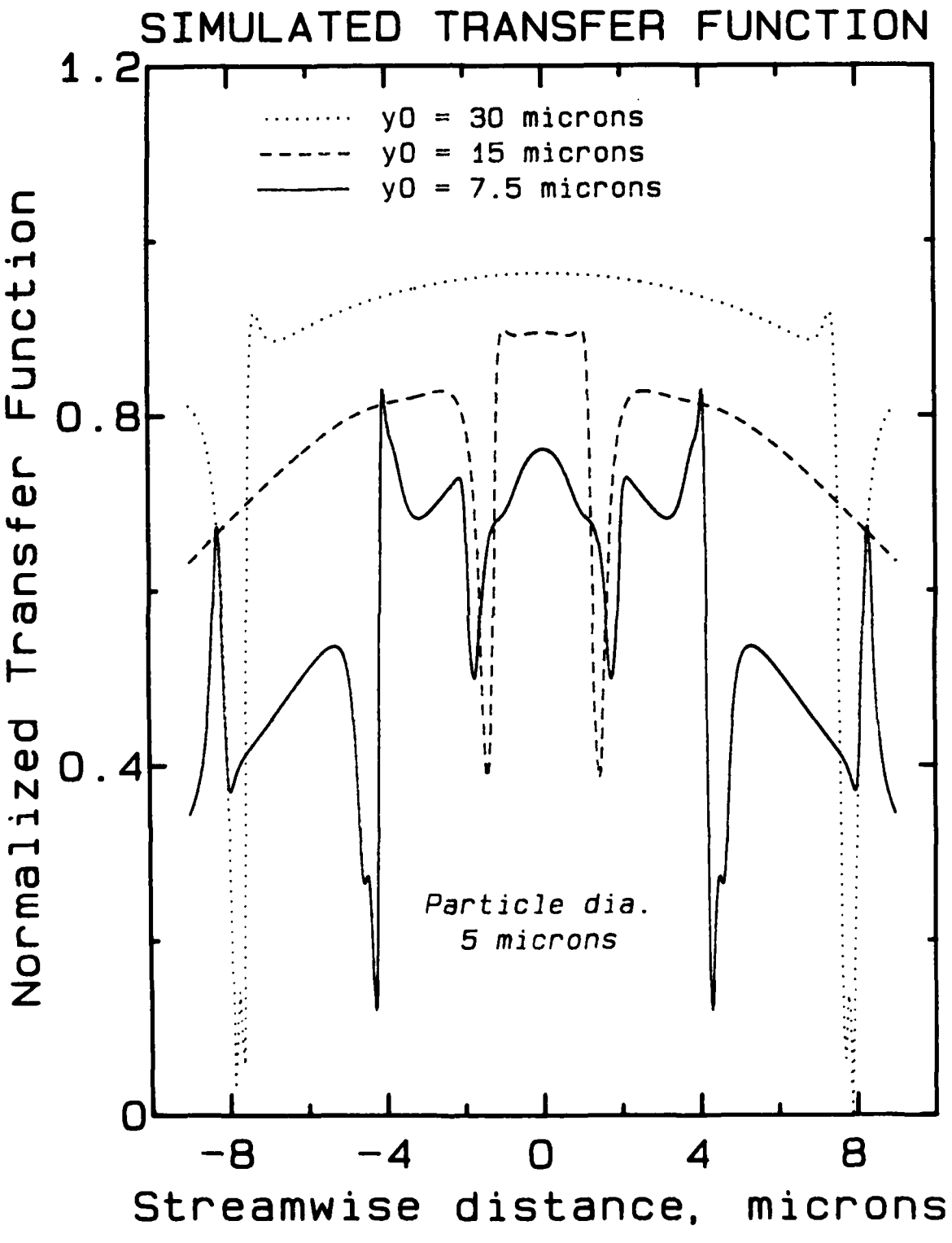

Fig. 4.14. Behavior of the transfer function near the wall.

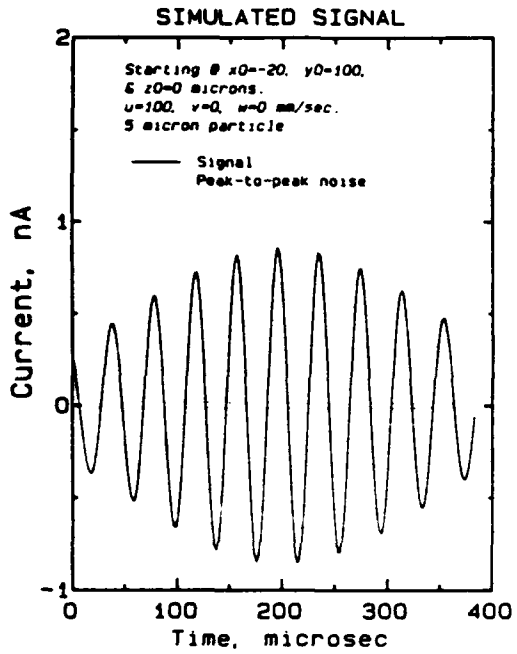

(a) No normal or spanwise velocity

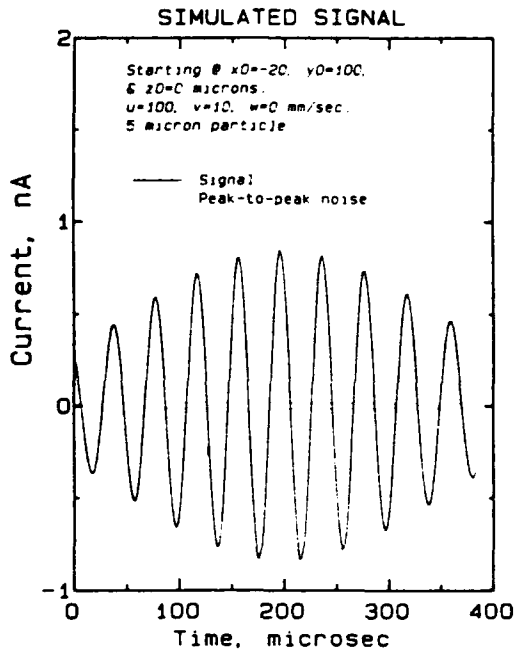

(b) Normal velocity

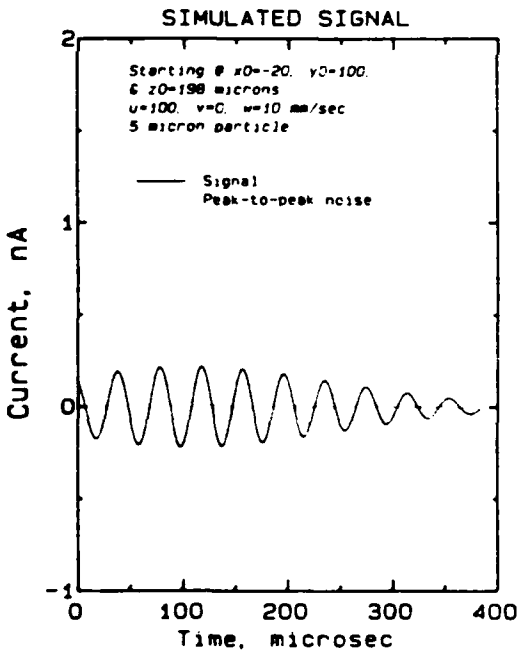

(c) Near-edge signal with spanwise velocity

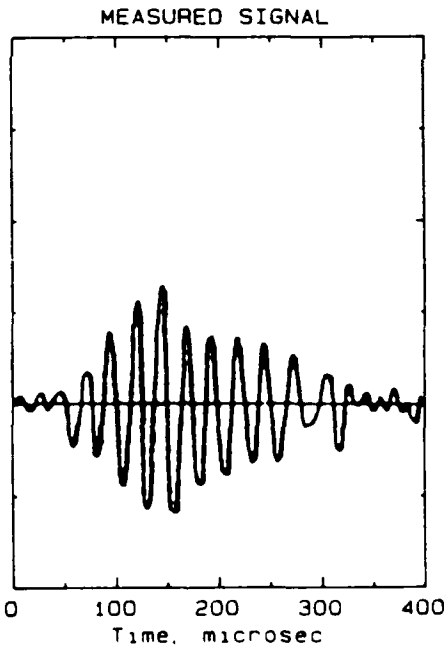

(d) A typical measured signal

Fig. 4.15. Comparison of a measured signal with the simulated signals.

(e) A measured signal without frequency shifting.

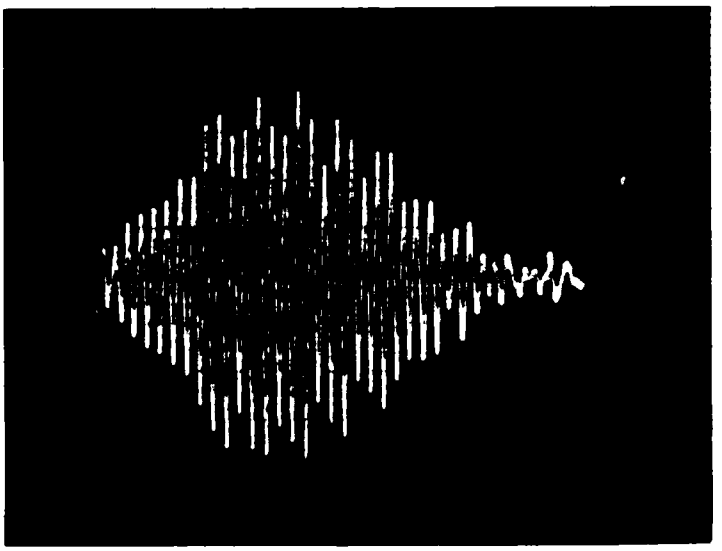

(f) A measured signal with frequency shifting.

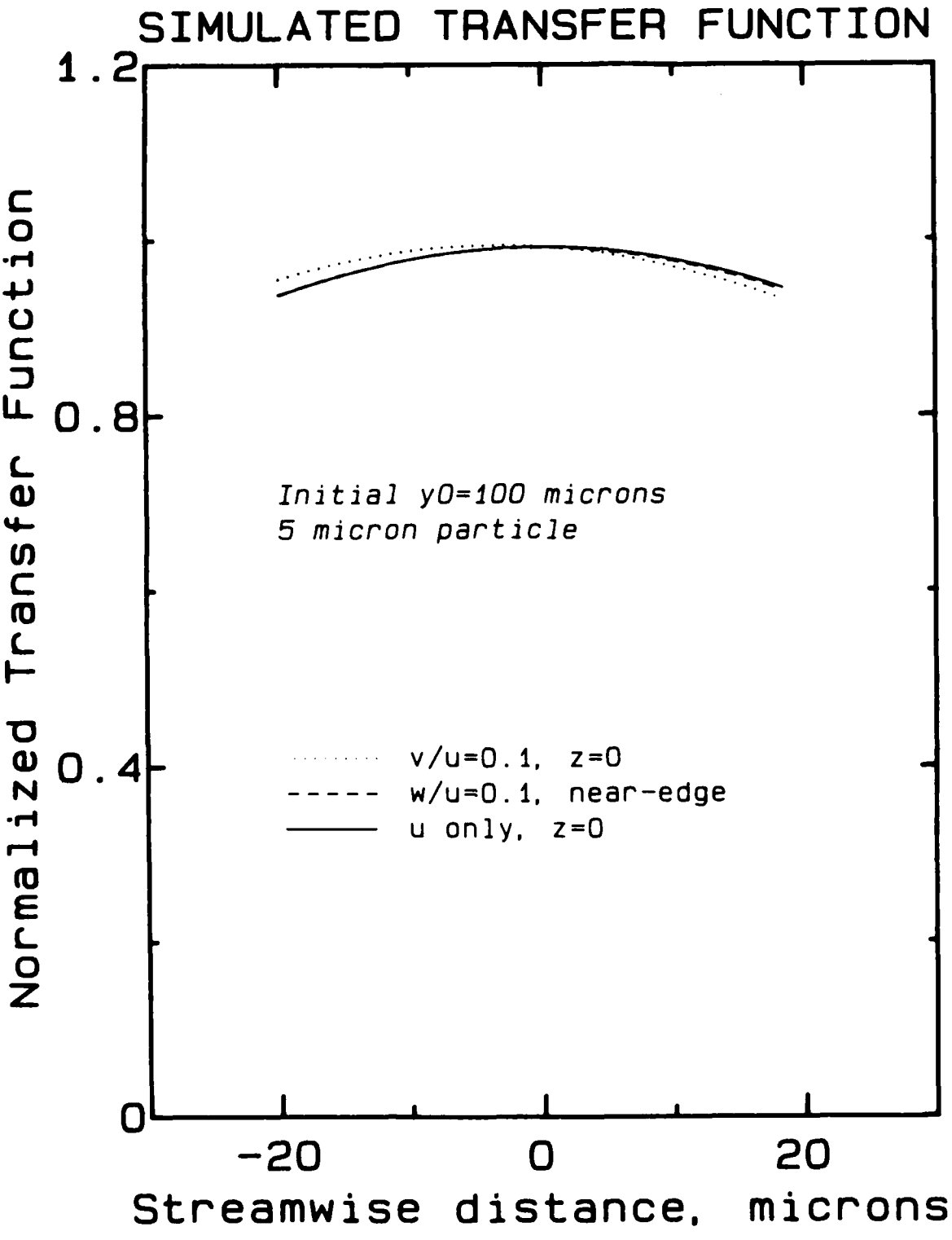

Fig. 4.16. Behavior of the transfer function in the measuring volume.

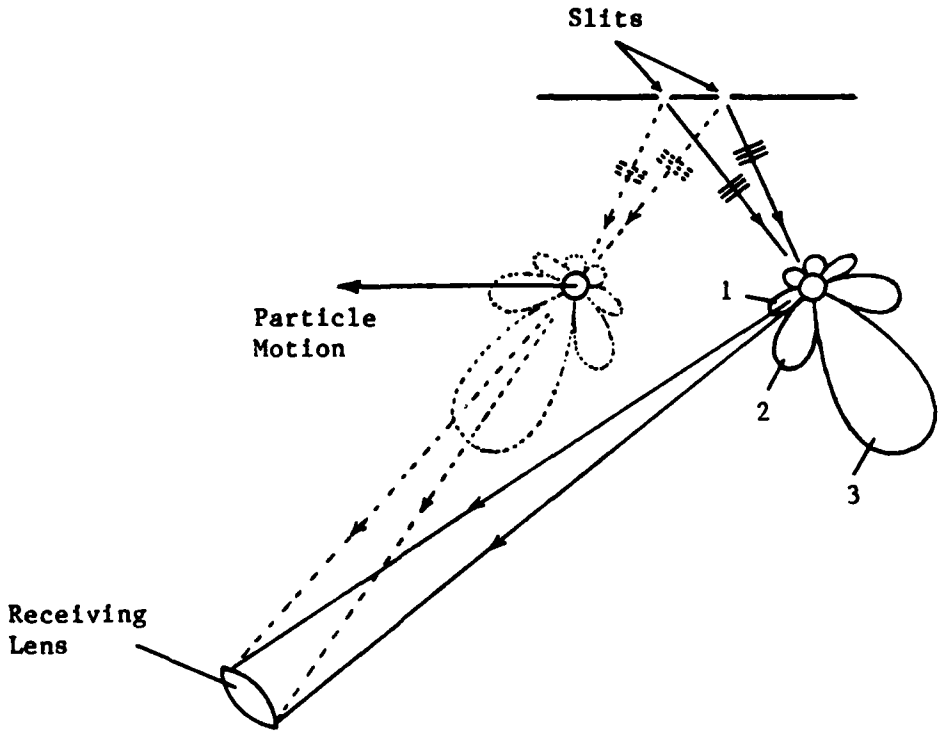

(a) Schematic representation of the intensity lobes sweeping across the receiving aperture.

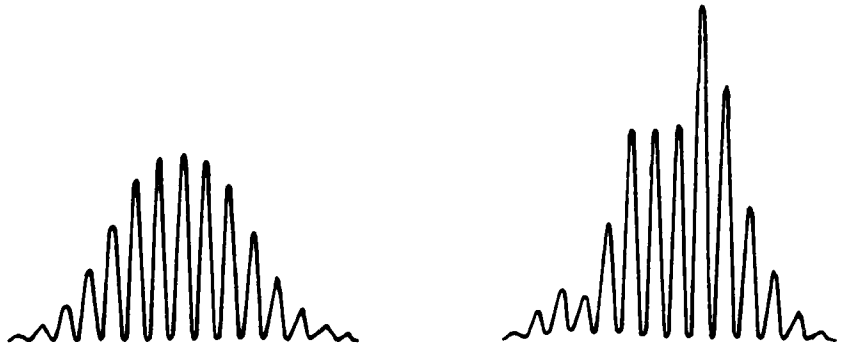

(b) Difference in the signal shape for the cases of isotropic and anisotropic scattering.

Fig. 4.17. Intensity modulation due to anisotropic scattering.

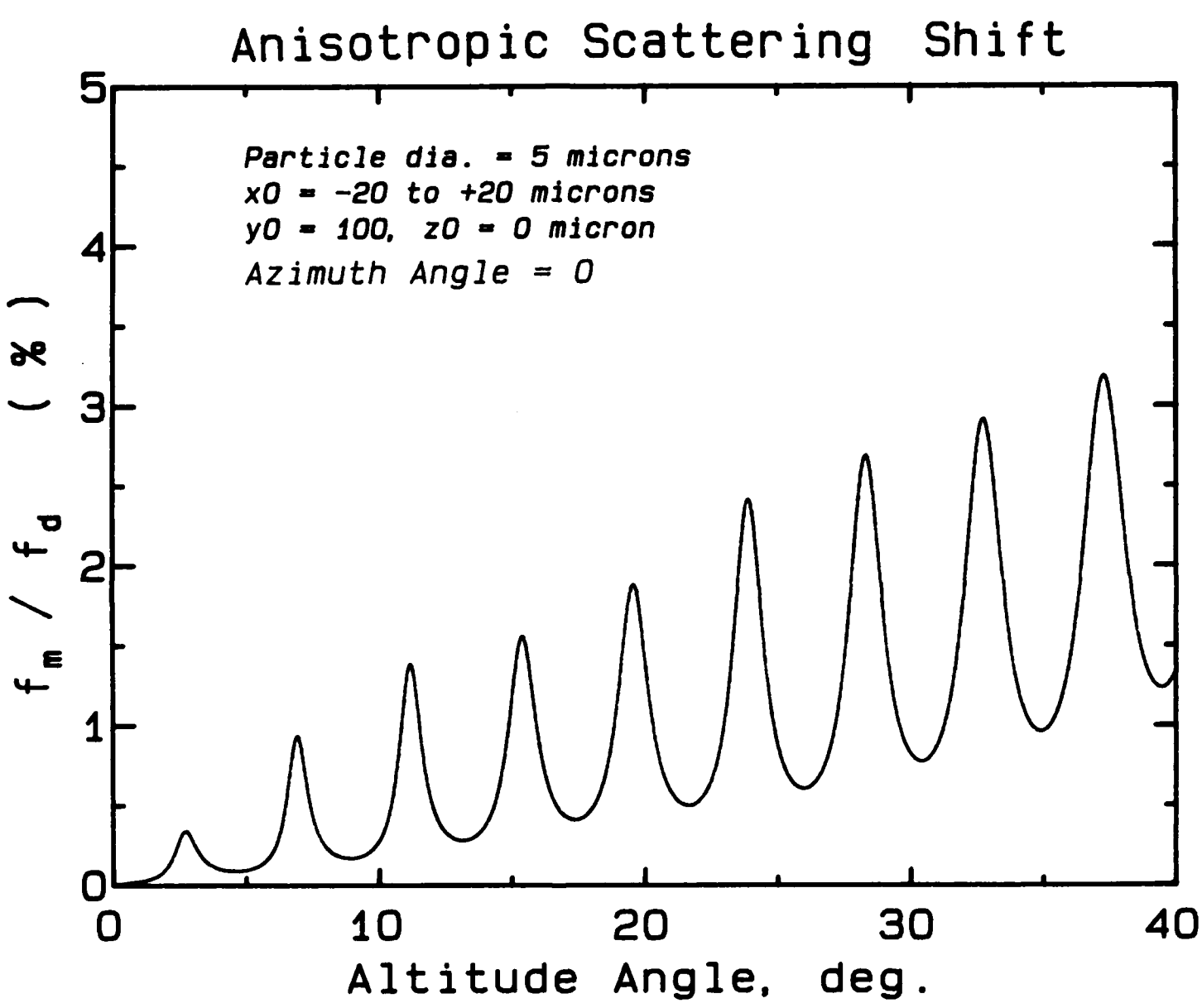

Fig. 4.18. Local value of anisotropic scattering shift in the side-scatter.

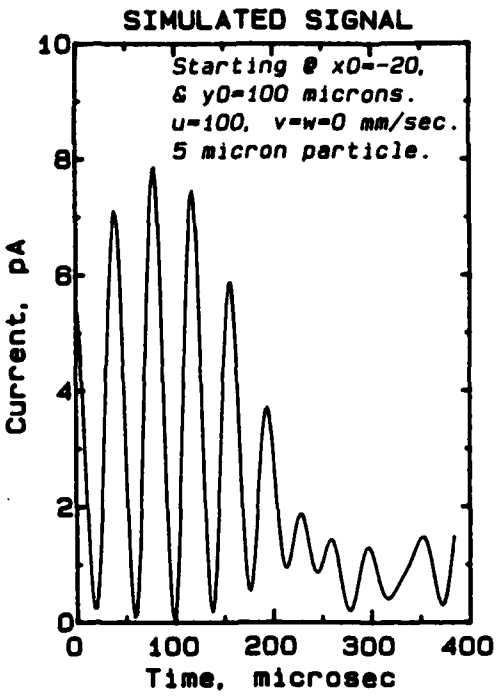

(a) M-polarization: Small aperture.

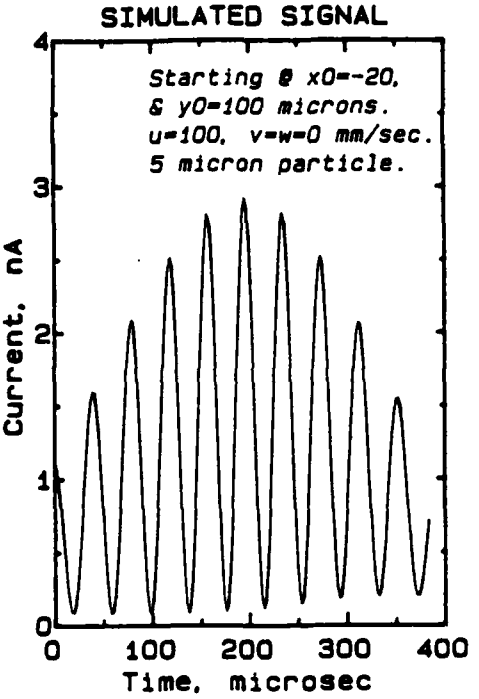

(b) M-polarization: Large aperture.

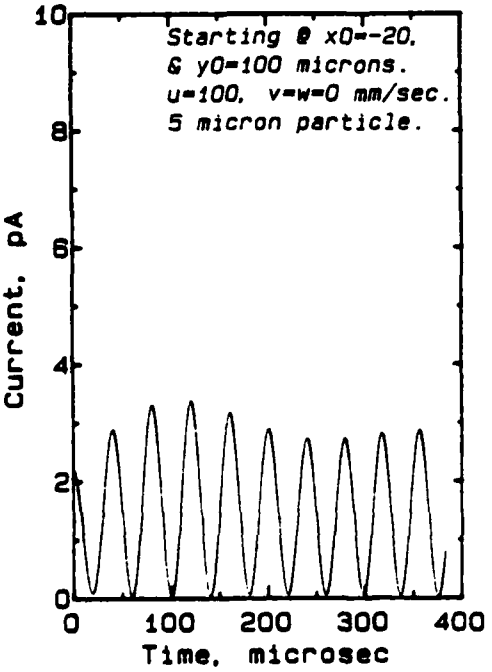

(c) E-polarization: Small aperture.

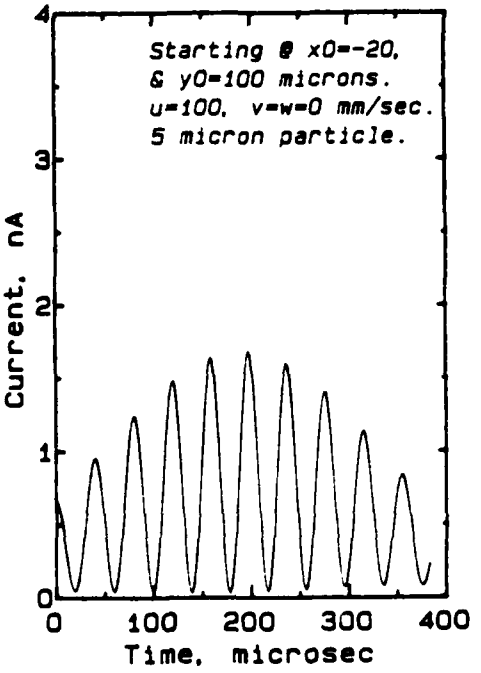

(d) E-polarization: Large aperture.

Fig. 4.19. An examination of intensity modulation due to anisotropic scattering: Receiving aperture at $\theta_c = 20°$, $\phi_c = 15°$.

Chapter 5

THE OPTICAL ARRANGEMENT

5.1 The Schematic Design of Focusing Optics

A schematic of the optical arrangement required for this device is shown in Fig. 5.1. A single-wavelength laser beam (see Table 5.2 for detailed specifications) is passed through a train of optical elements referred to as focusing optics. The final element in the focusing optics is a pair of slits which produces cylindrical waves as discussed earlier. Other optical elements constituting the focusing optics are described later in this chapter. The light scattered by particles in the measuring volume is collected by another optical setup known as receiving optics. The receiving optics of conventional LDV system have been adopted in the present apparatus. The focusing optics are very unconventional.

The laser head produces a laser beam with circular cross-section. The intensity of light is maximum at the center and diminishes away from it, following a Gaussian distribution. The $1/e^2$ diameter of the beam is typically 1-2 millimeters. The purpose of the focusing optics is to transform such a beam into two closely-spaced thin sheets of laser light which are focused on the slits. The sheets are 5 microns wide, 10 microns apart and have elliptic cross-sections as mentioned in Chapter 4. It is also possible to obtain a slight shift in the frequency of one of the sheets in order to facilitate measurement of flow reversal.

The schematic design of the focusing optics is illustrated in Fig. 5.2. It consists of a pair of slits, a cylindrical lens and a beam generator. The function of the slits has already been described in the previous chapters. The cylindrical lens is used to squeeze the laser beams into very thin sheets which are focused onto the two slits.

The beam generator accomplishes the following three functions:

1. Beam splitting
2. Frequency shifting
3. Beam merging

The incoming laser beam is split into two beams with approximately equal power in each beam. The frequency of one of the beams could be shifted if desired. After frequency shifting, the beams are merged and passed through the cylindrical lens. Since the cylindrical lens is small in size, the two beams are overlapped on the lens with no apparent spacing between them. Nevertheless, the beams are at a small adjustable angle (fraction of a degree) which allows focusing them on two separate slits.

5.2 Cylindrical Lens

The cylindrical lens performs important functions which require a high degree of precision. This section deals with the theoretical basis of these functions as well as practical aspects of selection and use of the cylindrical lens.

5.2.1 Functions of Cylindrical Lens

The functions of the cylindrical lens may be explained in terms of certain established optical phenomena. It is known from the optics of Gaussian laser beams that a positive lens focuses laser beams to a spot. Normally, for a given laser beam, the spot size is small for smaller focal length and occurs in the vicinity of geometrical focal plane. In the case of a cylindrical lens, the circular beam is focused to a thin line whose width corresponds directly to the focal length. This feature of a cylindrical lens is used to form the sheets. Figure 5.3 shows changes in the cross-section of a laser beam as it passes through a cylindrical lens. The waist of the beam is coincided with a slit in the present system. The lens is movable normal to the slits with a high precision. This arrangement permits maximum power transmission through the slits.

Another phenomenon of interest related to a cylindrical lens is illustrated in Fig. 5.4. According to geometrical optics, a bundle of parallel rays in the plane of a thin cylindrical lens (Fig. 5.4) is focused on a point. Also, two rays at an angle α_b are focused at two points seperated by a distance S, such that

$$S = \alpha_b f_c \tag{5.1}$$

where f_c is the focal length of the lens. Laser beams may be modeled as a bundle of rays. Hence two beams approaching a cylindrical lens at a certain angle would be focused at different locations in the focal plane. The spacing between the two waists would be roughly proportional to the angle between the beams. Based upon Eqn. (5.1), the beam angle is estimated to be 0.1 degree for the present system. Since the waist-spacing must accurately match the slit-spacing, the angle between the beams is kept adjustable.

As shown in Fig. 5.4, displacement of the lens parallel to the focal plane by a certain amount results in movement of the focused spot by the same amount. This is strictly valid only under the approximation of geometrical optics. With a relatively complex relationship between displacement of the lens and displacement of the waist, this phenomenon occurs in the case of a laser beam too. In the present device, it is used to locate the laser beams properly over the slits.

5.2.2 Performance of the Cylindrical Lens

The present system incorporates a precision plano-cylindrical lens (Melles Griot Model 01 LCP 000). The nominal focal length of the lens is 6.35 mm. It is one of the highest quality, small-focal-length cylindrical lenses commercially available. In order to ascertain the size of the laser waist produced by this lens, we may use the following formula suggested by Self (1983).

$$\frac{w_o}{w_{o1}} = \frac{1}{\{[1 - s_1/f_c]^2 + (z_{R_1}/f_c)^2\}^{1/2}} \tag{5.2}$$

where

$$z_{R_1} \equiv \pi w_{o1}^2/\lambda \ . \tag{5.3}$$

This formula provides the ratio of the waist after the lens to that before it expressed in terms of focal length, wavelength of laser and distance s_1 of first waist from the lens. First waist occurs inside the laser cavity as shown in Fig. 5.3. The path length from this waist to the lens would vary from one application to the other. We have considered two cases with s_1 = 0.5 m and 2 m. The resulting waist size

and beam width in the vicinity of the waist are shown in Fig. 5.5. The beam profile is known to be parabolic near the waist and follows the following relation (Self, 1983):

$$w = w_o [1 + (z/z_R)^2]^{1/2} \qquad (5.4)$$

where z is the distance along the direction of propagation of the laser beam.

Figure 5.5 is based on an original waist of 0.55 mm and a wavelength of 0.5145 micron. Since the second waist occurs inside the glass substrate of the slits, the wavelength in Eqn. (5.4) has been modified accordingly. The refractive index of glass is taken as 1.5 for this purpose. It may be pointed out that w as evaluated from Eqn. (5.2), does not include the effect of glass substrate. However, it may be shown that presence of the glass disc does not affect the waist size significantly. According to Fig. 5.5, a smaller waist is produced if the lens is located farther from the laser head. In practice, it may not always be true. At larger distances, the beam diverges and cannot be handled properly by a lens of small width. In the present device, the lens width is 6 mm; best performance is obtained from the central portion only. Figure 5.5 also indicates that laser beam diverges faster in the vicinity of a smaller waist making it difficult to focus it on a slit. In general, the slit should be within a few microns of the waist along z-axis in order to obtain maximum power transmission. It also requires a submicron precision in lateral positioning, i.e., the lens displacement parallel to plane of the slits should be controllable to a fraction of a micron. In the present system, the lens is moved normal and parallel to the slit-plane using two motorized translators (Model 17009/18009 of Oriel Corporation). The translators have a rated resolution of 0.02 micron. The least count in the digital readout of the position is one-tenth of a micron. The lens is also rotatable about an axis normal to the slit plane. This arrangement is shown in Fig. 5.6. The rotational stage (Model 470-A of Newport Corporation) has a sensitivity of 21 microradians which is less than 1 % of the width-to-length ratio of each slit; hence, it satisfactorily aligns laser waists with the slits. A rotational base is used to mount the lens assembly to the outer casing of the focusing optics.

5.2.3 Experimental Evaluation of Cylindrical Lens

The performance of the cylindrical lens has been described in terms of a simple model based on thin lens theory. In practice, a lens of small focal length has substantial thickness. Furthermore, there may be imperfections in the curvature of the surface. Also, spherical abberation is likely to affect the final waist size because incident beam covers a large portion of the lens width. It was found appropriate to evaluate the lens experimentally in order to ascertain the influence of above-mentioned effects on the shape and size of the waist. Two types of experiments were conducted.

(1) Chopping Experiments

The parameters of the laser beam were deduced by chopping it with a knife-edge and observing variation in laser power transmitted through the chopper. Versions of this method have been proposed by other researchers in the past. Arnaud et al. (1971), Skinner and Whitcher (1972), Suzaki and Tachibana (1975), and Firester et al. (1977) are some of the earlier users of this technique. The experimental setup for chopping is shown in Fig. 5.7. The focusing lens is large enough to collect almost all the light after diffraction from the knife edge. Power is measured using a fast-response photodiode. In the present setup, the response time of the photodiode is 10 ns. The total chopping time may easily be kept large enough to avoid the effects of photodiode delay on the desired signal. Photodiode output as a function of time may be displayed on an oscilloscope screen. Characteristics of this display are used to evaluate the waist-size as well as the intensity distribution in the plane of the waist.

In the case of a Gaussian intensity distribution the power variation with time follows an error function. Significant deviations from a symmetric error function were noticed in certain experiments. This situation corresponds to a non-Gaussian distribution of intensity in the waist. Dark and bright regions appear in the waist-plane if the laser beam is not centered properly on the lens.

As shown in Appendix D, for a symmetric error function the beam waist may be expressed as follows:

$$2w_o = 2.97\ v_c\ \Delta t \qquad (5.5)$$

where v_c is the speed of the chopper blade and Δt the time interval between the drop in power from 75% to 25% of the total power in the beam being chopped.

In order to measure the waist, the lens is moved back and forth from the chopper and rotated about an axis normal to it until the sharpest drop in power is observed on the oscilloscope. Details of the chopping method, including the required sensitivity of the above-mentioned adjustments, is documented in Appendix D.

According to chopping experiments, the beam waist was found to be 5 ± 1 microns. In contrast to prediction based on the thin lens theory, there is no significant decrease in the beam waist with increasing distance from the laser head.

(2) Scanning Experiments

The size and intensity distribution of the waist were further explored by scanning the waist across a slit. As shown in Fig. 5.8, the scanning experiment may be conducted with the assembled focusing optics. Hence it measures the beam waist inside the glass substrate and not in air as in the case of chopping experiments. The motion of the lens was monitored to a precision of 0.1 micron using the motorized translators. The power in transmitted laser light is measured using a collecting lens and a photodiode connected to a power-meter. The result of a scanning run for an improperly aligned beam is shown in Fig. 5.9. Two large peaks, in the power output in Fig. 5.9(a), represent the two slits which are 10 microns apart. The smaller peaks indicate that intensity distribution is not Gaussian and consists of fringes as interpreted in Fig. 5.9(b). Evidently, a number of bright bands of varying intensity occur in the waist-plane. This problem may be remedied by properly centering the incoming laser beam on the lens. The result of scanning for a properly aligned beam is shown in Fig. 5.10. The secondary peaks in the intensity of the waist plane have been suppressed but not completely eliminated.

Assuming a Gaussian profile, the waist of the beam may be evaluated from a measurement of the full-width of a hump at half the maximum power (FWHM). The $1/e^2$ size of the waist is 1.7 times FWHM. This factor is based on a small ratio of slit-width to waist-width which is applicable to the present arrangement. However, it must be modified for larger slits or smaller waists as described in Appendix D. According to Fig. 5.10, the beam waist is approximately 5 microns. This substantiates the theoretical inference that the presence of glass substrate does not affect the waist size.

5.3 Beam Generator

The purpose of beam generator has been discussed earlier. Several options were considered for achieving the stated functions of this unit. Two different designs are discussed in this section. An outline of a potentially promising design has been given alongwith a detailed account of the idea being tested now.

5.3.1 Single-Component Design

All three functions of the beam generator described in Section 5.1, could be accomplished by a single component. An acousto-optic modulator with a suitable range of variable frequency may be used to split a beam into a shifted and unshifted beam. A discussion of theory and modern applications of acousto-optic phenomenon has been presented by Adler (1967). It is known that close to the modulator exit, the two beams would be well-merged. This arrangement is shown in Fig. 5.11. The angle between the beams depends upon the shift-frequency in accordance with the following relations.

Angle between the beams:
$$\alpha_b = \frac{\lambda}{\Lambda} \tag{5.6}$$

Wavelength of sound:
$$\Lambda = \frac{c_s}{f_s} \tag{5.7}$$

where, c_s is the speed of sound in the medium and f_s is the frequency of sound waves. Sound frequency is imparted to one of the output beams, known as shifted beam.

If the cell is short, then several output beams with varying intensity and frequency shift (in multiple of f_s) would appear in the output. In order to eliminate higher modes, the cell length must satisfy the following relation.

Length of the cell:
$$\ell_{am} \gg \frac{\Lambda^2}{2\pi\lambda} \tag{5.8}$$

This condition is knwon as Bragg reflection condition; hence the name Bragg cell for the device. For a certain tilt of the cell relative to the incoming beam, this device would divide most of the energy between an unshifted beam and a first mode shifted beam. For a given cell material and laser light, the length of the cell satisfying the Bragg condition is inversely proportional to square of the shift-frequency, i.e.,

$$\frac{\ell_{am_2}}{\ell_{am_1}} = \left(\frac{f_{s_1}}{f_{s_2}}\right)^2 \tag{5.9}$$

We may estimate the desirable frequency shift from the following data:

$S = 10$ microns, $\lambda = 0.5145$ micron

$f_s = 6.35$ mm $c_s = 5000$ m/s (glass)

Substituting the above data in Eqns. (5.1), (5.6), and (5.7).

$$f_s = 15.3 \text{ MHz}$$

Since f_s is directly proportional to α_b, an estimated ± 10% desirable adjustability in α_b would require f_s to be adjustable by ± 1.5 MHz.

Some of the technical difficulties with the manufacture of such a Bragg cell are as follows:

(1) The proposed operating range, ± 1.5 MHz, is higher than that normally achieved with such devices. A significant drop in efficiency occurs at off-design conditions.

(2) Knowing that commercially available 40 MHz cells are 65 mm long, length of the proposed cell for equivalent performance may be

calculated from Eqn. (5.9). According to this criterion the proposed cell should be 440 mm long which is obviously not feasible in practice. Hence a compromise is to be made by permiting a part of the input power in undesirable higher-mode beams.

(3) In order to adjust the beam angle (and hence waist-spacing) with a high degree of precision, the shift frequency should be accurately adjustable. This requirement may offer difficulties in designing pertinent electronics.

According to the preliminary analysis of a single-component design presented here, such an arrangement is permissible. However, it offers some design challenges which need further investigation.

5.3.2 Discrete-Component Design

In the present hardware, separate components are used to accomplish the functions of the beam generator stated in section 5.1. Commercial LDV components (from TSI Incorporated) are employed for splitting the laser beam into two parts and shifting the frequency of one of the beams by 40 MHz. As shown in Fig. 5.12, the shifted and unshifted beams are brought to a partial mirror which allows half of each beam to propagate towards the cylindrical lens. The other halves are rejected to a beam-dump. In contrast to the single-component design, this arrangement allows operation without frequency shifting as well; i.e., a Bragg cell is not necessarily needed for generating two beams at a slight angle.

All the mirrors, including the partial mirror, are made up of dielectric coatings on glass which preserve polarization. The mirrors are mounted in standard mirror mounts (see Table 5.3 for specifications). These mounts allow tilting about two axes permitting independent positioning of each beam. According to the manufacturer's specifications, the mirror mounts have a sensitivity of 2 arc-seconds, which corresponds to a 0.5° rotation of the adjusting knob. Sensitivity is a small fraction (0.5%) of the required angle between the two beams. Hence, it is possible to obtain the desirable angle repeatedly with manual adjustments. Another parameter of interest is the displacement of the beam on the lens resulting from a certain amount of mirror tilt. Since mirror tilts during alignment are likely to be of the order of the angle

between the beams, displacement corresponding to nominal beam angle (0.1°) is considered an appropriate measure of this effect. The value of this parameter for each mirror is listed below.

Mirror-1:	770 microns
Mirror-2:	730 microns
Mirror-3:	550 microns
Partial Mirror:	500 microns

It may be noticed that beam displacement is particularly large for mirrors 1 & 2 which handle the right-hand side beam as shown in Fig. 5.12. Hence, special care is required in locating this beam than the left-hand side beam whose tilt and position is controlled by Mirror 3 and the partial mirror. This precaution has been taken into account in devising the alignment procedure for the instrument presented in Chapter 6.

Each laser beam may be displaced without changing the angular orientation by tilting the corresponding mirrors in the same sense. This idea is illustrated in Fig. 5.13(a). By tilting Mirrors 1 & 2 through angles θ_m each, a laser beam may be displaced approximately by an amount $\theta_m d_m$, where d_m is the distance between the mirrors. Since the distance d_m is known to be 25 mm for each pair of the mirrors, the sensitivity and the range of displacement may be estimated using the manufacturer's data as follows.

Sensitivity:	0.25 micron
Range:	± 1.9 mm

The sensitivity of displacement using mirror tilts appears satisfactory; however, the range is found inadequate. Additional means of displacing the laser beams have been incorporated in the present hardware. As shown in Fig. 5.13(b), displacement of one mirror has the same effect as simultaneous tilting of two mirrors. The present setup allows movement of one mirror in each pair. This arrangement is used for initial coarse centering of laser beams on the cylindrical lens. Final alignment is accomplished using high sensitivity mechanism of mirror tilting.

Various concepts associated with adjustment of position and angular orientation of laser beams have been illustrated with examples of adjustments in the plane of the incoming beams. Similar adjustments are needed normal to this plane. Details of all the alignments are considered in the next chapter.

Finally, it may be pointed out that the present hardware would be easily extendable to a two-point shear stress measuring system. The pair of beams rejected to the beam-dump has the same angular spacing as the one focused on the slits. The extra beams could be channeled to another assembly of cylindrical lens and slits for the second-point measurement.

5.4 Receiving Optics

A schematic of the receiving optics is shown in Fig. 5.14. A train of lenses is used to produce an image of the pinhole in the probe volume. The image region is known as the measuring volume. Light scattered by the particles in the measuring volume, passes through the pinhole and generates a signal in the photomultiplier tube. The current output from the photomultiplier is a direct measure of intensity fluctuation in the scattered light. This signal is amplified and transmitted to a counter signal processor which provides a digital output corresponding to the signal frequency. In the present arrangement, this output is tranfered directly to the memory of a laboratory computer (MINC-11). The computer saves and further processes the data.

Significant parameters of the receiving optics for three type of experiments are listed in Table 5.1. In order to obtain stronger signals, it is convenient to swing the receiving optics to a significant angle ($\sim 20°$) from the side-scatter towards the foward-scatter. As shown in Fig. 5.15(a), it results in the influx of direct light from the slits into the receiving optics. Though the direct light produces additional noise, the overall signal quality improves. This arrangement also results in detection of erratic signals from a very near-wall region. The signal processor is setup to discard such signals. Furthermore, as explained in Chap. 7, particle concentration diminishes in the close vicinity of the wall; hence, the non-representative signals are not expected to cause any serious errors in the measurement. The

signal corresponding to direct light (or zero velocity) may be filtered out in the first two cases described in Table 5.1. However, in the case of spanwise turbulence measurement, because of flow reversals, the direct light cannot be distinguished from valid signals. As illustrated in Figure 5.15(b), in an attempt to isolate the direct light a small receiving angle was used for the latter measurements.

The receiving assembly is mounted on a precision traverse mechanism in order to move the measuring volume within the viscous sublayer and locate it properly in the x and y bounds specified earlier. In the present setup, a tilt platform is used for this purpose. Movement of the measuring volume in the streamwise and normal directions is controlled by means of micrometers calibrated to microns. Displacements of the measuring volume per micron-displacement at the micrometers are as follows.

	Laminar Facility	Turbulent Facility
Normal to the wall:	10.5 microns	4.2 microns
Streamwise direction:	6.5 microns	2.6 microns

The above-mentioned sensitivity of adjustment meets the requirements satisfactorily for turbulent flow but only marginally for laminar flow. Improvements in receiving optics traverse are recommended for future experiments.

5.5 Hardware Requirements

Photographs of various components of the focusing optics are presented in Figs. 5.16 through 5.19. The hardware includes some of the standard LDV components from TSI Incorporated alongwith a selection of special parts. A detailed listing of all the components together with a brief description of relevant functions is presented here.

5.5.1 Standard Components

As pointed out earlier, beam splitting and frequency shifting in the focusing optics are achieved using standard LDV components. Also, most of the receiving optics are composed of standard hardware. A list of these parts is presented in Table 5.2.

5.5.2 Special Parts

A number of important functions in the optical arrangement of laser beams are accomplished using special parts obtained either from sources other than LDV component suppliers or manufactured locally. The pair of slits on chromium-coated glass was produced at the Integrated Circuit Laboratory of the Electrical Engineering Department at Stanford University. The outer casing of the device, lens holder, beam dump and several mounts and supports shown in the photographs were fabricated in the Mechanical Engineering Machine Shop at Stanford.

Table 5.2 presents a list of special parts obtained from commercial sources.

Table 5.1

PARAMETERS OF THE RECEIVING OPTICS

	Laminar Experiments	Turbulent Flow	
		Streamwise Measurements	Spanwise Measurements
Receiving Angle	22°	17°	5°
Receiving-Cone Angle	6°	12°	12°
Pinhole Diameter	50 microns	200 microns	130 microns
Pinhole Image Diameter	~ 100 microns	~ 150 microns	~ 100 microns

Table 5.2

STANDARD LDV COMPONENTS

Part No.	Source	Part Name	Function
95-4	Cooper Laser-Sonic	Laser Head with Etalon	Provides a laser beam: Wavelength 0.5145 μm; Max. Power: 1 W, CW argon-ion laser; TEM_{oo} mode, Beam dia.: 1.35 mm; Beam divergence: 0.6 mrad.
9102-12	TSI	Polarization Rotator	Aligns polarization axis with beam-splitter surface.
9115-1	TSI	Beamsplitter	Divides incoming beams into two parts in the focusing optics.
9180-12	TSI	Frequency Shift Assembly	Shifts frequency of one beam in the focusing optics.
9119 or 9118	TSI	Focusing Lens	Collects scattered light.
9140	TSI	Receiving Assembly	Focuses scattered light on photomultiplier pinhole.
9160	TSI	Photo-multiplier System	Converts optical signal into electrical signal.
1980B	TSI	Counter System	Measures frequency of the signal.

Table 5.3

SPECIAL PARTS

Part No.	Source	Part Name	Function
01LCP000	Melles Griot	Cylindrical Lens	Focuses laser beams on the slits.
17009/ 18009	Oriel Corp.	Motorized Translators	Positions cylindrical lens above the slits.
470A	Newport Corp.	Rotational Stage	Aligns cylindrical lens parallel to the slits.
10D20/ BD.1	Newport Corp.	1" Mirrors	Position beams in the beam generator.
10B20/ BS.1	Newport Corp.	1" Beam-splitter	Positions and merges beams in the beam generator.
MM2-1A	Newport Corp.	Mirror Mounts	Hold and align mirrors and the partial mirror.
04PIP011 04PIP013	Melles Griot	Pinhole 25/50 microns	Determines measuring volume size.
36	Newport Corp.	Tilt platform	Positions the measuring volume.

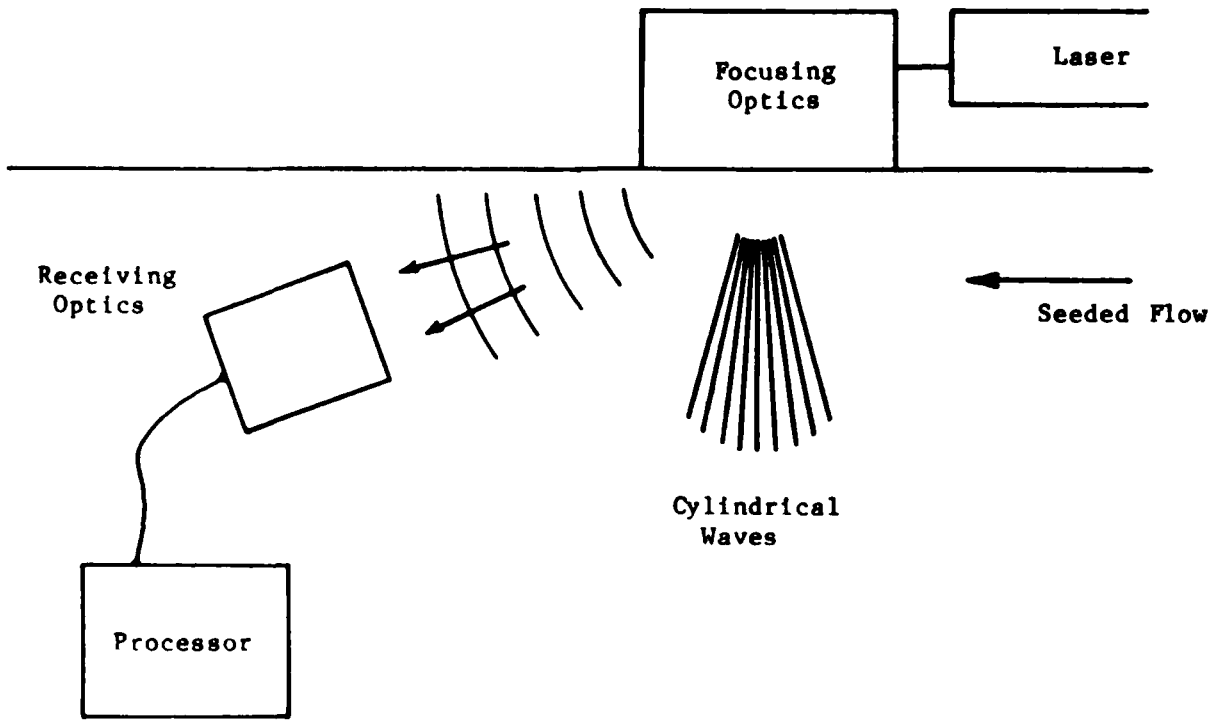

Fig. 5.1. Optical arrangement — schematic.

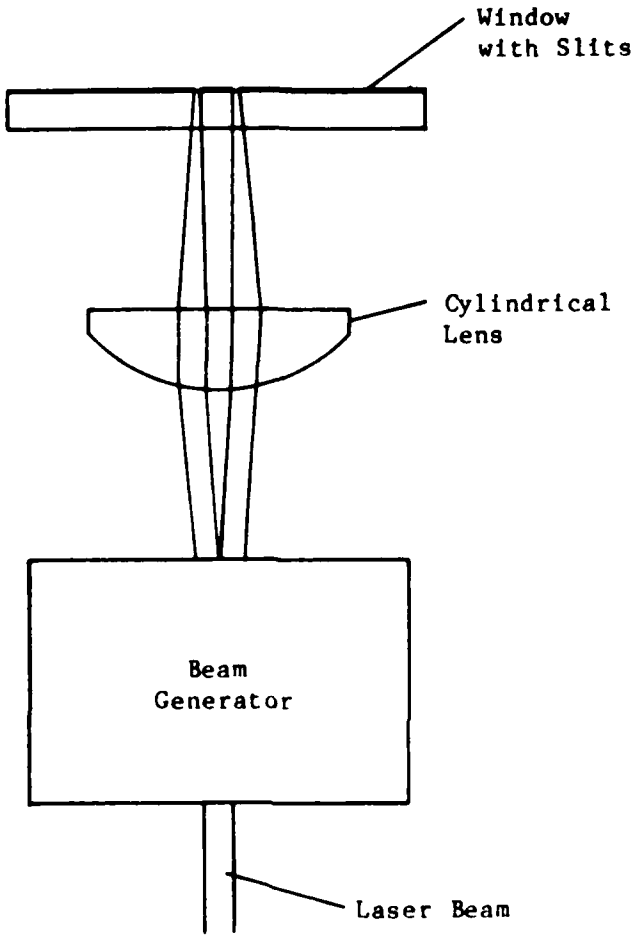

Fig. 5.2. Focusing optics -- schematic.

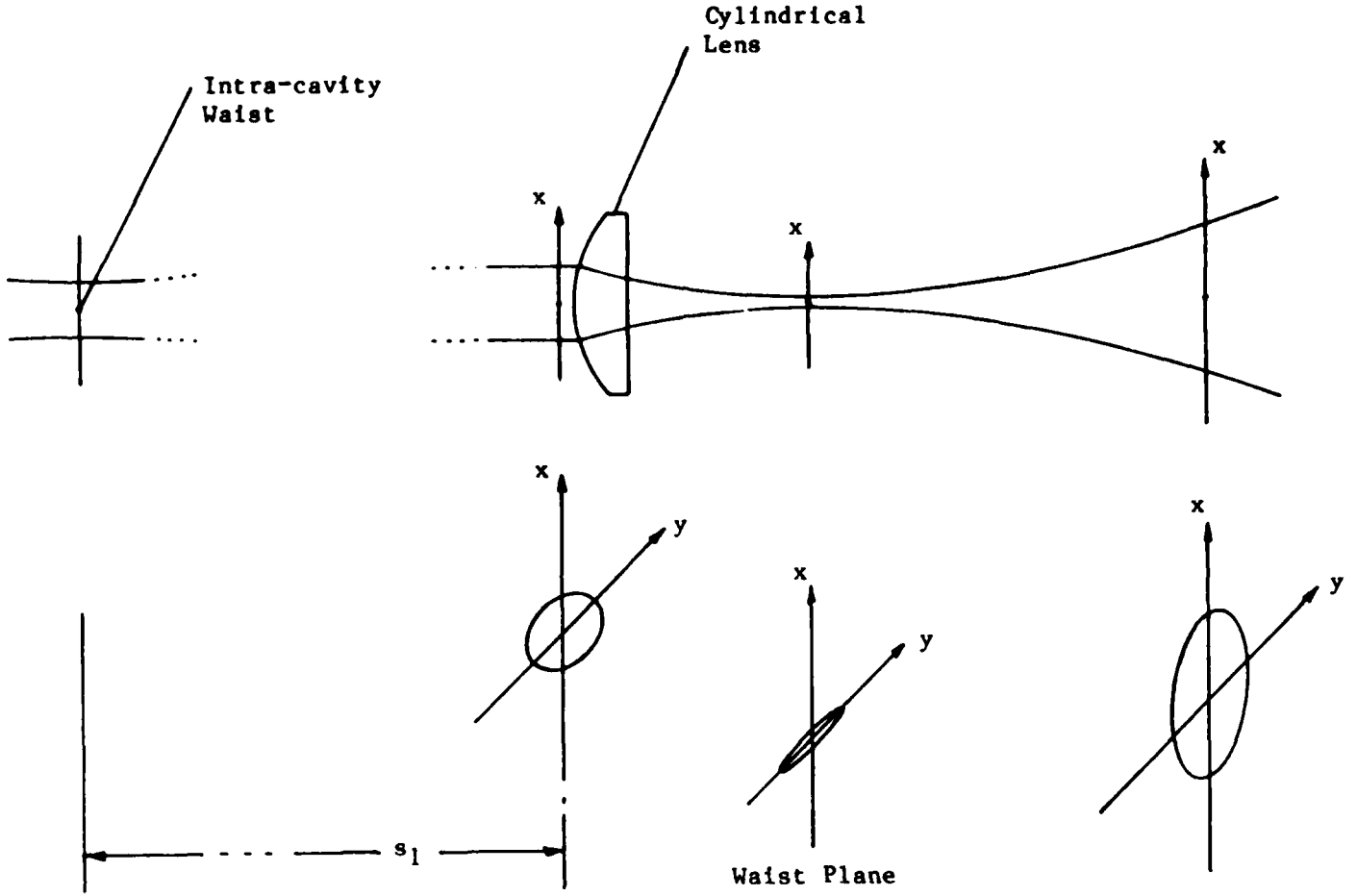

Fig. 5.3. Cross-section of laser beam before and after passage through a cylindrical lens.

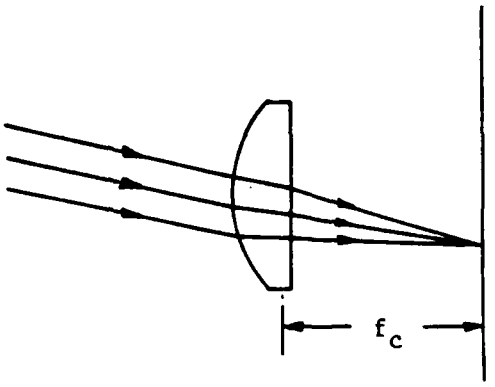

(a) Parallel rays focus on a point in the focal plane

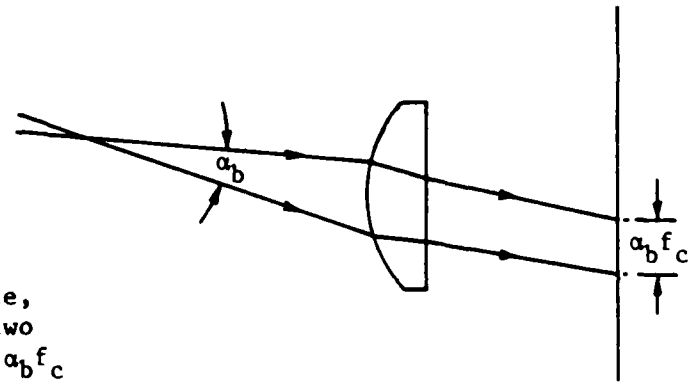

(b) Rays at an angle, α_b, focus at two points spaced $\alpha_b f_c$

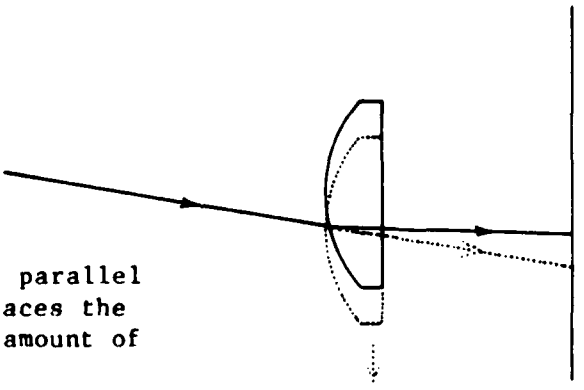

(c) Displacement of lens parallel to focal plane displaces the focused spot by the amount of lens displacement

Fig. 5.4. Illustration of the relevant principles of geometrical optics.

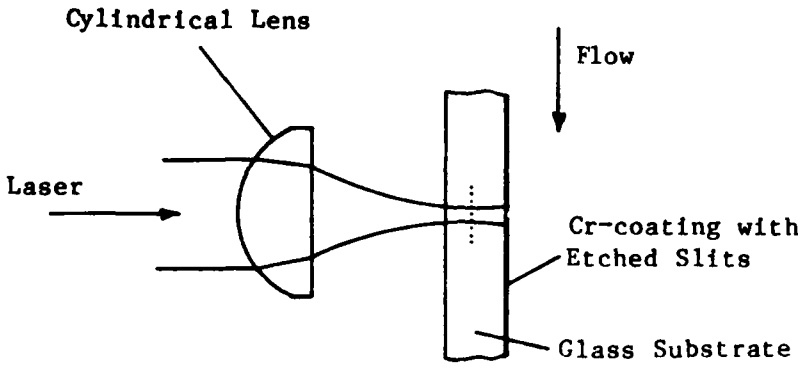

(a) De-focused laser sheet near the slit

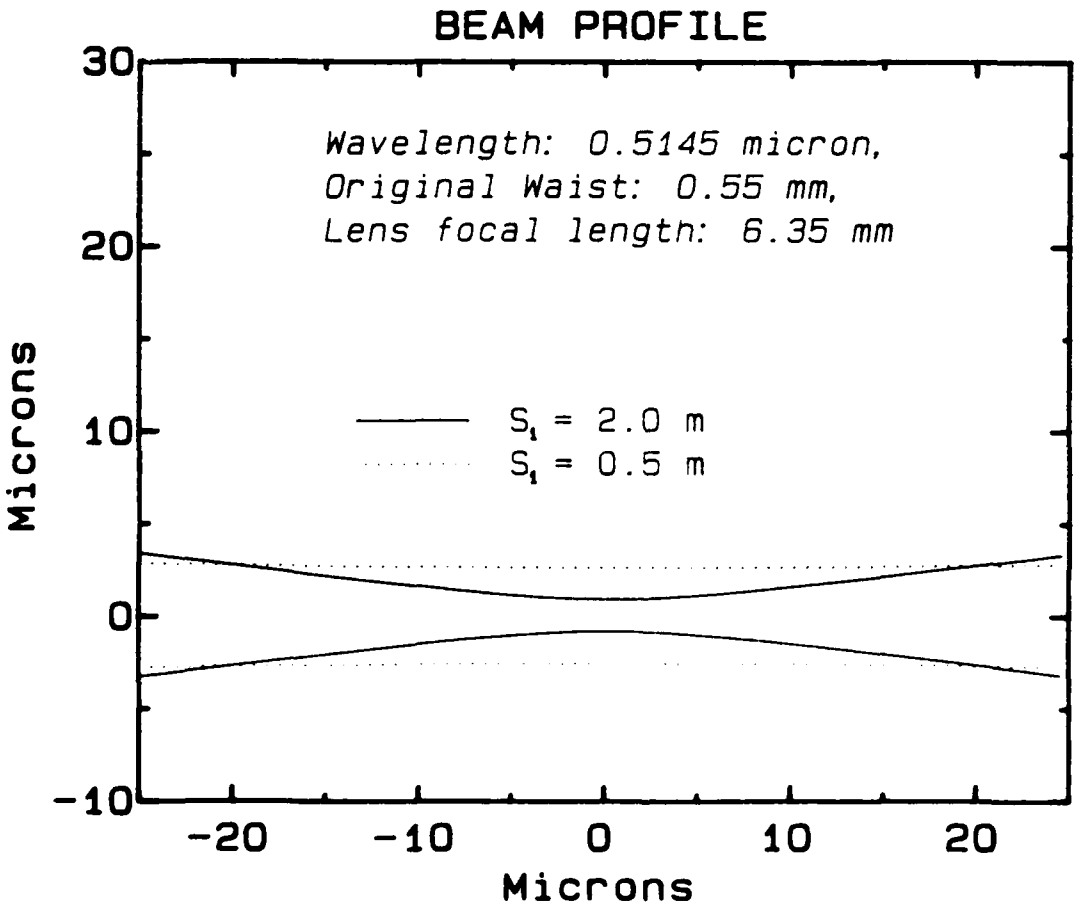

(b) Calculated beam profile in the glass substrate

Fig. 5.5. Laser-beam profile in the vicinity of the waist.

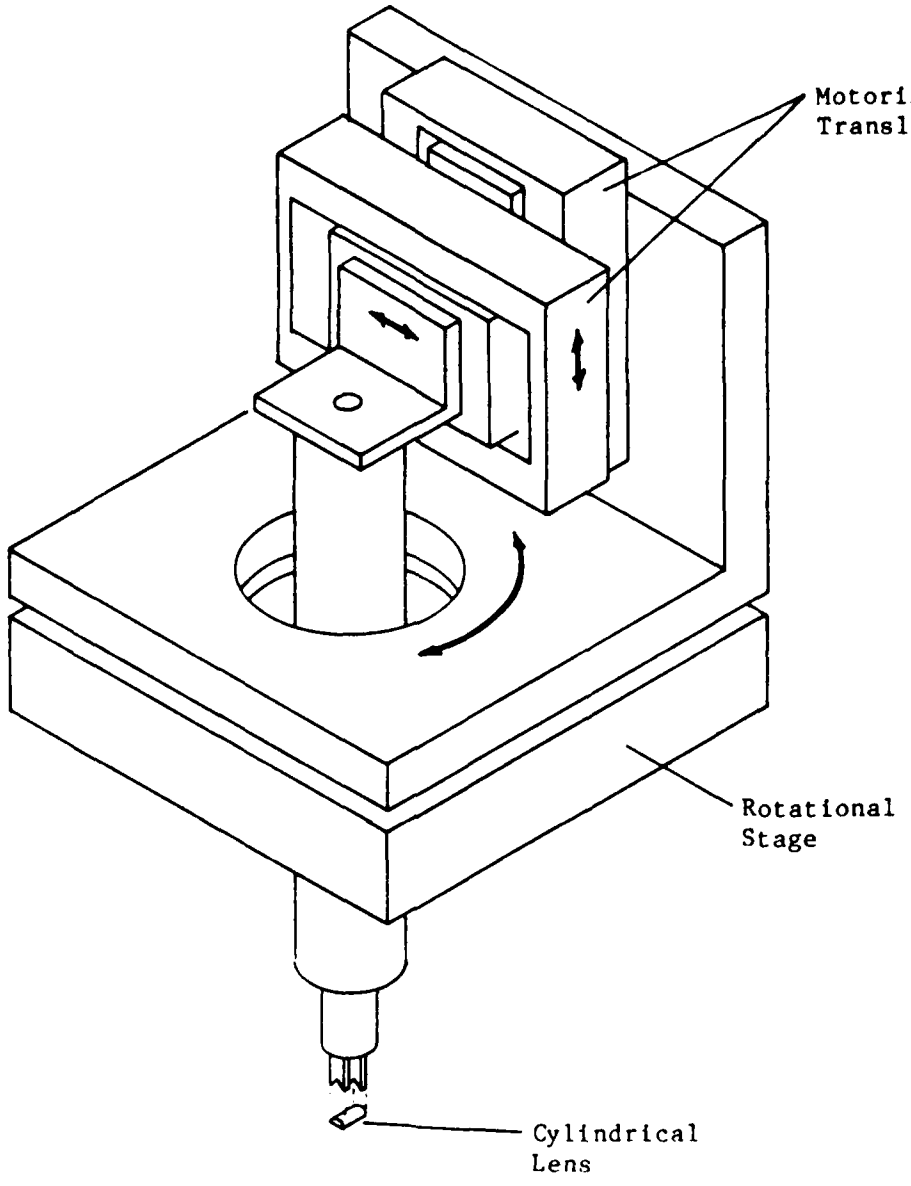

Approximately half scale.
Only relevant features illustrated.
Also see Figs. 5.18 and 5.19.

Fig. 5.6. Cylindrical lens translators.

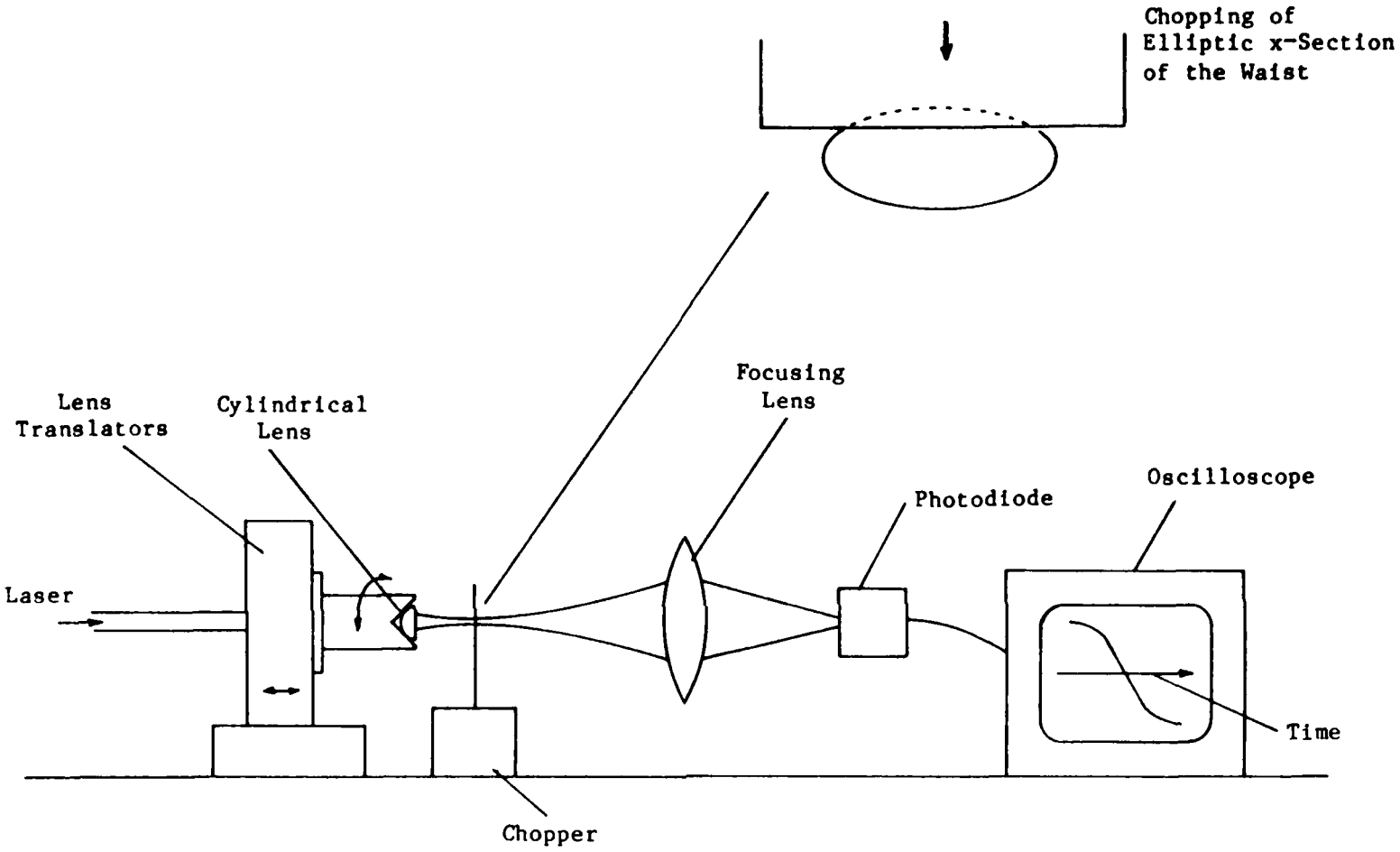

Fig. 5.7. Experimental setup for chopping.

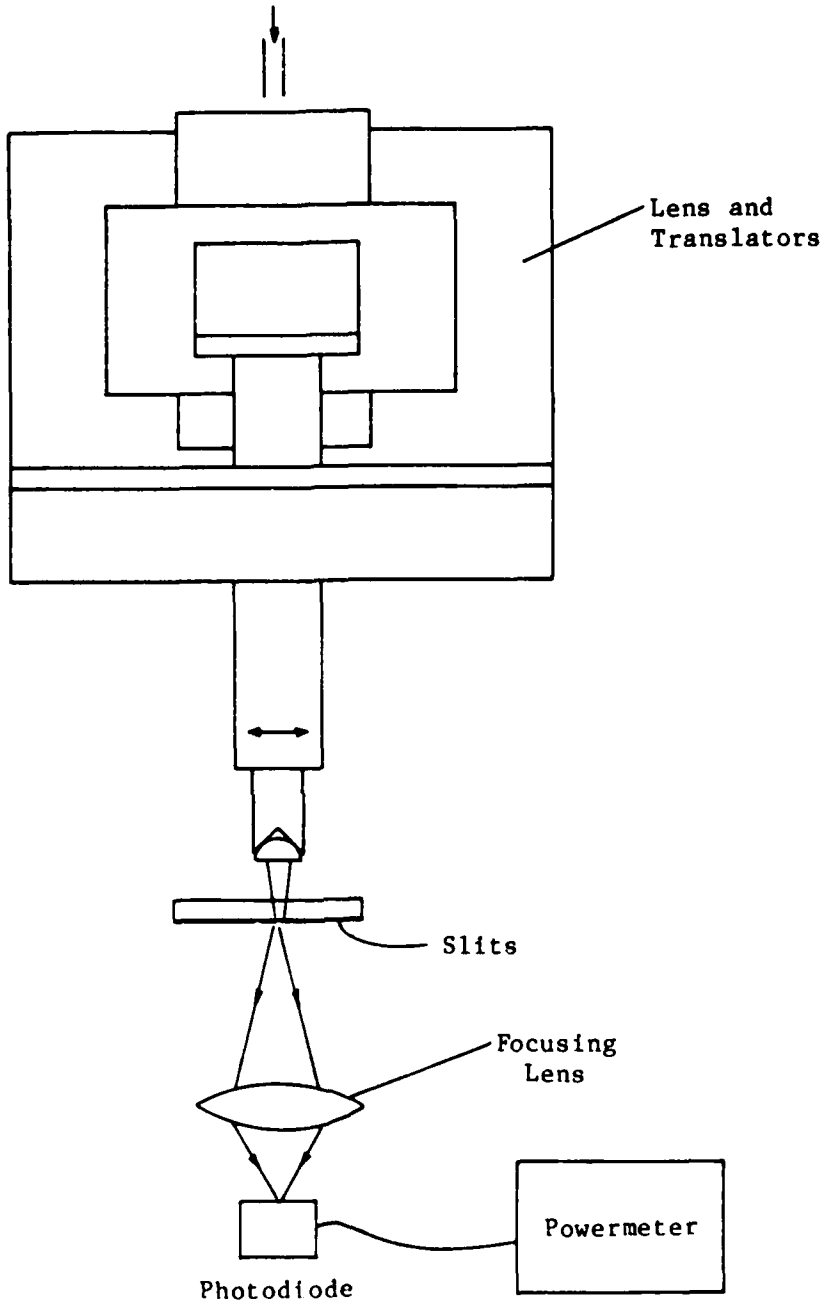

Fig. 5.8. Experimental setup for scanning.

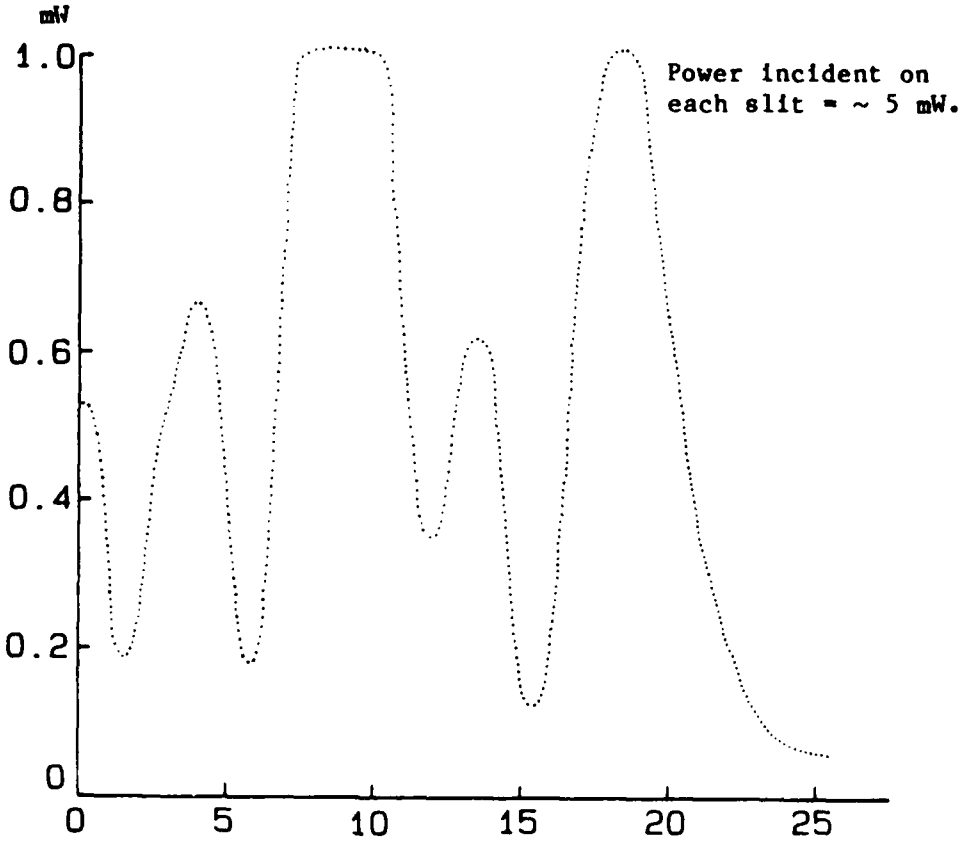

(a) Power transmission

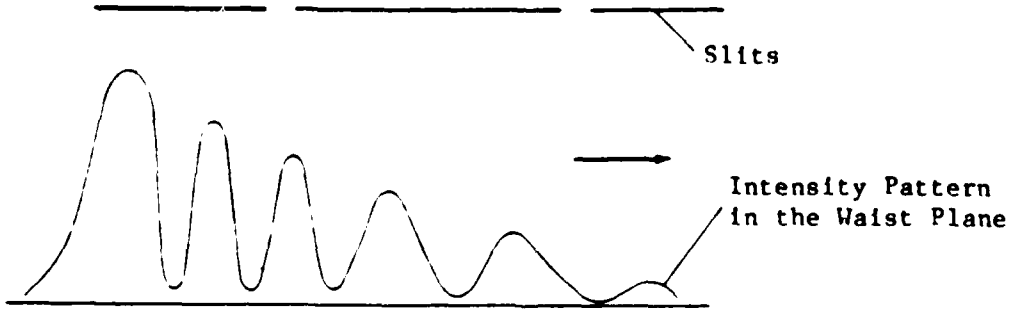

(b) Interpretation of scanning data

Fig. 5.9. Scanning output for poor alignment.

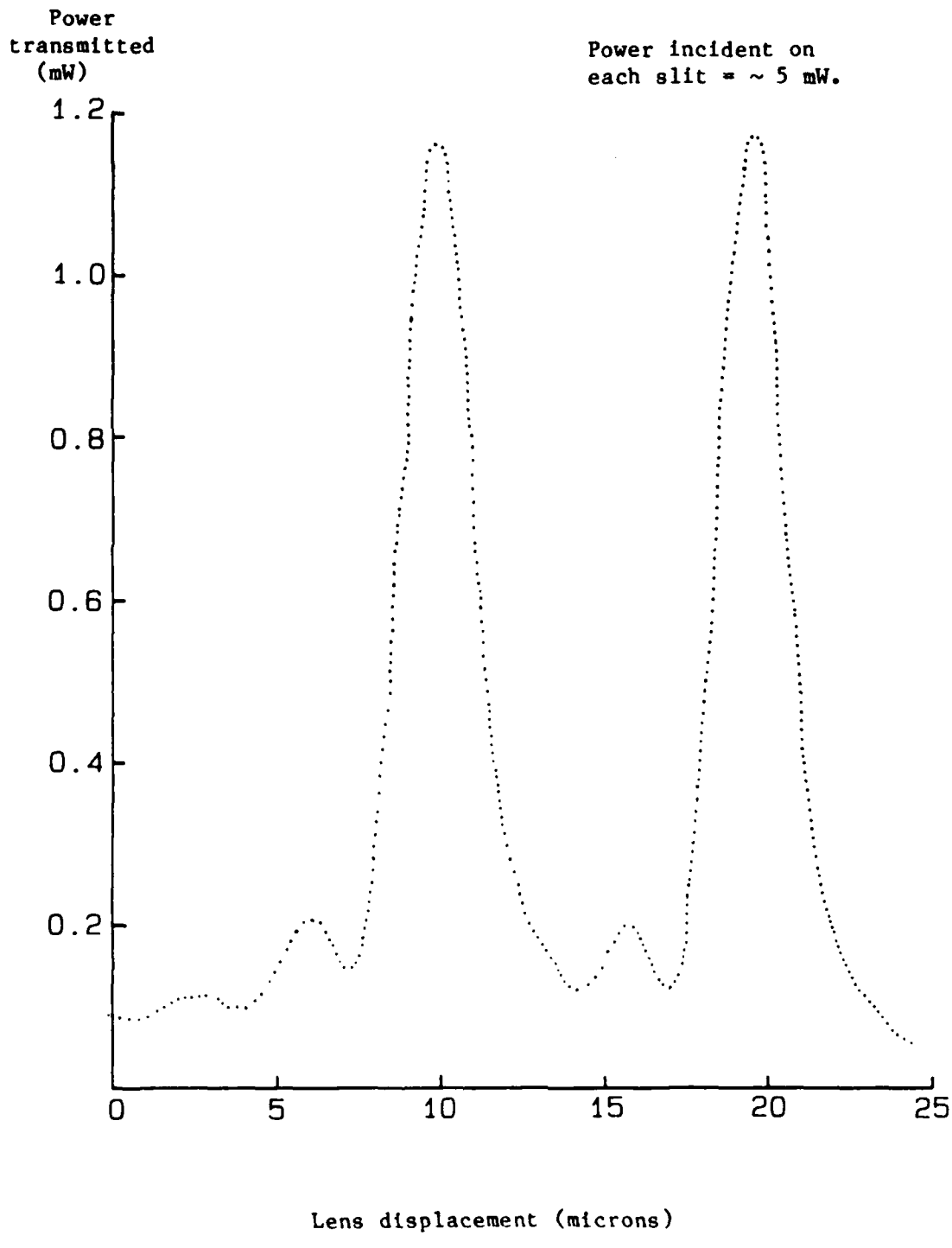

Fig. 5.10. Scanning output for good alignment.

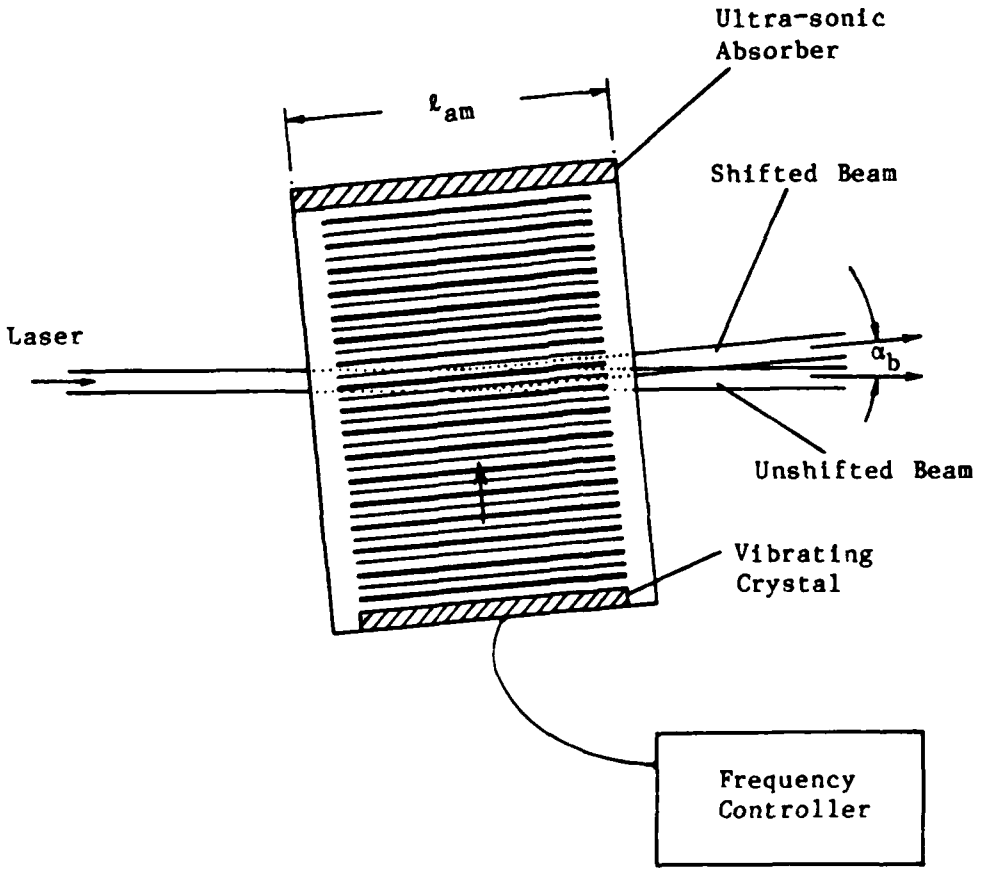

Cell tilt
exaggerated

Fig. 5.11. Single-component beam generator.

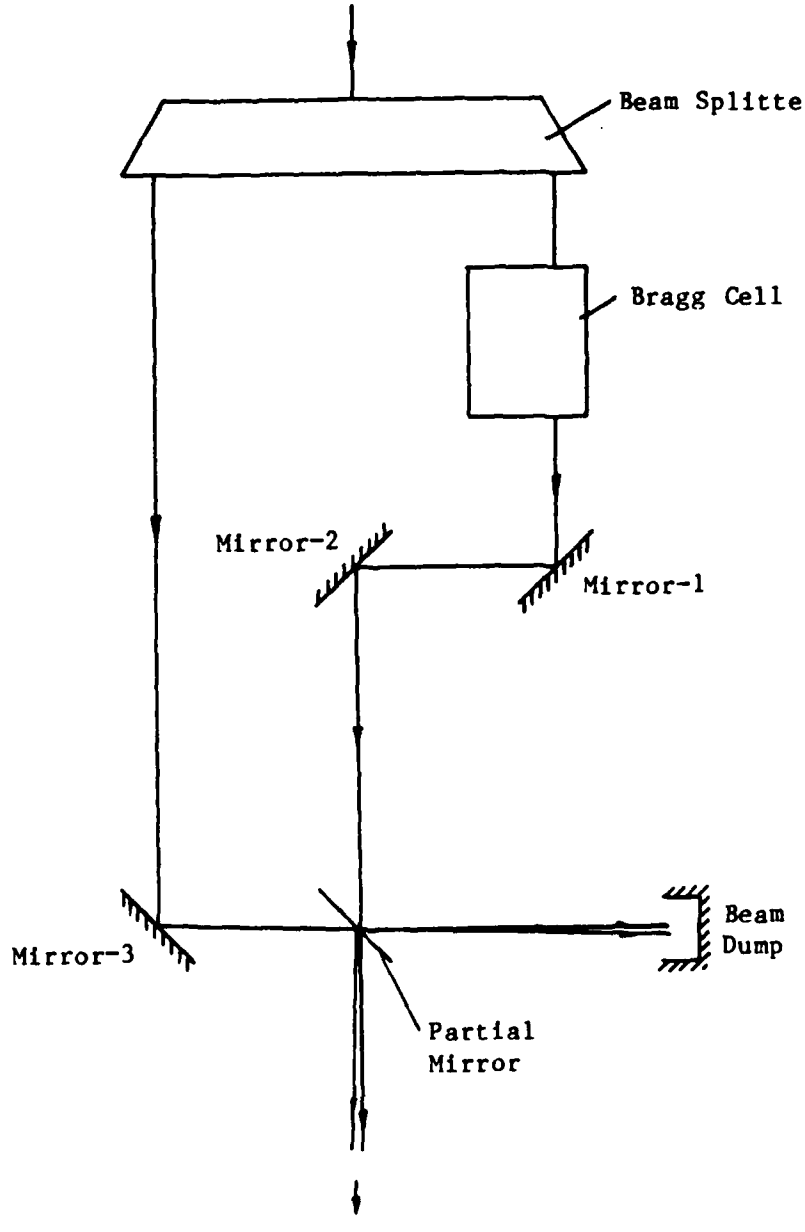

Fig. 5.12. Beam generator: discrete-component design.

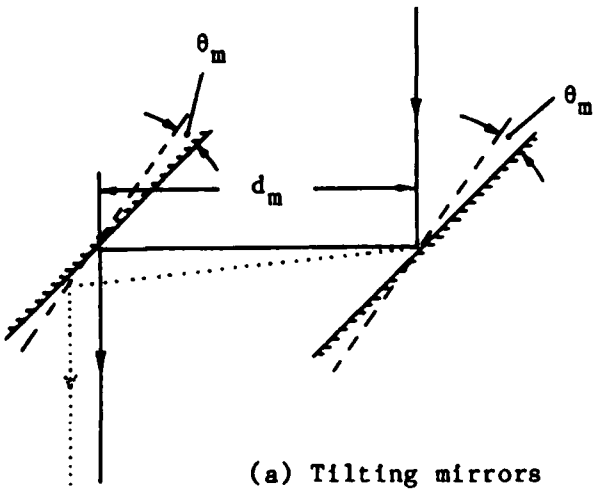

(a) Tilting mirrors

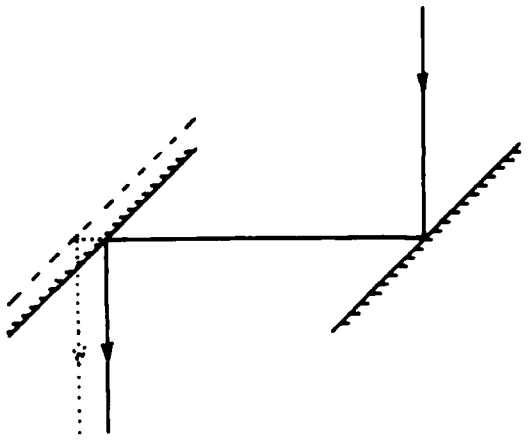

(b) Displacing one mirror

Fig. 5.13. Laser-beam displacement with fixed angular orientation.

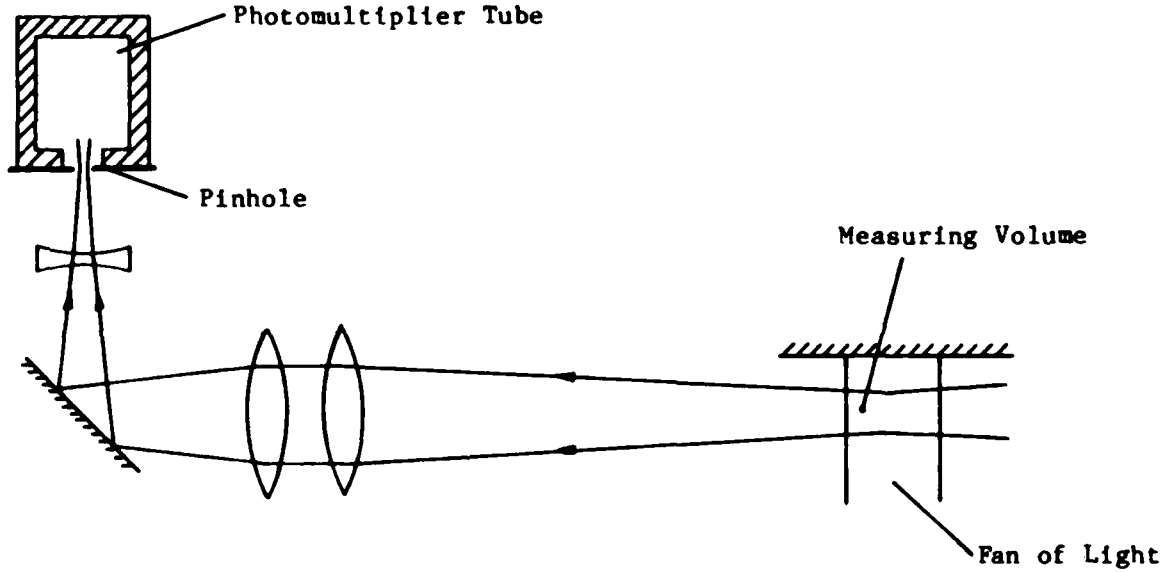

Fig. 5.14. Receiving optics — schematic.

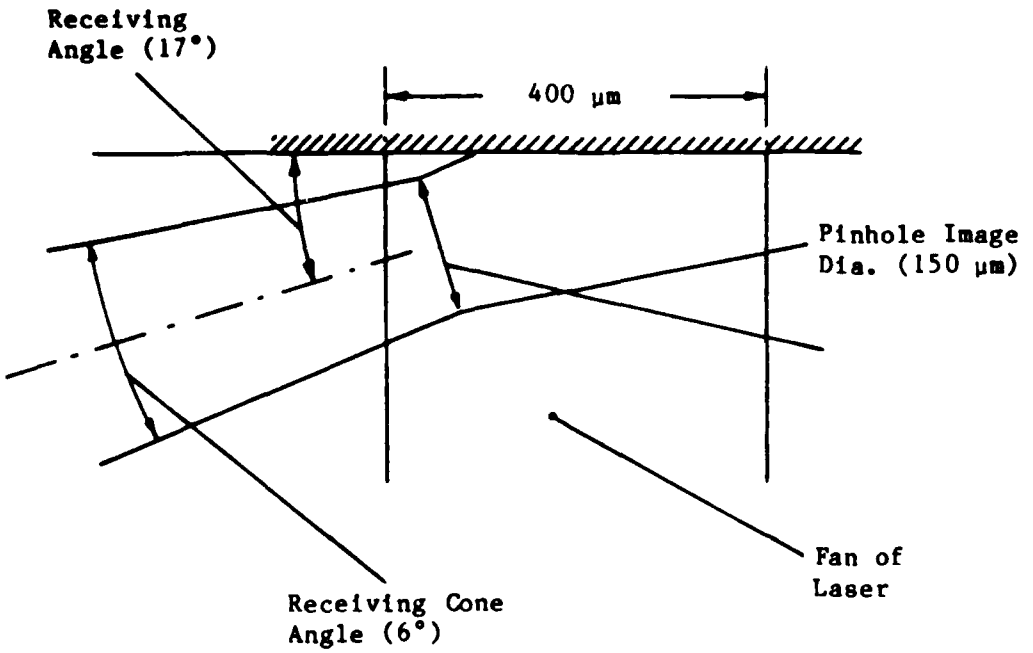

(a) Setup for streamwise measurements

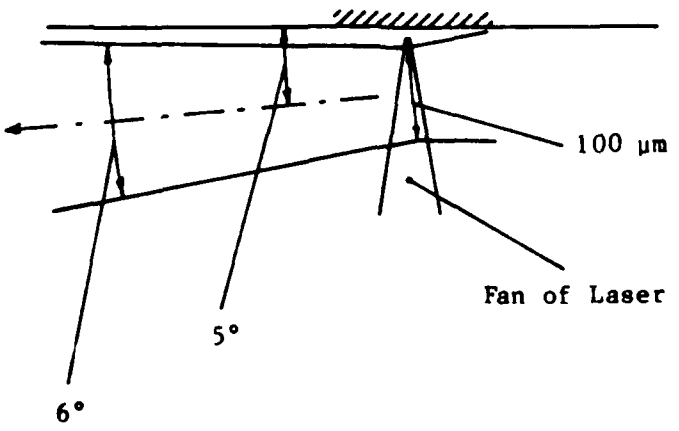

(b) Setup for spanwise measurements

Fig. 5.15. Measuring volume: size, shape, and location (mean flow normal to the paper).

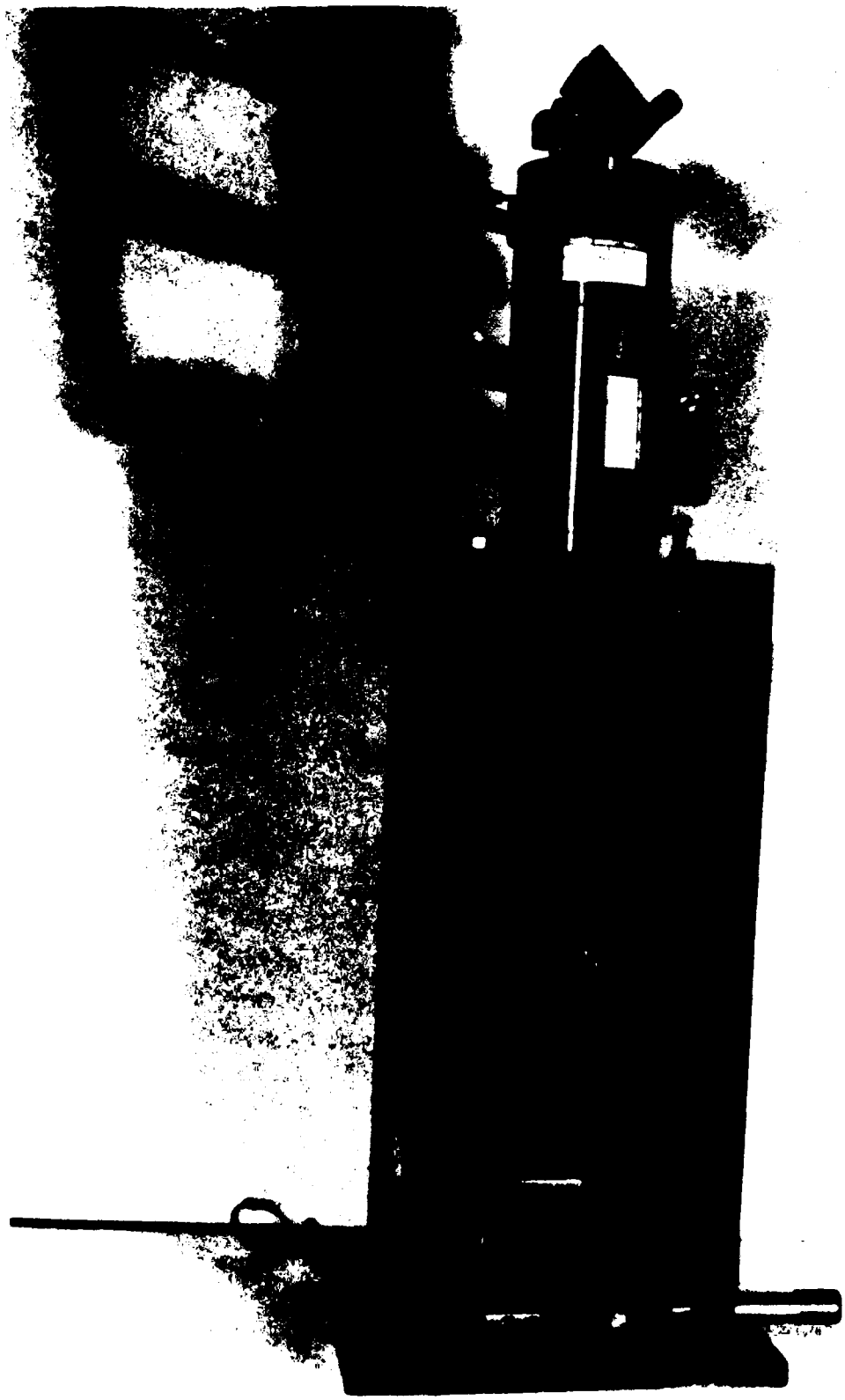

Fig. 5.16. Assembled focusing optics.

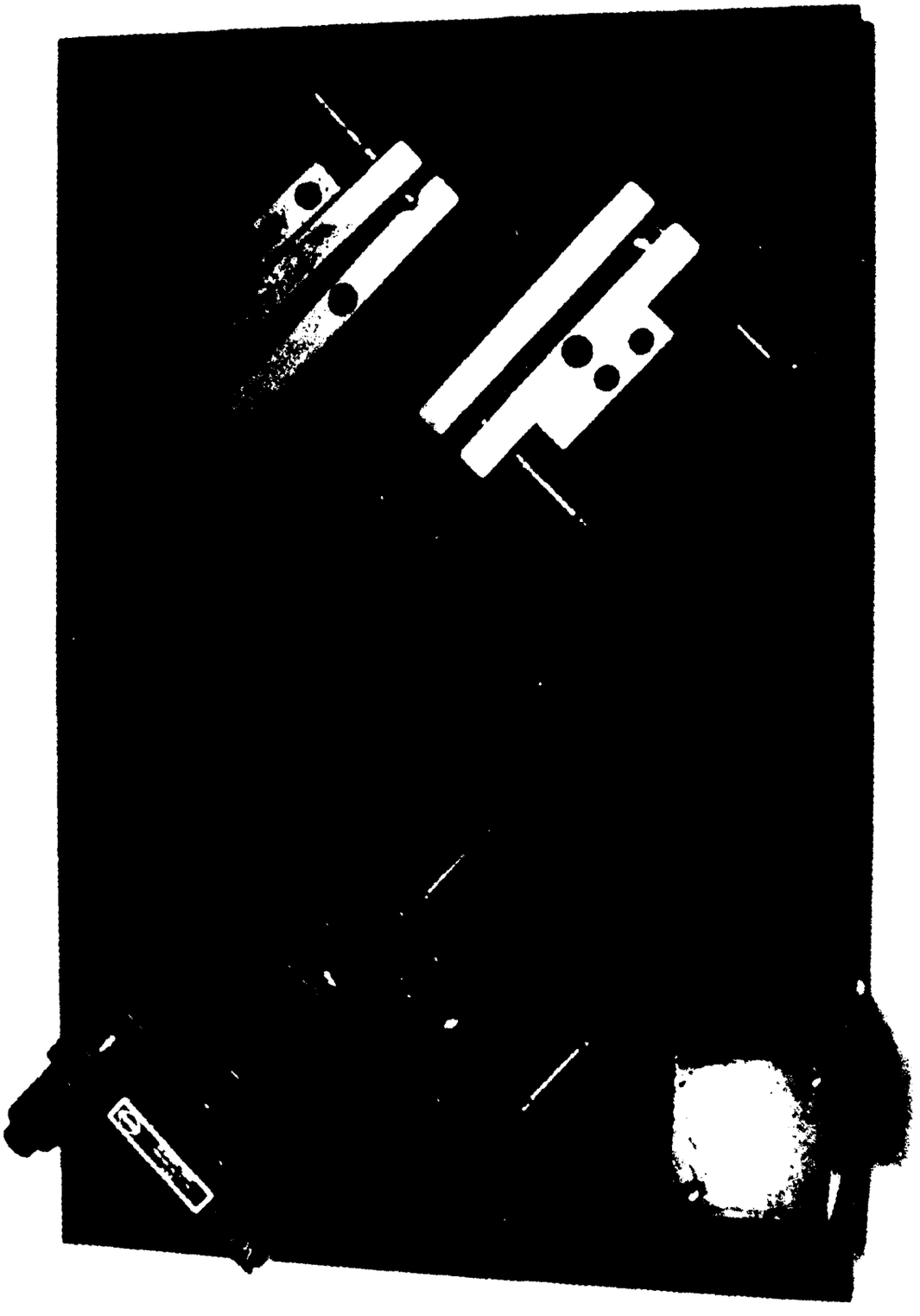

Fig. 5.17. Beam merger: front-plate removed.

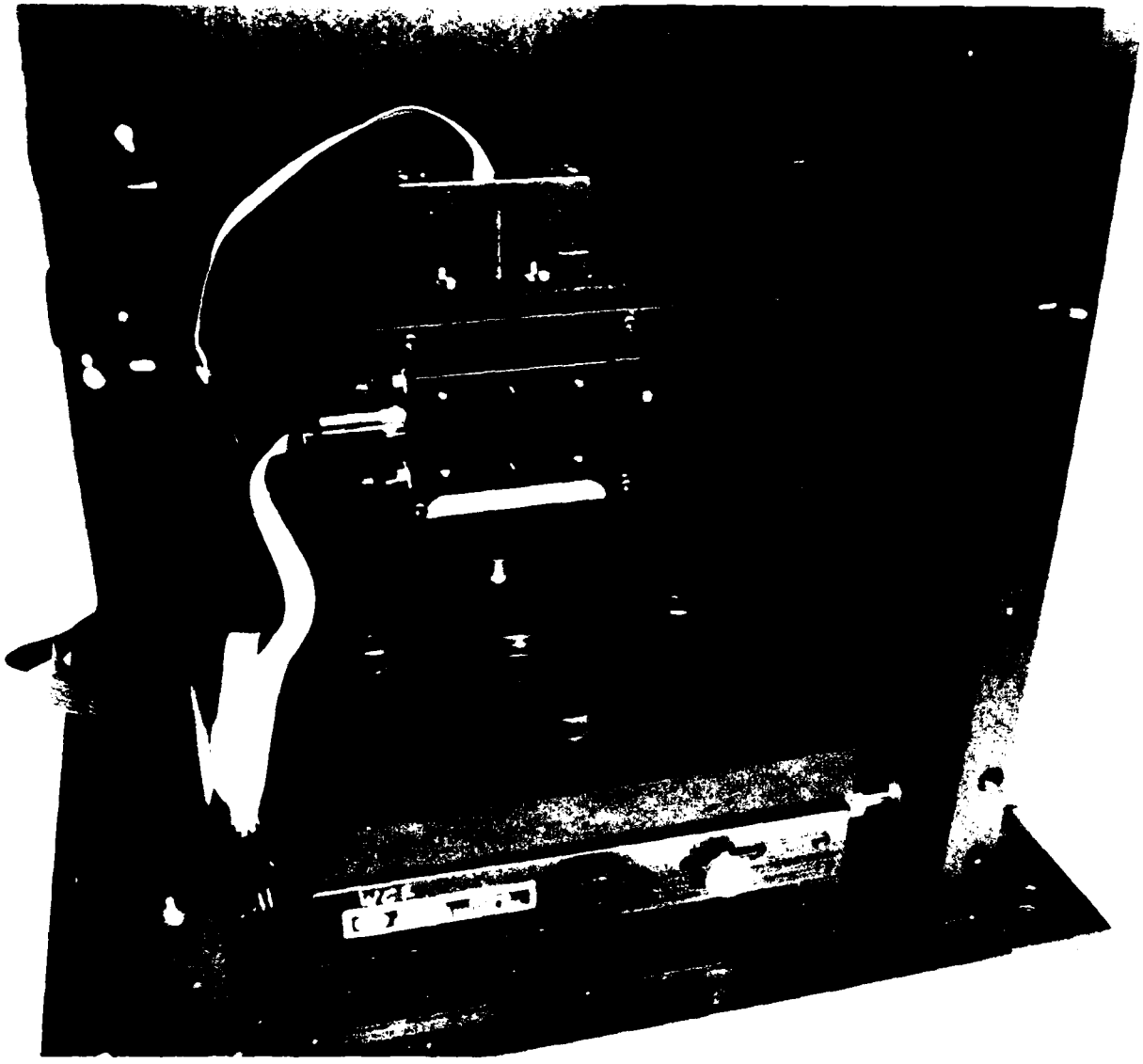

Fig. 5.18. Lens translators in the assembly.

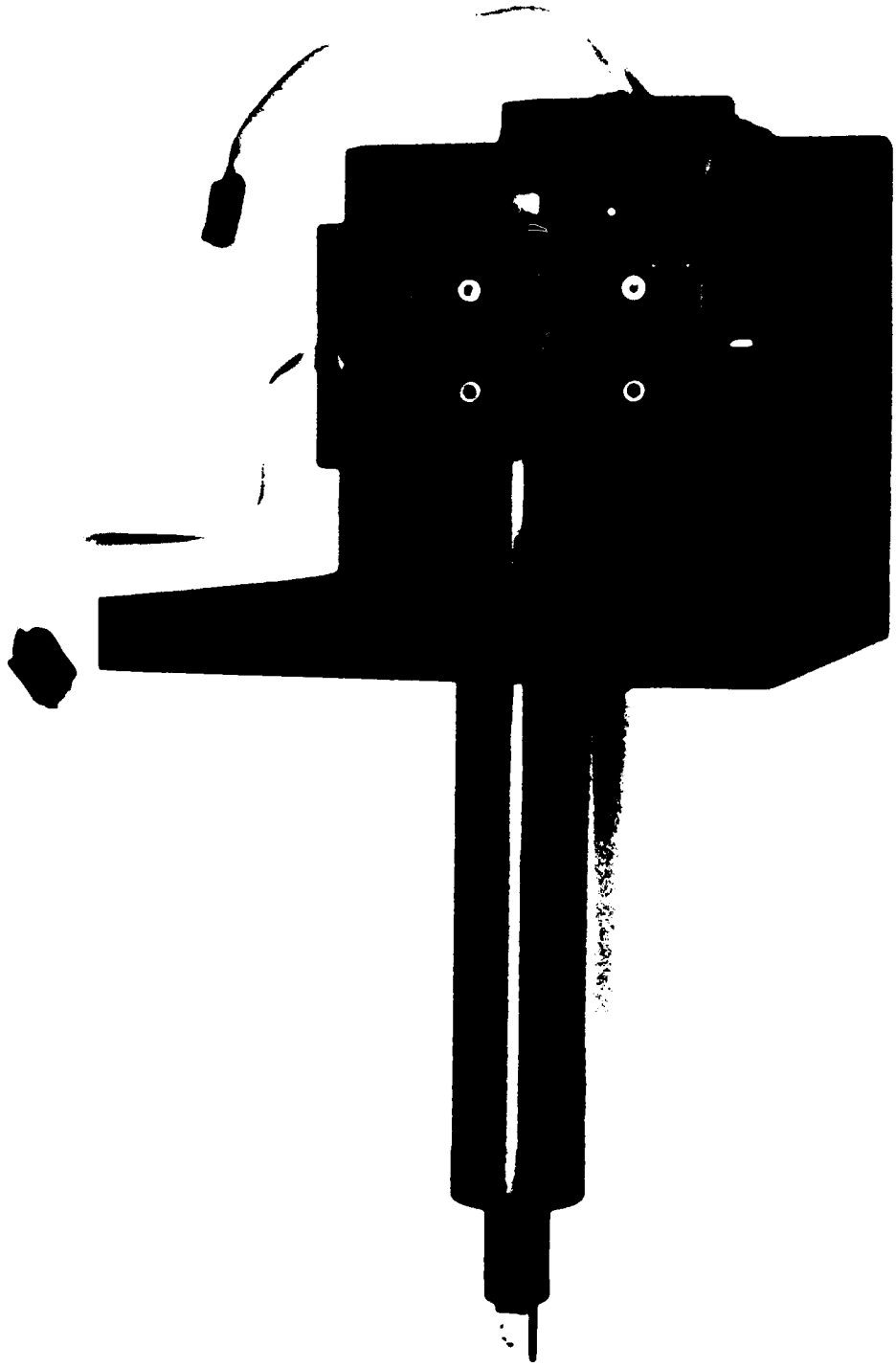

Fig. 5.19. Lens holder and translators.

Chapter 6

TUNING PROCEDURES

6.1 Overview

The present device incorporates two motorized translators and a number of manually adjustable knobs and levers. In order to produce the best cylindrical waves, all the adjustable parts must be brought to the correct position simultaneously. Considering a large number of degrees of freedom (more than ten), it appears a difficult task. However, the governing optical principles allow for independent tuning of various modules of the device. Several of these modules need to be adjusted only once, i.e., prior to installation of the instrument on a flow channel. The optical principles used to simplify the tuning procedure are discussed in the next section. The material in this chapter includes a description of the pre-installation adjustments as well as an appropriate installation procedure. Guidelines for maintainence of tuning are also provided.

6.2 The Underlying Concepts

The rationale for allowing various adjustments in the beam generator and the lens assembly has been elaborated in Chapter 5. The present discussion focuses on two observations which simplify the alignment of various components in the device. It may be shown that small displacement or tilt of the beam splitter or beam merger does not affect the angular spacing between the output beams. This idea has been illustrated schematically in Fig. 6.1. It allows the user to adjust the mirror tilts in the beam merger prior to installation on a flow channel. If the location and the tilt of the components are not exactly duplicated during installation then pertinent misalignment may be corrected simply by re-aligning the in-going beam.

The second concept of interest is illustrated in Fig. 6.2. It shows a cylindrical lens with a yaw with respect to the slit-plane. Under such a conditions, the illuminating sheet approaches the slit obliquely. It is known that oblique illumination produces an asymmetric diffracted field which is stronger in the direction of illumination.

Hence an asymmetric diffraction pattern is an indication of lens yaw. The direction of yaw may be ascertained from the asymmetry of the diffracted field.

Besides the concepts described above, certain elements of optics, such as the idea of ghost images, are used to facilitate alignment. These ideas are elaborated at appropriate places in the following discussion.

6.3 Pre-installation Adjustments

Various parts of the instrument are assembled into modules prior to installation on a flow channel. Three of these modules, i.e. the beam merger, the lens holder, and the lens translator assembly, require precise positioning of various components in them. These alignments are robust and do not drift over extended periods of use. The procedure for assembling these modules is described in this section.

6.3.1 Experimental Setup for Initial Adjustments

For initial adjustments, the focusing optics are installed on a replica of the test channel which allows access to the slits for the sake of measuring the laser power transmitted through them. This arrangement is shown in Fig. 6.3. This exercise may be done at the actual flow channel if power-measuring assembly could easily be installed on the flow-side of the slits. Notice that a pair of tiltable mirrors is needed prior to the focusing optics. These mirrors are used for proper injection of the laser beam into the focusing optics.

6.3.2 Mirror Tilts in the Beam Merger

The beam merger is illustrated in some detail in Fig. 6.4. Various mirror mounts are shown attached to the back plate. Mirror mounts 2 and 4 are bolted to the front and the back plate through slotted holes which allow vertical adjustment. The beam dump may also be displaced vertically in a similar fashion. The partial mirror is placed in mount #4 with the partially reflecting surface facing down. Each mirror mount is equipped with one ball-type pivot and two micrometer screws. Figure 6.5 shows locations of the pivots and the adjusting screws for the present

setup. The screws may be turned using a 1/8" ball driver, and the outer casing of the focusing optics is provided with holes to access the screws. The function of each screw is described in Table 6.1. This table specifies the motion of each beam resulting from clockwise turning of a knob. Counter-clockwise motion would displace the beams in the opposite direction.

In order to set the mirror tilts in the beam merger, the focusing optics are setup to obtain two laser beams at the beam merger entrance. This can be accomplished by following the first five steps of the installation procedure outlined in Section 6.3. The Bragg cell must be rotated out of the beam path in this setting. The beam merger may be aligned using the following procedure:

(1) Mount mirrors in place. Locate mirror mounts 2 and 4 and the beam dump approximately at the middle of their respective slots. Also, leave all the adjusting screws about at the middle of the adjusting range.

(2) Slide the beam merger into the appropriate grooves in the outer casing. Inspect the location of beam incidence on each mirror. Examine one beam at a time by blocking the other. Check to be sure that

   (i) The beams hit the mirrors near their center.

   (ii) The two beams arrive at the partial mirror at the same spot.

   (iii) The rejected beams reach the entrance of the beam dump.

   (iv) The transmitted beams are centered on the slits.

(3) Try to approach the above-mentioned conditions as closely as possible by sliding mirror mount Nos. 2 and 4 and the beam dump in the respective slots.

(4) Use the adjusting knobs to bring the beams closer, locating them over the slits while maintaining a near-normal incidence on the slit plane. The following guidelines would simplify this process.

   (i) While maintaining laser power at a low level ($\sim$ 20 mW), look at the slits from the flow-side to ascertain if the

beams are centered on them. Avoid direct exposure to the laser.

(ii) Try to find the reflected spots on the input mirrors. Maintain the reflected spots next to the in-going beam. As illustrated in Fig. 6.6, the two spots should be on the opposite sides of the input beam.

(iii) Use mirror mount knobs for the functions proposed in Table 6.2. Notice that linear and angular motions are coupled, e.g., if knob 3 is used to displace the right-hand beam sideways, the angular orientation of the beam would also change. It would require a readjustment of knob 4 to make the beam nearly normal to the slit plane. This would in turn reduce the amount of linear displacement achieved. Hence, in order to obtain a certain amount of displacement, several iterations of these two steps would be needed. After some experience, the user may turn knobs 3 and 4 simultaneously in order to displace the beams efficiently.

(5) As the beams merge, dark and bright fringes appear in the region of overlap. The fringes may be observed by interposing a piece of paper in the path of the merged beams and looking at it through a pair of laser goggles. Move the beams back and forth slightly to align the fringes approximately parallel to the length of the slits. Also, adjust the beams sideways to obtain appoximately three fringes per millimeter. This would correspond to an angle of ~ 0.1 degree between the two beams which is desired for focusing them at a spacing of 10 microns.

At the end of the last step, the merged beams should be centered on the slits and the two reflected spots on the input mirrors should be spaced equally from the in-going beam. If this condition is not achieved satisfactorily, some of the previous steps may be repeated. Further refinements in the mirror tilts are obtained during the final steps of pre-installation alignments succeeding the adjustment of lens yaw.

6.3.3 Lens Yaw

Before starting the adjustment of the cylindrical lens for yaw, the lens translator assembly should be installed in place. This assembly consists of two miniature motorized translators and one rotational stage. While assembling the rotational stage, the micrometer should be adjusted so that the bracket holding the motorized stages is not crooked.

The cylindrical lens is mounted at the end of a long tube as shown in Fig. 6.7. This tube is connected to a bracket through three bolts. The bracket in turn is bolted to the lens translator assembly.

The axis of the lens holding tube should be aligned precisely with the merged beams. Otherwise, as described in Section 6.1, an asymmetric and weak diffraction pattern would be produced. Proper alignment is achieved by inserting a stack of thin metallic washers at the right-hand side bolt between the tube and the bracket. Without any washers the tube would be crooked to the right. A 0.001-inch-thick washer would move the lens by about 1/64 inch. In the present setup, washers of thickness 0.001 and 0.002 inch are used. In order to ascertain the total thickness of washers needed, a "hole-burning method" is employed. The hole-burning method is also used to check the alignment after insertion of the estimated thickness of washers. This method may be described as follows.

(1) Replace the cylindrical lens with a thin piece of paper (preferably 0.002-0.005 inch thick) cut to the right size. The side of the paper facing the laser beams should be painted flat-black.

(2) Mount the tube in place and slide the beam merger in. Keeping the laser power low, check if the merged laser beam is entering the lens tube at its center. It may be accomplished by mounting a paper mask on the bracket (Fig. 6.7). The mask may be marked with the center of the tube. Laser goggles must be worn prior to inserting the mask. If the tube is not centered, traverse it sideways using the horizontal motorized translator until the center of the beam is located at the center of the tube.

(3) Remove the mask. Turn the laser power up to ~ 1 Watt for 30-45 seconds. This would burn a hole in the blackened paper mounted at the lens location. Remove the beam merger and the lens tube to examine the location of the burnt hole.

The hole-burning method is very convenient for determining the position of a laser beam at a location not accessible mechanically or visually. However, excessive use of this method would result in deposition of smoke on the optics.

6.3.4 Final Steps

Final refinements in the tuning of three modules under consideration are achieved through the following steps:

(1) While maintaining laser power at a low level, block the left beam.

(2) Using the horizontal translator, scan the right beam over the slits to determine the maximum power transmitted.

(3) Repeat the previous step while moving the cylindrical lens vertically in increments of 100 microns in the direction of increasing peak power. Upon approaching the correct focus, use 10 micron increments.

(4) After focusing the cylindrical lens, align it with the slits length-wise. This is accomplished in a manner similar to the previous step by using the micrometer of the rotational stage instead of the vertical translator. Recommended values for the coarse and the fine adjustments are 200 microns and 20, microns respectively.

(5) Record a power profile and estimate the width of the waist as suggested in Section 5.2.3. Also examine the intensity distribution in the focal plane. Take appropriate corrective measures if the results are not satisfactory. These may include readjustment of lens yaw or re-evaluation of the lens using the chopping method.

(6) Locate the waist over the right-hand side slit if the reflected spot occurs to the right of the in-going beam and vice versa.

Release the left beam. Examine the fan visually. It would probably not be very strong.

(7) Block the right-hand side beam. Turn knob 7 slowly until maximum power is obtained. It should be close to the maximum power from the right beam.

(8) If the power transmission from the left beam is low, displace it sideways using knobs 7 and 8 (as described in Section 6.2.2) to maximize the power. After this adjustment, a strong symmetric fan should be seen upon releasing the right beam.

This would complete the pre-installation adjustments. The beam merger and the lens holder may be removed from the casing in order to move the instrument to the flow channel. The individual modules must not be dis-assembled and handled with care in order to prevent accidental misalignment.

6.4 Installation and Start-up

The instrument may be installed on a flow channel through the following steps:

(1) Install the slit-holding plug, the outer casing, the lens translator assembly and the input mirrors. A chopper may be installed in the path of the in-going beam. As explained later, such a chopper could be used in conjunction with the receiving optics to locate the laser sheets precisely over the slits.

(2) Align the laser beam normal to the slit plane locating it over the slits. Use the first input mirror to displace the beam and the second one to keep it normal to the slit plane. The reflected beam should coincide with the in-going beam.

(3) Insert the polarization rotator. Determine the polarization axis using an axis finder. Align it roughly with the slits.

(4) Install the beam splitter. Set the polarization rotator for equal power in the two beams produced by the beam splitter.

(5) Install the Bragg cell and align it according to the manufacturer's instructions. The standard method requires an alignment mask

to help recover the origional position of the laser beam after frequency shifting. The standard alignment mask cannot be used in the present setup; however, a homemade paper mask would serve the stated purpose. If frequency shifting is not desired, then rotate the Bragg cell out of the beam path.

(6) Slide the beam merger in. Check if the merged beams are located over the slits. Also, look for two reflected beams on either side of the in-going beam. If these conditions are not met then re-align the in-going beam using the input mirrors as in step 2.

(7) Remove the beam merger. Mount the lens holder and insert the beam merger again. Bolt the beam merger down to the outer casing.

(8) Block the left beam. Look up for the diffraction pattern produced by the right beam. Traverse the lens sideways to obtain the brightest light pattern from a slit. Locate the right beam over the correct slit; so that, the other slit would be illuminated upon releasing the left beam.

(9) If it is found difficult to maximize the power transmission, merely by visual examination, then turn on the chopper and display the photomultiplier output on an oscilloscope. Traverse the lens sideways till the amplitude of the signal on the oscilloscope reaches its peak value.

(10) Release the left beam. In the case of no frequency shifting, one should obtain a strong fan without further alignment. Block the right beam to examine the brightness of the diffraction pattern produced by the left beam. It may be done visually or through the oscilloscope as explained earlier. If frequency shifting is used then slight adjustment of knob 7 may be required for satisfactory focusing of the left beam.

If serious difficulties are encountered in obtaining correct alignment using the above procedure, then the pre-installation adjustments should be repeated.

After aligning the focusing optics and roughly locating the receiving optics in the vicinity of the measuring volume, the user may look for Doppler signals from the flow. Using the micrometers on the

traverse mechanism of the receiving optics, the measuring volume may be gradually moved closer to the wall. This would result in an increase in the average signal frequency, reaching a maximum value which would be invariant over a considerable displacement normal to the wall. This region may be recognized as the viscous sublayer. The signal from a very near-wall region exhibits certain special characteristics when examined without high-pass filtering. As explained in Section 4.6, these characteristics may be used to locate the measuring volume properly. In the present system, the measuring volume center is located approximately 100 microns from the wall.

6.5 Maintenance of Tuning

Over extended periods of use, various components of the system are likely to drift slightly. Usually, the effect of such a drift may be corrected by relocating the cylindrical lens using the horizontal translator. Often this can be done by eye, maximizing the transmitted power. If this procedure fails to produce satisfactory realignment then remove the beam merger and the lens holder from the outer casing and repeat steps 6 through 10 of the installation procedure outlined in the previous section. If the alignment is still poor, the entire installation procedure should be repeated.

Table 6.1

EFFECT OF CLOCKWISE TURNING OF THE MIRROR MOUNT KNOBS IN THE BEAM MERGER

Knob #	Beam moved	Motion of the beam
1	Right	Forward
2	Right	Backward
3	Right	Right
4	Right	Right
5	Left	Forward
6	Left	Backward
7	Left	Left
8	Left	Left

Table 6.2

APPLICATIONS OF MIRROR MOUNT KNOBS IN THE BEAM MERGER

Knob No.	Beam Handled	Type of Intended Motion	Direction of Motion
1	Right	Linear	Back & Forth
2	Right	Angular	Back & Forth
3	Right	Linear	Sideways
4	Right	Angular	Sideways
5	Left	Angular	Back & Forth
6	Left	Linear	Back & Forth
7	Left	Angular	Sideways
8	Left	Linear	Sideways

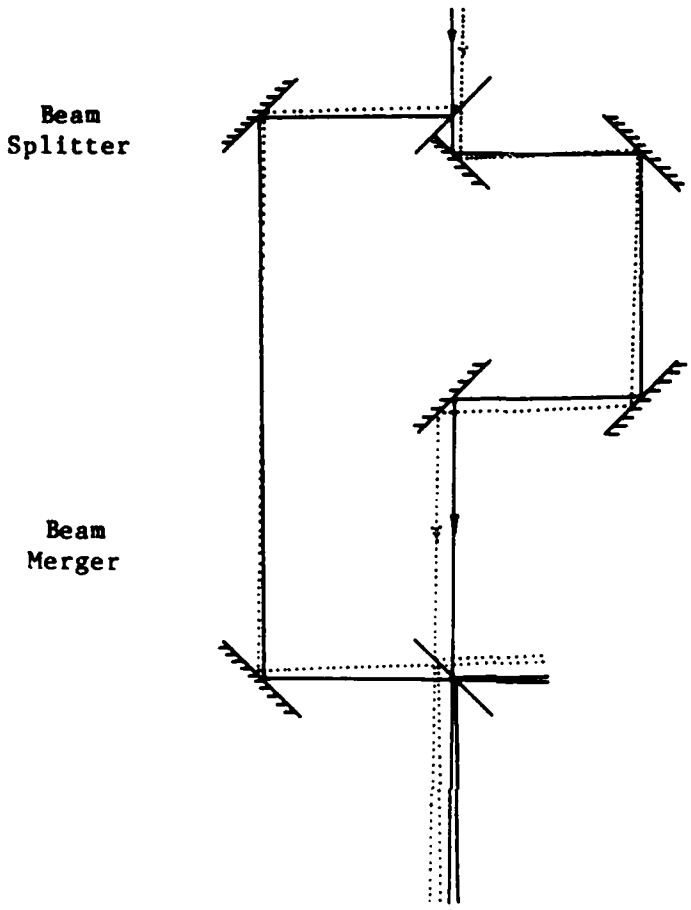

The pair of the laser beams at the beam merger exit is displaced because of the misalignment in the input beam. However, the angle and the spacing between the two beams in the pair are unaffected. It is also true of misalignments of the beam splitter and the beam merger as units.

Fig. 6.1. Self-aligning characteristics of the focusing optics.

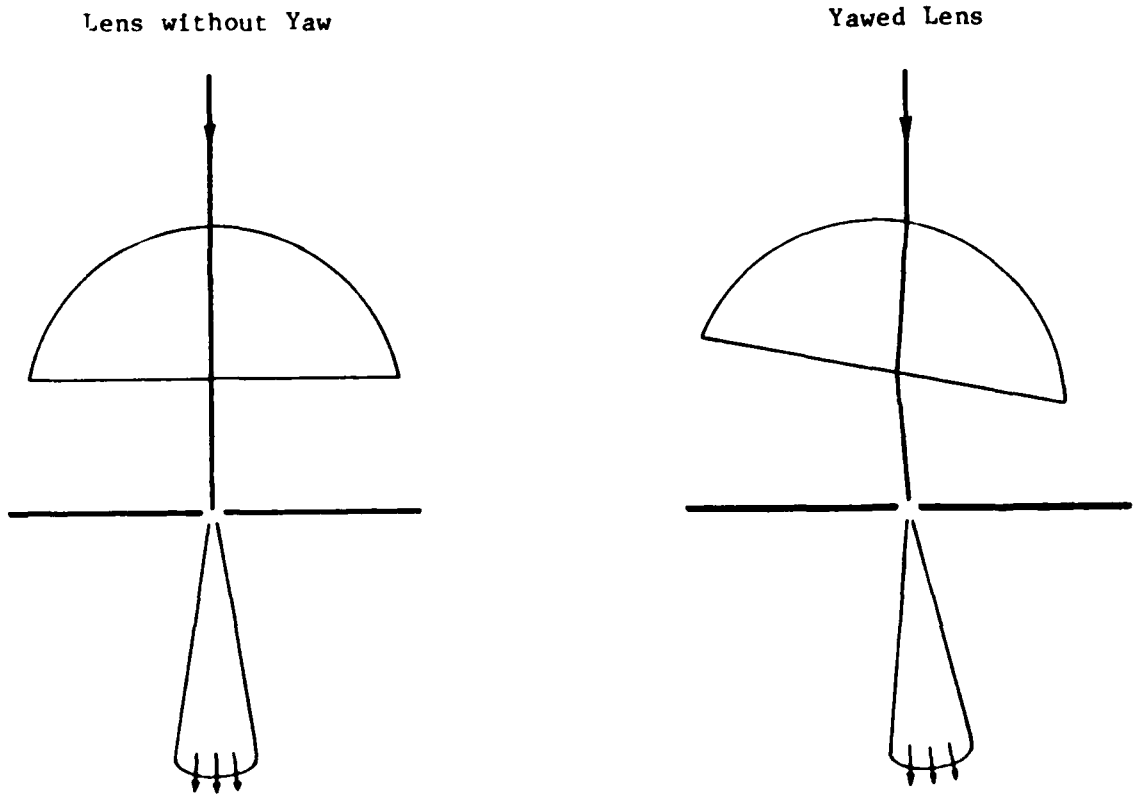

Fig. 6.2. Asymmetry of diffraction pattern, caused by a tilted lens.

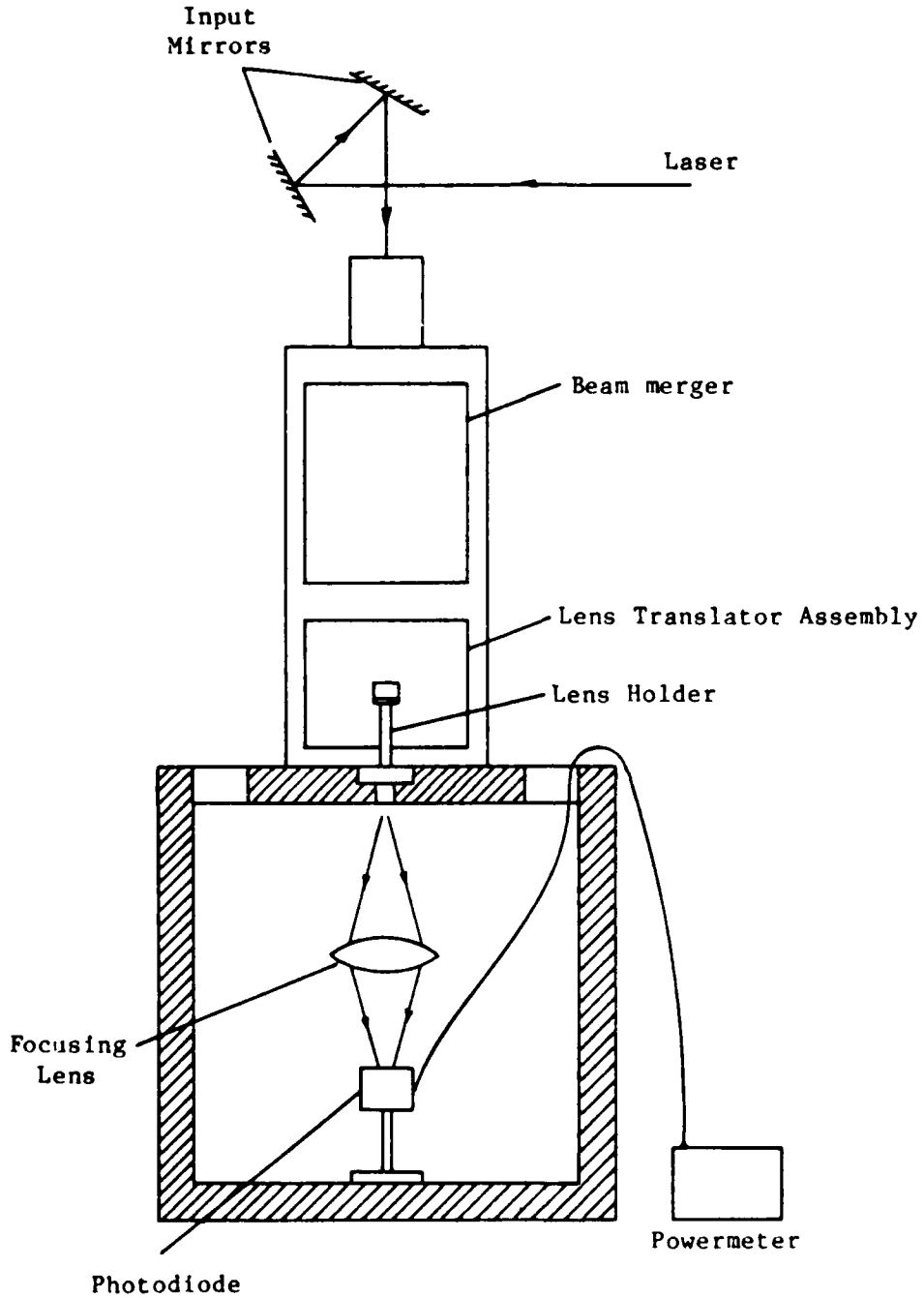

Fig. 6.3. Experimental setup for pre-installation alignments.

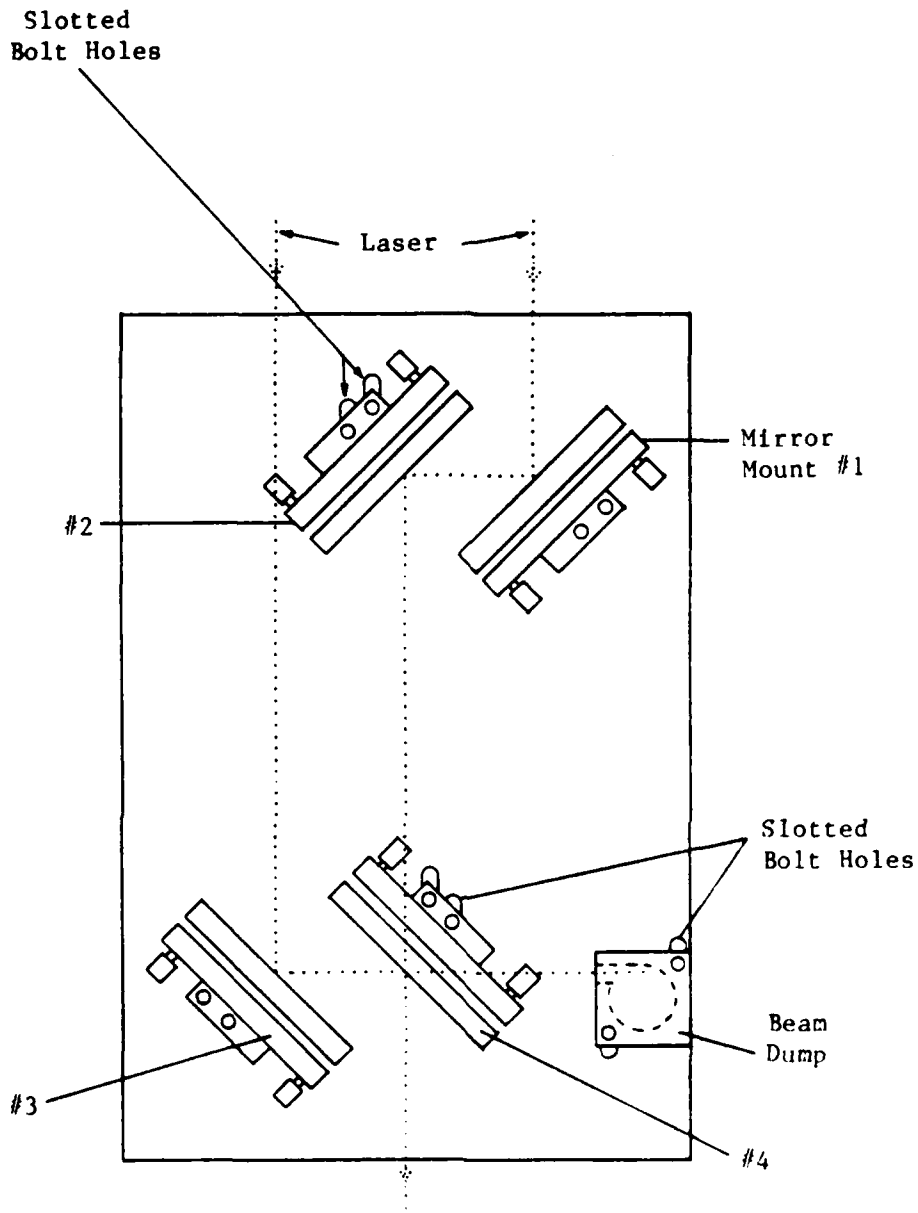

Fig. 6.4. Mirror mounts in the beam merger (front plate removed).

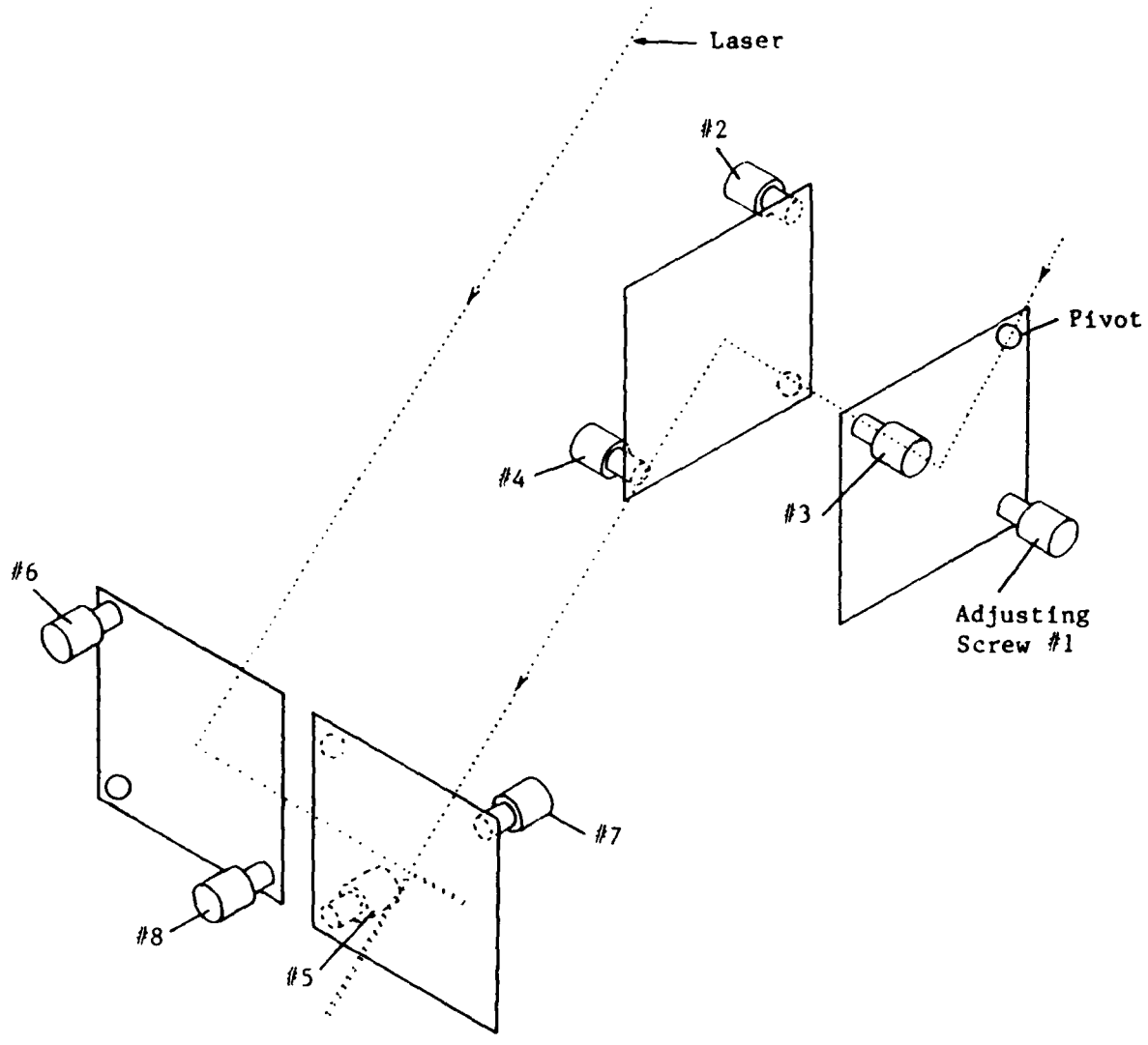

Fig. 6.5. Locations of pivots and adjusting screws in the mirror mounts.

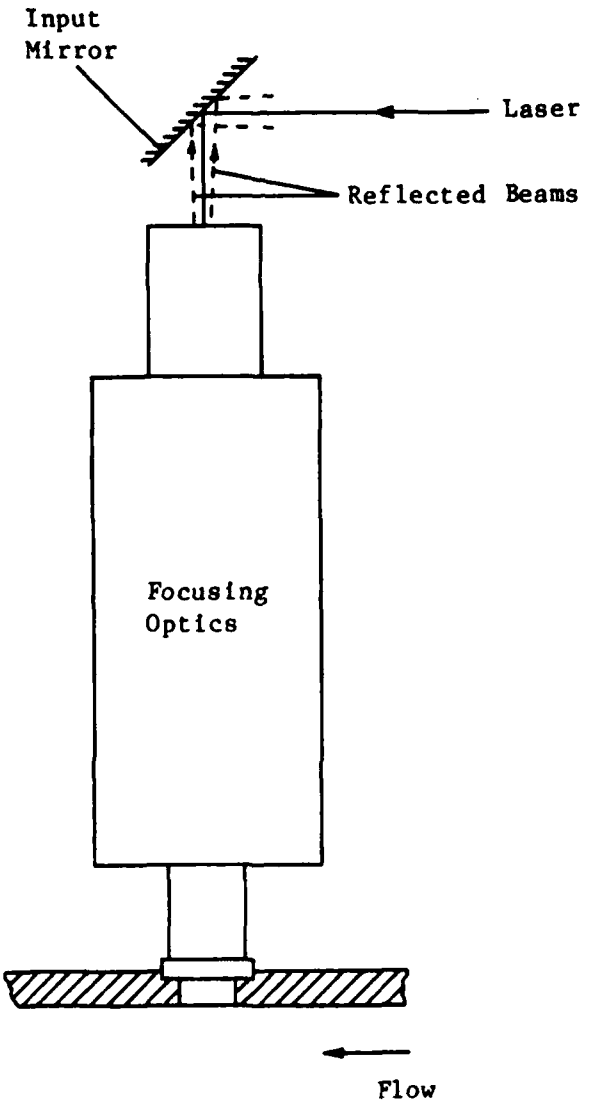

Fig. 6.6. Appearance at the input mirrors of laser beams reflected from the slit plane.

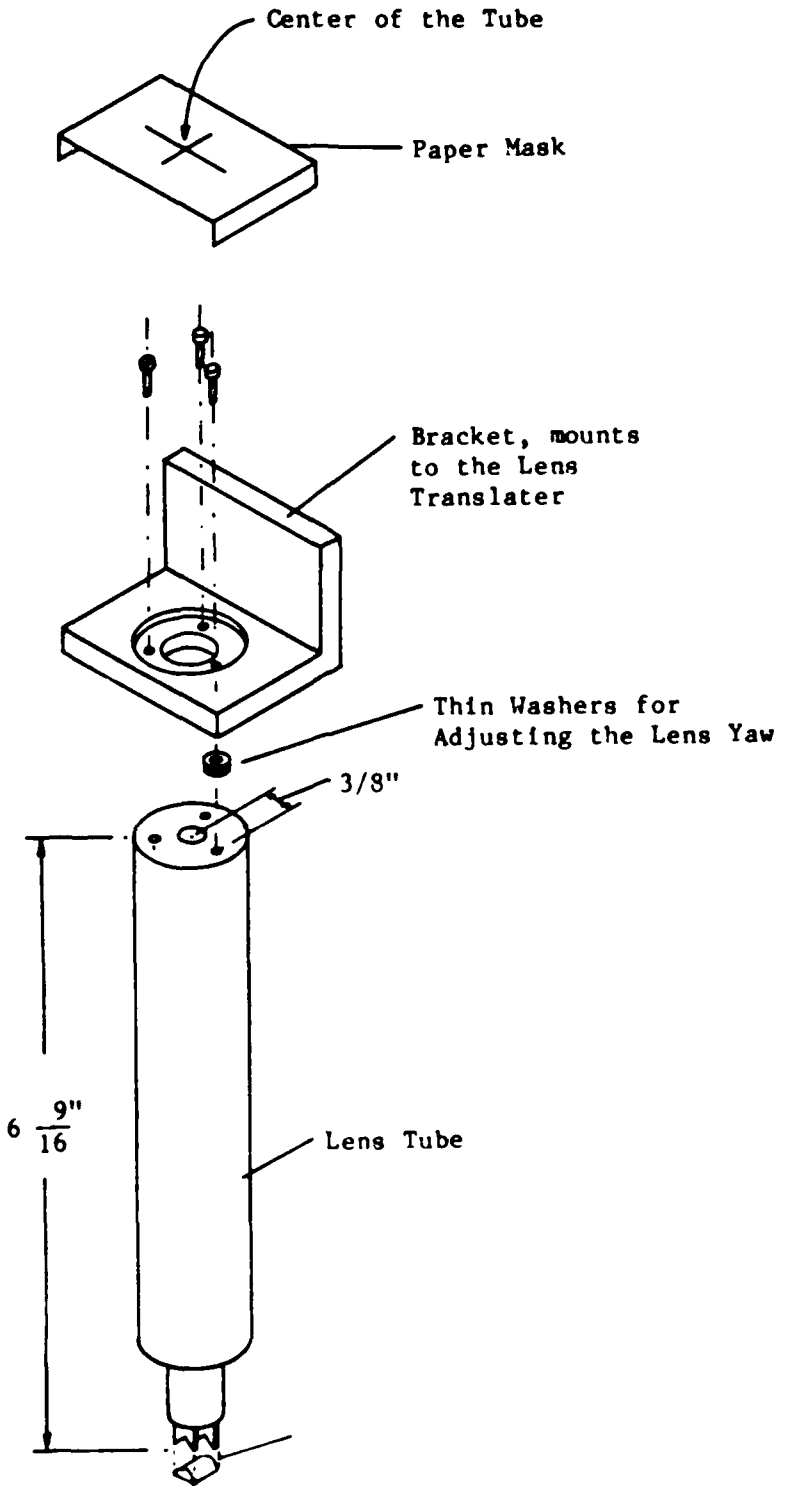

Fig. 6.7. Lens holder and paper mask used for centering the laser beam.

Chapter 7

SELECTION OF SEED PARTICLES

7.1 Desirable Properties

The selection of scattering particles is based on their ability to produce a discernible and representative signal without causing any undesirable side-effects. According to the results of scattering calculations presented in Chapter 4, particles of diameter larger than 2 microns would produce discernible signals in the present device.

In order to explore whether a particular arrangement would generate representative signals, it must be emphasized that an LDV system measures velocity of the scattering center of a particle as sensed by the receiving optics. This measurement is meaningful if the scattering-center velocity is either coincident with the fluid velocity or can unambiguously be related to it. The relationship between the particle velocity and the scattering-center velocity is complex, but the discrepancy is tolerable, as shown in Chapter 4. The matter of present interest is the relationship between particle velocity and fluid velocity. The current system operates very close to the wall, where flow behavior of the particles is more complex than it is in a standard situation for LDV measurement. In this chapter, practical implications of the peculiarities in flow behavior are identified through a simple analysis. It is shown that migration of particles from the near-wall region may result in a serious reduction of data rate. However, this can be offset by seeding particles through the wall a short distance upstream of the measuring location.

Durst et al. (1981) have discussed the properties required for scattering particles in various applications. It is not difficult to find particles which are harmless to the experimental setup. The present experiments were conducted with naturally occuring particles in the tap water filtered to 5 microns. Polystyrene latex and silicon carbide particles were also used in various runs of experiments. All these particle materials are clean and safe to use.

Optical properties of the particles are considered in Chapter 4. The signal-to-noise ratio is the key parameter for evaluating the feasibility of a certain type of particles. Particle diameters less than 2 microns are found to have inadequate signal-to-noise ratio. Usually, a high refractive index improves the signal quality in an LDV system. However, for the receiving location in the present system, it is not obvious that a particularly high refractive index is always advantageous.

Standard criteria for evaluating flow behavior of the particles in laser velocimetry systems are based on the assumption of homogeneous turbulence and do not take into account velocity gradients across the particle. In the vicinity of the wall, the velocity gradient is large and affects the particle path and the velocity. A particle in the near-wall region may be set in rotation and gradually moved away from the wall. Also, the phenomena of burst and sweep in the turbulent boundary layer are likely to affect transport of particles between near-wall and outer regions.

A schematic picture of particle motion is presented in Fig. 7.1. The first phase of particle motion is dominated by the Magnus effect, the Saffman effect and gravitational sedimentation. In this phase the waviness in the particle path is caused by fluctuations in the normal velocity. The migration of particles away from the wall is determined principally by particle rotation (i.e., Magnus effect). Outside the viscous sublayer, the particle path is determined chiefly by the fluid motion which goes through a sequence of events known as bursts and sweeps. As discussed by Cantwell (1981), discrepancies exist among various works regarding the origin of the bursts. It is not well-understood, whether an active exchange of fluid takes place between the viscous sublayer and the outer region during burst-sweep cycles. However, conservative estimates can be made by assuming that, once migrated, a particle is not likely to be transported back into the sublayer. Hence, only the migration phase is studied in this chapter.

The rate of migration is generally much slower than that of turbulence fluctuations. This allows one to use a stationary solution for studying the frequency response. Furthermore, it permits one to ignore high-frequency motion during evaluation of overall migration.

This idea is illustrated in Fig. 7.2. The concepts of frequency response and migration are further elaborated in the following sections.

7.2 Frequency Response

For homogeneous turbulence, equations of particle motion have been solved by various investigators, such as Hjelmfelt and Mockros (1966) and Chao (1964). The former authors have presented a solution for the stationary response of a particle to a single frequency of fluctuation in fluid velocity whereas the later author has proposed a scheme entailing the entire spectrum of turbulence frequencies. The present study is restricted to single-frequency response; the highest turbulence frequency is used to obtain a conservative estimate.

In order to obtain a solution for near-wall particle motion, Rizk and Elghobashi (1984) have proposed certain modifications in the above-mentioned solutions. These modifications account for increase in the viscous drag due to presence of the wall and also incorporate Saffman's lift force due to particle slip in a shearing flow. The additional viscous drag dampens the particle motion relative to the fluid. The lift force acts as a periodic force normal to the wall and generally increases the particle velocity amplitude beyond the amplitude of the fluid velocity.

The mathematical formulation for streamwise and normal motion using the criteria of Rizk and Elghobashi and that for homogeneous turbulence due to Hjelmfelt and Mockros are presented in Appendix E. Based on these criteria, the response of silicon carbide, dust and polystyrene latex particles has been evaluated. The ratio of the particle velocity amplitude to that of the fluid velocity is plotted as a function of the particle diameter in Fig. 7.3. All the computations are based on a turbulence frequency of 1000 Hz and normal-to-streamwise velocity ratio of 0.1. The turbulence frequency was chosen as the reciprocal of the Kolmogoroff microtime scale whose value near the wall may be approximated by the mean-wall velocity gradient. It may be noticed that, under the worst conditions, the particle velocity is within 1% of the fluid velocity for particle diameters less than 10 microns.

The particle response in the spanwise direction would be similar to that in the streamwise direction. The present evaluation indicates that frequency response in the sublayer would be different from that in the outer region but would not offer any extraordinary difficulties for laser velocimetry applications.

7.3 Particle Migration

Migration of particles away from or towards the wall may take place through various mechanisms. Sedimentation causes a vertical motion of the particle relative to the fluid. In the case of a horizontal wall, it results either in deposition of the particles on the surface or migration away from it. For a flow bounded by a vertical wall, the slip caused by sedimentation would result in a lift force normal to the wall. This lift force may be calculated from an expression proposed by Saffman (1965, 1968). The present measurements were taken near a horizontal top surface of a water channel. Since the scattering particles were heavier than water, migration away from the wall was expected due to sedimentation. The equilibrium migration velocity may be evaluated by equating the gravitational force to the viscous drag (Stokes' law):

$$v_{ms} = \frac{d_p^2(\rho_p/\rho - 1)\, g_c}{18\, \nu} \tag{7.1}$$

Besides sedimentation-related migration, there is a mechanism of migration due to shear which is independent of particle density. Vasseur and Cox (1976) have developed the following approximate formula for the migration velocity of a neutrally buoyant particle:

$$v_{mn} = \frac{55}{4608} \frac{d_p^3 g^2}{\nu} \tag{7.2}$$

There are certain inconsistencies in the assumptions underlying the above equation. Hamour (1984) has removed these inconsistencies by seeking a more complex solution. This solution suggests that Eqn. (7.2) consistently overestimates the migration velocity. In order to obtain a conservative estimate of migration, Eqn. (7.2) is used in the subsequent derivations.

The migration length is defined as the streamwise distance traveled by a particle while migrating from the lower bound in y of the measuring volume to the upper bound. This parameter may be expressed by:

$$L_m = \frac{g(y_{max}^2 - y_{min}^2)}{2(v_{ms} + v_{mn})} \tag{7.3}$$

Values of the migration length for various materials are plotted in Fig. 7.4. These results are based on the values of specific gravity of 1.06, 2.5 and 3.2 for polystyrene latex, dust, and silicon carbide, respectively. The velocity gradient is taken as 1000 s^{-1} and values of y_{max} and y_{min} have been specified as 150 and 50 microns, respectively.

It is obvious that heavy particles such as those of silicon carbide are not useful for measurement unless seeded a short distance upstream of the measuring volume. In a channel of length not exceeding a few meters, light particles such as those of polystyrene latex are likely to stay in the y-limits of the measuring volume. These deductions have been verified experimentally in the present test facility. The final data sets were taken in a flow seeded with polystyrene latex particles.

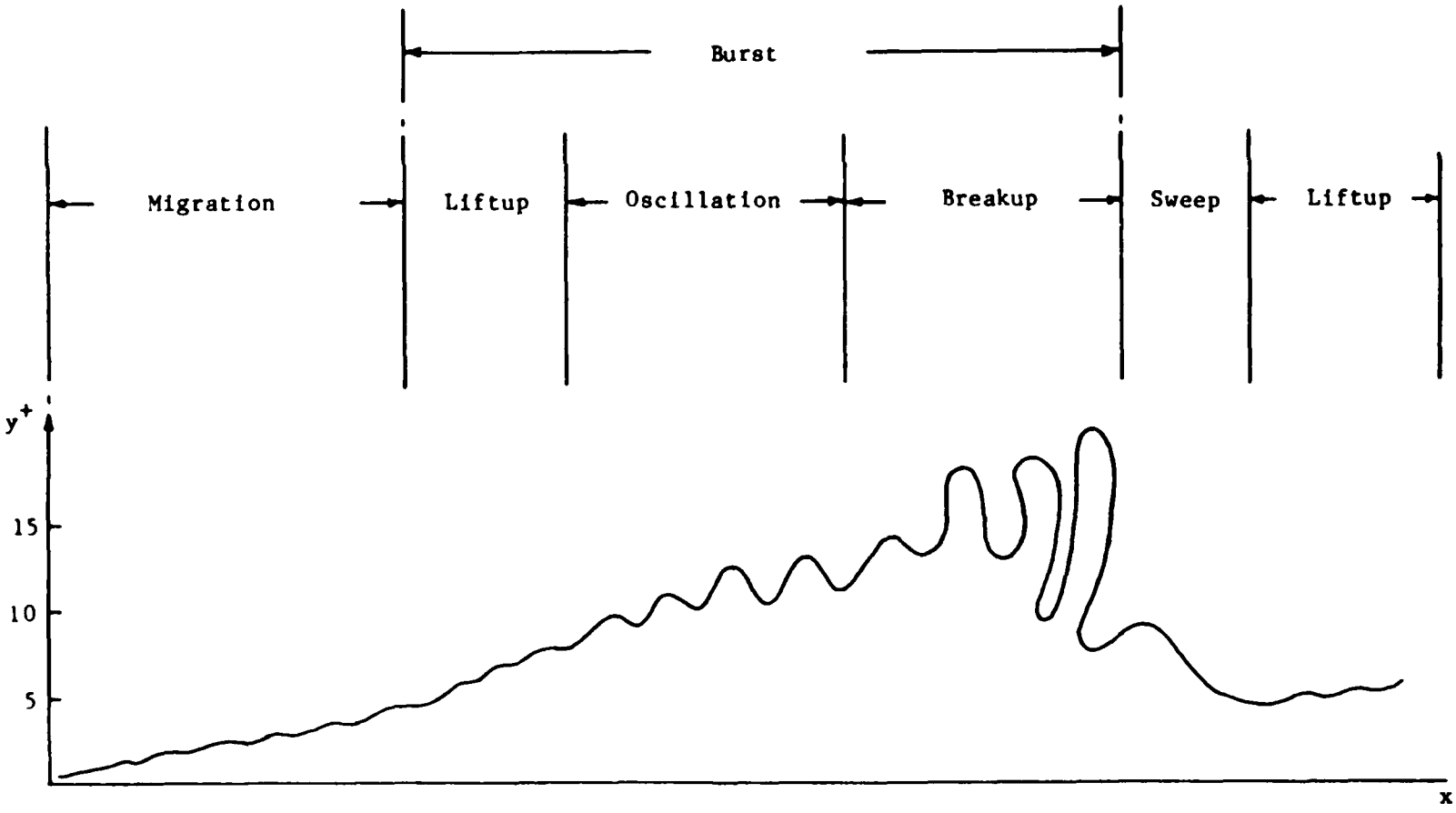

Fig. 7.1. Schematic representation of the particle path in the sublayer.

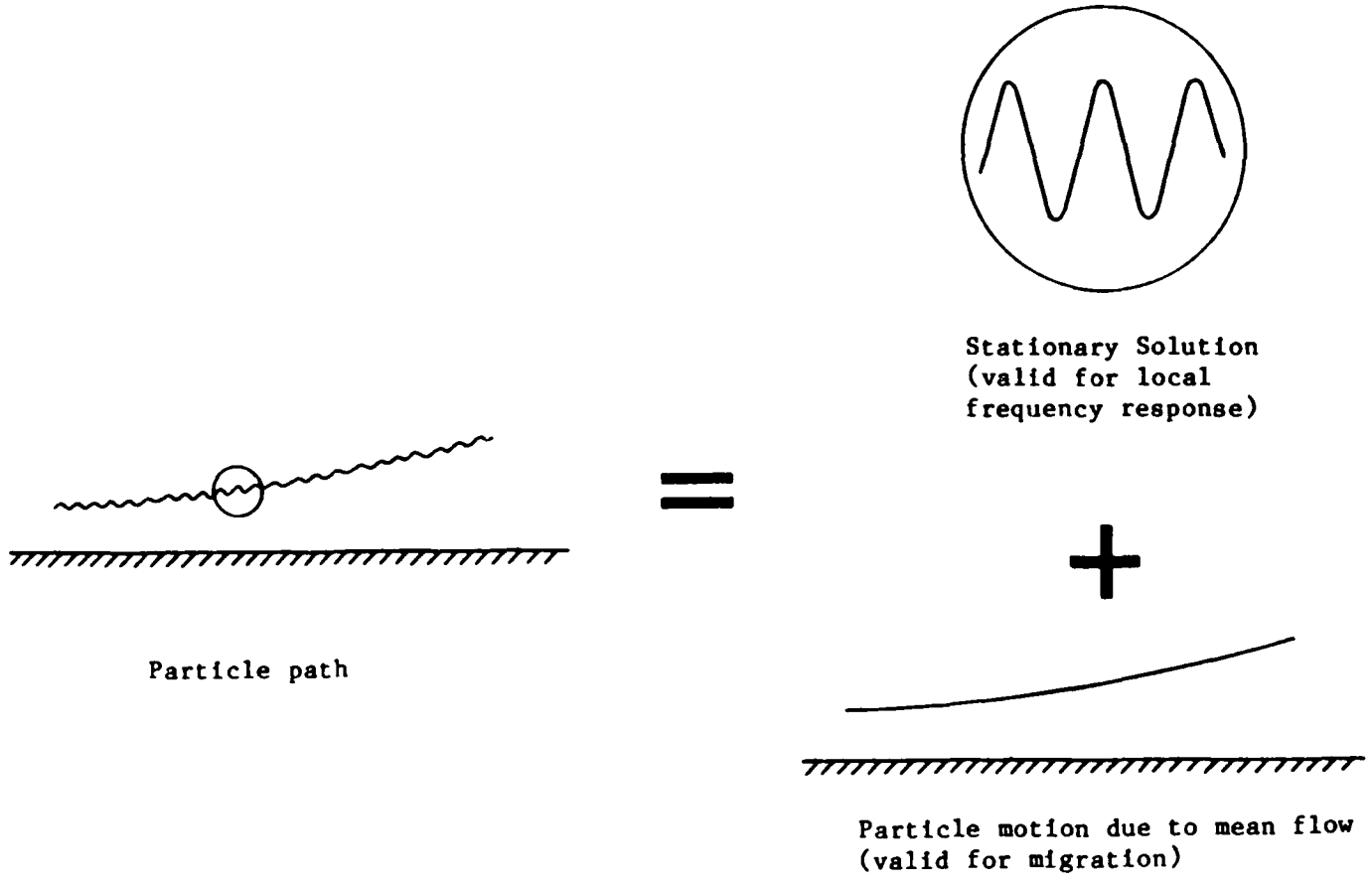

Fig. 7.2. Dichotomy of particle motion.

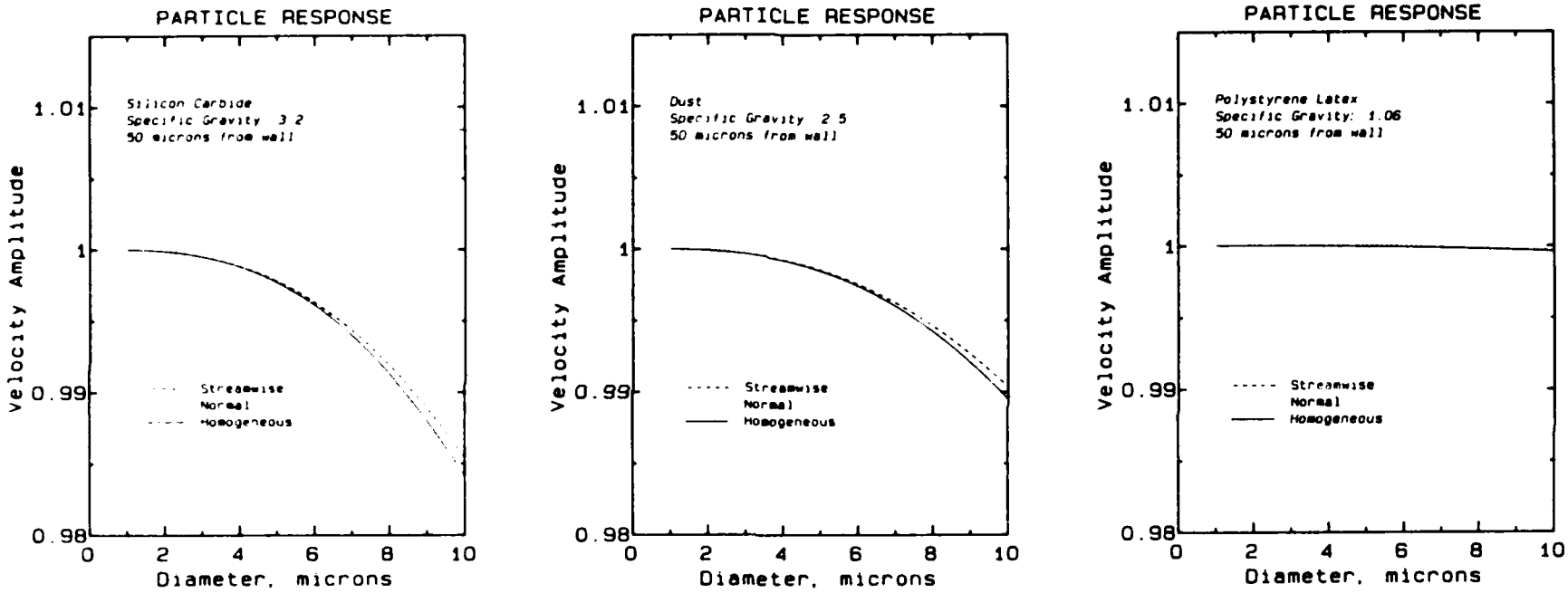

Fig. 7.3. Stationary response for particles of various materials.

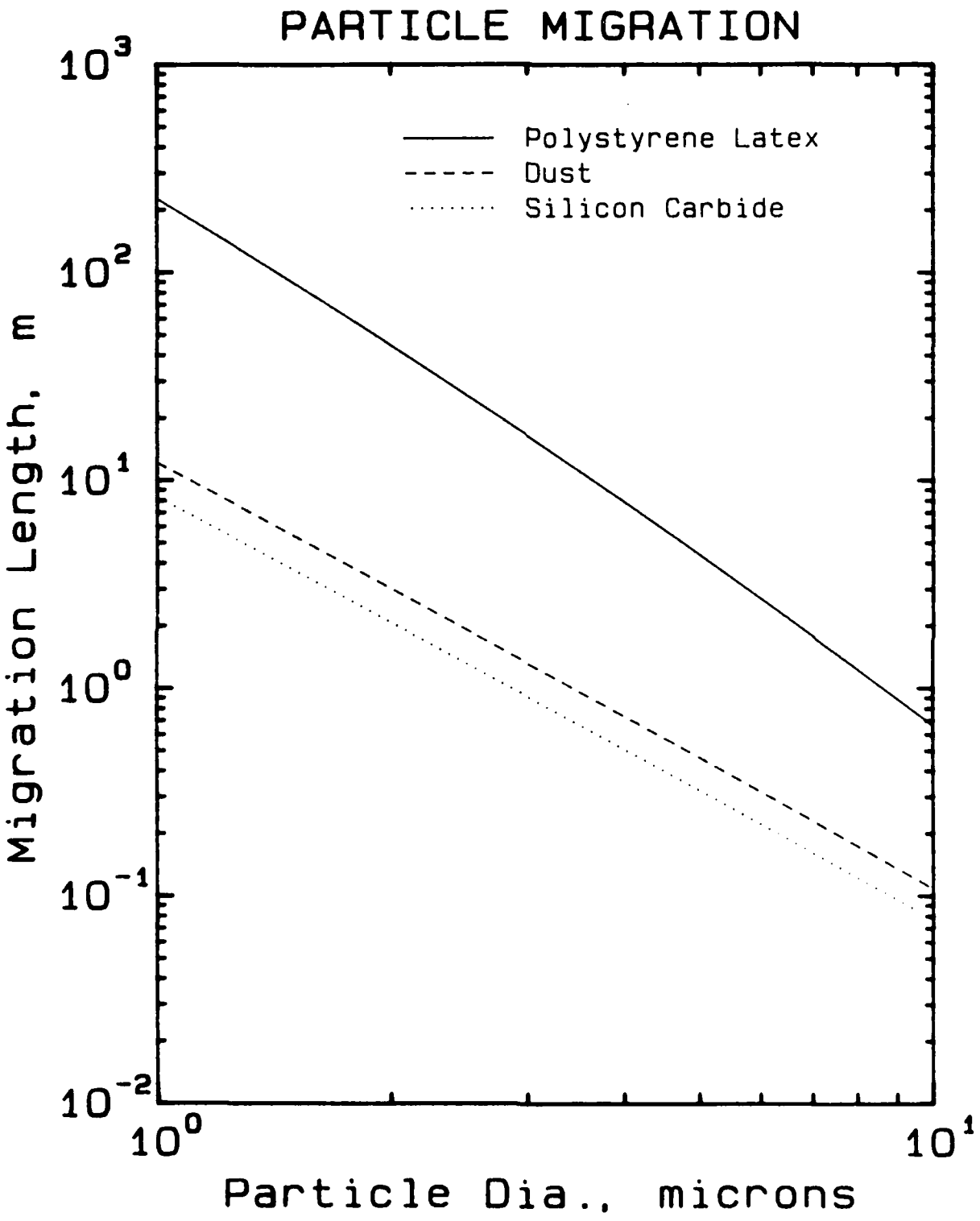

Fig. 7.4. Migration characteristics for particles of various materials.

Chapter 8

EVALUATION IN LAMINAR FLOW

Prior to testing in a turbulent boundary layer, the first version of the instrument (using unpackaged optics) was evaluated in a laminar flow channel. The purpose of this evaluation was to qualify the instrument in a well-understood flow situation. The anticipated particle behavior was also verified through these experiments. A laminar flow water tunnel was built to create steady skin friction comparable with turbulent boundary layer of the intended application of the device.

8.1 Laminar Flow Facility

The laminar channel has a rectangular cross-section of 3" × 1/8". Measurements were made at a distance of 12" from the entrance. Hence a condition close to plane Poiseuille flow was obtained. A scaled diagram of the facility is shown in Fig. 8.1. The tunnel stood vertically on an optical table and provides an easy access for the optical setup described earlier. This arrangement allowed testing of the unpackaged device on an optical bench. As shown in the photographs in Fig. 8.2, the unpackaged device had a horizontal train of optical elements and required the flow channel to be vertical. (The packaged version of the instrument is vertical and suits a horizontal channel.)

Flow was maintained through the channel by a pump-and-tank assembly in a closed loop. Water was seeded with Polyvinyltoluene Latex microspheres of diameter 2.0 microns. These particles have a density of 1.027 g/ml and a refractive index of 1.60. The signal rate was found to correspond closely to a uniform distribution of seed particles throughout the channel cross-section which indicates that the effect of shear on the particle path is negligible.

As shown in Fig. 8.3, the receiving optics in this arrangement were located at an angle of 22° from the side. The receiving optics were set up with a front lens of focal length 600 mm and a pinhole of diameter 50 microns in front of the photomultiplier tube. This combination produces a nearly cylindrical measuring volume of diameter 100 microns and a receiving cone angle of 6°.

The receiving assembly was positioned in place by first moving it close to the wall to obtain a signal of the form shown in Fig. 4.12(d), which has two distinct peaks due to laser light from the two slits. The near-wall signals were qualified according to the criteria described in Section 4.6. The receiving assembly was then moved away from the wall to locate the measuring volume center roughly at 100 microns from the wall.

8.2 Results and Discussion

The signal frequency was found to be fairly insensitive to small changes in the location of the measuring volume and the size of the pinhole. The results of the experiments are plotted in Fig. 8.4. The theoretical estimate in the plot is based on the following relationship for plane Poiseuille flow,

$$\tau^* = 12\ Re_H \tag{8.1}$$

where

$$\tau^* = \frac{\tau}{\frac{\rho}{2}\left(\frac{\nu}{H}\right)^2} \tag{8.2}$$

The above expression is obtained from the parabolic velocity profile of the flow under consideration. A discussion of this flow may be found in standard text books such as Schlichting (1979).

The dots on the plot correspond to the mode and the error bars to 95% confidence limits for the data recorded. The mode of a data record is understood to represent the steady laminar flow and the scatter can be attributed to occasional fluctuations in flow. Note that the data are in good agreement with the known laminar wall shear-stress behavior.

Scale: approx. 1/12

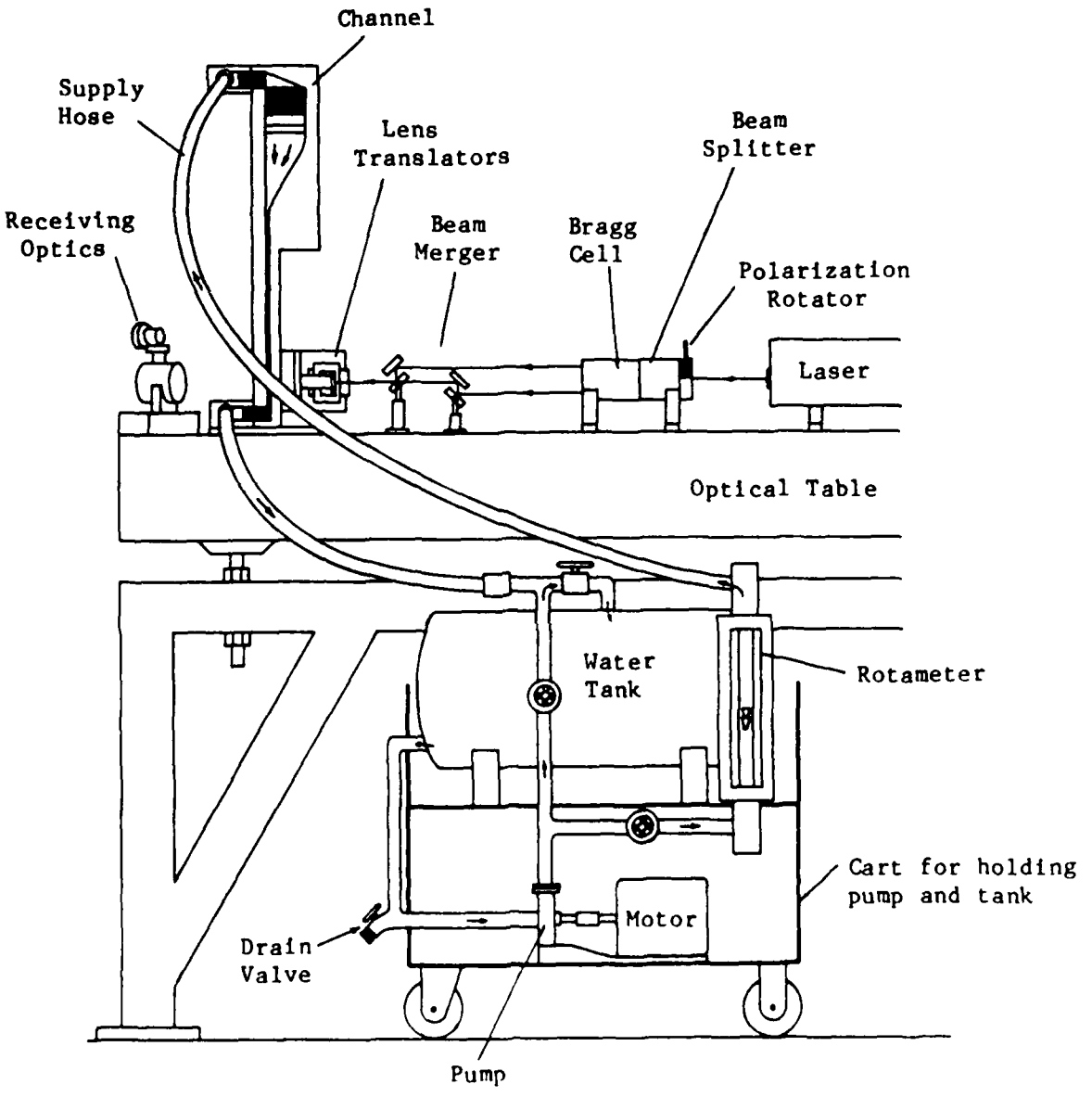

Fig. 8.1. Laminar demonstration facility: unpackaged optics, bench-top channel, and accessories.

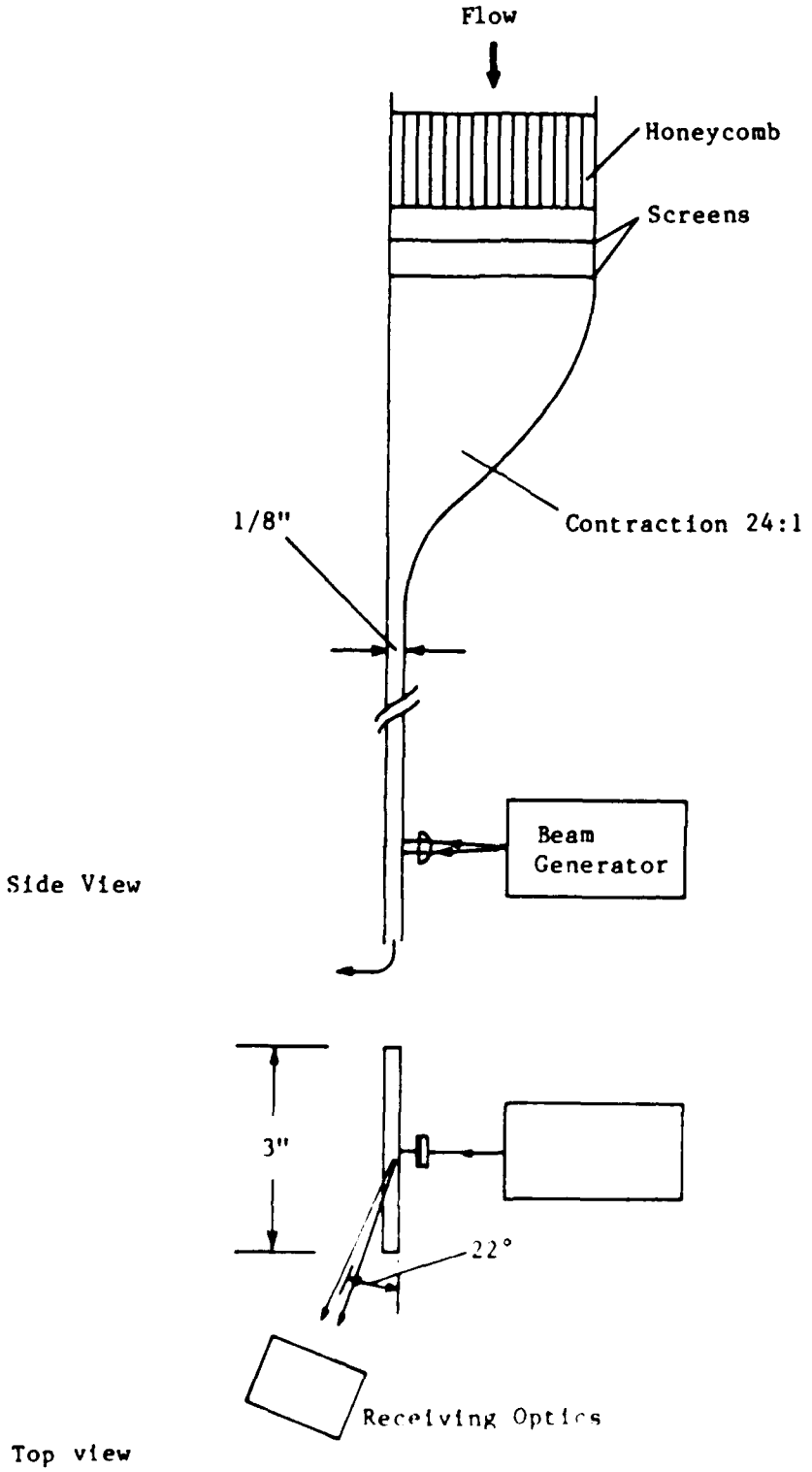

Fig. 8.3. Laminar channel: some significant features.

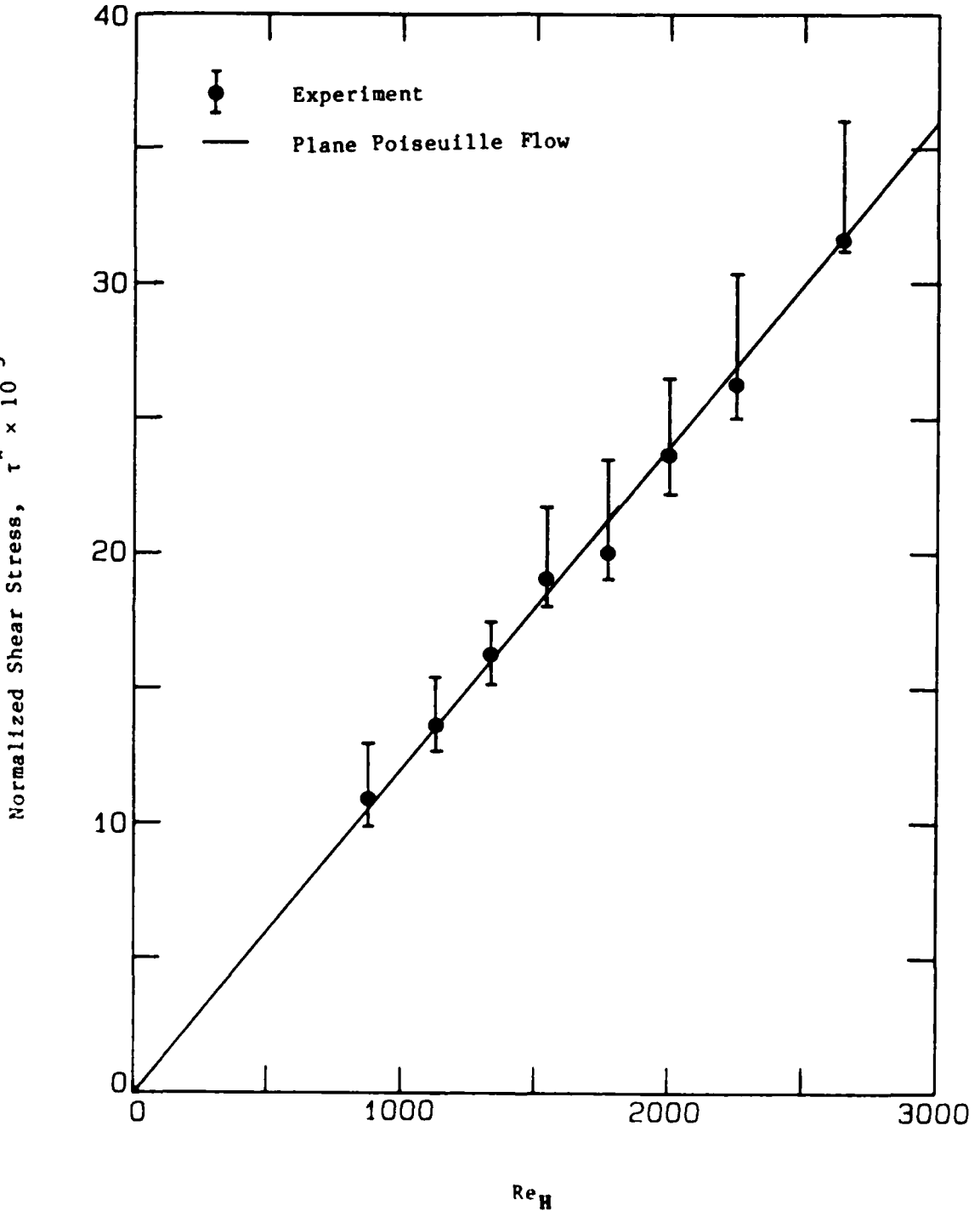

Fig. 8.4. Skin friction in laminar channel flow.

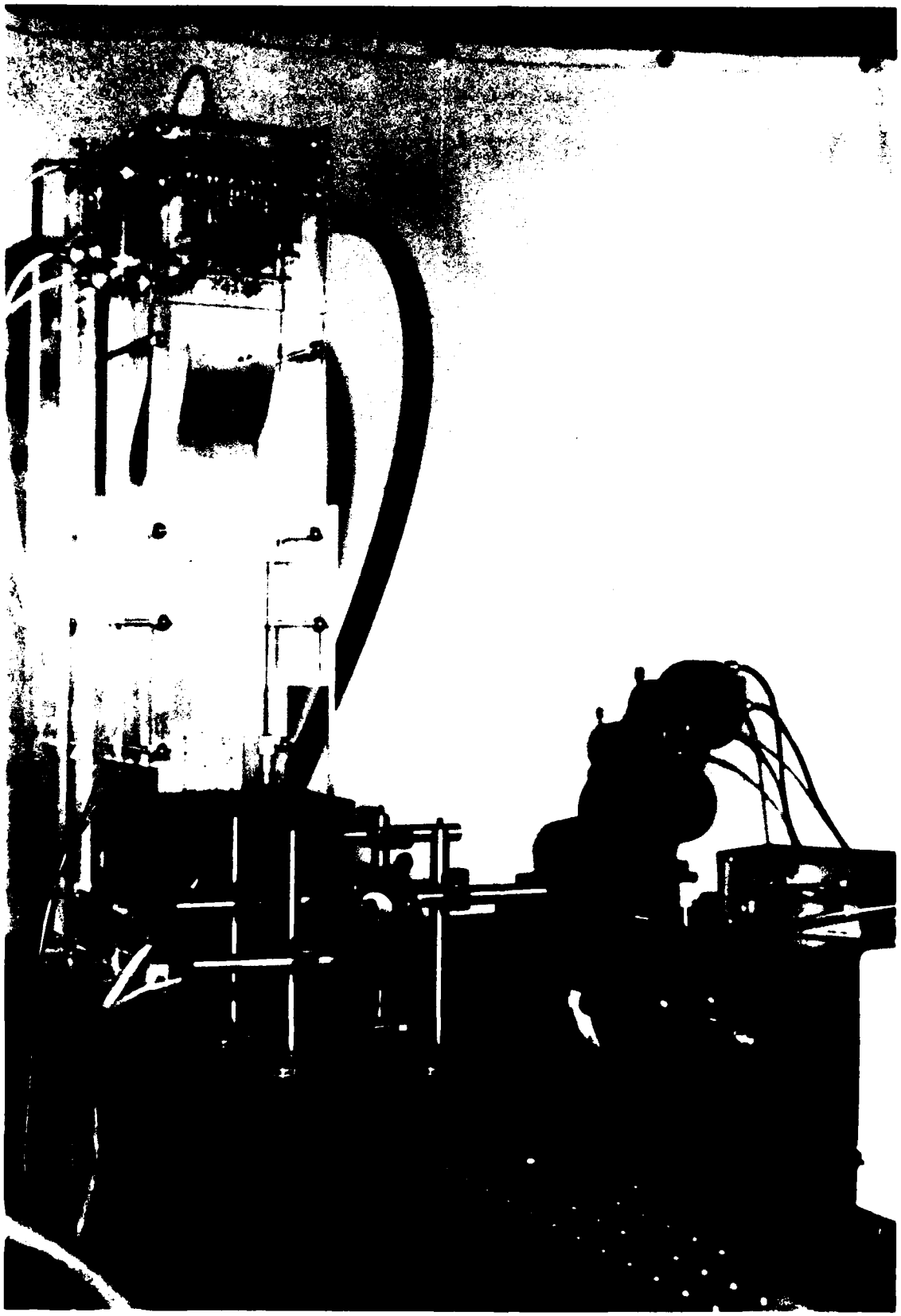

Fig. 8.2(a). Laminar flow measurements: experimental setup.

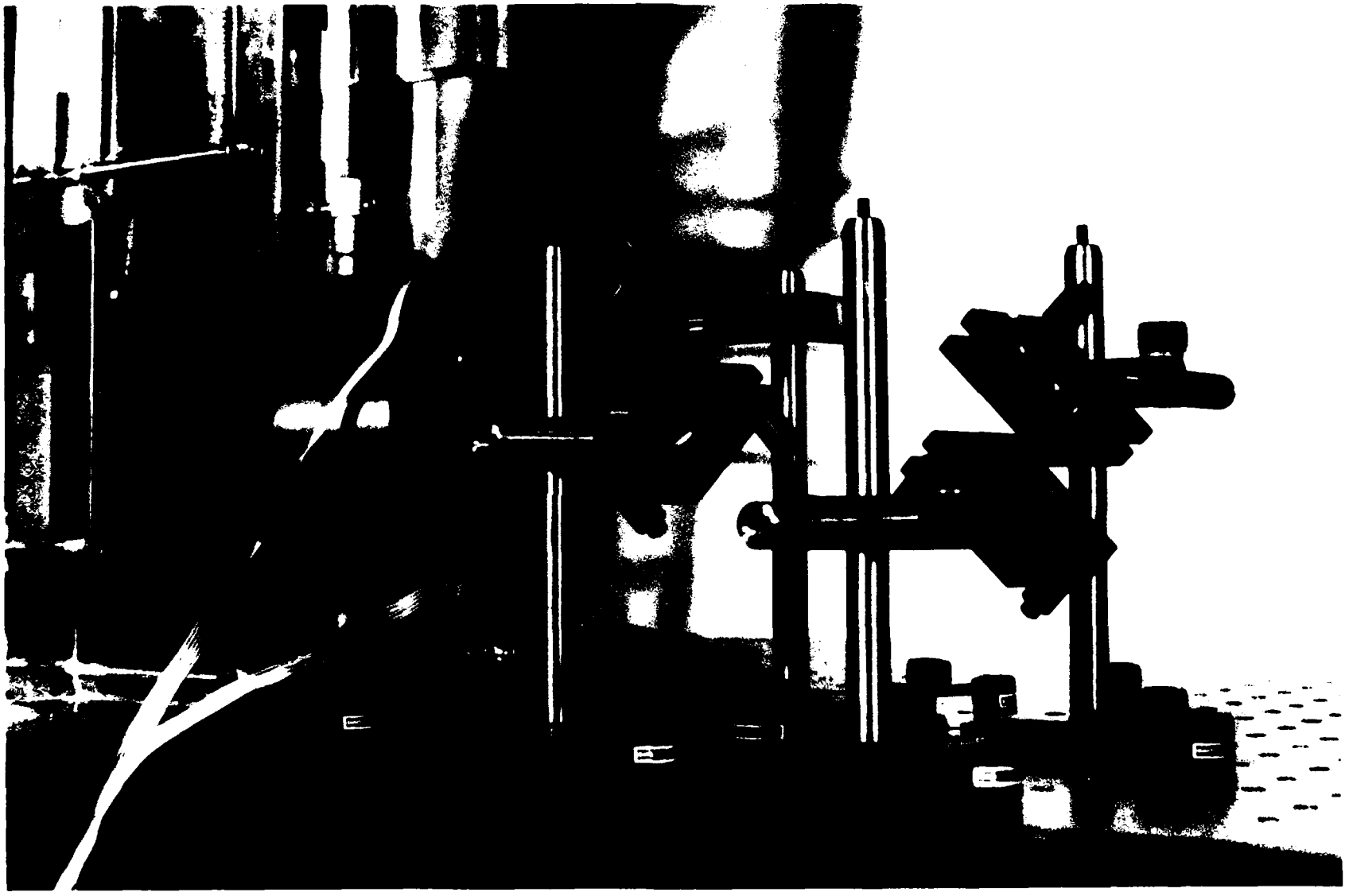

Fig. 8.2(b). Laminer flow measurement: beam merger and lens translators.

Chapter 9

MEASUREMENTS IN A TURBULENT BOUNDARY LAYER

Following an evaluation in laminar flow, the packaged instrument was constructed and used for measurements in a zero-pressure-gradient turbulent boundary layer. The results of these experiments have not only further validated the technique but have also provided new data valuable to researchers in this field. The present measurements consist of large samples of the velocity gradient in the streamwise and spanwise directions. Various statistical parameters of these data are presented and discussed later in this chapter. In order to correlate these data to other parameters of the boundary layer, a profile of the streamwise velocity was also recorded at the location of skin friction measurement.

9.1 Turbulent Flow Facility

The turbulence measurements were made in an existing facility, described in detail by Jayaraman et al. (1982). In this facility, measurements are made in a boundary layer growing on the top surface of a water tunnel of rectangular cross-section. It was found that near-wall measurements are strongly influenced by presence of air bubbles in the flow. In order to eliminate the bubbles, some modifications were made. In the original system, the gate valve used to oscillate the flow discharged water into the sump as a free-falling stream. This arrangement caused entrainment of a large amount of air into the flow. Since the present experiments could be conducted with a steady flow, the oscillating gate valve was replaced by a closed conduit which discharged water below the fluid surface in the sump. The existing apparatus was also supplemented with a de-aeration system, illustrated in Fig. 9.1. A small portion of the flow in the system ($\sim$ 5%) was passed through a venturi consisting of a sudden expansion from 1/2" to 2" in diameter. The pressure drop across the venturi allowed maintaining a vacuum of $\sim$ 25" of mercury downstream. At this pressure, the suspended air bubbles were easily separated from water by swirling it in a separation chamber. The air-bubbles accumulated on the center of the centrifugal separation chamber and rose to the air-water interface in a separation

column. The separated air was continuously removed by a vacuum pump connected to the column.

Two sets of fine and course valves were used to adjust the flow rates of air and water through the separation chamber, so that a high vacuum was obtained and the air-water interface in the separation column was maintained at a fixed level. However, in practice, the air-water interface drifted over long periods of operation. A control system was used to maintain the interface between two float switches. The water level in the separation column was allowed to rise till it reached the upper float. At this point a solenoid valve shut off the air flow. The separated air collected in the column and lowered the water level till it went below the lower float. This actuated the solenoid valve open and the cycle was repeated.

9.2 Flow Qualification

The quality of the flow in the turbulent boundary layer facility was studied and documented by earlier users, Jayaraman et al. (1982) and Brereton (1986). As described earlier, the existing facility was modified; hence, a re-examination of the flow was warranted. However, the present evaluation of the boundary layer has been restricted to the following:

- Measurement of a velocity profile at the location of the shear stress measuring device;
- Application of Coles' scheme of boundary layer classification to the mean profile;
- Evaluation of mean profile parameters (displacement thickness, momentum thickness, Reynolds number etc.) as well as turbulence parameters;
- Measurement of probability density function (PDF) of streamwise velocity at $y^+ = 16.9$.

The rest of this section consists of a description of Coles' method and a discussion of the boundary layer parameters.

9.2.1 Coles' Scheme of Boundary Layer Classification

Coles (1962) has suggested a procedure for classifying turbulent boundary layers using the similarity laws developed by Prandtl and von Kármán. In this scheme the experimental data are fitted to a profile of the form:

$$u^+ = \frac{1}{\kappa} \ln y^+ + c + \frac{2\Pi}{\kappa} \sin^2\left(\frac{\pi}{2}\frac{y}{\delta}\right) \qquad (9.1)$$

where $u^+ = u/u^*$ and $y^+ = u^* y/\nu$. Knowing the free-stream velocity, $\overline{U}$,

$$U^+ = \frac{1}{\kappa} \ln \delta^+ + c + \frac{2\Pi}{\kappa}$$

or

$$\Pi = \frac{\kappa}{2}\left(U^+ - \frac{1}{\kappa} \ln \delta^+ + c\right) \qquad (9.2)$$

Substituting the value of Π from (9.2) in (9.1),

$$u^+ = \frac{1}{\kappa} \ln y^+ + c + \left[U^+ - \frac{1}{\kappa} \ln \delta^+ - c\right] \sin^2\left(\frac{\pi}{2}\frac{y}{\delta}\right) \qquad (9.3)$$

After choosing fixed values of κ and c, a given set of data may be fitted to the above equation by adjusting the parameters u^* and δ. The value of Π corresponding to a least-squares fit has a special significance in the present scheme of flow qualification. Using $\kappa = 0.41$ and $c = 5.0$, a constant-pressure boundary layer is expected to have a value of $\Pi \simeq 0.62$. The value of Π is larger for an adverse pressure gradient. For a supposedly zero-pressure-gradient flow, a significant deviation from $\Pi = 0.62$ is an indication of a non-standard boundary layer, resulting usually from the presence of secondary flows and/or poor choice of boundary layer tripping device. Furthermore, according to Coles (1968), the optimum value of u^* is slightly, though consistently, smaller than the friction velocity evaluated from other methods. Hence, the estimate of C_f based on u^* is usually one to two percent smaller than expected C_f.

The success of this method in classifying boundary layers and estimating skin friction does not imply that the recommended numerical values of κ and c are necessarily definitive. Despite minor

refinements, the present values are basically adduced from the earliest experimental explorations of these constants. The modern expertise in producing standard flow situations and instrumentation for measuring such flows has yet to be employed systematically in order to re-evaluate the numerical values of these constants. It is in fact evident from certain experimental results that the values of these constants are likely to be higher than the classical values. Also, numerical simulations of Spalart (1986) indicate a dependence of κ on Reynolds number; suggesting an increase in κ with increasing Re_{δ_2}.

For the boundary layer under consideration, the velocity profiles of raw and normalized data are shown in Fig. 9.2. The values of δ, Π, and u^* for the best fit to Eqn. (9.3) are listed in Table 9.1. The value of Π is 3.5% higher than the expected value for a zero-pressure-gradient boundary layer. The scatter above the wall functions of eqn. (9.1) is about 0.5 % of free-stream velocity. As obvious from figure 9.2(b), the scatter in the data is not random. In fact, it indicates that the slope of the log-linear region is smaller than expected. Hence, according to Coles' criterion, this boundary layer has certain minor anomalies. It is regrettable that, due to lack of time, we did not have an opportunity to resolve these apparent abnormalities.

9.2.2 Parameters of the Boundary Layer

Table 9.1 contains values of various thicknesses of the boundary layer and other standard parameters such as, shape factors and Reynolds numbers. All the parameters are evaluated from the best fit to Eqn. (9.1) (referred to as standard functions) as well as from direct parabolic interpolation of the data. No significant differences were found between the results from the two methods. Table 9.1 also contains the value of the friction coefficient as obtained from the correlation of Ludwieg and Tillmann (1949); i.e.,

$$C_f = 0.246 \times 10^{-0.678H} Re_{\delta_1}^{-0.268} \qquad (9.4)$$

The value of C_f from this correlation is in close agreement with the value from the optimum u^* for Coles' fit to the data. It should be

noticed that the Reynolds number of the flow (Re_{δ_2} = 3700) is fairly high and reliable numerical simulations of such a flow are not available.

The present measuremets indicate about 2% turbulence in the free-stream. Earlier measurements in the same flow, as documented in a microfiche report by Jayaraman et al. (1982) indicated less than 1% turbulence in the free-stream. The higher value of "apparent turbulence" in the present measurements is believed to be caused by the higher vibration level of the new LDV system. The distribution of the fluctuating component of streamwise velocity is presented in Fig. 9.3. The probability density function of the velocity was also recorded at a y-location near the wall (yu^*/ν = 16.9). It is shown in Fig. 9.4. The skewness and flatness factors at this location are -0.23 and 2.8, respectively. These numbers are in reasonable agreement with the results reported by Eckelmann (1974). Visual observations of Schraub and Kline (1965) indicate that beyond y^+ = 10, the high-speed streaks are wider than the low-speed streaks which results in negative skewness factor for the PDF. However, in closer proximity to the wall ($y^+ < 10$), the opposite is true about the width of the low- and high-speed streaks; hence, a positive value of the skewness factor is expected.

9.3 Measurements of Streamwise Skin Friction

The results of the present experiments are listed in Table 9.2. For the sake of comparison, data from a selection of experiments and numerical simulations describing similar flow situations are also included. For boundary layer flows, the reported Reynolds number is based on momentum thickness and free-stream velocity. Whereas for channel flows, it is expressed in terms of centerline velocity and half-width of the channel. Similarly, C_f is defined in terms of free-stream velocity for boundary layer flow and centerline velocity for channel flow. In the case of pipe flow, radius and the centerline velocity are used as characteristic length and velocity respectively. Any exception to this convention has be stated in the footnotes to Table 9.2.

The earliest measurements by Mitchell & Hanratty (1966) had shown a Gaussian distribution of skin friction which is now considered incorrect and the anomaly is generally attributed to the lack of spatial resolution; especially along the spanwise direction. Also, notice that measurements of Eckelmann (1974) in an oil channel have been repeated recently by Alfredsson et al. (198( ). The authors have rendered earlier measurements inaccurate on account of unreliability of the analog linearization of hot-film data which has now been replaced by digital linearization.

The present technique was used in two different modes; i.e., with and without shifting the frequency of light illuminating one of the slits. The results from the two modes of application are slightly different. The differences between the two measurements are illustrated in Fig. 9.5. A plausible explanation of this discrepancy is as follows. In order to eliminate the low-frequency noise, the detected signal was high-pass filtered. Whereas the filter frequency was sufficiently lower than the lowest signal frequency for a rotating fan, it appears to interfere with the signal frequencies for the stationary fan. In the latter case, the filter was set at a center-frequency of ~ 7 kHz, which is represented by the vertical line in Fig. 9.5. This may have resulted in elimination of some low frequency signals as well as distortion of such signals during passage through the filter. A clustering of signals near the filter-frequency is also evident from Fig. 9.5. Unfortunately, due to lack of time, this interpretation of the discrepancies in the two measurements could not be verified experimentally. However, for the current purpose, the results of measurements with frequency-shifting are considered more accurate. Hence, only these results are used for further reducing the data.

9.3.1 Mean Flow Near the Wall

The skin friction coefficient from DCW measurement is 4% higher than the estimate based on the Ludwieg-Tillmann correlation. The mean value of the velocity gradient is shown in Fig. 9.6(a). The near-wall data points from the conventional LDV are also plotted in this figure. The near-wall mean velocity seems to approach the wall behavior as

recorded by the present technique. For the conventional measurement, the origin of the y-axis was identified by by a visual examination of the interaction between the measuring volume and the wall. The standard receiving assembly and the eye-piece were used as a microscope while the measuring volume was gradually moved towards the wall. This method has a repeatability of ± 0.1 mm. A zero-shift within this uncertainty range has provided a good continuity between the two type of measurements depicted in Fig. 9.6(a).

In Fig. 9.6(b), the velocity profile has been normalized with the measured value of wall velocity gradient. The logarithmic region of the profile has a smaller slope than that stipulated in Coles scheme of boundary layer classification. The corresponding value of κ is about 0.46.

9.3.2 Wall Turbulence

In Fig. 9.7, the measured wall turbulence is compared with the data of near-wall turbulence from conventional LDV. The latter type of measurements could not be conducted nearer to the wall than $y^+ = 7$. Hence, a conclusive comparison cannot be made. However, there is no obvious disagreement between the two type of measurements.

The probability density function of the normalized wall shear $(\tau - \overline{\tau})/\tau'$ is plotted in Fig. 9.8. The measured data have been distributed into bins of size $\tau'/5$. An attempt to use smaller bin size results in larger scatter in the PDF. This may be attributed to a relatively small size of the sample. The dotted line in Fig. 9.8 corresponds to the PDF of wall shear stress from the numerical simulation of Kim et al. (1986).

9.4 Measurement of Spanwise Velocity Gradient

As discussed in Chapter 5, the spanwise measurements are difficult to make because of the need to eliminate the influx of unscattered light into the receiving optics. Attempts were made to approach the wall closely, while isolating the slits from the measuring volume. The value of $\partial w'/\partial y$ was found to increase with the approach of the wall. A final steady value could not be identified from the present realiza-

tions. The results presented in Table 9.3 are from the closest location to the wall reached during these experiments.

It is obvious from the data presented in this table that an enormous discrepancy exists in the reported statistics of spanwise flow near the wall. A non-zero value of skewness factor in various studies is an indication of inability to identify accurately the spanwise direction and/or inadequate sample size. Similarly, the mean values of $\partial w/\partial y$ are also non-zero in some of the measurements. The mean value from the experiments of Sirkar and Hanratty (1970) is estimated to be 3% of the streamwise mean value. The present measurements have a mean value of 0.24% (though from the alignment of the instrument with respect to the tunnel, it was expected to be about -1% of the streamwise value).

In Table 9.2, the term "turbulence intensity" implies the limiting value of $w'/\bar{u}$ at the wall. The computed value of this parameter is much larger than the measured values. This discrepancy may be explained as follows. Numerical simulation of Kim et al. indicates that, unlike the streamwise fluctuation, the spanwise component does not vary linearly in the vicinity of the wall. It becomes linear only in a region smaller than $y^+ = 1$. The simulations of viscous sublayer performed by Chapman and Kuhn (1985) have yielded similar results. These numerical findings are in agreement with the present experimental observation that the value of fluctuation in the spanwise gradient does not become invariant with respect to y-location even if the measuring volume covers as small a region in y^+ as three wall units. Instead, it continues to increase with the approach of the wall. The strong non-linearity in variation of w' with respect to y would also render other experimental techniques inaccurate because of their dependence on existence of a thermal or concentration layer within a purely viscous hydrodynamic sublayer.

The probability density function of the spanwise measurement is presented in Fig. 9.9. Notice that because of the poor resolution, the bin size could not be reduced below $0.4\ \tau'$. The present results are compared with the numerical simulation of Kim et al. (1986) at $y^+ = 5.4$. At this y-location, the turbulence intensity from the simulation agrees with the experimental result. The overshoot at the center may

AD-A178 629 DUAL CYLINDRICAL WAVE LASER-DOPPLER METHOD FOR MEASUREMENT OF SKIN FRICTI..(U) STANFORD UNIV CA DEPT OF MECHANICAL ENGINEERING A A NAQWI ET AL. JAN 87 3/3

UNCLASSIFIED ARO-19976.3-EG DAAG29-83-K-0056 F/G 20/4 NL

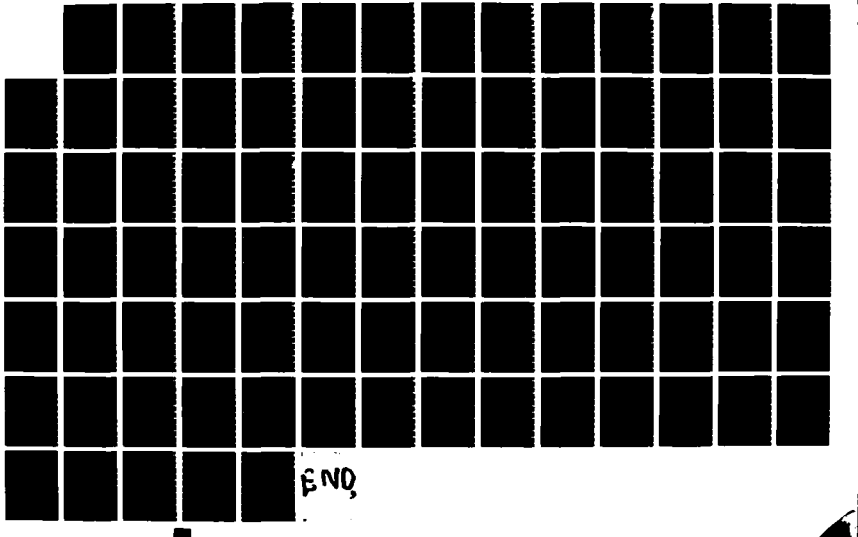

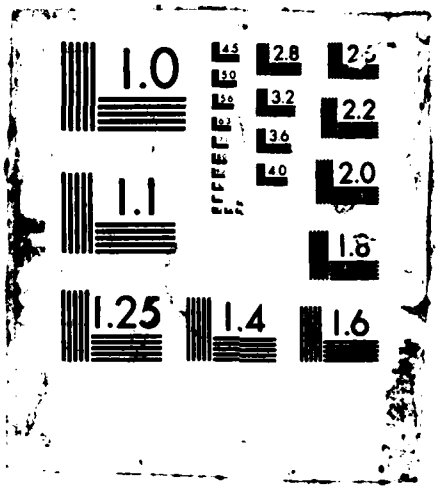
1.0
1.1
1.25
1.4
1.6
2.8
3.2
3.6
4.0
2.2
2.0
1.8

have been caused by the influx of some unscattered light during the measurement. Or it may be a result of the sampling bias. Signals from slower-moving particles have a large number of cycles and are more likely to be detected than faster-moving particles.

Table 9.1

PARAMETERS OF THE TURBULENT BOUNDARY LAYER

Coles' Scheme

Fitting Range:	1.69 mm to 26.6 mm (14 data points)
δ:	45.3 mm
u^*:	31.3 mm/s
Π:	0.642
Scatter (rms):	0.0049 $\overline{U}$
C_f:	0.00305

Integral Parameters

	Standard Functions	Parabolic Interpolation
δ_1	7.08 mm	7.05 mm
δ_2	5.04 mm	5.02 mm
δ_3	181.3 mm	180.7 mm
H	1.404	1.405
Re_{δ_1}	5200	5180
Re_{δ_2}	3700	3690
G	7.38	7.39
C_f (Ludwieg & Tillmann)	0.00304	0.00304

Table 9.2

CHARACTERISTICS OF SKIN FRICTION IN TURBULENT FLOW

Reference	Type of Flow	Measuring Technique	Reynolds Number	C_f x 10^4	Turbulence Intensity	Skewness Factor	Flatness Factor
Mitchell & Hanratty (1966)	Water in Pipe	Electro-Chemical Probe	40000	59	0.32	~ 0	~ 3
Eckelmann (1974)	Oil Channel	Flush Hot Film	2800-4100	54-51	0.24	0.75	3.7
Simons & Blinco (1974)	Water in Open Channel	Flush Hot Film	10000[a]	47[a]	0.39	0.89	3.7
Kim et al. (1986)	Channel Flow	Full Simulation	3300	60.4	0.364	0.90	4.15
Alfredsson et al. (1986)	Air B. Layer	Hot Wire on Wall	(2.6×10^6)[b]	--[c]	0.39	1.0	4.8
	Oil Channel	Hot Film on Wall	2600-3500	--[c]	0.36	1.1	4.8
	Water Channel	Flush Hot Film	5000	--[c]	0.40	1.0	4.2
Present Work	Water B. Layer	DCW: Bragg Shifted	3700 (1.6×10^6)[b]	31.8	0.38	0.78	4.0
	Water B. Layer	DCW: No Bragg Shift	3700	32.6	0.41	0.87	3.7

[a]Based on hydraulic diameter (cross-sectional area/wetted perimeter) and bulk velocity.
[b]Based on distance from the tripping device and the free-stream velocity.
[c]Reported to be consistent with Clauser plot; numbers not available.

Table 9.3

CHARACTERISTICS OF SPANWISE VELOCITY GRADIENT IN TURBULENT FLOW

Reference	Type of Flow	Measuring Technique	Reynolds Number	Turbulence Intensity	Skewness Factor	Flatness Factor
Sirkar & Hanratty (1970)	Water in Pipe	Electro-Chemical Probe	19000	0.098[a] (0.09)[b]	0.20[a]	2.3[a]
Py (1973)	Water Channel	Electro-Chemical	3500-12500	0.115	--	--
Kreplin & Eckelmann (1979)	Oil Channel	Flush Hot Film	2800-4100	0.065	0[c]	5.4
Kim et al. (1986)	Channel Flow	Full Simulation	3300	0.194	-0.02	7.0
Present Study	Water B. Layer	DCW	3700	0.111	0.028	4.6

[a]Deduced from Fig. 8 of the reference.

[b]Reported by the authors.

[c]Assumed; the instrument lacks directional sensitivity.

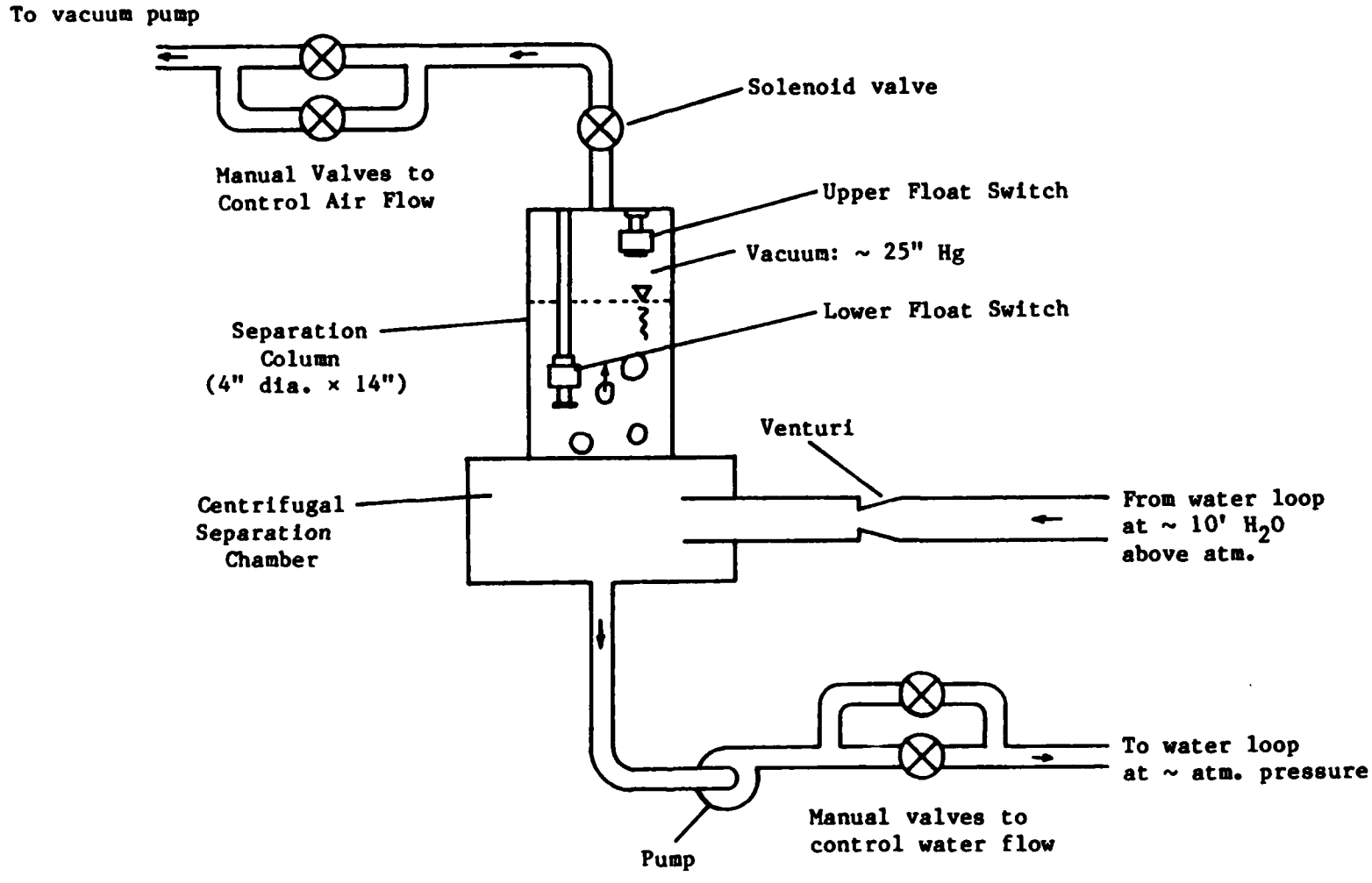

Fig. 9.1. The de-aeration system.

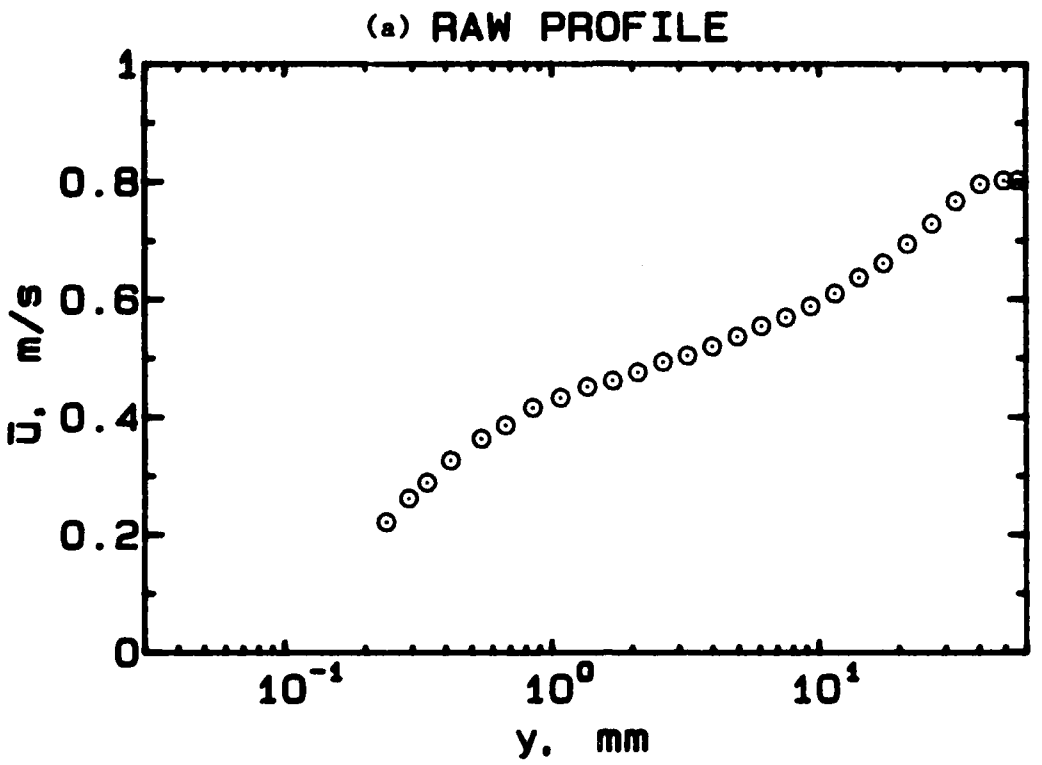

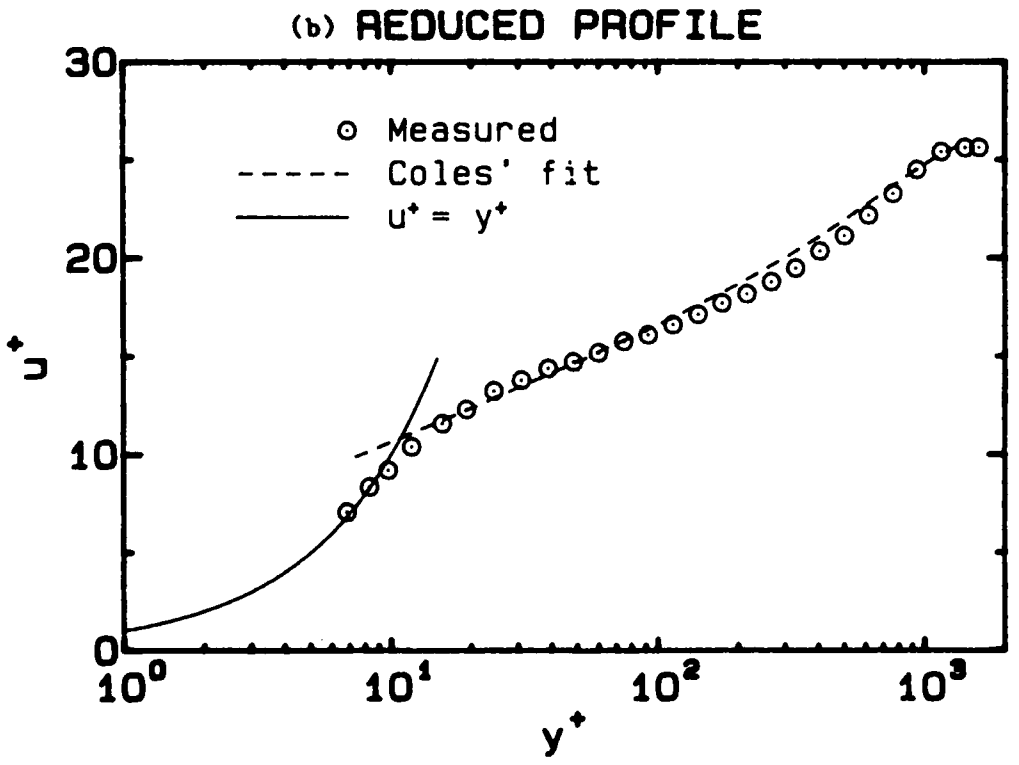

Fig. 9.2. Mean velocity in the boundary layer.

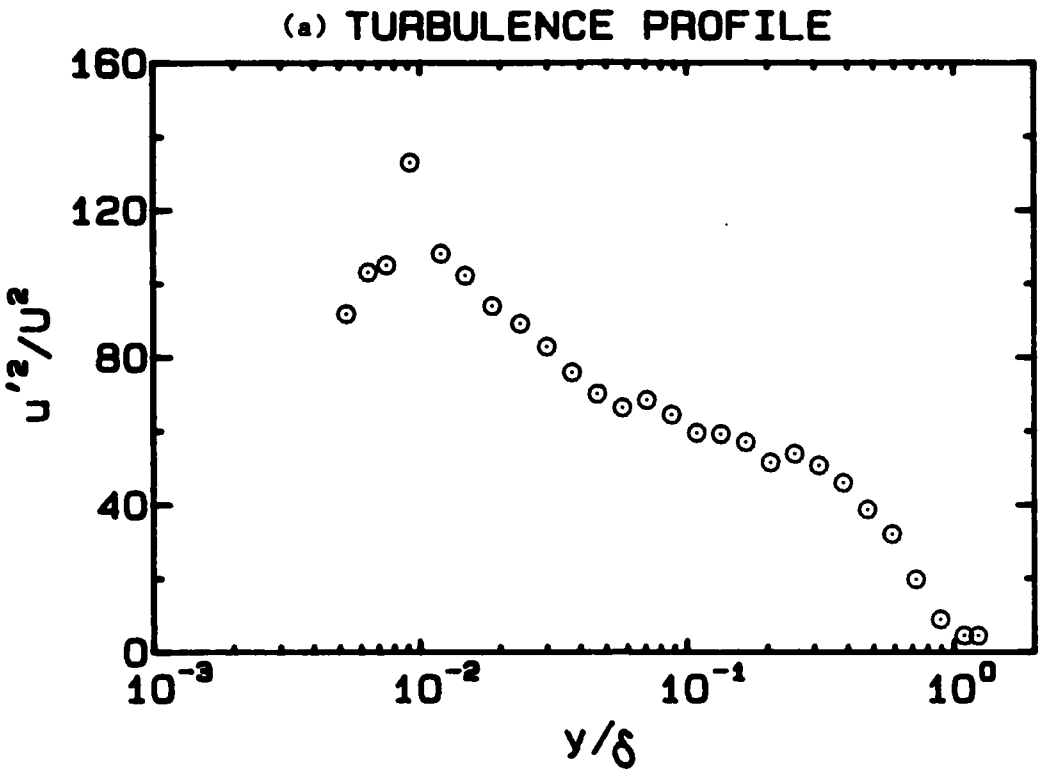

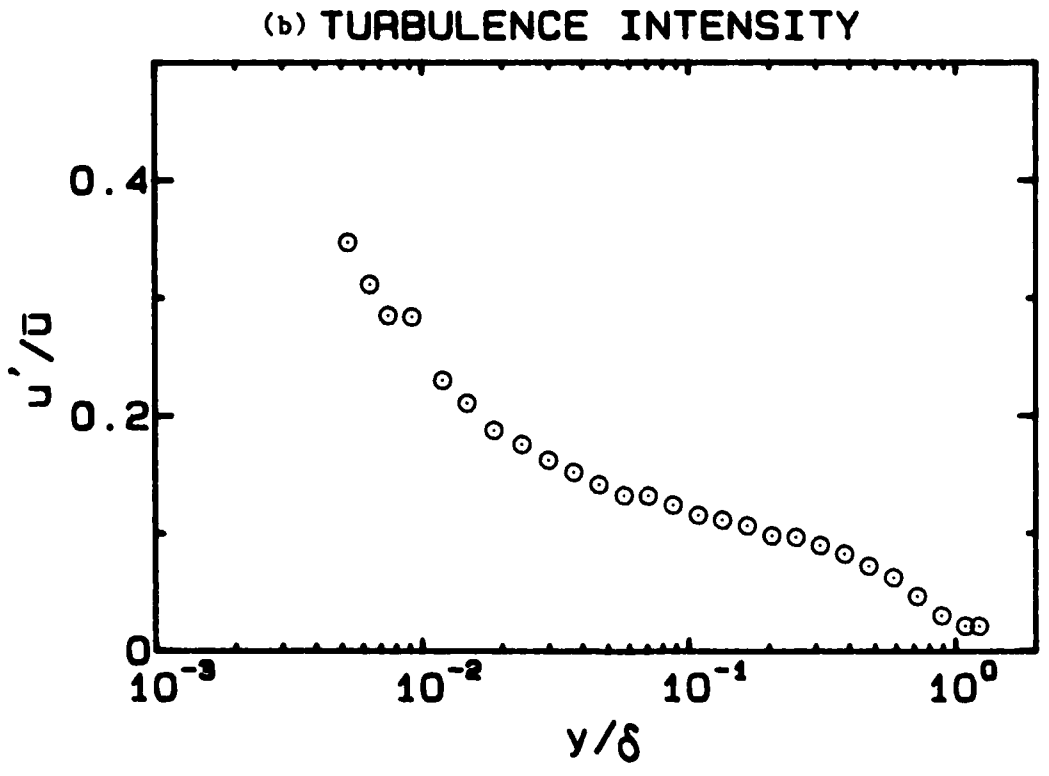

Fig. 9.3. Turbulence in the boundary layer.

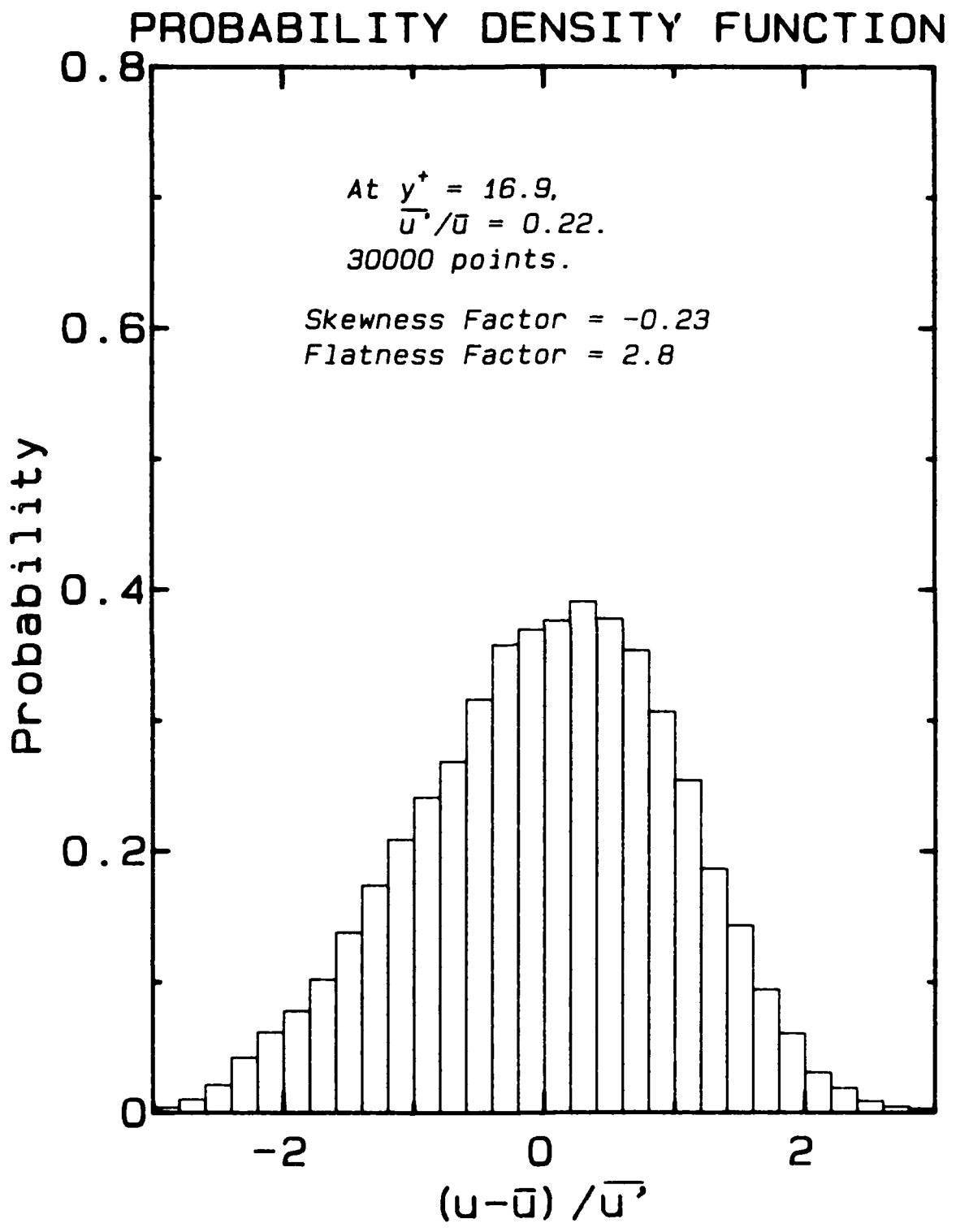

Fig. 9.4. Probability function of the streamwise velocity at a near-wall point.

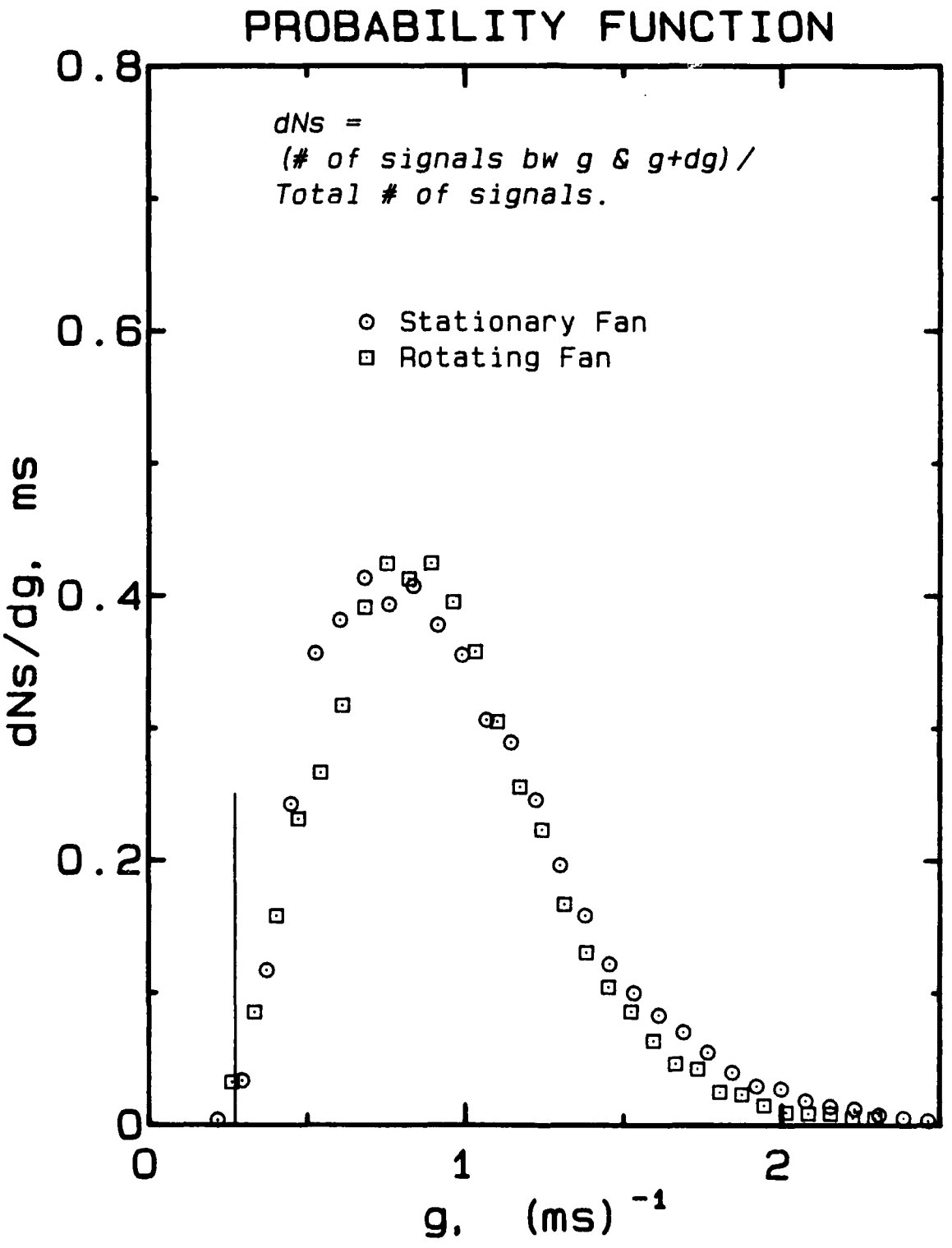

Fig. 9.5. Probability functions for experiments with and without Bragg shifting.

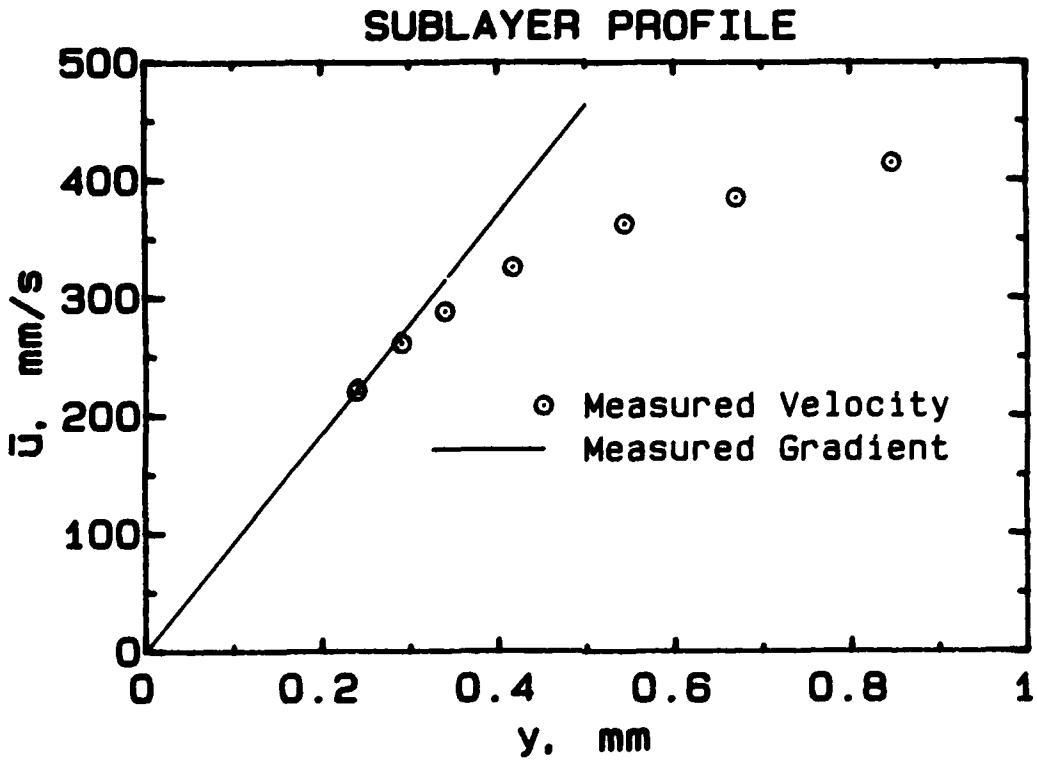

(a) Near-wall data

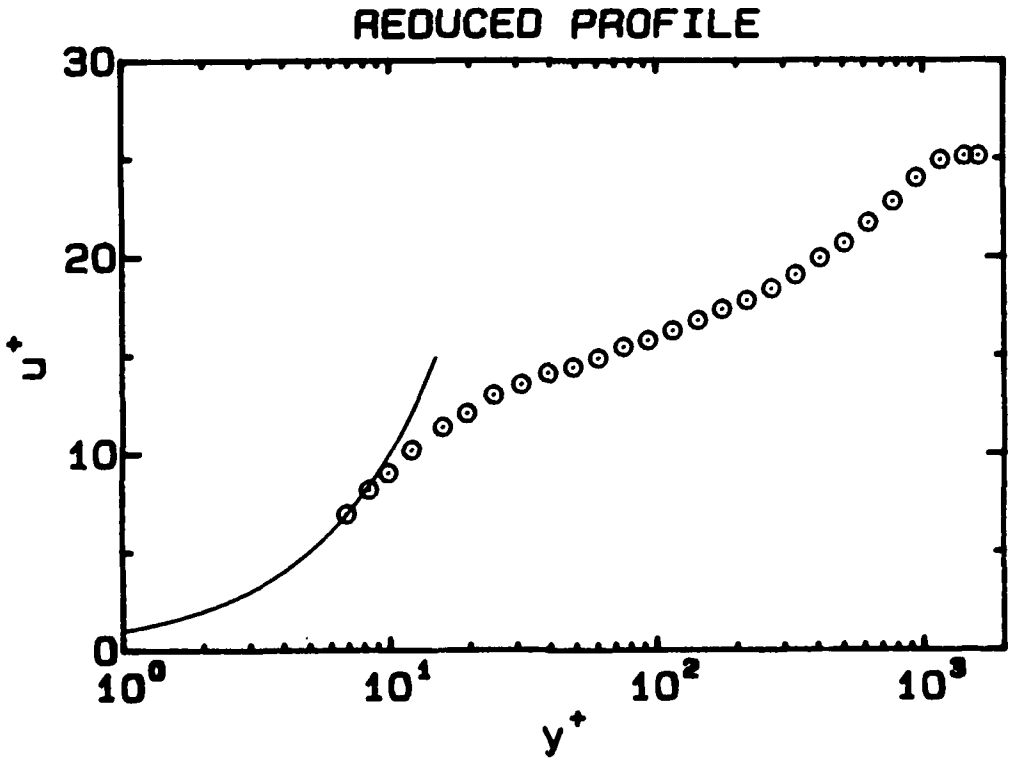

(b) Complete reduced profile

Fig. 9.6. Mean velocity: in the boundary layer and at the wall.

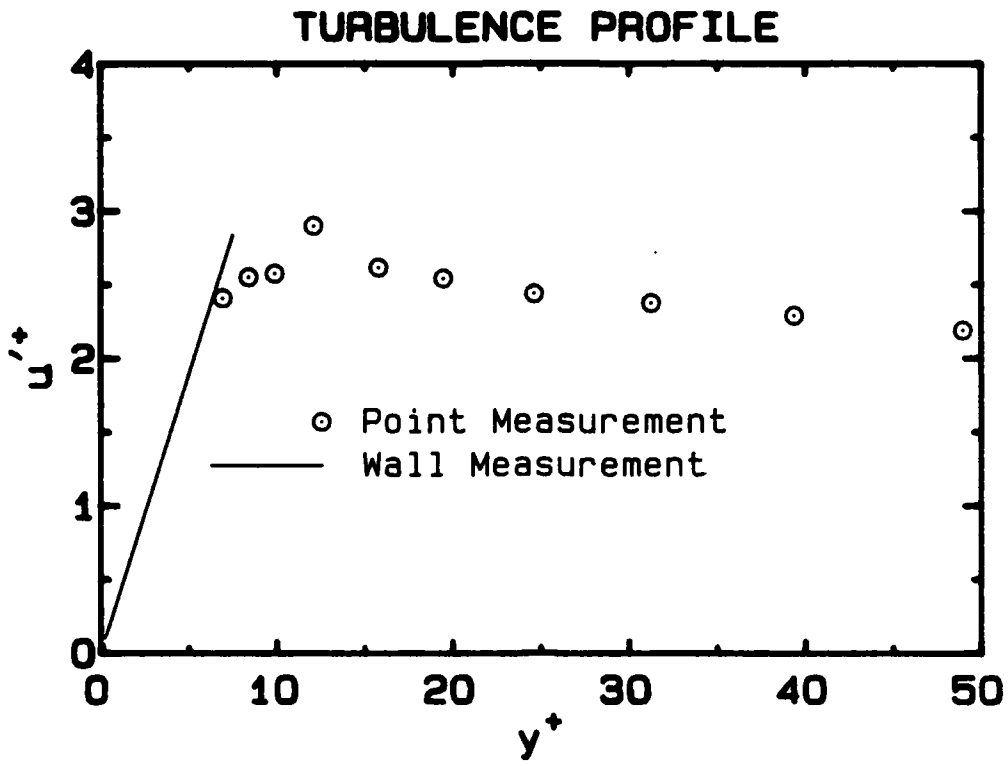

(a) Turbulence velocity

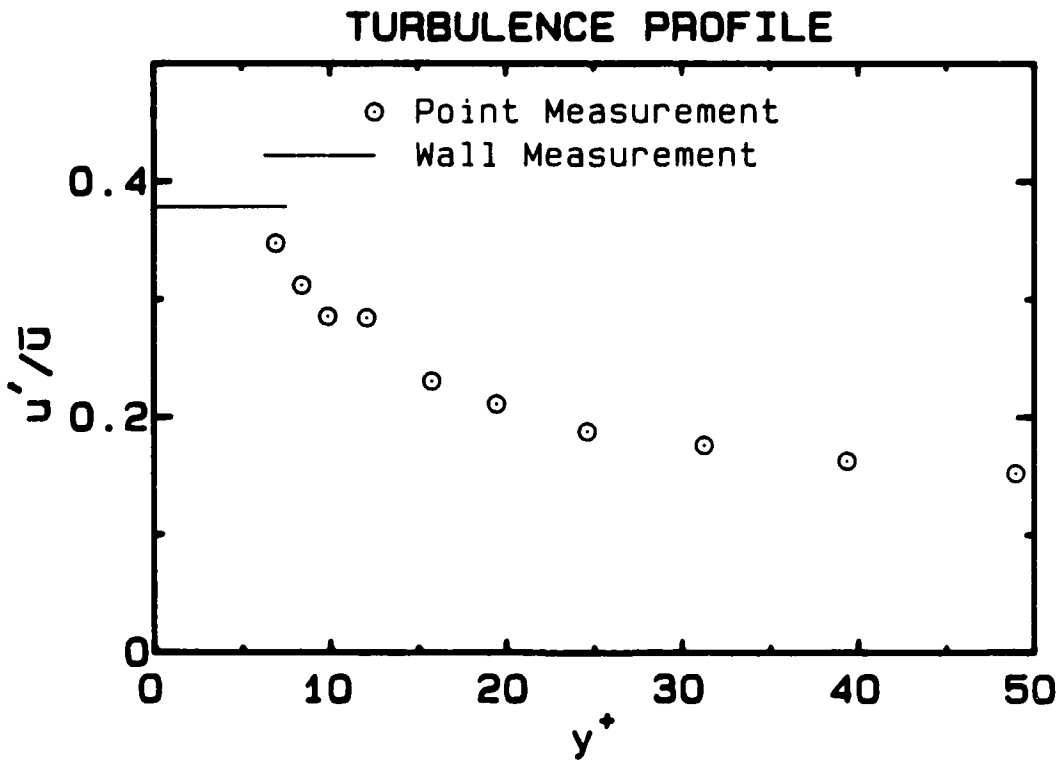

(b) Turbulence intensity

Fig. 9.7. Turbulence: in the boundary layer and at the wall.

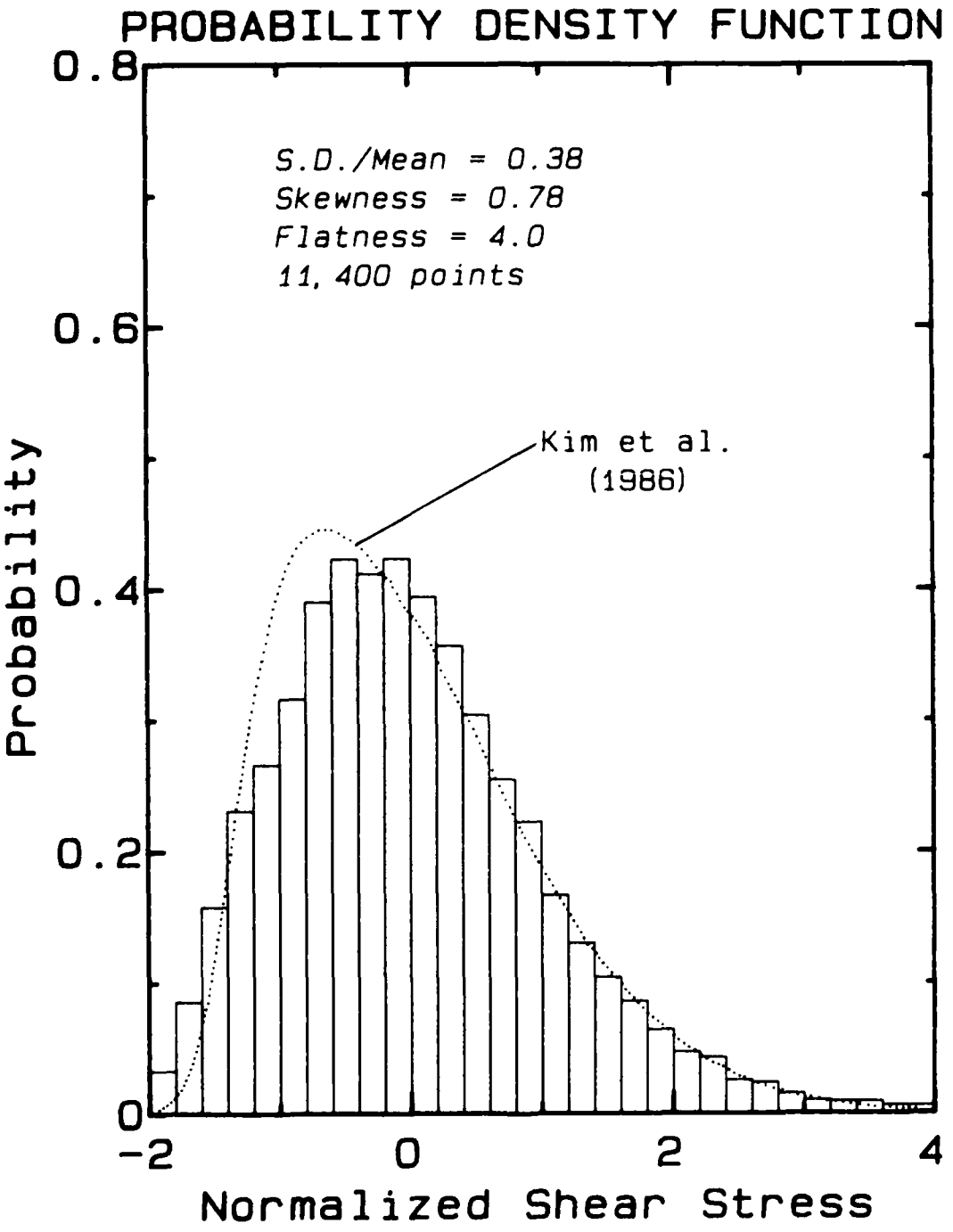

Fig. 9.8. Probability density function of skin friction.

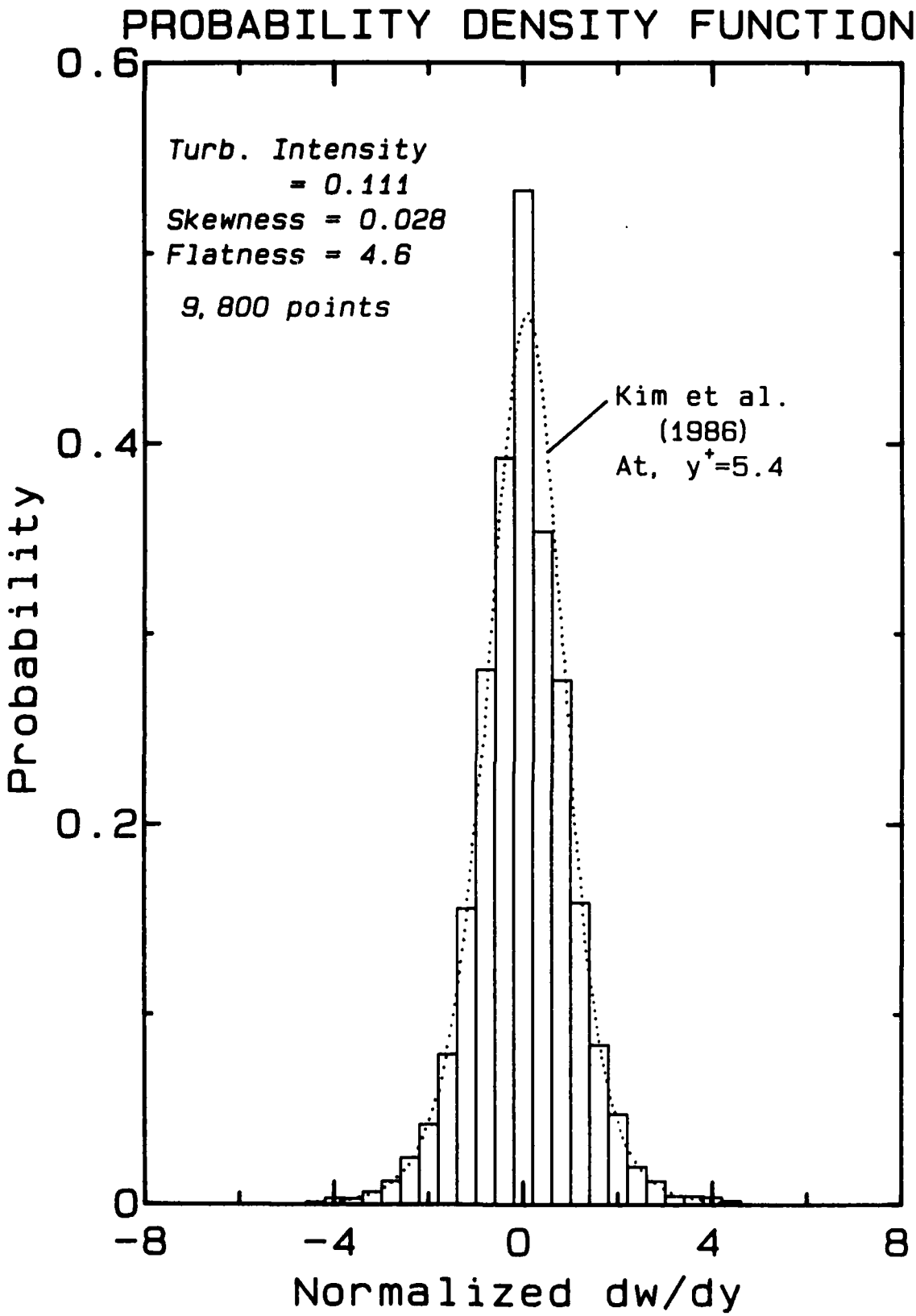

Fig. 9.9. Probability density function of the spanwise velocity gradient.

Chapter 10

CONCLUSIONS AND RECOMMENDATIONS FOR FUTURE WORK

In the previous chapters, the principle and design of a laser-Doppler device for measurement of wall velocity gradient have been described. The results of some simple measurements in a turbulent boundary layer are also presented. In the present chapter, the important lessons from this experience have been summarized into formal conclusions. Also, the unresolved issues are being formulated into guidelines for the future work.

10.1 Conclusions

The present measurements of skin friction in a turbulent boundary layer are in agreement with the latest understanding among the researchers that the value of turbulence intensity at the wall is about 35-40% and the distribution is highly skewed towards the higher values. The exploration of the spanwise velocity gradient seems to be supportive of the suggestion that the velocity profile in this direction does not reach linearity till $y^+ < 1$. A reliable quantitative value for the spanwise velocity gradient could not be obtained.

The present experience with applications of the instrument has unraveled certain advantages and disadvantages of the device which were not obvious at the beginning of this work. It is hoped that a discussion of these lessons can place the present technique in perspective with the existing alternative methods.

10.1.1 Advantages of DCW Method

The main advantage of this technique is the simplicity of the relationship between the signal and the measurand. Though the signals can be impaired by the velocity bias and secondary optical effects, the uncertainty range is small as compared to the alternate techniques. The two other well-recognized techniques are based on heat transfer and mass transfer analogies; these have been in practice for about 40 years and 20 years, respectively. Despite long periods of development and application, these methods have involved enormous uncertainties in the

measurements. The large differences between the two measurements in the oil channel, presented in Table 9.2, may be cited as an example of vulnerability of these methods. The reason for such vulnerability is the fact that the interaction of these devices with the flow is complex and not well-understood. The present method may be regarded as a giant step forward in simplifying the interaction between the instrument and the flow. The relationship between the signal frequency and the measurand is linear and known with a high accuracy from the optical parameters alone; hence, it does not require calibration in the flow.

With the present technique, it is easy to change the size of the measuring volume and vary its location. Hence, it would allow one to verify the linearity of the velocity profile being measured. This feature has enabled us to infer the reported trend of w' with respect to y from measurements at various y-locations. However, the results have been documented only for the smallest value of y approached. In hindsight, it may be suggested that a systematic record of the measured gradient versus size and location of the measuring volume be taken for the sake of qualifying the linearity of the gradient.

The present instrument provides a high spanwise resolution. Besides the fact that the spanwise extent can be made conveniently small, the individual signals are not integrated over the entire spanwise width. Usually, there is one particle in the measuring volume at a time. Hence in general, each signal corresponds to only the path it travels through the illuminated region and not the whole measuring volume. This may be contrasted with the heat transfer or mass transfer devices which yield a signal integrated over the entire sensing element. Also, in order to maintain a reasonable signal-to-noise ratio, the size of the element cannot be made very small in the latter techniques.

To conclude the discussion of advantages of the system, the ability to make a non-intrusive measurement may be recalled.

10.1.2 Disadvantages of DCW Method

As compared to the alternate devices mentioned above, the present instrument is more complex in construction. It is more bulky and expensive as well.

Since this device requires delicate alignments, it is sensitive to vibration. The present application has shown that the instrument does function on a water channel without any special vibration control but the quality of measurement would certainly improve if the vibration could be reduced to submicron level. This is more relevant to measurement of the spanwise component, which requires a smaller measuring volume.

The collection of unscattered light by the receiving optics reduces the signal-to-noise ratio. It may also generate spurious signals in the case of spanwise measurements. Necessary safeguards including vibration control are needed to overcome this shortcoming.

In the measurements taken so far, the signal rate has been too low to allow evaluation of energy spectra. This happens because the signals are weak in side-scatter and the scattering particles are scarce in the vicinity of the wall. The means of improving the signal rate suggested in Chapter 7 remain to be implemented.

10.2 Recommendations for Future Work

The concept of DCW has been proven feasible. Some results related to wall parameters in a turbulent boundary layer have been obtained. These results may be considered as validation of earlier findings, rather than new results. However, the limited experience with the use of this device has established certain advantages of the technique which justify further development and application.

There is a need to disseminate the technology; proliferation is vital to the survival and further development of a technique like this, which requires advanced skills as well as considerable capital investments. Further evaluation in simple flow situations (such as constant pressure boundary layer and channel flow) would be helpful in further improving and perfecting the device. Independent experimentation at different institutions would provide ideal conditions for maturation of the technique.

It is strongly recommended that an appropriate use of optical fibers and integrated optics be considered for the next version of the

device. Optical fibers carrying laser light may be coupled to special waveguides which would project it in the form of cylindrical waves. This arrangement would be less susceptible to the vibration of the flow facility and would make transportation of the probe easier. The receiving optics may also be replaced by appropriate integrated optics to collect the scattered light. These integrated optics may be coupled to an optical fiber leading to a photomultiplier tube. In an ideal arrangement, all the optical fibers would be connected to a small plug containing all the integrated optics.

Improvement of the signal rate and SNR would certainly enhance the utility of the device; wall seeding may be attempted as the first step towards this goal.

Experimentation in a thicker boundary layer would inevitably provide better insights into the functioning of the device. In particular, it would be helpful in verifying the stipulated behavior of w' in the sublayer.

The following goals may be suggested for further applications in the immediate future:

(1) A critical examination of the existing correlations for skin friction in a turbulent boundary layer.

(2) Re-evaluation of the constants in the universal logarithmic velocity profile; examination of their dependence on the Reynolds number of the flow, using the DCW system to determine the shear velocity.

(3) Documentation of the turbulence and higher-order statistics of the near-wall flow in order to examine their relationship to the outer flow or the bulk flow.

(4) Measurement of correlations that would provide additional information about the structural features of the sublayer, e.g., correlation of the wall shear stress with near-wall velocity.

Appendix A

AN OVERVIEW OF RELEVANT CONCEPTS IN THE ELECTROMAGNETIC THEORY OF LIGHT

Inclusion of this appendix in the report needs an explanation, because a description of electromagnetic theory of light can easily be found in textbooks on physical optics. The present discussion is only a cursory survey intended to state clearly the concepts and assumptions underlying various mathematical formulations employed in this report for design and description of the present device. It includes a selection of elementary and advanced material relevant to the system under consideration, which is not found in one place in the literature. A general reference for the material in the following pages is Born and Wolf (1980); other references are mentioned at appropriate places. The nomenclature in the current presentation is fairly consistent with common practice in electromagnetic theory. Since a number of these symbols are used to denote different physical quantities in fluid mechanics, a separate listing of nomenclature is included for this appendix.

The concepts of "anisotropic scattering shift" (or "fringe displacement") and "dipole approximation for vector diffraction" presented in this appendix are being proposed by the present author.

A.1 Nomenclature

a	Width of optical slit.
$\vec{B}$	Magnetic induction.
c	Speed of light in a material medium.
c_o	Speed of light in a vacuum.
C_s	Scattering coefficient in Mie scattering theory.
$\vec{D}$	Electric displacement.
$\vec{e}$	Electric field amplitude vector.
$\vec{E}$	Electric field.
$\vec{e}_\theta$, $\vec{e}_\phi$	Unit vectors used for expressing the scattering coefficient.

$\hat{h}$ Magnetic field amplitude vector.

$\hat{H}$ Magnetic field.

i $\sqrt{-1}$

$\hat{i}, \hat{j}, \hat{k}$ Unit vectors along x,y,z respectively.

Imag(U) Imaginary part of U.

$\hat{J}$ Electric current.

k Wavenumber, $2\pi/\lambda$.

$\hat{M}, \hat{P}$ Inhomogeneity functions on a primary wavefront.

n Refractive index of the medium.

n_p Complex refractive index of scattering particle.

$\hat{p}$ A vector along the direction of polarization.

$p(t)$ Strength of a dipole.

Q Weighting function in dual integral solution.

Real(U) Real part of U.

$\hat{s}$ A vector along the direction of propagation of light.

$U(P)$ Scalar field at point P in space.

$\hat{V}_{t_1}$ Vector tangential to a wavefront in $x_o y_o$ plane.

$\hat{V}_{t_2}$ Vector tangential to a wavefront in $y_o z_o$ plane.

x,y,z Spatial coordinates.

x_o, y_o, z_o Spatial coordinates for diffracted field, Fig. A.2.

Greek Symbols

α Angle of propagation of a plane wave in dual integral solution of diffraction problem.

α_o Angle of incident plane wave in the case of diffraction from a half-plane.

β $\cos \alpha$.

δ Dirac delta function.

ϵ Dielectric constant.

ζ Optical path in geometrical optics.

λ Wavelength in a medium.

μ Magnetic permeability.

$\vec{\Pi}_e$ Hertz electric vector.

$\vec{\Pi}_m$ Hertz magnetic vector.

ρ Charge density.

σ Electrical conductivity.

ϕ Phase of diffracted field.

Special Symbols

$\vec{\nabla}$ $\frac{\partial}{\partial x}\vec{i} + \frac{\partial}{\partial y}\vec{j} + \frac{\partial}{\partial z}\vec{k}$

∇^2 $\vec{\nabla} \cdot \vec{\nabla}$

Subscripts

x x-component of a vector.

y y-component of a vector.

z z-component of a vector.

Superscripts

(i) Incident electric or magnetic field.

(s) Scattered electric or magnetic field.

$\hat{}$ Distance normalized with wavenumber $(2\pi/\lambda)$.

A.2 Maxwell's Equations

These equations provide a generalized description of certain well-known phenomena in electromagnetics. A steady state flow of electrons under the influence of an electric field $\vec{E}$ is known to produce a magnetic field $\vec{H}$ (e.g., magnetic field around a current-carrying

wire). This phenomenon may in general be described by the following differential equation:

$$\vec{\nabla} \times \vec{H} = \frac{4\pi}{c} \vec{J}$$

where, $\vec{J}$ depends on $\vec{E}$ and the material properties.

For the sake of generalization, $\vec{H}$ is defined to be independent of the properties of the material in which it is produced. $\vec{H}$ is considered an entity which could sustain itself in vacuum; magnetic response of the material medium on the other hand is termed magnetic induction $\vec{B}$ and is considered a function of $\vec{H}$ as well as properties of the material. Similarly, electric field $\vec{E}$ is also considered independent of matter; its interaction with material substances results in electric displacement $\vec{D}$. Many texts on electricity use the term electric field for electric displacement. The notion of existence of electric and magnetic fields external to material media has in fact been introduced to extend the jurisdiction of electromagnetics to vacuum so that propagation of light across the space could be interpreted as an electromagnetic phenomenon without requiring to hypothesize the existence of ether.

It is also observed that an unsteady current, i.e., an accumulation or dispersion of electrons, not only affects $\vec{H}$ but also starts a feedback from $\vec{H}$ to $\vec{E}$. Since $\vec{E}$ cannot be specified independent of $\vec{H}$ under such conditions, another equation is needed to close the problem. The closed set of equations is given below:

$$\vec{\nabla} \times \vec{H} - \frac{1}{c} \dot{\vec{D}} = \frac{4\pi}{c} \vec{J} \qquad \text{(A.1)}$$

$$\vec{\nabla} \times \vec{E} + \frac{1}{c} \dot{\vec{B}} = 0 \qquad \text{(A.2)}$$

where $\vec{J}$ and $\vec{D}$ depend on $\vec{E}$ and material properties and $\vec{B}$ depends on $\vec{H}$ and material properties.

The unsteady part of the current is conventionally represented in terms of rate of change of $\vec{D}$. Magnetic induction and electric displacement follow the relevant continuity equations, like other conservative fields in a continuum.

$$\vec{\nabla} \cdot \vec{D} = 4\pi\rho \qquad (A.3)$$

$$\vec{\nabla} \cdot \vec{B} = 0 \qquad (A.4)$$

The non-zero right-hand side in (A.3) signifies the fact that electric displacement is associated with the movement of electrons which might accumulate in one location and produce a net charge ρ, whereas magnetic induction results from alignment of magnetic dipoles. Accumulation of magnetic mono-poles is not a known phenomenon in classical physics.

Historically, Eqns. (A.1) and (A.2) were first derived as integral equations over a finite control volume and subsequently reduced to partial differential equations. The integral form may be found in elementary texts on electromagnetics, e.g. Ramo, Whinnery and Van Duzer (1984).

Equations (A.1) through (A.4) are known as Maxwell's equations. These equations indicate the possibility of existence of mutually supported $\vec{H}$ and $\vec{E}$ fields even in the absence of an electric current $\vec{J}$. It is shown later that such fields would propagate with a velocity c_o in vacuum. The value of c_o from pure *electromagnetic* measurements matches well with the speed of light. Hence interpretation of light as an electromagnetic wave has been hypothesized.

It is also worth mentioning that the manner in which we perceive the existence of electric or magnetic field is by assessing its ability to do work; viz ability to move electrically charged bodies or magnetic poles. The Maxwell's equations can be transformed into an energy law so that each term represents a form of energy. In this form the term

$$\frac{c}{4\pi} \iint_S (\vec{E} \times \vec{H}) \cdot \hat{n}\, dS$$

determines the energy flux across the surface of a control volume where dS is a surface element and $\hat{n}$ is a unit vector normal to it. Evaluation of this term leads to a fringe pattern in the case of light from two sources which is the basis of fringe model discussed in Chapter 1. The fringe model is conceptually simple but since its mathematical description takes a more complex form than the original mathematical

representation of the phenomenon (viz, Maxwell's equations), it is not suitable for an extensive analysis.

Finally, a rather simple but important deduction from the Maxwell's equations can be discussed briefly. Application of Maxwell's equations to a control volume surrounding a surface discontinuity in the space yields the boundary conditions for the $\hat{E}$ and $\hat{H}$ fields. Continuity of the $\hat{E}$ and $\hat{H}$ fields is required if both the media are dielectric, e.g., glass-air interface. Another case of particular interest is one of an infinitely thin sheet of infinite electrical conductivity interposed between two dielectric media. This is an idealization of diffraction from apertures in a thin metallic layer. In this case, the tangential component of the electric field vanishes on the interface whereas the tangential component of the magnetic field goes through an abrupt change of the amount $4\pi\hat{J}/c$, where $\hat{J}$ is the current density induced in the interface.

A.3 Linear Optics

The constitutive equations relating $\hat{J}$ and $\hat{D}$ to $\hat{E}$ and $\hat{B}$ to $\hat{H}$ may be very complex for certain materials, but the media involved in the present system, (i.e., air, water, glass, chromium, etc.) can be assumed to follow the following linear relations:

$$\hat{J} = \sigma\hat{E} \tag{A.5}$$

$$\hat{D} = \varepsilon\hat{E} \tag{A.6}$$

$$\hat{B} = \mu\hat{H} \tag{A.7}$$

where, σ, ε, and μ are called electrical conductivity, dielectric constant and magnetic permeability respectively. If the material is homogeneous and isotropic these properties would be constant throughout. Such is the case of common lenses and mirrors whereas acousto-optic modulators (cells with standing sound waves) and birefringent media are examples of anisotropic systems.

It should be mentioned here that the above relations are strictly speaking, valid for bodies at rest only. For bodies in linear motion

with constant speed, Lorentz transform may be used to adapt these equations to the moving frame of reference. In the case of non-relativistic speeds, the effect of Lorentz transform is confined to a frequency shift. Mathematically this shift is identical to the classical Doppler shift. This is the reason for combining Doppler effect with the electromagnetic theory in the wave model of the device, proposed in Chapter 2. The problem becomes more complex if the body interacting with the electromagnetic waves is rotating, such as a rotating particle in the measuring volume of an LDV system. Concepts from general relativity may be empolyed to formulate the phenomenon mathematically.

It should also be remarked that the constitutive equations are more complex and generally nonlinear in the cases where electric and/or magnetic fields excite electrons in atoms and result in phenomena such as self-focusing, electro-optic modulation, flouresence or laser emission. These phenomena are subjects of nonlinear optics. An introductory exposition of mildly non-linear phenomena in optics is available in the text on optoelectronics by Haus (1984); phenomena such as flouresence and laser emission are generally treated as subjects of quantum electronics and not as variants of electromagnetics. The present formulation of electromagnetic phenomena applies only to propagation of light in homogeneous and isotropic media. It may however be easily extended to anisotropic materials such as wave plates or polarizers by using different values of dielectric constant and magnetic permeability for various components of $\vec{E}$ and $\vec{H}$.

A special case in linear optics is one of non-conducting media. Maxwell's equations for this case reduce to wave equations in $\vec{E}$ and $\vec{H}$.

$$\vec{\nabla}^2 \vec{E} - \frac{\varepsilon\mu}{c_o^2} \ddot{\vec{E}} = 0 \qquad \text{(A.8)}$$

$$\vec{\nabla}^2 \vec{H} - \frac{\varepsilon\mu}{c_o^2} \ddot{\vec{H}} = 0 \qquad \text{(A.9)}$$

where speed of light = $c_o/\sqrt{\varepsilon\mu}$.

The above equations in conjunction with (A.1) and (A.2) may be used to demonstrate that $\vec{E}$ and $\vec{H}$ vectors are normal to one another and also normal to the direction of propagation of light energy as shown in Fig. A.1(a).

The well-known laws of reflection and refraction can be derived by satisfying the surface discontinuity boundary conditions for a plane wave approaching the interface between two media with different dielectric constant and magnetic permeability.

An electromagnetic wave is called harmonic if all the components of $\vec{E}$ and $\vec{H}$ oscillate with the same frequency.

An electromagnetic wavefront is linearly polarized at a point if both x and y components of $\vec{E}$ (and $\vec{H}$) are in-phase or completely out-of-phase; as a result the vector $\vec{E}$ vibrates along one fixed line in space called the axis of polarization. If E_x and E_y as shown in Fig. A.1(b) are of equal amplitude and out-of-phase by 90°, the vector $\vec{E}$ would rotate in a circle, producing circularly polarized light. In general, a harmonic wave is elliptically polarized.

The nature of polarization is irrelevant for the optical elements which follow Eqns. (A.8) and (A.9) and have identical physical orientation relative to $\vec{E}$ and $\vec{H}$ fields (i.e., axisymmetric relative to the direction of propagation). All the components of $\vec{E}$ and $\vec{H}$ follow identical equations and boundary conditions for such elements. Ordinary spherical lenses are examples of this type of optical elements. Propagation of light through such elements can be expressed in terms of a single wave equation; hence the notion of scalar waves applies. Cylindrical lenses and dielectric beamsplitters have different physical orientation relative to the $\vec{E}$ and $\vec{H}$ fields and hence are sensitive to polarization. Similarly, electromagnetic waves cannot be treated as scalar waves while passing through a polarizer, because different speeds of light are encountered in different directions. Another case for which scalar wave formulation is not adequate is the passage of light through an optical element employing a metallic film, because it is an electrically conducting medium and Eqns. (A.8) and (A.9) are not valid locally; Eqns. (A.1) through (A.4) with appropriate electrical conductivity should be used for an exact solution. Metallic mirrors, beam

splitters and diffraction gratings are examples of such elements. Dielectric mirrors and beamsplitters are used in the present system in order to preserve the state of polarization in the beam generator and elsewhere. However, a pair of slits etched in a chromium coating is used for diffraction of light in the final stage of the focusing optics. This element is slightly sensitive to polarization of incident light as shown in Appendix B.

A.4 Scalar Diffraction

A solution to the problem of diffraction of light from an aperture in a screen may become exceedingly complex depending upon the thickness and the material of the screen. The term scalar diffraction refers to a solution of the problem which describes the entire phenomenon in terms of a single wave equation. In other words, it ignores the conductivity of the screen but still assumes that the screen effectively blocks light over its infinitesimal thickness ("absorbing screen"). This approach is incosistent with electromagnetic theory of light, nevertheless it has yielded reasonably accurate prediction of diffraction at relatively larger distances from the screen. This theory is unable to describe the state of polarization after diffraction. However, it is useful in estimating wavefronts and energy flux if the state of polarization after diffraction is evaluated by other means.

A solution of wave equation pertinent to diffraction of monochromatic waves, known as Rayleigh-Sommerfeld formula is given below (Goodman, 1968):

$$U(P_o) = \frac{1}{i\lambda} \iint_S U(P_1) \frac{\exp(ikr_o)}{r_o} (\vec{n} \cdot \vec{r}_o) \, dS \qquad (A.10)$$

This formula is expressed in terms of the nomenclature of Fig. A.2. It is valid for distances sufficiently larger than the wavelength of light. In this report, it is used for investigation of wavefronts produced by a finite slit.

Two simplifications of this formula are well-known.

(1) Fresnel approximation:

Rayleigh-Sommerfeld equation can be simplified if the diffracted field is observed in front of the aperture and not at large oblique angles. Assuming that the dimensions of the apperture are sufficiently smaller than the distance at which the diffracted field is observed, the factor $\vec{n}\cdot\vec{r}_o$ may be taken as unity. The distance $\vec{r}_o$ in the denominator is approximated by y_o, whereas in the phase function the following relation is used for r_o.

$$r_o = y_o\left[1 + \frac{1}{2}\left(\frac{x_o - x}{y_o}\right)^2 + \frac{1}{2}\left(\frac{z_o - z}{y_o}\right)^2\right]$$

This leads to the following formula:

$$U(x_o,y_o,z_o) = \frac{\exp(iky_o)}{i\lambda y_o}\exp\left[i\frac{k}{2y_o}(x_o^2 + z_o^2)\right] \qquad (A.11)$$

The finite limits of integration are replaced by infinity, using the principle of stationary phase; (see Nayfeh (1981) for a discussion on the concept of stationary phase). The nomenclature for the above expression is elucidated in Fig. A.3. It is valid in general for

$$y_o^3 \gg \frac{\pi}{4\lambda}\left[(x_o - x)^2 + (z_o - z)^2\right]^2_{max}$$

The Fresnel formula is used to derive the equation for propagation of Gaussian laser beams. Since a screen to cut-off the light at a particular cross-section is not employed in this case, the inconsistency associated with the so-called absorbing screen is removed.

(2) Fraunhofer approximation:

When the distance from the screen is very large, one more term in the integrand of Eqn. (A.11) may be dropped to obtain the following formula:

$$U(x_o,y_o,z_o) = \frac{\exp(iky_o)\,\exp\left[i\,\frac{k}{2y_o}\,(x_o^2 + z_o^2)\right]}{i\lambda y_o} \times \int_{-\infty}^{\infty} U(x,z)\,\exp\left[-i\,\frac{k}{y_o}\,(x_o x + z_o z)\right] dxdz \qquad (A.12)$$

It is valid under the following condition:

$$y_o \gg \frac{k(x^2 + y^2)_{max}}{2}$$

Equation (A.12) is simply a Fourier transform of the wave function at the screen. It provides the basis for Fourier Optics dealt with formally by Goodman (1968).

A.5 Geometrical Optics

A simplification of Maxwell's equations for small wavelengths is commonly used for studying propagation of light through imaging and focusing systems. The analysis can be started with time harmonic field of the following form:

$$\vec{E} = \vec{e}(\vec{r})\,\exp\,[ik\,\zeta(\vec{r})]$$

$$\vec{H} = \vec{h}(\vec{r})\,\exp[ik\,\zeta(\vec{r})] \qquad (A.13)$$

Time dependence has been suppressed in the above equations. The function $\zeta(\vec{r})$ is used to specify the wavefronts; changes in phase of the wave are governed solely by $\zeta(\vec{r})$.

On substituting (A.13) into Eqns. (A.1) and (A.2) and ignoring the terms involving $1/ik$ (i.e., assuming wavelength to be smaller than other dimensions), one obtains

$$\left(\frac{\partial\zeta}{\partial x}\right)^2 + \left(\frac{\partial\zeta}{\partial y}\right)^2 + \left(\frac{\partial\zeta}{\partial z}\right)^2 = n^2(x,y,z) \qquad (A.14)$$

The above equation governs the evolution of wavefronts in the space irrespective of the wavelength. A surface of constant ζ represents a wavefront and vectors normal to such a surface are refered to as rays of light. Rays represent the local direction of propagation of light. Being independent of the wavelength information, the rays may be considered the sole descriptors of the phenomenon under the premises of this

formulation. Propagation of a ray through a medium with a known spatial distribution of refractive index can be determined from Eqn. (A.14). Solutions of (A.14) for a variety of standard cases, such as propagation of a ray through a thin lens, are simple and require only a geometrical construction for a complete description -- hence the term geometrical optics.

It may be recalled now that the laws of reflection and refraction in general are deducible by applying surface discontinuity boundary conditions to a plane wave. These laws, in the limit of geometrical optics are valid for each ray hence do not require the incident wavefronts to be a plane.

A.6 Vector Diffraction Theory for Idealized Screens

Scalar diffraction formula as discussed earlier fails to provide information regarding the state of polarization. It is also not valid very close to the screen. For the present application the state of polarization as well as the nature of the fields very close to the screen are of significant value. An exact solution of Maxwell's equations for a real screen is too complex and not treated in detail in the literature. An idealized case of immense value is the one which assumes the screen to be infinitesimally thin and perfectly conductive. Considering the fact that the screen in the present system is significantly thinner than the wavelength of the light and is made up of chromium which has high electrical conductivity, the above mentioned solution would be a close approximation to the real system.

A.6.1 Dual Integral Formulation

The case of particular interest under this formulation is one of a plane screen. For a two dimensional problem (i.e., no variation along the z-axis), the total field can be divided into two parts -- E-polarization and H-polarization, as shown in Fig. A.4. Each of these cases may be reduced to a single wave equation which is valid over the entire space and must satisfy a set of boundary conditions on the screen. The boundary conditions follow directly from Maxwell's equations as discussed in Section A.1. A complete mathematical representation in the case on E-polarization is as follows:

$$\frac{\partial^2 E_z}{\partial x^2} + \frac{\partial^2 E_z}{\partial y^2} + \frac{\partial^2 E_z}{\partial z^2} = 0 \qquad \text{(A.15)}$$

$$H_x = \frac{1}{ik}\frac{\partial E_z}{\partial y}, \quad H_y = -\frac{1}{ik}\frac{\partial E_z}{\partial x},$$

$$E_x = E_y = H_z = 0 \qquad \text{(A.16)}$$

Boundary Conditions:

(1) $E_z = 0$, on metal,

(2) H_x and H_y goes through abrupt changes $4\pi J_y/c$ and $4\pi J_x/c$, respectively, on the metal.

It is convenient to divide the total field into an incident field and a scattered field; i.e.,

$$\vec{E} = \vec{E}^{(i)} + \vec{E}^{(s)}$$

$$\vec{H} = \vec{H}^{(i)} + \vec{H}^{(s)}$$

Both the incident and the scattered fields satisfy the above equations independently. Since the incident light is not obstructed on the aperture, the scattered field is zero in the aperture plane. This fact allows to state the second boundary condition as follows:

$$\vec{H}^{(s)} = 0 \quad \text{on the aperture.}$$

The solution of (A.15) may in general be expressed as an angular spectrum of plane waves in terms of polar coordinates (r,θ).

$$E_z^{(s)} = \int_C P(\cos\alpha)\, e^{ikr\cos(\theta-\alpha)}\, d\alpha, \quad y > 0 \qquad \text{(A.17)}$$

It may be shown easily that $e^{ikr\cos(\theta-\alpha)}$ satisfies Eqn. (A.15) for both real and complex values of α. The path of integration C and the weighting function $Q(\cos\alpha)$ are unknown in the above expression. It is found appropriate to choose limits of integration such that, $\cos\alpha = -\infty$ to $+\infty$; the resulting expression is a Fourier integral. The plane waves corresponding to real values of α (i.e., $\cos\alpha = -1$ to $+1$) are

homogeneous and do not attenuate whereas those corresponding to complex α attenuate and disappear at larger distances from the screen; their presence however is essential for accurate determination of near-surface distribution of the field and the current density. It may be remarked at this point that Rayleigh-Sommerfeld formula of scalar diffraction theory does not incorporate any attenuating (or evanescent) waves. It actually describes the diffracted field as a spectrum of spherical waves which lack a physical interpretation at the center of the individual waves. However, the attenuation length of the evanescent waves scales with the wavelength of light and a solution ignoring such waves is not likely to be in large error if the distance from the screen is sufficiently larger than the wavelength.

The boundary conditions for this formulation take the following form.

$$\int_{-\infty}^{\infty} \frac{Q(\beta)}{\sqrt{1-\beta^2}} e^{ikx\beta}\, d\beta = -E_z^{(i)} \quad \text{on metal} \ ,$$

$$\int_{-\infty}^{\infty} Q(\beta)\, e^{ikx\beta}\, d\beta = 0 \ , \quad \text{on the aperture} \ ,$$

where, $\beta = \cos\alpha$. This formulation is refered to as dual integral equations. These integrals must be solved mutually to deduce an expression for $Q(\beta)$. Advanced mathematical techniques are employed for this purpose. The resulting expression is usually in the form of a series expansion. Once an analytical expression for $Q(\beta)$ is obtained, E_z and other field components can be expressed explicitly in the integrals of the form of Eqn. A.17.

A.6.2 Diffraction of a Plane Wave by a Half-Plane

The weighting function $Q(\beta)$ of dual integral equations takes a rather simple form for the case of a plane wave incident on a half-plane. The simplicity of this solution has motivated its application to more complex problems.

In the case of a unit amplitude E-polarized wave incident at an angle α_o on the half-plane.

$$Q(\cos\alpha) = \frac{i}{\pi}\frac{\sin\frac{1}{2}\alpha_o \sin\frac{1}{2}\alpha}{\cos\alpha + \cos\alpha_o}$$

The resulting expressions for the diffracted field are as follows:

$$E_z = \frac{e^{-\frac{1}{4}i\pi}}{\sqrt{\pi}} e^{ikr}\,[G(u) - G(v)] \tag{A.18}$$

$$H_x = -\frac{e^{-\frac{1}{4}i\pi}}{\sqrt{\pi}} e^{ikr}\,\{\sin\alpha_o[G(u) + G(v)] + i\sqrt{\left(\frac{2}{kr}\right)}\sin\tfrac{1}{2}\alpha_o\cos\tfrac{1}{2}\theta\} \tag{A.19}$$

$$H_y = \frac{e^{-\frac{1}{4}i\pi}}{\sqrt{\pi}} e^{ikr}\{\sin\alpha_o\,[G(u) - G(v)] - i\sqrt{\left(\frac{2}{kr}\right)}\sin\tfrac{1}{2}\alpha_o\sin\tfrac{1}{2}\theta\} \tag{A.20}$$

Similarly, for an H-polarized field,

$$H_z = \frac{e^{-\frac{1}{4}i\pi}}{\sqrt{\pi}} e^{ikr}\,[G(u) + G(v)] \tag{A.21}$$

$$E_x = \frac{e^{-\frac{1}{4}i\pi}}{\sqrt{\pi}} e^{ikr}\,\{\sin\alpha_o\,[G(u) - G(v)] - i\sqrt{\left(\frac{2}{kr}\right)}\cos\tfrac{1}{2}\alpha_o\sin\tfrac{1}{2}\theta\} \tag{A.22}$$

$$E_y = -\frac{e^{-\frac{1}{4}i\pi}}{\sqrt{\pi}} e^{ikr}\,\{\cos\alpha_o\,[G(u) + G(v)] - i\sqrt{\left(\frac{2}{kr}\right)}\cos\tfrac{1}{2}\alpha_o\cos\tfrac{1}{2}\theta\} \tag{A.23}$$

where

$$G(\gamma) = e^{-i\gamma^2}\int_{\gamma}^{\infty} e^{i\beta^2}\,d\beta \tag{A.24}$$

$$u = -\sqrt{(2kr)}\cos\tfrac{1}{2}(\theta - \alpha_o) \tag{A.25}$$

$$v = -\sqrt{(2kr)}\cos\tfrac{1}{2}(\theta + \alpha_o) \tag{A.26}$$

It should be noted that these expressions determine the strength, direction of propagation as well as the state of polarization of the field at a given point in space.

A.6.3 Diffraction from a Slit

The value of a nondimensional slit width, defined as ka/2 plays an important role in the solution of slit diffraction problem. A slit may be called narrow if this parameter is less than one and wide otherwise. The dual integral equations can be solved relatively easily for a narrow slit as shown by Tranter (1954). The present device involves a wide slit (ka/2 = 8.1). Millar (1958) has sought a solution for a wide slit. The solution is available in terms of improper integrals which are difficult to be evaluated numerically. However certain portions of the solution are expressed in a series expansion in the inverse ratio of nondimensional slit width.

Karp and Russek (1956) have proposed a procedure in which the two edges of the slit are considered as two half-planes and the standard solution for a half-plane is utilized. Light diffracted by each edge is considered as a second incident wave for the other edge and so on. Multiple diffractions result in the development of a series which exhibits fast convergence in the case of a wide slit.

A.6.4 Geometrical Theory of Diffraction

Keller (1957, 1962) has proposed a geometrical theory of diffraction which is a further development and generalization of the procedure of Karp and Russek. This theory allows application of canonical solutions of the diffraction problem to the apertures of complex shapes. Though this procedure is not used for the present problem of finite slits, it would be instructive to briefly examine such an application. The diffracted field for the finite slit would be described by one primary field for each edge and one for each corner. Each of these eight primary fields would produce seven secondary fields upon impinging the other edges or corners and so on. This method may actually become quite complex in the presence of several edges and corners. A relatively simple approach to the problem of vector diffraction from a narrow aperture is presented in the following section.

A.7 Vector Diffraction under the Dipole Approximation

This section presents a simplified approach for determining the direction of polarization for a diffracted field. The present formulation is based on the notion of an electric dipole which consists of two electric charges fluctuating in strength with a certain amplitude and frequency. The charges are brought closer and merged into one another while amplitude of their strengths is increased in a manner that the product of the charge-strength amplitude and spacing between the charges reaches a finite value. A dipole has a direction of vibration which determines the nature of the field radiated by it. The direction of E-vector at a point in this field can be determined from a knowledge of the local direction of propagation of light and the direction of vibration of the dipole. Hence if any field of known direction of propagation could be reconstructed locally from a dipole of known direction of vibration, the direction of its electric vector can be specified. The local direction of light propagation in the case of a diffracted field can be deduced from the Rayleigh-Sommerfeld formula. The present formulation suggests that this field could be reconstructed from a dipole whose direction of vibration would be same as the polarization of the incident field in the plane of the screen.

This simplification is being refered to as dipole approximation in this report. Under this approximation linearly polarized light produces linearly polarized diffracted field and the direction of polarization in the diffracted field can be deduced from the local direction of propagation and the direction of polarization of the incident light.

In practice there would be some ellipticity in polarization of the diffracted field but it is not expected to be significant. This prediction is based on a knowledge of the scattering characteristics of particles under comparable conditions, i.e., forward scattering for micron-size particles. As shown by Adrian and Earley (1976), ellipticity is negligible under such conditions.

A.7.1 Huygens-Fresnel Principle

Huygens-Fresnel principle is an intuitive conception of the propagation of light as a wave, according to which each point on a primary wavefront may be considered as a source of a secondary wavelet. Interference between secondary wavelets produces various patterns of intensity in the case of diffraction from an aperture. An envelope of the secondary wavelets may be regarded as a new wavefront.

A.7.2 Formulation of Light Propagation as an Inhomogeneous Wave

The "sources of wavelets" in Huygens-Fresnel principle can be modeled as inhomogeneities in the governing wave equations. This in fact is a means of invoking the boundary condition on a primary wavefront.

Considering an electromagnetic wave in vacuum, we introduce the following relations:

$$\vec{D} = \vec{E} + 4\pi\vec{P} \tag{A.27}$$

$$\vec{B} = \vec{H} + 4\pi\vec{M} \tag{A.28}$$

where $\vec{P}$ and $\vec{M}$ are non-zero only in a region of inhomogeneity. Substitution of these relations into Maxwell's equations for nonconducting media leads to the following equations for the electric and magnetic fields.

$$\vec{E} = \vec{\nabla} \times \left(-\frac{1}{c}\dot{\vec{\Pi}}_m + \vec{\nabla} \times \vec{\Pi}_e\right) + \left(\nabla^2 \vec{\Pi}_e - \frac{1}{c^2}\ddot{\vec{\Pi}}_e\right) \tag{A.29}$$

$$\vec{H} = \vec{\nabla} \times \left(\frac{1}{c}\dot{\vec{\Pi}}_e + \vec{\nabla} \times \vec{\Pi}_m\right) + \left(\nabla^2 \vec{\Pi}_m - \frac{1}{c^2}\ddot{\vec{\Pi}}_m\right) \tag{A.30}$$

where $\vec{\Pi}_e$ and $\vec{\Pi}_m$ be referred to as Hertz vectors following the convention of dispersion theory. Hertz vectors follow the inhomogeneous wave equations.

$$\nabla^2 \vec{\Pi}_e - \frac{1}{c^2}\ddot{\vec{\Pi}}_e = -4\pi\vec{P} \tag{A.31}$$

$$\nabla^2 \vec{\Pi}_m - \frac{1}{c^2} \ddot{\vec{\Pi}}_m = -4\pi\vec{M} \qquad \text{(A.32)}$$

A solution to these equations is given as follows:

$$\vec{\Pi}_e = \iiint \frac{\vec{P}(t-R/c)}{R}\, dV \qquad \text{(A.33)}$$

$$\vec{\Pi}_m = \iiint \frac{\vec{M}(t-R/c)}{R}\, dV$$

where R is the distance from the point of interest to the volume element dV.

In order to further simplify the problem we may set $\vec{M} = 0$, i.e. we may specify a suitable $\vec{P}$ on a primary wavefront so that it reproduces the actual field at a later point.

A simple inhomogeneity, at a point defined by position vector $\vec{r}_o$ may be given by the following relation:

$$\vec{P}(\vec{r},t) = p(t)\, \delta(\vec{r} - \vec{r}_o)\, \vec{n} \qquad \text{(A.35)}$$

where $\vec{n}$ is a unit vector and δ is the Dirac delta function. It may be mentioned at this point that three terms, electric dipole, sources of secondary wavelets and simple inhomogeneity actually refer to the same entity.

Using the mathematical tools discussed here, we can formulate the problem of diffraction from an aperture as a wave motion resulting from an spectrum of simple inhomogeneities (or dipoles) in the aperture plane. In order to properly satisfy the boundary condition at the aperture, the vibration axis of these inhomogeneities must be same as the polarization of the incident wave.

A.7.3 Field Produced By an Electric Dipole

The field of a single electric dipole can be obtained by substituting Eqn. (A.35) into (A.33) and the value of $\vec{\Pi}_e$ thus obtained into (A.29) and (A.30). The expressions for $\vec{E}$ and $\vec{H}$ can be simplified for the case of $R >> \lambda/2\pi$. The simplified expressions are given below.

$$E \sim H \sim \frac{\ddot{p}(t-R/c)}{c^2 R} \sin\theta \qquad (A.36)$$

The coordinate system for this expression is illustrated in Fig. (A.5). It may be noticed that $\vec{E}$ lies in the plane containing the direction of propagation and the direction of vibration. This condition alongwith the requirement that $\vec{E}$ must also be in a plane normal to the direction of propagation, is sufficient for specification of the direction of $\vec{E}$. This provides a criterion for determining the polarization from the direction of propagation and the direction of dipole vibration. In order to apply this criterion to the diffracted field it should be established that the entire spectrum of dipoles in the aperture could be replaced by an equivalent dipole with a vibration axis not significantly different from the vibration axis of individual dipoles in the spectrum. A preliminary judgement in this respect can be made by examining the orientation of an equivalent dipole for a field produced by two dipoles at various locations in the aperture.

A.7.4 Equivalent Dipole

Figure A.6 shows two dipoles at $(x_1,0,z_1)$ and $(x_2,0,z_2)$ vibrating along z-axis. In this coordinate system, Eqn. (A.36) for a unit dipole can be written as follows:

$$\vec{E} = \frac{xz\vec{i} - y_o z\vec{j} - (x^2+y_o^2)\vec{k}}{R^3} \qquad (A.37)$$

where R is the distance of a dipole at $(x,0,z)$ from the point of observation $(0,y_o,0)$. Direction of propagation is given by

$$\vec{i}_R = \frac{-x\vec{i} + y_o\vec{j} - z\vec{k}}{R} \qquad (A.38)$$

where

$$R = \sqrt{x^2 + y_o^2 + z^2}. \qquad (A.39)$$

If the fields for the two dipoles are represented by $\vec{E}_1$ and $\vec{E}_2$ and directions of propagation by $\vec{i}_{R_1}$ and $\vec{i}_{R_2}$, then the combined field is given by

$$\vec{E} = \vec{E}_1 + \vec{E}_2 \tag{A.40}$$

and the resultant direction of propagation is represented as follows:

$$\vec{I}_R \sim |\vec{E}_1| \vec{I}_{R_1} + |\vec{E}_2| \vec{I}_{R_2} \tag{A.41}$$

Since the vibration axis $\vec{n}$ of the resultant dipole lies in the plane of $\vec{E}$ and $\vec{I}_R$, the following vector relation holds:

$$\vec{n} \cdot (\vec{E} \times \vec{I}_R) = 0 \tag{A.42}$$

The resultant dipole may be chosen to lie in xz plane such that

$$\vec{n} = n_x \vec{I} + n_z \vec{k} \tag{A.43}$$

Equations (A.40) through (A.43) may be solved to obtain an expression for n_x/n_z. Employing expressions of the form of (A.37), (A.38), and (A.39) to represent the field and the direction of propagation for each dipole, the following relation is obtained.

$$\frac{n_x}{n_z} = - \frac{R_1 R_2 (x_2 - x_1) \left(z_2 \sqrt{x_1^2+y_o^2} - z_1 \sqrt{x_2^2+y_o^2}\right)}{R_2^4 \sqrt{x_1^2+y_o^2} + R_1 R_2 \left[z_1 z_2 + \sqrt{(x_1^2+y_o^2)(x_2^2+y_o^2)}\right] \left(\sqrt{x_1^2+y_o^2} + \sqrt{x_2^2+y_o^2}\right) + R_1^4 \sqrt{x_2^2+y_o^2}} \tag{A.44}$$

The above expression clearly shows that n_x would be small as compared to n_z if the difference between x_2 and x_1 is small. It also shows a dependence on the difference between z_1 and z_2. Hence, the equivalent dipole would be tilted only slightly from the original vibration axis if the aperture is sufficiently smaller than the distance between the point of observation and the aperture. Equation (A.44) may be used to make an order-of-magnitude estimate for the tilt of the equivalent dipole. If the tilt could be ignored conveniently, then the dipole approximation is valid. It should be noted that this approximation does not require the aperture to be small enough to be represented by a single dipole. It only requires the equivalent dipole for reconstruc-

tion of the field at a given point to be parallel to the polarization of the incident light, which is a much less restrictive condition.

A.7.5 Explicit Expressions for Vector Diffraction

An expression for diffracted field, known as Rayleigh-Sommerfeld formula has been given in Section A.3. It is convenient for the current purpose to represent this expression in terms of the coordinates of Fig. A.3 as follows:

$$U(\hat{x}_o, \hat{y}_o, \hat{z}_o) = \text{Real}(U) + i\ \text{Imag}(U) \tag{A.45}$$

where

$$\text{Real}(U) = \frac{\hat{y}_o}{2\pi} \iint_S U(\hat{x}, \hat{z}) \frac{\sin \hat{r}_o}{\hat{r}_o^2} d\hat{z}\, d\hat{x} \tag{A.46}$$

$$\text{Imag}(U) = \frac{-\hat{y}_o}{2\pi} \iint_S U(\hat{x}, \hat{z}) \frac{\cos \hat{r}_o}{\hat{r}_o^2} d\hat{z}\, d\hat{x} \tag{A.47}$$

$$\hat{r}_o = \sqrt{\hat{y}_o^2 + (\hat{x}_o - \hat{x})^2 + (\hat{z}_o - \hat{z})^2}$$

Intensity of the field is given by

$$I \sim [(\text{Real}(U)]^2 + [\text{Imag}(U)]^2 \tag{A.48}$$

Phase of the field at a given point $(\hat{x}_o, \hat{y}_o, \hat{z}_o)$ can be evaluated as follows:

$$\phi(\hat{x}_o, \hat{y}_o, \hat{z}_o) = \tan^{-1} \frac{\text{Imag}[U(\hat{x}_o, \hat{y}_o, \hat{z}_o)]}{\text{Real}[U(\hat{x}_o, \hat{y}_o, \hat{z}_o)]} \tag{A.49}$$

Since a wavefront passing through a given point has a fixed phase, the following equation can be proposed for the surface of a wavefront containing $(\hat{x}_o, \hat{y}_o, \hat{z}_o)$.

$$\frac{\text{Imag}(U)}{\text{Real}(U)} = \tan \phi \tag{A.50}$$

Upon substitution from (A.46) and (A.47) for Real(U) and Imag(U), the following equation for the wavefront is obtained:

$$\iint_S U(\hat{x},\hat{z}) \frac{\cos(\hat{r}_o - \phi)}{\hat{r}_o^2} d\hat{z}\, d\hat{x} = 0 \qquad (A.51)$$

Equation (A.51) may be used to evaluate two vectors tangential to the wavefront at a point $(\hat{x}_o,\hat{y}_o,\hat{z}_o)$. Cross product of these vectors would be normal to the wavefront representing the local direction of wave propagation. The tangential vectors may conveniently be chosen to lie in the x_oy_o and y_oz_o planes. Explicit expressions for $\partial x_o/\partial y_o$ and $\partial z_o/\partial y_o$ are needed for constructing these vectors. Differentiating (A.51) with respect to $\hat{y}_o$ for a fixed $\hat{z}_o$ and variable $\hat{x}_o$, the following expression is obtained:

$$\frac{\partial x_o}{\partial y_o} = \frac{A_1}{A_2} \qquad (A.52)$$

where

$$A_1 = \hat{y}_o \iint_S A\, d\hat{z}\, d\hat{x} \qquad (A.53)$$

$$A_2 = -\iint_S A(\hat{x}_o - \hat{x})\, d\hat{z}\, d\hat{x} \qquad (A.54)$$

$$A = \frac{U(\hat{x},\hat{z})\,[\hat{r}_o \sin(\hat{r}_o - \phi) + 2\cos(\hat{r}_o - \phi)]}{\hat{r}_o^4} \qquad (A.55)$$

The corresponding tangential vector may be expressed as follows:

$$\vec{V}_{t_1} = A_1\vec{I} + A_2\vec{J} \qquad (A.56)$$

Similarly, by differentiating Eqn. (A.51) with respect to $\hat{y}_o$ for a fixed $\hat{x}_o$ and variable $\hat{z}_o$, an expression for the second tangential vector can be obtained.

$$\vec{V}_{t_2} = A_3\vec{J} + A_1\vec{K} \qquad (A.57)$$

where

$$A_3 = -\iint_S A(\hat{z}_o - \hat{z})\, d\hat{z}\, d\hat{x} \qquad (A.58)$$

A vector in the direction of wave propagation can now be defined as follows:

$$\vec{s} = \vec{V}_{t_1} \times \vec{V}_{t_2} = A_1A_2\vec{i} - A_1^2\vec{j} + A_1A_3\vec{k} \qquad (A.59)$$

Under dipole approximation, a vector along the direction of polarization, $\vec{p}$ would lie in the plane defined by propagation vector $\vec{s}$ and the polarization vector $\vec{n}$ of the incident field. Hence, $\vec{p}$ can be expressed as a linear combination of $\vec{s}$ and $\vec{n}$.

$$\vec{p} = \vec{s} + K\vec{n}$$

Since $\vec{p}$ must also be normal to $\vec{s}$,

$$\vec{p} \cdot \vec{s} = 0$$

which yields the value of K.

$$K = -\frac{|\vec{s}|^2}{\vec{n} \cdot \vec{s}}$$

Hence the polarization vector may be expressed as follows:

$$\vec{p} = (\vec{n} \cdot \vec{s})\,\vec{s} - |\vec{s}|^2\,\vec{n} \qquad (A.60)$$

Vectors $\vec{s}$ and $\vec{p}$ may be normalized with the corresponding magnitudes for later applications.

This completes the set of equations needed to evaluate a diffracted field, its direction of propagation and the sense of polarization. These equations are further simplified for the case of a long finite slit and used for simulation of the signal produced by the device under consideration.

A.7.6 An Alternative Approach

The vector form of Kirchhoff's theory of diffraction is available in optics texts (e.g., Jones (1964)). It may be possible to use this theory to arrive at a mathematical formulation similar to the one given above. We did not have an opportunity to explore this possibility.

A.8 Mie Scattering Theory

Maxwell's equations were solved by Gustav Mie in 1908 for scattering of a uniform plane wave by a homogeneous isotropic spherical particle. This solution is exact and applies to particles with complex refractive indices. The imaginary part of the refractive index (known as extinction coefficient) accounts for absorption of light energy by the particle and can be associated to its electrical conductivity. The extinction coefficients and the refractive indices of common materials are available in references on optical materials such as Driscoll, W.G., and Vaughan, W. (1978).

A.8.1 Summary of the Results

Results of Mie theory are found in many different forms in the literature. It is convenient for the present application to follow the form used by Adrian and Earley (1976). The coordinates used in this formulation are shown in Fig. A.7. A set of rectangular coordinates $\vec{s}$, $\vec{p}$, and $\vec{s} \times \vec{p}$ is defined in terms of the direction of incident light propagation $\vec{s}$ and polarization $\vec{p}$. A set of polar coordinates (r,θ,ϕ) is used to express the solution for the scattered wave. Unit vector $\vec{r}$ represents the direction in which the properties of scattered light are needed. Unit vector $\vec{e}_\phi$ is normal to the plane of $\vec{s}$ and $\vec{r}$, whereas $\vec{e}_\theta$ is normal to $\vec{r}$ and $\vec{e}_\phi$. Coordinate transformation is done using the following relations.

$$\vec{e}_\phi = \frac{\vec{s} \times \vec{r}}{|\vec{s} \times \vec{r}|} \tag{A.61}$$

$$\vec{e}_\theta = \vec{e}_\phi \times \vec{r} \tag{A.62}$$

$$\cos\theta = \vec{s} \cdot \vec{r} \tag{A.63}$$

$$\sin\theta = |\vec{s} \times \vec{r}| \tag{A.64}$$

$$\cos\phi = \frac{\vec{p} \cdot \vec{r}}{\sin\theta} \tag{A.65}$$

$$\sin\phi = \frac{(\vec{s} \times \vec{p}) \cdot \vec{r}}{\sin\theta} \tag{A.66}$$

Scattered electric field for a unit incident field is given by

$$\vec{E}_s = C_s(\theta,\phi)\,\frac{e^{-ikr}}{kr} \tag{A.67}$$

where $\vec{C}_s$ is known as scattering coefficient and represents deviation of scattered wave from a homogeneous spherical wave. In the far field of scattering the following equation determines the scattering coefficient.

$$\vec{C}_s = A(\theta)\sin\phi\,\vec{e}_\phi + B(\theta)\cos\phi\,\vec{e}_\theta \tag{A.68}$$

$$A(\theta) = -i\sum_{n=1}^{\infty}\left[a_n \Pi_n(\cos\theta) + b_n T_n(\cos\theta)\right] \tag{A.69}$$

$$B(\theta) = i\sum_{n=1}^{\infty}\left[a_n T_n(\cos\theta) + b_n \Pi_n(\cos\theta)\right] \tag{A.70}$$

$$a_n = \frac{S_n'(\beta)\,S_n(\alpha) - mS_n'(\alpha)\,S_n(\beta)}{S_n'(\beta)\,\phi_n(\alpha) - m\phi_m'(\alpha)\,S_n(\beta)} \tag{A.71}$$

$$b_n = \frac{mS_n'(\beta)\,S_n(\alpha) - S_n'(\alpha)\,S_n(\beta)}{mS_n'(\beta)\,\phi_n(\alpha) - \phi_n'(\alpha)\,S_n(\beta)} \tag{A.72}$$

$$S_n(\alpha) = \sqrt{\pi\alpha/2}\,J_{n+1/2}(\alpha) \tag{A.73}$$

$$C_n(\alpha) = (-1)^n\sqrt{\pi\alpha/2}\,J_{-(n+1/2)}(\alpha) \tag{A.74}$$

$$\phi_n(\alpha) = S_n(\alpha) + iC_n(\alpha) \tag{A.75}$$

$$\Pi_n(\zeta) = \frac{2n+1}{n(n+1)}\,P_n'(\zeta) \tag{A.76}$$

$$T_n(\zeta) = \frac{2n+1}{n(n+1)}\left[\zeta P_n'(\zeta) - \left(1-\zeta^2\right)P_n''(\zeta)\right] \tag{A.77}$$

$$\alpha = \pi a/\lambda \tag{A.78}$$

$$\beta = m\alpha \tag{A.79}$$

$$m = n_p/n \tag{A.80}$$

where $J_{n+1/2}$ is the Bessel function of order $(n+1/2)$ and $P_n(\zeta)$ is the Legendre polynomial of order n.

It is worth mentioning that the coefficients a_n and b_n are complex in general. Hence the scattered wave changes phase with changing values of θ and ϕ.

For the purpose of computation, the series expansions for $A(\theta)$ and $B(\theta)$ need to be truncated. The following criterion has been suggested by Gucker et al. (1962) for a significant number of terms in the series.

$$n = 7 + 1.2\alpha \quad , \quad \text{for} \quad \alpha \geq 10 \tag{A.81}$$

For $\alpha < 10$, Adrian and Earley (1976) suggest the following criterion:

$$n = 2(\alpha + 1) \tag{A.82}$$

A.8.2 Anisotropic Scattering Shift and Intensity Modulation

Calibration of laser velocimetry systems is normally based upon a "moving point-source model" of the scattering particle exhibiting a Doppler shift in the frequency of the scattered light. Since scattering particles are generally larger than the wavelength of the light, this model has certain limitations. The scattered wave has a variation in intensity and phase over a spherical surface around the particle. This phenomenon may be explained in terms of the Huygens-Fresnel principle (Sec. A.7.1). The scattered wave may be considered as an interference pattern produced by a number of secondary waves originating from the particle. Figure A.8 shows a portion ABC of the spherical surface and a polar diagram of intensity variation over it. In the vicinity of point A, intensity is large and varies slowly; hence, this portion of the scattered wave may be attributed to a single secondary wave. Near point B, the intensity shows a sharp spatial variation. This effect may be interpreted as the emergence of another secondary wave which is out of phase with respect to the first wave. Hence, the two waves

interfere destructively near B, causing a drop in intensity. Apparently, the second wave grows stronger near point C, while the first secondary wave diminishes in strength. Hence, it is expected that a change in phase of about 180° would take place between A and C. In other words, neighboring intensity lobes would be out of phase. Typically, the angular extent of an intensity lobe is given by λ/d_p; hence, anisotropic scattering effects are stronger for particles with diameter significantly larger than the wavelength of the light.

Motion of the particle in certain LDV systems may result in exposure of significantly different parts of the scattered wave to the receiving aperture during a single measurement. The rate of change of the phase under such conditions would cause a shift in the frequency of the light in addition to the Doppler shift deduced from a point-source model. The additional shift is related to the anisotropic scattering characteristics of the particle and may appropriately be called anisotropic scattering shift. Furthermore, there may occur a modulation of signal intensity due to various lobes sweeping across the receiving aperture. For the present device, these effects are examined in Chap. 4.

The anisotropic scattering shift may also be interpreted as a Doppler shift resulting from motion of the "virtual center" of the scattered wave with respect to the geometrical center of the particle. The scattered wave at a given orientation appears to be emanating from a center in the vicinity of the geometrical center of the particle. The scattering center moves with respect to the geometrical center if the scattered wave orientation is changed at the receiving aperture. Hence it must be emphasized that the signal from an LDV setup is a measure of the scattering-center velocity and not necessarily the particle velocity.

Yet another way of conceptualizing the scattering-related frequency shift is an interpretation based on a fringe model. Because of its finite size the scattering particle displaces fringes (by refraction and other complex phenomena covered by the Mie theory). The amount of fringe displacement may vary from fringe-to-fringe causing the "effective fringe spacing" to be different from the "undisturbed fringe

spacing". It may be pointed out that a common method of calibrating an LDV system employs scattering from a disc of known rotating speed. Since the scattering characteristics of a rotating disc are in general different from that of a particle, there may be an uncertainty associated with such calibration.

Fringe displacement is likely to be more significant in the case of apertures located very close to the measuring volume. Mazumder et al. (1981) have suggested a method of near-wall velocity measurement which employs a microscope objective in the wall for receiving the signal. This particular method appears more prone to fringe displacement than common LDV.

The present device involves diverging fringes which undergo different displacements because of the changing orientation of fringes across the measuring volume. This effect has been examined in Chap. 4.

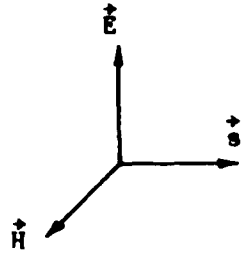

(a) Direction of propagation relative to $\vec{E}$ and $\vec{H}$ fields

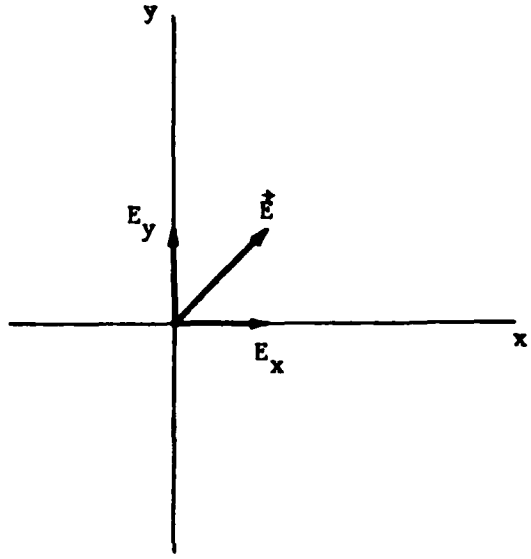

Components of $\vec{E}$ along fixed coordinates in a plane normal to the direction of propagation

Fig. A.1. Propagation of electromagnetic waves.

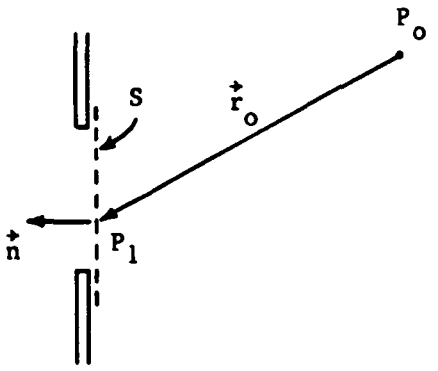

Fig. A.2. Rayleigh-Sommerfeld formulation of diffraction from an aperture.

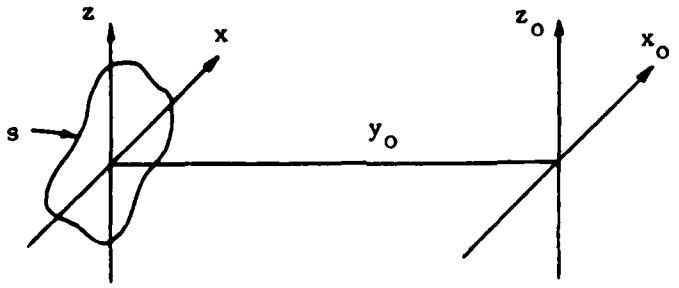

Fig. A.3. Coordinates for scalar diffraction.

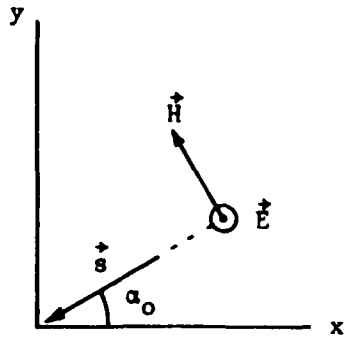

(a) E-polarization

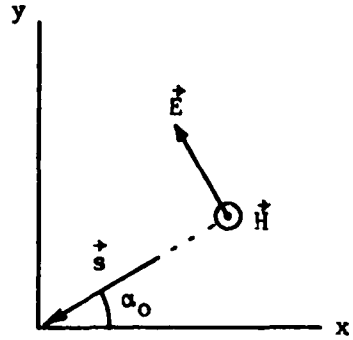

(b) H-polarization

Fig. A.4. Two-dimensional problem in vector diffraction theory.

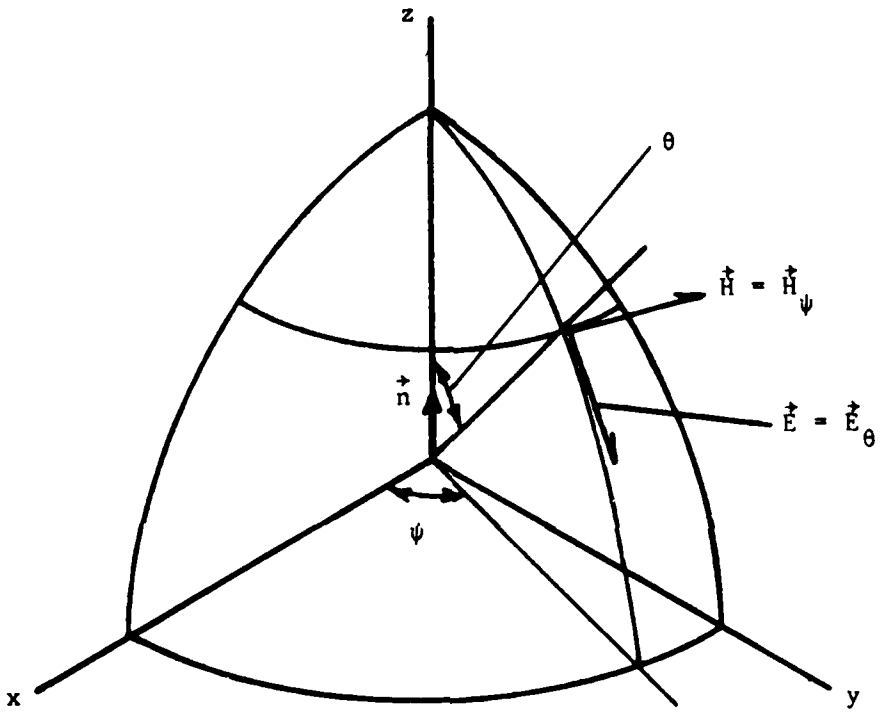

Fig. A.5. Coordinates for the field of a dipole.

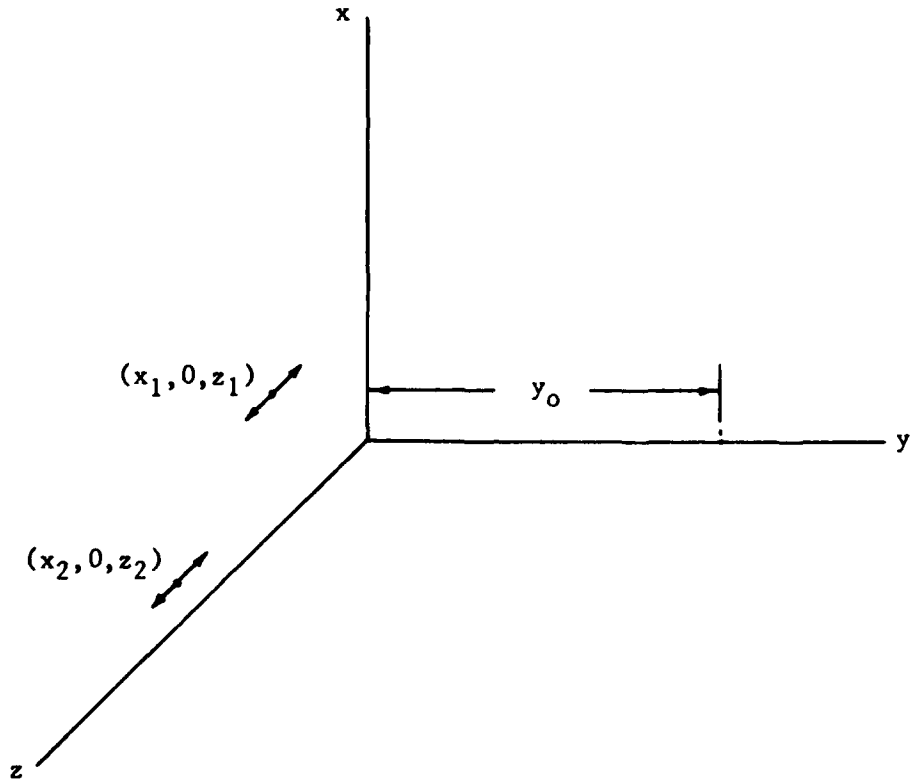

Fig. A.6. Specification of a dipole-pair for evaluating the slope of the equivalent dipole.

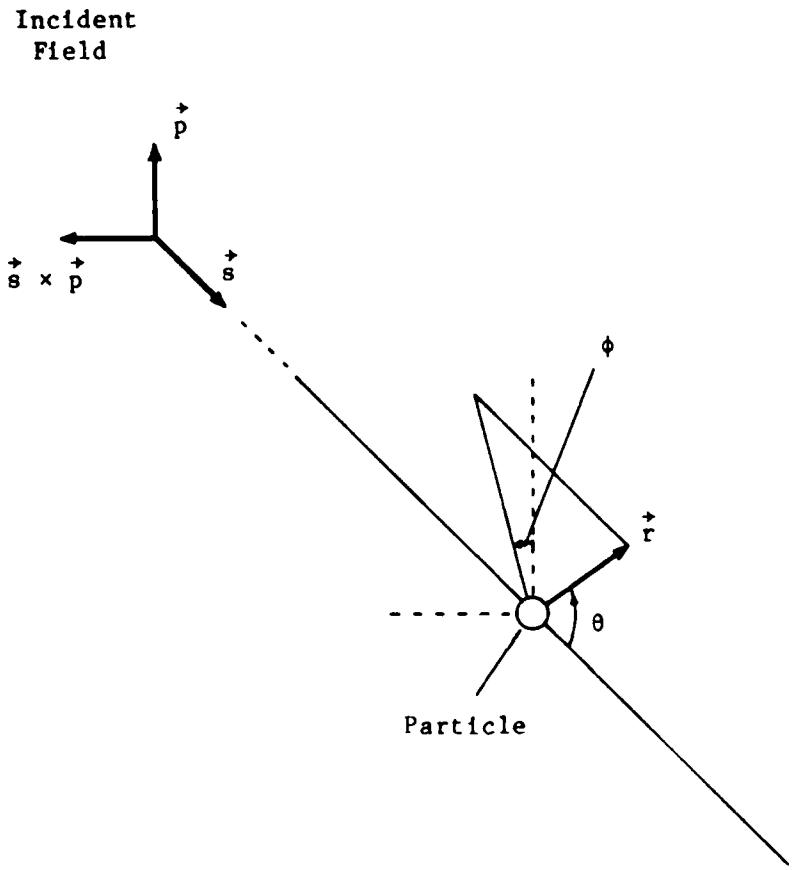

Fig. A.7. Coordinates for Mie scattering theory.

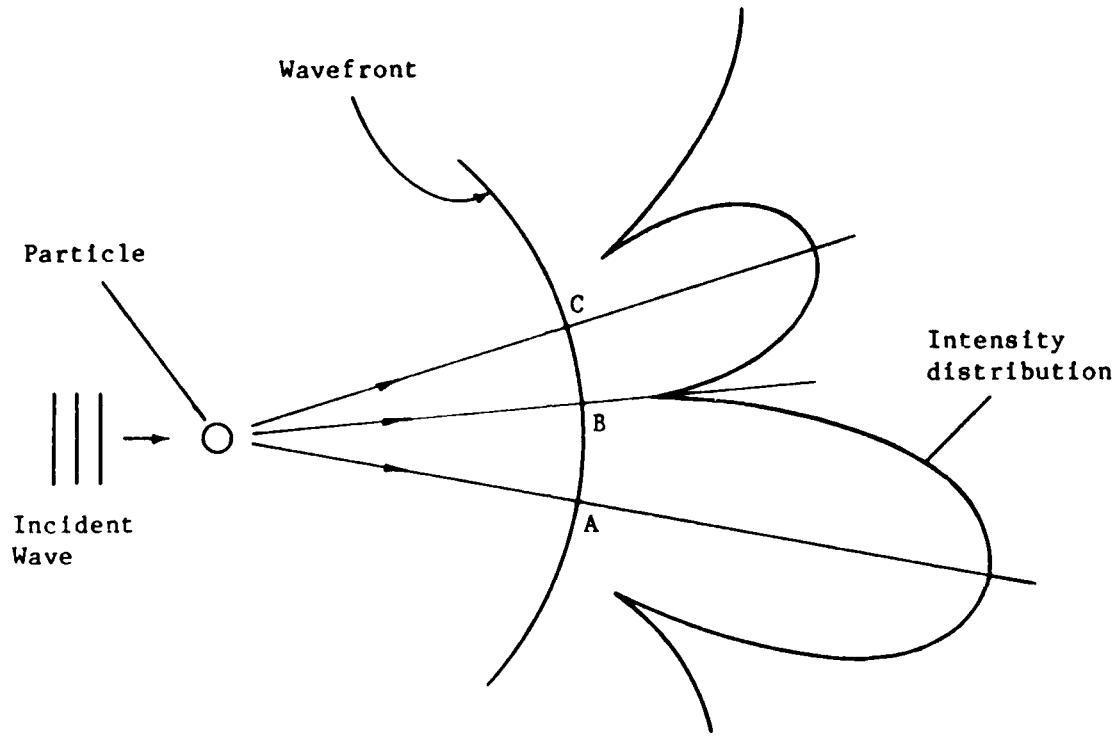

Fig. A.8. Anisotropic scattering from large particles.

Appendix B

POLARIZATION EFFECTS IN SLIT DIFFRACTION

The purpose of this appendix is to examine the effect of changes in polarization of the laser light incident on the slits. Two cases are considered, i.e.,

(1) E-field parallel to the slits;

(2) H-field parallel to the slits.

These shall hereafter be refered to as Case (1) and Case (2). A simplified mathematical model has been used to derive expressions for the shape of the wavefronts and the transfer function of the device for the two cases. According to present analysis, the wavefronts are more flat than circular for Case (1) and more peaked relative to a circular arc for Case (2). However, these deviations from the circularly cylindrical shape are small and do not affect the transfer function significantly. It must be emphasized that the mathematical formulation used here is approximate and excessively simplified. It is considered suitable for the purpose of comparing the two cases of different polarization but not recommended for modeling the system.

B.1 Nomenclature

For the sake of convenience, some exceptions to the nomenclature of the main text have been made. Symbols ϕ, ψ, χ, and r have been redefined in this appendix. Figures (B.1) and (B.2) may be consulted for the relevant definitions.

B.2 Shape of the Wavefronts

For diffraction of light by an infinitely long slit in a perfectly conducting screen, Keller (1957) has recommended the following expression:

$$e = -\left(\frac{1}{2\pi\hat{r}}\right)^{1/2} e^{-i\left(\hat{r}+\frac{\pi}{4}\right)} f_s(\phi) \qquad (B.1)$$

where

$$f_s(\phi) = i \frac{\sin[\hat{a}(\sin\phi)]}{\sin\frac{\phi}{2}} \pm \frac{\cos[\hat{a}(\sin\phi)]}{\cos\frac{\phi}{2}}$$

In the second term of the above expression, plus sign corresponds to Case (1) and the minus sign to Case (2). The variable e in Eqn. (B.1) represents electric field for Case (1) and magnetic field for Case (2). This equation is based on the assumption of far-field diffraction by a slit illuminated with a uniform plane wave incident normally to the screen. It is further assumed that the total field at a point is the sum of the fields produced by diffraction from each edge of the slit; the interaction between the edges being ignored.

The equation of a wavefront may be deduced from Eqn. (B.1), as a surface of constant phase, i.e.,

$$-\hat{r} + \tan^{-1}\left(\pm \frac{\tan(\hat{a}\sin\phi)}{\tan\frac{\phi}{2}}\right) = \text{constant} \qquad \text{(B.2)}$$

where, range of second term: 0 to π;

+ sign: Case (1);

- sign: Case (2).

The angle of slope ψ has been defined in Fig. B.1. It may be evaluated by differentiating Eqn. (B.2).

$$\tan\psi = \frac{\hat{r}}{d\hat{r}/d\phi} \qquad \text{(B.3)}$$

$$= \pm \frac{\hat{r}[\tan^2\frac{\phi}{2} + \tan^2(\hat{a}\sin\phi)]}{\hat{a}\sec^2(\hat{a}\sin\phi)\cos\phi\tan\frac{\phi}{2} - \frac{1}{2}\tan(\hat{a}\sin\phi)\sec^2\frac{\phi}{2}}$$

where $0 \leq \psi < \pi$,

+ sign: Case (1);

- sign: Case (2).

Since $\psi = 90°$ for a truly circular arc, the wavefronts would be too flat or too peaked for $\psi < 90°$ or $\psi > 90°$, respectively; provided that $\phi \geq 0$. However, the following numerical example would illustrate that deviation from the circular structure is marginal.

Given: $r = 50\ \mu m$, $\lambda = 0.3868\ \mu_m$,

$\phi = 20°$ and $a = 1\ \mu m$;

For Case (1), $\psi = 89.3$,

For Case (2), $\psi = 90.7$.

Differences between the two cases may be explained in physical terms. In Case (1), the electric field is parallel to the slit edges and therefore is completely absorbed at the edges; hence, bending of the wave around the edges is not as strong as in Case (2). Furthermore, one would expect less power transmission in Case (1). However, the slits in the present system are quite wide ($\hat{a} > 8$), so that the amount of power transmission depends only upon the area exposed to the laser (see Keller, 1961).

It may also be noticed that $\tan \psi$ is directly proportional to $\hat{r}$; hence, with increasing r, the value of ψ would approach 90°. Alternatively, with increasing distance from the slit, the wavefronts would become more circular.

B.3 Polarization Sensitivity of the Transfer Function

The above-mentioned model of wavefronts may be used to derive expressions for the transfer function $\mathbf{B}$ for the two case under consideration. Wavefronts produced by the two slits, spaced S, are considered in Fig. B.2(a). The angle of each wavefront with the horizontal may be expressed as follows:

$$\chi_\ell = \phi_\ell + \psi_\ell - \frac{\pi}{2} \quad ; \qquad \ell = 1, 2 \tag{B.4}$$

In Fig. B.2(b), the unit vectors normal to each wave are shown. It is obvious that the term $\hat{n}.\hat{i}$ may be evaluated as below:

$$\hat{n}.\hat{i} = \sin \chi_2 - \sin \chi_1$$

Upon substituting (B.4),

$$\hat{n}.\hat{i} = \cos(\phi_1 + \psi_1) - \cos(\phi_2 + \psi_2) \tag{B.5}$$

Using Eqns. (2.8), (2.11) and (2.14) of Chapter 2,

$$B = \frac{\hat{n}.\hat{l}}{2S} \tag{B.6}$$

The above expression is valid for a streamwise linear velocity profile without any normal component. Inserting (B.5) into (B.6), the following expression for the transfer function is obtained.

$$B = \frac{1}{2S}\left[\cos(\phi_1 + \psi_1) - \cos(\phi_2 + \psi_2)\right] \tag{B.7}$$

For a given location (x,y), the angles ϕ_1 and ϕ_2 may be evaluated as follows:

$$\begin{aligned} \tan\phi_1 &= -(x + S) \;; \quad -\frac{\pi}{2} < \phi_1 \leq \frac{\pi}{2} \\ \tan\phi_2 &= -x + S \;; \quad -\frac{\pi}{2} < \phi_2 \leq \frac{\pi}{2} \end{aligned} \tag{B.8}$$

Similarly,

$$\begin{aligned} \hat{r}_1 &= \hat{y}\sqrt{1 + (x + S)^2} \\ \hat{r}_2 &= \hat{y}\sqrt{1 + (x - S)^2} \end{aligned} \tag{B.9}$$

Eqs. (B.8) and (B.9) may be used in conjunction with (B.3) to evaluate the necessary angles for deducing B from (B.7).

For a range of $x = 0$ to 0.2 and $y = 50$ μm, the normalized transfer functions are represented in Fig. B.3(a). The transfer function for a circular wavefront is also shown for comparison. Case (2) appears to have the smallest deviation from the nominal value. But as illustrated in Fig. B.3(b), the advantage of Case (2) over Case (1) is only marginal because both the cases exhibit less than 1% deviation from the case of circular wavefronts. Hence, it may be concluded that the transfer function is fairly insensitive to the polarization of the light illuminating the slits and the circular-wave model is a good approximation for either mode of polarization. To conclude, it may be recalled that the present hardware conforms to Case (1) of polarization.

$\psi > 90°$: Less flat than circular

$\psi < 90°$: More flat than circular

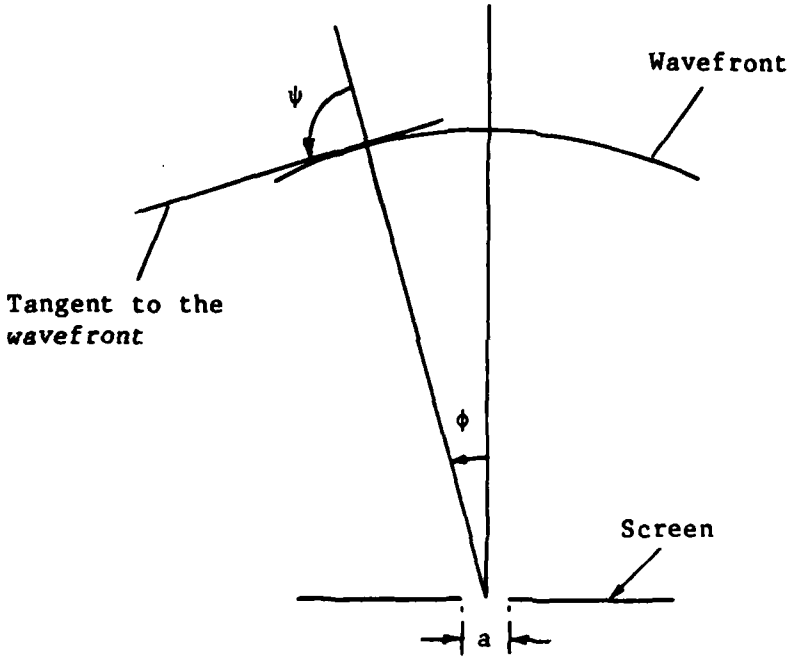

Fig. B.1. Flatness of the wavefronts.

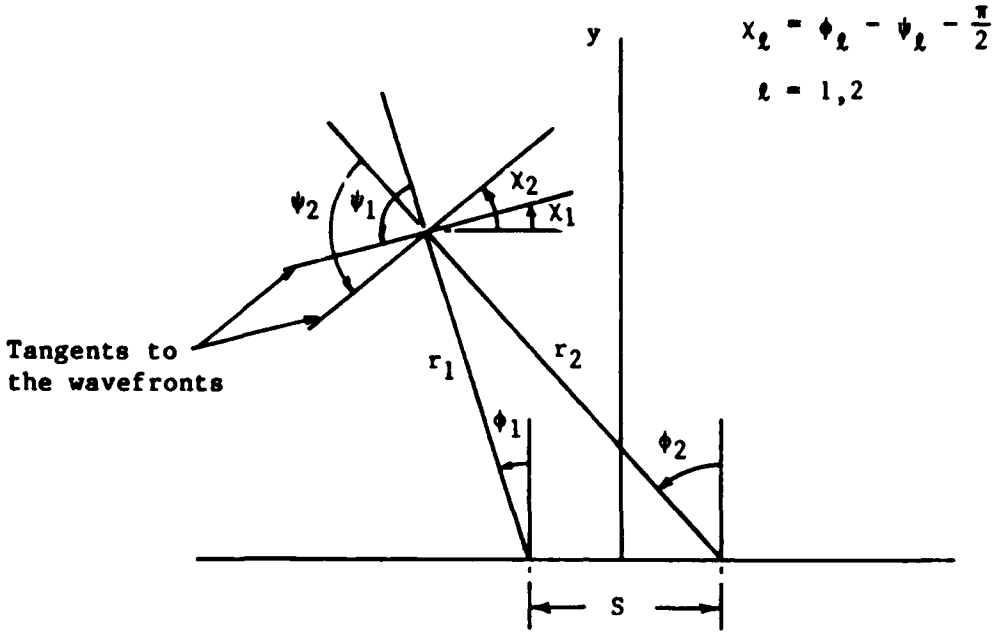

(a) Geometry of the wavefronts produced by a pair of slits

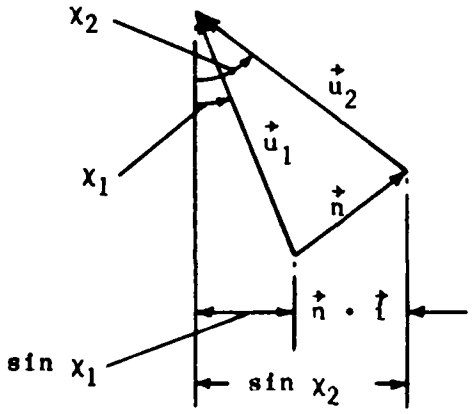

(b) Evaluation of $\vec{n} \cdot \vec{l}$ from geometry of the wavefronts

Fig. B.2. Interaction of the wavefronts emanating from a pair of slits.

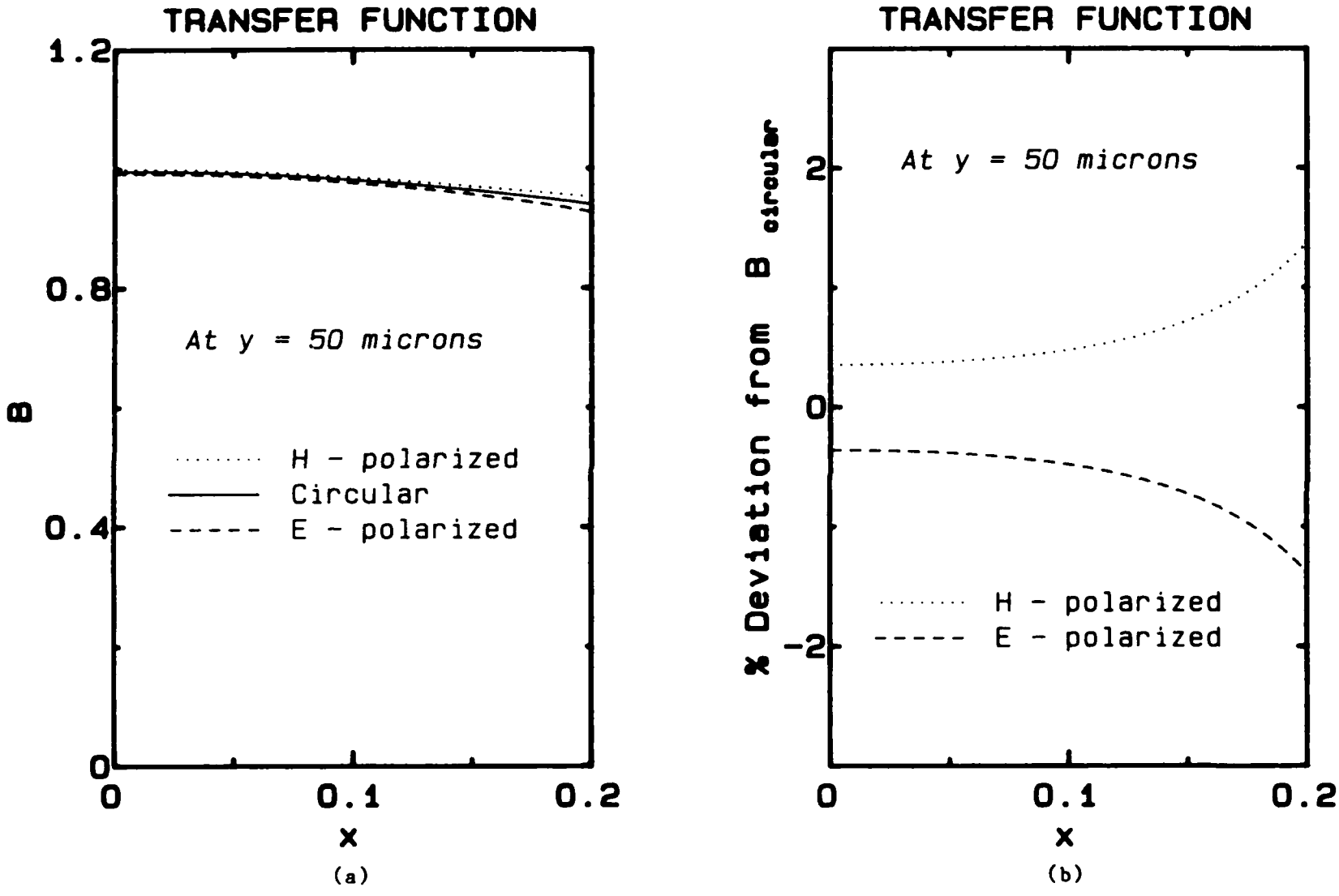

Fig. B.3. Comparison of polarization-sensitive models of the transfer function with the circular-wave model.

Appendix C

OPTICS-RELATED VARIATIONS IN THE TRANSFER FUNCTION

The instantaneous velocity gradient may be deduced from the following expression.

$$g = \frac{\lambda}{B\,S} f_d \tag{C.1}$$

where, f_d is the frequency of the signal after removing the Bragg shift. The accuracy of a single measurement is determined by the uncertainties in various parameters on the right-hand side of Eq. (C.1). The quantities λ and S are known fairly accurately (within 1%); whereas, accuracy of f_d is determined by the SNR of the signal discussed in Chap. 4. The purpose of the present discussion is to evaluate the uncertainty in parameter B.

It may be mentioned at this point that the uncertainty in a single measurement does not completely describe the accuracy of a statistical sample. The measured samples are known to be biased because of several reasons. Adams et al. (1984) have given a comprehensive summary of the sources of bias and various methods for bias correction. Typically, a bias correction method would require the right-hand side of Eq. (C.1) to be multiplied by a weighting function prior to reduction of the data. The accuracy of this function would be an additional factor in the uncertainty analysis of the statistical parameters. The present results have been reported without any bias correction.

C.1 The Statistics of B

A probability density function (PDF), p_B, for B may be introduced; so that, the mean and the mean-square values of B may be expressed as follows:

$$\bar{B} = \int_{-\infty}^{\infty} B\, p_B\, dB$$

$$\overline{B^2} = \int_{-\infty}^{\infty} B^2\, p_B\, dB \tag{C.2}$$

where,

$$\int_{-\infty}^{\infty} p_B \, dB = 1$$

As shown in Chap. 2, B depends upon several variables. In general, p_B would be a joint probability function of all these variables. However, some simplification may be made by taking into account the fact that the measured signal frequency is averaged over the path traversed by the scattering particle through the measuring volume. If the fluid-related uncertainties are isolated, the path-averaged transfer function would be represented as below:

$$B = \frac{\left[1 + (x_m + S)^2\right]^{1/2} - \left[1 + (x_m - S)^2\right]^{1/2}}{2x_m S}$$

In this form, B is a function of y only. Hence, the probability of a certain value of B being effective may be defined as the probability of signal generation from the corresponding y-location. To further simplify the problem, p_B may be specified as the joint probability of particle arrival and signal detection at the appropriate y-location. These functions are illustrated schematically in Fig. C.1. At this stage, it would be helpful to consider a numerical example of p_B.

C.2 A Model for PDF of B

In order to estimate the optimum value of B and the associated uncertainty, the following models may be used for the probability functions shown in Fig. C.1:

- PDF of signal detection: Uniform between y_{min} and y_{max} and zero beyond this range;
- PDF of particle arrival: Exponentially rising from zero at the wall to an asymptotic value in the free-stream.

Hence, the PDF of signal generation would be given as follows:

$$p_B \sim 1 - e^{-y/\delta_p}, \quad y_{min} < y < y_{max}$$
$$p_B = 0, \quad y \leq y_{min}, \quad y \geq y_{max} \tag{C.4}$$

A more relevant parameter is the amplitude distribution function, defined as below:

$$A_B(B) \sim \int_{-\infty}^{B} p_B \, dB \tag{C.5}$$

An appropriate multiplier is needed on the right-hand side of the above equation. In the normalized form, the largest value of A_B would be unity.

Equations (C.3) and (C.4) may be combined to express p_B as a function of B rather than y. Subsequently, p_B may be used with Eqs. (C.2) and (C.5) to evaluate the mean, the variance and the amplitude distribution function of B. Calculations have been performed for two values of δ_p, i.e., 0.1 and 10 mm, which are comparable with the thicknesses of the sublayer and the turbulent layer respectively. The results are presented in Table C.1 and Fig. C.2.

Table C.1

Statistical Parameters of B

The following results are based on:

$S = 10$ μm, $y_{min} = 50$ μm, $y_{max} = 150$ μm, and $\alpha_m = 0.15$.

δ_p	Mean	Standard Deviation
0.1 mm	0.9865	0.00138
10 mm	0.9867	0.00117

Despite large differences between the values of δ_p for the two cases, the statistical parameters of interest are very close. The mean value of B may be specified as 0.987. According to Fig. C.2, 95% of the variations in B lie in the range of -0.26% to +0.13% of the mean value.

It may be concluded that the optics-related variations are not a main source of uncertainty in the measurements. Also, the present data have been reduced with $B = 1$, which may have resulted in underestimating the skin friction by $\sim 1\%$.

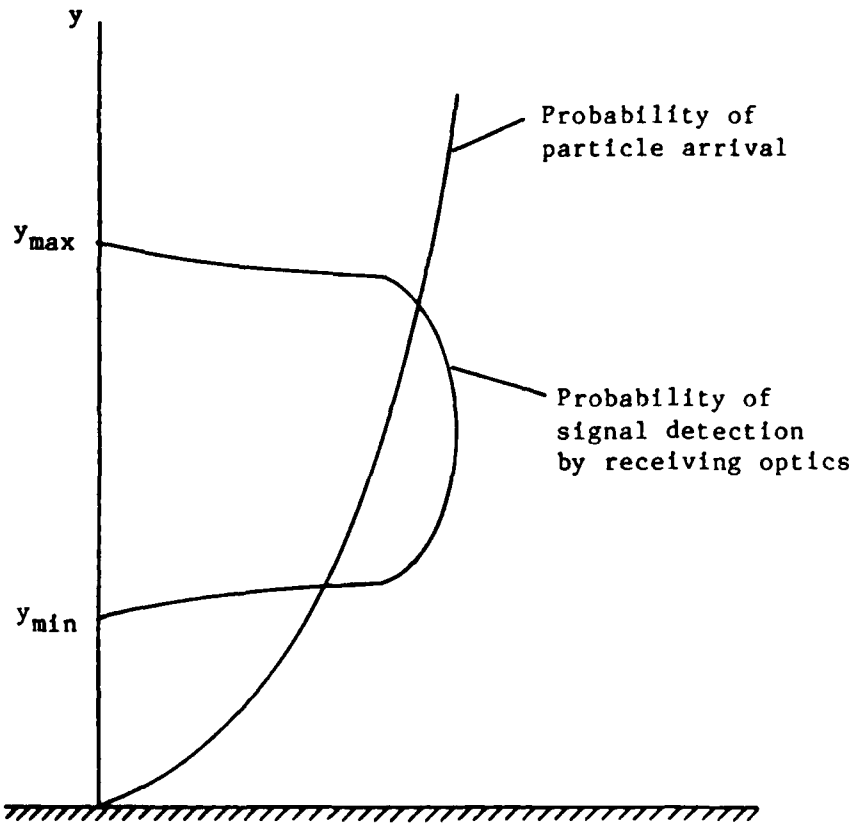

Fig. C.1. Schematic representation of the probability functions that determine the likelihood of signal generation from a y-location.

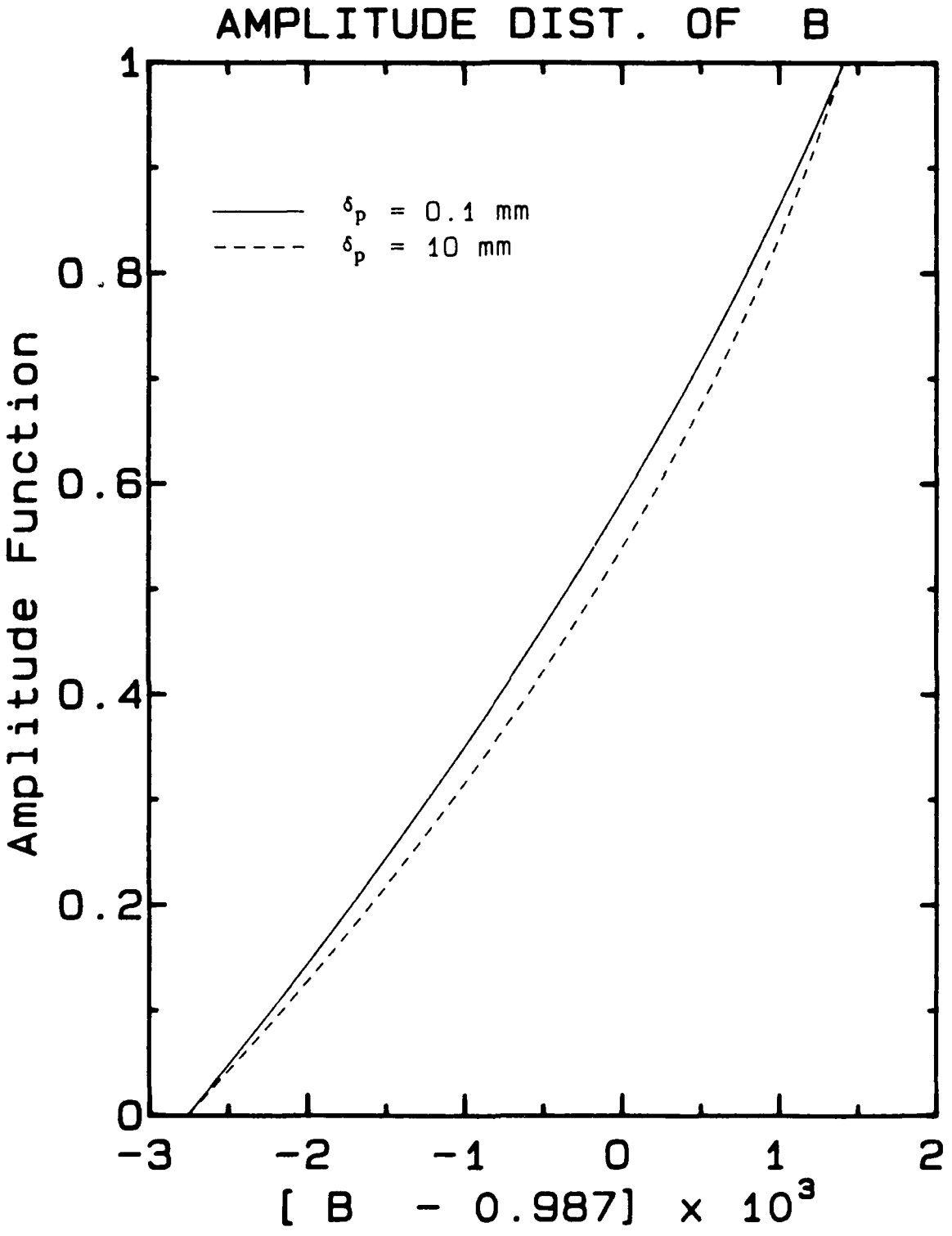

Fig. C.2. Amplitude distribution function of B.

Appendix D

CHOPPING AND SCANNING METHODS

Two useful methods for studying the intensity characteristics of laser beams, especially at a focused spot, are explained. The following discussion includes a description of the methods, the ways of interpreting the results and precision requirements for the adjustable parameters. Some nonstandard nomenclature is used to facilitate derivation of expressions used in Chap. 5. However, this auxiliary nomenclature is not extended beyond this appendix.

D.1 The Chopping Method

The experimental setup for this method has been illustrated in Fig. 5.7. For measuring very small or narrow laser beams (micron-size), the chopping edge should be precisely straight and sufficiently thin. A sharp-edged metallic coating on a glass disc would probably be a convenient device for this purpose. However, a good quality razor blade was found to give satisfactory results for the present experiments. As the beam is chopped, the detected power drops with time. The relationship between power and time is refered to as "power profile". Analytical expressions for the power profile are derived and used for establishing a criterion for interpreting the results. Sensitivity of the measurement to various adjustments is also deduded from the expressions for power profile.

D.1.1 Analysis of the Power Profile

A laser beam of elliptic cross-section is shown in Fig. D.1. The intensity distribution over the cross-section may be expressed as follows:

$$I(x,y) = I_o \exp\left[-2\left(\frac{x^2}{L^2} + \frac{y^2}{W^2}\right)\right] \qquad (D.1)$$

where I_o is intensity at the center. It diminishes to I_o/e^2 on the periphery of an ellipse, with W and L as semi-minor and semi-major axes, respectively.

The total power in the beam may be evaluated as below:

$$P_T = \int_{-\infty}^{\infty} I(x,y)\, dxdy = \frac{\pi}{2} abI_o \qquad (D.2)$$

The power in the chopped beam may be worked out by considering a chopper AB, shown in Fig. D.1. The orientation of the chopper may be specified by the angle from the minor axis, ϕ and the distance from the center, h; so that, line AB is defined by

$$x \sin \phi + y \cos \phi = h \qquad (D.3)$$

After transforming the coordinates to $x_1 = x/L$ and $y_1 = y/W$, and rotating the chopper so that it lies parallel to the x_1-axis, power in the chopped beam may be expressed as follows:

$$P = ab\, I_o \int_{x_1=-\infty}^{\infty} \int_{y_1=-\infty}^{h'} \exp\left[-2(x_1^2 + y_1^2)\right] dx_1 dy_1 \qquad (D.4)$$

$$= \frac{\pi}{4} ab\, I_o\, \mathrm{erfc}(-\sqrt{2}\, h')$$

where

$$h' = h/\sqrt{W^2 \cos^2 \phi + L^2 \sin^2 \phi} \qquad (D.5)$$

Defining nondimensional power as $p^* = P/P_T - 1/2$,

$$p^* = -\frac{1}{2} \mathrm{erf}(\sqrt{2}\, t^*) \qquad (D.6)$$

If the chopper is moving with a speed v_c,

$$h' = -t^* = -t/\tau \qquad (D.7)$$

where

$$\tau = \sqrt{W^2 \cos^2 \phi + L^2 \sin^2 \phi}/v \qquad (D.8)$$

The above expression is valid for a large chopper moving with a constant linear speed over the portion of the beam cross-section containing most of the energy. For special cases of

$$\phi = 0^\circ \quad , \quad \tau = W/v_c \quad ,$$

and

$$\phi = 90^\circ \quad , \quad \tau = L/v_c \quad .$$

For a fast photodiode, the power profile is transfered exactly as a voltage profile at the output of the photodiode. However, if the response of the photodiode is not satisfactory, a first-order model of the following form may be used:

$$t_c \frac{dQ}{dt} + Q = P \tag{D.9}$$

where Q is photodiode output and t_c is the characteristic time of the photodiode. For a step input, $P = 1$, the time required by Q to reach a value of 0.9 from 0.1 is referred to as "10%-90% rise time". This parameters is frequently quoted by the manufacturers. It is related to the characteristic time through the following relation:

$$t_c = 0.455 \times (\text{10\%-90\% rise time})$$

The response equation may be nondimensionalized as follows:

$$\frac{1}{\hat{t}} \frac{dq^*}{dt^*} + q^* = p^* \tag{D.10}$$

where

$$\hat{t} = \tau/t_c \quad \text{and} \quad q^* = \frac{Q}{P_T} - \frac{1}{2}$$

Integrating from $t^* = -\infty$ to t^*,

$$q^* = p^* + \frac{1}{2} \exp[-\hat{t}(t^* - \hat{t}/8)] \operatorname{erfc}[\sqrt{2}\,(\hat{t}/4 - t^*)] \tag{D.11}$$

For the measurements reported in Chap. 5, the photodiode rise time was 10 ns. For a reasonable chopper speed, the value of $\hat{t}$ lies in the range of 10000-20000; hence for all practical purposes, $q^* = p^*$.

D.1.2. A Criterion for Interpretation of the Measurements

The points of I_o/e^2 intensity lie in the wings of the power profile where the slope is very small with respect to the time axis. Hence, these points cannot be located very accurately. It was found appropriate to measure the time interval, Δt, between the drop in power from $P/P_T = 3/4$ to $1/4$. This would correspond to variation in p^* from $1/4$ to $-1/4$. From Eq. (D.6), at

$$p^* = \pm 0.25, \quad \sqrt{2}\, t^* = \mp 0.476 \quad .$$

Using the definition of t^* from Eq. (D.7),

$$\Delta t/\tau = 2 \times 0.476.$$

For the case of $\phi = 0$ (measurement of waist), the above expression may be written as follows:

$$2W = 2.97\, v_c\, \Delta t \qquad (D.12)$$

Knowing the chopper speed and the time interval Δt, the $1/e^2$-waist width may be obtained from the above equation.

D.1.3 Sensitivity of the Adjustments

In order to obtain accurate results from the chopping method, the test lens and the chopper should be adjustable relative to the laser beam. In the case of a cylindrical lens of small focal length, the two most sensitive adjustments are as follows:

- The chopping edge should be precisely parallel to the major axis of the elliptic waist.
- The chopper path should coincide closely with the focal plane.

If the chopping edge is tilted by a small angle ϕ, Eq. (D.8) may be simplified to the following expression:

$$\tau = \sqrt{W^2 + \phi^2 L^2}\Big/ v_c$$

It is obvious that, in order to accurately measure W, the angle ϕ must satisfy the condition

$$\phi \ll W/L \ .$$

The precision requirement for this adjustment may be appreciated from the following numerical example, which is representative of the experiments reported in Chap. 5:

$$W = 2\ \mu m, \quad L = 500\ \mu m,$$

To keep the error below 10%, $\phi = 0.1°$. During the present experiments, ϕ was adjusted by rotating the lens. Finer adjustment was obtained by raising and lowering the chopper relative to the laser beam.

The effect of the other major source of error (i.e., a gap between the chopper plane and the focal plane) may be ascertained by considering the parabolic increase in the laser width away from the waist. The measured waist, W' may be expressed as follows:

$$W' = W\left[1 + \left(\frac{\lambda \delta z}{\pi W^2}\right)^2\right] \approx W\left[1 + \frac{1}{2}\left(\frac{\lambda \delta z}{\pi W^2}\right)^2\right] \tag{D.13}$$

where δz is the displacement of the chopper from the waist.

If $\lambda = 0.5\ \mu m$ and $W = 2\ \mu m$, then in order to keep the error below 10%, $\delta z = 10$ micron. A standard micrometer with a least count of 1 micron was used for the present experiments.

D.2 The Scanning Method

The experimental setup for this method has been described in Chap. 5 (see Fig. 5.8). For the case of perfect alignment, the slit and the waist are shown in Fig. D.2. Since the scanning experiments are conducted with the assembled focusing optics, this condition may be achieved closely using the precision translators. Hence, this scheme is analyzed only for the case of ideal alignment.

Using the intensity distribution given by Eq. (D.1), power transmitted through the slit in Fig. D.2 may be expressed as

$$P = I_o \int_{x=-b}^{b} \int_{y=y-a}^{y+a} \exp\left[-2\left(\frac{x^2}{L^2} + \frac{y^2}{W^2}\right)\right] dydx$$

$$= \frac{\pi WLI_o}{4} \operatorname{erf}\left(\frac{\sqrt{2}\, b}{L}\right) \left\{ \operatorname{erf}\left[\frac{\sqrt{2}\,(y+a)}{W}\right] - \operatorname{erf}\left[\frac{\sqrt{2}\,(y-a)}{W}\right] \right\} \tag{D.14}$$

For the cases of a very narrow and a very wide slit, the power profile is illustrated in Fig. D.3. In the case of a narrow slit, the power profile may be simplified as follows:

$$P = \sqrt{2\pi}\, aLI_o \operatorname{erf}\left(\frac{\sqrt{2}\, b}{L}\right) \exp\left[-2\left(\frac{y}{W}\right)^2\right] \tag{D.15}$$

In the case of a wide slit, the overlap between the two error functions involving y (in Eq. (D.14)) is insignificant. Hence, each wing of the power profile may be viewed as a chopping profile and interpreted according to the criteria outlined in the previous section.

The scanning data from a relatively narrow slit may be interpreted by measuring the full width of the profile at half the maximum power (FWHM). Since the maximum power occurs at $y = 0$,

$$P_{max} = \frac{\pi WLI_o}{2} \operatorname{erf}\left(\frac{\sqrt{2}\, b}{L}\right) \operatorname{erf}\left(\frac{\sqrt{2}\, a}{W}\right) \tag{D.16}$$

For very narrow slit, Eq. (D.15) yields

$$P_{max} = \sqrt{2\pi}\, aLI_o \operatorname{erf}\left(\frac{\sqrt{2}\, b}{L}\right) \tag{D.17}$$

The values of y-coordinates for FWHM may be evaluated from $P = P_{max}/2$. Using Eqs. (D.14) and (D.16),

$$\operatorname{erf}\left(\frac{\sqrt{2}\, a}{W}\right) = \operatorname{erf}\left(\frac{\sqrt{2}\,(y+a)}{W}\right) - \operatorname{erf}\left(\frac{\sqrt{2}\,(y-a)}{W}\right) \tag{D.18}$$

For a very narrow slit, Eq. (D.15) and (D.17) lead to the following expression:

$$\frac{1}{2} = \exp\left[-2\left(\frac{y}{W}\right)^2\right]$$

Or

$$\frac{2W}{FWHM} = \left(\frac{2}{\ln 2}\right)^{1/2} \approx 1.7 \qquad (D.19)$$

A numerical solution of Eq. (D.18) is plotted in Fig. D.4. It may be noticed that the narrow slit approximation is valid within 1.5% for the values of FWHM exceeding 4 times the slit width. For very small values of FWHM, the parameter 2W/FWHM decreases very sharply. It is not advisable to use FWHM for deducing the waist width if it is smaller than 1.5 times the slit width. However, chopper approximation would provide accurate results for such cases. As mentioned in Chap. 5, the narrow slit approximation is suitable for the present system. Finally, it may be pointed out that the above analysis is based on the assumption that the power transmitted through a slit is the same as the power incident on the exposed area of the slit. As discussed in Sec. 3.3.4, this assumption is not valid for very narrow slits, but it is acceptable for the present system.

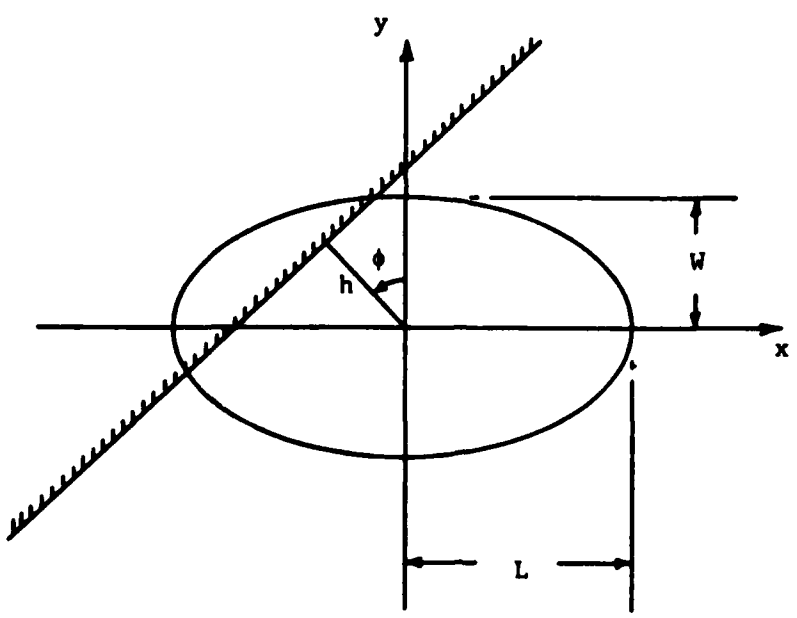

Fig. D.1. Chopping of an elliptic laser beam.

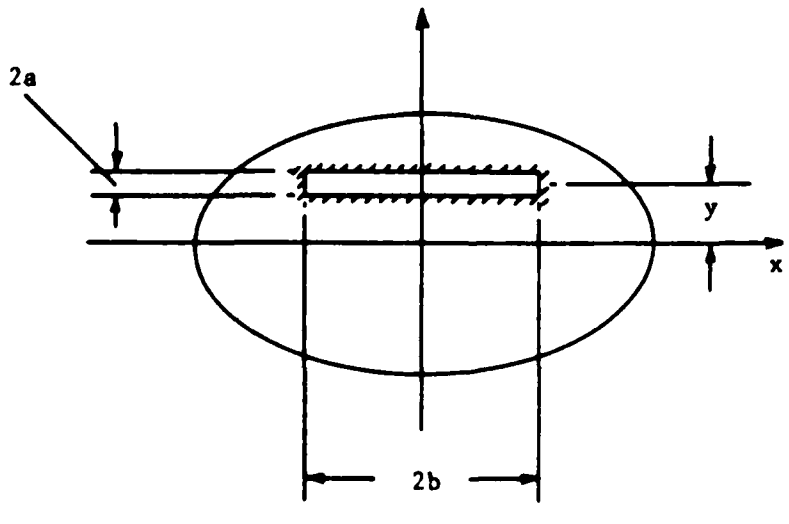

Fig. D.2. Scanning of an elliptic laser beam.

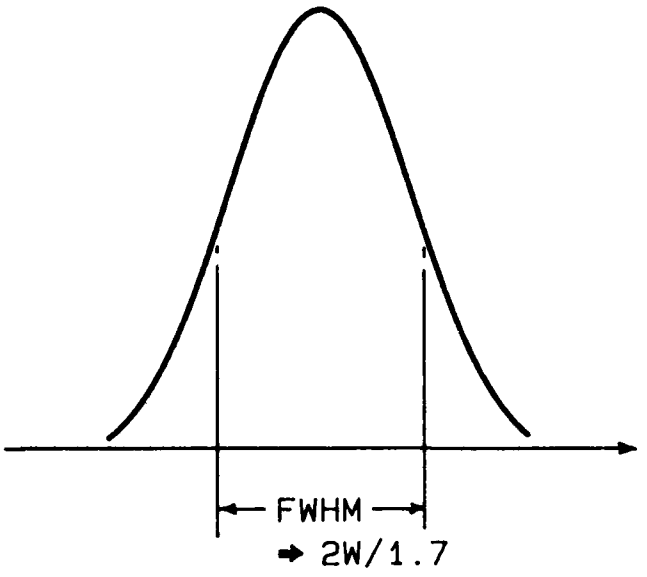

(a) Power profile for a narrow slit.

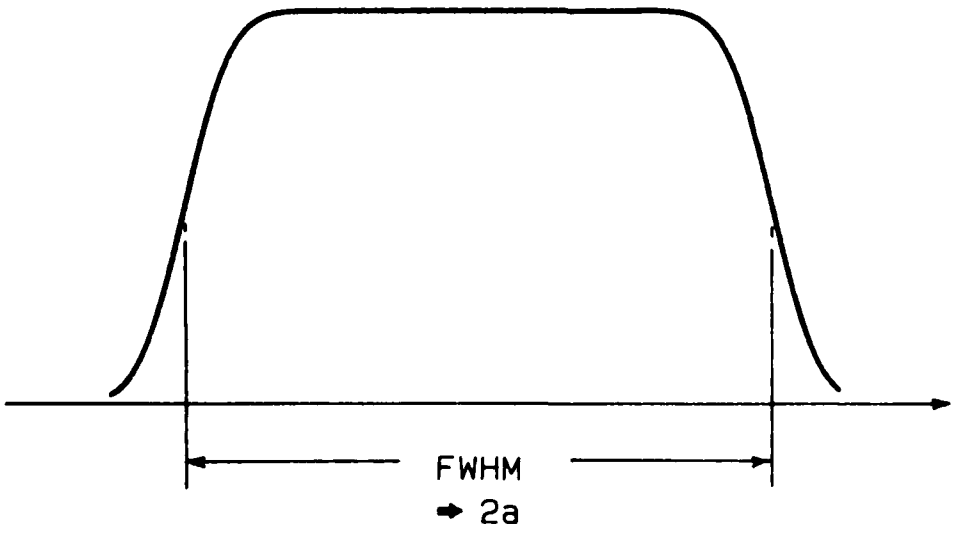

(b) Power profile for a wide slit.

Fig. D.3. Power profiles for the scanning method.

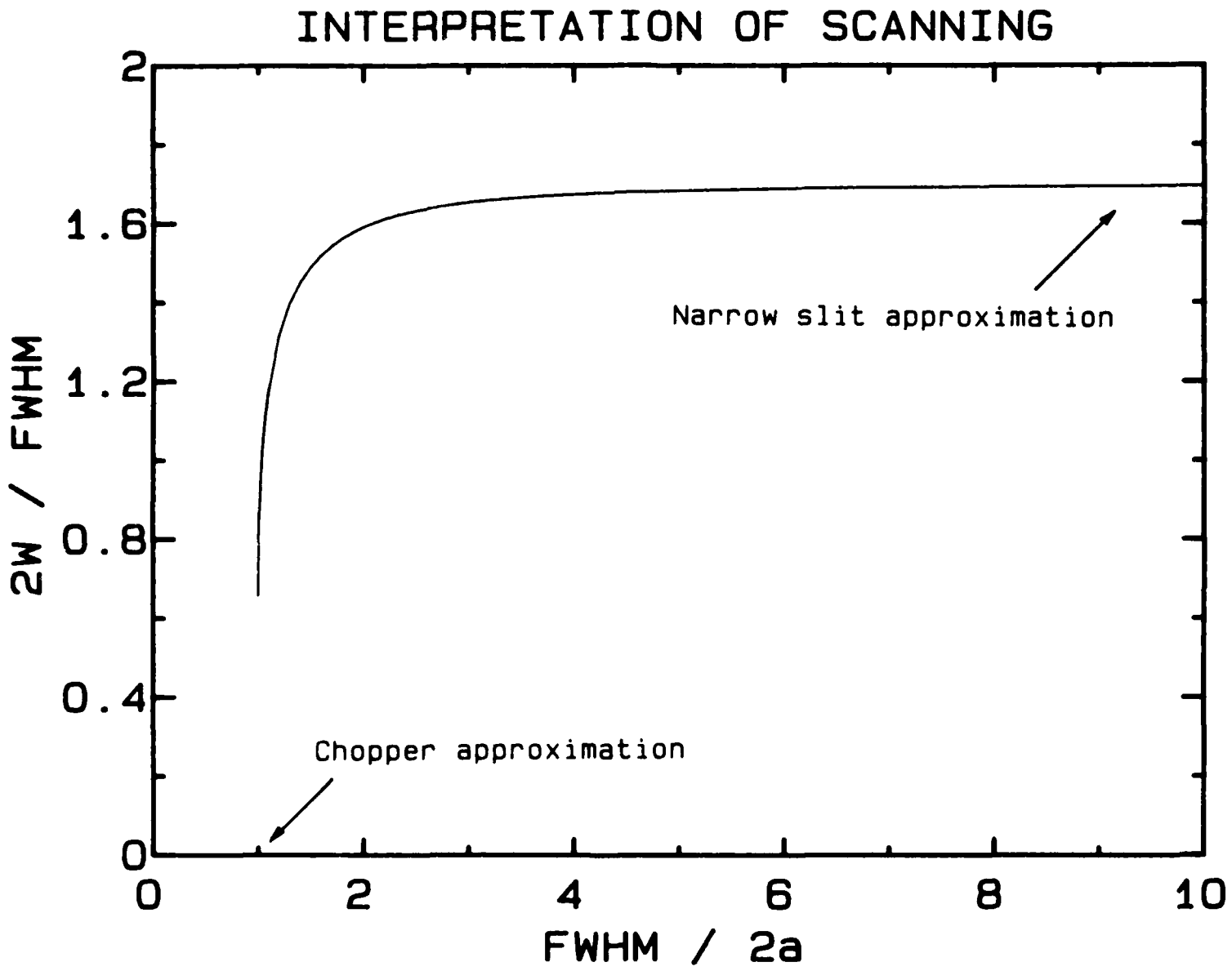

Fig. D.4. Interpretation of the scanning data.

Appendix E

STATIONARY SOLUTION OF PARTICLE-FLUID INTERACTION IN A TURBULENT FLOW

The data presented in Figure 7.3 are based on the stationary solution of the simplified equations of particle motion in a turbulent flow. These equations have evolved through the efforts of a number of investigators over several decades; the underlying concepts and assumptions may be found in the papers by Hjelmfelt and Mockros (1966) and Rizk and Elghobashi (1985).

E.1 Nomenclature

The notations for the primary parameters involved in the problem are defined below. The secondary parameters are introduced for convenience. Definitions of such parameters are given at appropriate places.

d_p Particle diameter (1-10 microns)

i $\sqrt{-1}$

K Saffman's constant, 1.615

r $\tilde{u}_x/\tilde{u}_y = u_x/u_y$, neglecting phase difference between u_x and u_y (0.1)

s Ratio of particle density to fluid density (Polystyrene latex: 1.06, Dust: 2.5, Silicon Carbide: 3.2)

u Fluid velocity

v Particle velocity

y Distance from the wall (50 microns)

Greek Symbols

ν Kinematic viscosity (1.0×10^{-6} m^2/s)

ω Turbulence frequency (1000 Hz)

Superscript

~ Fourier transform

• Time derivative

Subscripts

x Streamwise component

y Normal component

The values of d_p, r, s, y, ν, and ω for the present system are specified in parentheses in front of the definitions. These values are used for computing the results presented in Fig.7.3.

E.2 Differential Equations

The equations of particle motion (i.e., momentum balance) in the streamwise and normal direction are given below.

$$\dot{v}_x = \beta\dot{u}_x + \alpha\beta C_1(u_x - v_x) + \beta\left(\frac{3\alpha}{\pi}\right)^{1/2}\int_{-\infty}^{t}\frac{\dot{u}_x(\tau) - \dot{v}_x(\tau)}{\sqrt{t-\tau}}\,d\tau \quad (E.1)$$

$$\dot{v}_y = \beta\dot{u}_y + \alpha\beta C_2(u_y - v_y) + \beta\left(\frac{3\alpha}{\pi}\right)^{1/2}\int_{-\infty}^{t}\frac{\dot{u}_y(\tau) - \dot{v}_y(\tau)}{\sqrt{t-\tau}}\,d\tau + \gamma\theta\alpha\beta(u_x - v_x) \quad (E.2)$$

where

$$\alpha = \frac{12\nu}{d_p^2}$$

$$\beta = \frac{3}{2s+1}$$

$$C_1 = \left[1 - \frac{9}{16}\left(\frac{d_p}{2y}\right) + \frac{1}{8}\left(\frac{d_p}{2y}\right)^3 - \frac{45}{256}\left(\frac{d_p}{2y}\right)^4 \frac{1}{16}\left(\frac{d_p}{2y}\right)^5\right]^{-1}$$

$$C_2 = 1 + \frac{9}{8}\left(\frac{d_p}{2y}\right) + \frac{81}{64}\left(\frac{d_p}{2y}\right)^2$$

$$\gamma = K/3\pi$$

$$\theta = \frac{d_p}{(\nu/\omega)^{1/2}} \quad ;$$

$(\nu/\omega)^{1/2}$ represents Kolmogoroff microlength scale.

The case of homogeneous turbulence may be represented by setting $C_1 = 1$ in Eqn. (E.1).

E.3 Stationary Solutions

The following expressions are obtained by Fourier transforming Eqns. (E.1) and (E.2).

$$\frac{\tilde{v}_x}{\tilde{u}_x} = \frac{a + ib}{a + ic} \tag{E.3}$$

$$\frac{\tilde{v}_y}{\tilde{u}_y} = \frac{(a'+ib) + \phi(c+ia)\, r}{a' + ic} \tag{E.4}$$

where

$$a = C_1\alpha + (3\alpha\omega/2)^{1/2}$$

$$b = \omega + (3\alpha\omega/2)^{1/2}$$

$$c = \omega/\beta + (3\alpha\omega/2)^{1/2}$$

$$a' = C_2\alpha + (3\alpha\omega/2)^{1/2}$$

$$\phi = \frac{\gamma\theta\alpha\omega(1-\beta)}{\beta(a^2+c^2)}$$

The complex quantities represented by (E.3) and (E.4) contain basic information about the response of a particle to the fluctuations of fluid velocity in streamwise and normal directions, respectively. For a given frequency of fluctuations, the amplitude of these quantities represents the ratio of particle-velocity amplitude to the amplitude of the fluid velocity in the corresponding direction. The phase of this quantity depicts the phase difference between the particle velocity and the fluid velocity. Only the amplitude ratio has been evaluated in the present study. The case of homogeneous turbulence has been studied by setting $C_1 = 1$ in the expression for a and using it in Eqn. (E.4).

References

Abramowitz, M., and Stegun, I.A., 1970, Handbook of Mathematical Functions, Dover Publications Inc., New York.

Acharya, M., and Escudier, M.P., 1983, "Measurement of the Wall Shear Stress in Boundary Layer Flows", Proceedings of the Fourth International Symposium on Turbulent Shear Flows.

Adams, E.W., Johnston, J.P., and Eaton, J.K., 1984, "Experiments on the Structure of Turbulent Reattaching Flow," Thermosciences Division, Dept. of Mech. Engrg., Stanford Univ., California, Report MD-41.

Adler, R., 1967, "Interaction between Light and Sound," IEEE Spectrum, p. 42.

Alfredsson, P.H., Johansson, A.V., Haritonidis, J.H., Eckelmann, H., 1986, "On the Fluctuating Wall Shear Stress and the Velocity Field in the Viscous Sublayer", submitted to J. Fluid Mech.

Adrian, R.J., 1978, "Estimation of LDA Signal Strength and Signal to Noise Ratio," TSI Quarterly, IV: 1.

Adrian, R.J., and Earley, W.L., 1976, "Evaluation of [illegible] Performance Using Mie Scattering Theory," Minnesota Symposium on Laser Anemometry, Univ. of Minnesota Dept. of Conferences.

Adrian, R.J., and Orloff, K.L., 1977, "Laser Anemometer Signals [illegible] bility Characteristics and Application to Particle Sizing," Appl. Optics, 16: 677.

Arnaud, J.A., Hubbard, W.M., Mandeville, G.D., de la Clavière, B., Franke, E.A., and Franke, J.M., 1971, "Technique for Fast Measurement of Gaussian Laser Beam Parameters," Appl. Optics, 10 [illegible].

Bellhouse, B.J., and Schultz, D.L., 1966, "Determination of Mean [illegible] Dynamic Skin Friction, Seperation and Transition in Low-Speed Flow with a Thin-Film Heated Element," J. Fluid Mech., 24: [illegible].

Blackwelder, R.F., and Eckelmann, H., 1979, "Streamwise Vortices Associated with the Bursting Phenomenon," J. Fluid Mech., 94: [illegible].

Blinco, P.H., and Simons, D.B., 1974, "Characteristics of Turbulent Boundary Shear Stress", J. Engrg. Mech. Division, ASCE, 100: [illegible], 203.

Born, M., and Wolf, E., 1980, Principle of Optics (6th ed.), MacMillan Company, New York.

Brereton, G.J., 1987, Ph.D. Thesis, Stanford University, California.

Cantwell, 1981, "Organized Motion in Turbulent Flow", Ann. Rev. Fluid Mech.

Chao, B.T., 1964, "Turbulent Transport Behavior of [illegible] Particles in Dilute Suspension," Osterreichisches Ingenieur Archiv., 18 [illegible].

Chapman, D.R., and Kuhn, G.D., [illegible], "Navier-Stokes Computation of Viscous Sublayer Flow and the Limiting Behavior of Turbulence Near a Wall," AIAA [illegible]th Computational Fluid Dynamics Conference, [illegible]nati, Ohio.

Coles, D., 195[illegible], "The Law of the Wake [illegible] Turbulent Boundary Layer," J. Fluid Mech., 2 [illegible].

Coles, D., 196[illegible], "The Turbulent Boundary Layer [illegible] Compressible Fluid," RAND Corp., Rep. R[illegible]-PR.

Coles, D., 196[illegible], "The Young Person's Guide to the Data," Proc. Computation of Turbulent Boundary Layers, AFOSR-IFP-Stanford Conference.

Cook, W.J., and Giddings, T.A., [illegible], "Study of Wall Shear Stress and Shear Stress Meters in Separating Flow," Progress Report for the period August [illegible], May [illegible], to NASA Ames Research Center.

[illegible], W., and Reichardt, H., "Fundamentals of Physics," McGraw-Hill [illegible].

[illegible], P., [illegible], "The Combined Mean Temperature and Velocity Profile in Turbulent Flow," Ingenieur-Archiv, 104 [illegible].

[illegible], Hwang, A., and [illegible], "Laser Doppler Anemometry," Academic Press Inc. (London) Ltd.

[illegible], "The Structure of the Turbulent Sublayer and the Adjustment of Rough-Wall Turbulent Boundary Layers," J. Fluid Mech., 65 [illegible].

[illegible], Meyer, M.L., Hwang, P.C., [illegible], "Knife-edge Scanning Measurements of Sub-wave-length Focused Light Beams," Appl. Optics, 16 [illegible].

[illegible], and Adrian, R.J., [illegible], "Measurement of Fluid Velocity Fluctuations Using Laser Doppler Techniques," The Rev. of Sci. Instruments, 42 [illegible].

Goodman, J.W., [illegible], Introduction to Fourier Optics, McGraw-Hill Book Company.

Gucker, F.T., Rowell, R.L., and Ohki, G., 1962, "A Study of Intensity Functions for Dielectric Spheres Calculated from the Mie Theory: Table of Angular Functions π_n and τ_n of Orders 1 to 43 at 1° Intervals," Proc. 1st Nat'l. Conf. on Aerosols, Liblice, Czechoslovakia, 59.

Hamour, A., 1984, "Wall Effect on Lateral Migration of Spherical Particles in a Linear Shear Flow," Ph.D. Dissertation, Stanford University, USA.

Haus, H.A., 1984, Waves and Fields in Optoelectronics, Prentice-Hall, Inc., New Jersey.

Hershey, A.V., 1962, "Computing Programs for the Complex Fresnel Integral," NWL Report No. 1796, U.S. Naval Weapons Laboratory, Dahlgren, Virginia.

Hielmfelt, A.T., and Mockros, L.F., 1966, "Motion of Discrete Particles in a Turbulent Fluid," Appl. Sci. Res., 16: 149.

Jayaraman, R., Parikh, P., and Reynolds, W.C., 1982, "An Experimental Study of the Dynamics of an Unsteady, Turbulent Boundary Layer," Technical Report No. TF-18, Thermosciences Division, Department of Mechanical Engineering, Stanford University, Stanford, California, USA.

Jayaraman, R., Parikh, P. G., and Reynolds, W. C., 1982, "An Experimental Study of the Dynamics of an Unsteady, Turbulent Boundary Layer Data, Tables, and Plots," Microfiche report No. 1, Thermosciences Division, Department of Mechanical Engineering, Stanford University, Stanford, California, USA.

Jenkins, F.A., and White, H.E., 1957, Fundamentals of Optics, McGraw-Hill Book Company, Chap. 16.

Jones, D.S., 1964, The Theory of Electromagnetism, The MacMillan Co., New York.

Karp, S.N., and Russek, A., 1956, "Diffraction by a Wide Slit," J. Appl. Phys., 27, 886.

Keller, J.B., 1957, "Diffraction by an Aperture," J. Appl. Physics, 28: 426.

Keller, J.B., 1962, "Geometrical Theory of Diffraction," J. Opt. Soc. Am., 52: 116.

Keveloh, C., and Staude, W., 1983, "Determination of Velocity Gradients with Scattered Light Cross-Correlation Measurements," Applied Optics, 22, 333.

Kim, H.T., Kline, S.J., and Reynolds, W.C., 1971, "The Production of Turbulence Near a Smooth Wall in a Turbulent Boundary Layer," J. Fluid Mech., 50: 133.

Kim, J., Moin P., and Moser, R., 1986, "Turbulence Statistics in Fully Developed Channel Flow at Low Reynolds Number," submitted to J. Fluid Mech.

Klebanoff, P.S., 1954, "Characteristics of Turbulence in a Boundary Layer with Zero Pressure Gradient," NACA TN 3178.

Kline, S.J., Reynolds, W.C., Schraub, F.A., and Runstadler, P.W.,1967, "The Structure of Turbulent Boundary Layers," J. Fluid Mech., 30: 741.

Kreplin, H., and Eckelmann, H., 1979, "Behavior of the Three Fluctuating Velocity Components in the Wall Region of a Turbulent Channel Flow," Phys. Fluid, 22: 1233.

Laufer, J., 1953, "The Structure of Turbulence in Fully Developed Pipe Flow," NACA TN 2954.

Ludwieg, H., 1950, "Instrument for Measuring the Wall Shearing Stress of Turbulent Boundary Layers," TM 1284, NACA.

Ludwieg, H., and Tillmann, W., 1949, "Investigation of the Wall Shearing Stress in Turbulent Boundary Layers," TM 1285, NACA.

Mazumder, M.K., Wanchoo, S., McLeod, P.C., Ballard, G.S., Mozumdar, S., and Caraballo, N., 1981, "Skin Friction Drag Measurements by LDV," Appl. Optics, 20: 2832.

Millar, R.F., 1958, "Diffraction by a Wide Slit and Complementary Strip I & II," Proceed. Camb. Philos. Soc. (Math. & Physical Sciences), 54, 479.

Mitchell, J.E., and Hanratty, T.J., 1966, "A Study of Turbulence at a Wall Using an Electrochemical Wall Shear-Stress Meter," J. Fluid Mech., 26: 199.

Monson, D.J., and Higuchi, H., 1980, "Skin Friction Measurements by a New Non-intrusive Double Laser Beam Oil Viscosity Balance Technique," AIAA 13th Fluid and Plasmadynamics Conference, Snowmass, Colorado.

Nayfeh, A.H., 1973, Perturbation Methods, Wiley, New York.

Py, B., 1973, "Etude Tridimensionelle de la Sous-couche Visqueuse Dans une Veine Rectangulaire par des Measures de Transfert de Matiere en Paroi," Int. J. Heat Mass Transfer, 16: 129.

Rizk, M.A., and Elghobashi, S.E., 1984, "THe Motion of a Spherical Particle Suspended in a Turbulent Flow Near a Plane Wall," Phys. Fluid, 28: 806.

Ramo, S., Whinnery, J.R., and Van Duzer, T., 1984, Fields and Waves in Communication Electronics, John Wiley and Sons, New York.

Saffman, P.G., 1965, "The Lift of a Small Sphere in a Slow Shear Flow," J. Fluid Mech., 22: 385.

Saffman, P.G., 1968, Corrigendum to "The Lift of a Small Sphere in a Slow Shear Flow," J. Fluid Mech., 31: 624.

Sandborn, V.A., 1979, "Evaluation of the Time Dependent Surface Shear Stress in Turbulent Flows," ASME 79-WA/FE-17, ASME Winter Annual Meeting.

Schlichting, H., 1979, Boundary-Layer Theory, 7th Edition, McGraw-Hill Book Company.

Schraub, F.A., and Kline, S.J., 1965, Mech. Engrg Dept. Rept. MD-12, Stanford University.

Self, S.A., 1983, "Focusing of Spherical Gaussian Beams," Appl. Optics, 22: 658.

Sirkar, K.K., and Hanratty, T.J., 1970, "The Limiting Behaviour of the Turbulent Transverse Velocity Component Close to a Wall," J. Fluid Mech., 44: 605.

Skinner, D.R., and Whitcher, R.E., 1972, "Measurement of the Radius of a High-Power Laser Beam Near the Focus of a Lens," J. Phy. E, 5: 237.

Spalart, P.R., 1986, "Numerical Simulation of Boundary Layers: Part 3. Turbulence and Relaminarization in Sink Flows," NASA TM 88220.

Suzaki, Y., and Tachibana, A., 1975, "Measurement of the Micron Sized Radius of Gaussian Laser Beam Using the Scanning Knife-edge," Appl. Optics, 14: 2809.

Tranter, C.J., 1954, "A Further Note on Dual Integral Equations and an Application to the Diffraction of Electromagnetic Waves," Quart. J. Mech. and Appl. Math., VII: 318.

Vasseur, P., and Cox, R.G., 1976, "The Lateral Migration of a Spherical Particle in Two-Dimensional Shear Flows," J. Fluid Mech., 78: 385.

Westphal, R.V., Eaton, J.K., and Johnston, J.P., 1981, "A New Probe for Measurement of Velocity and Wall Shear Stress in Unsteady Reversing Flow," J. Fluid Engrg., 103: 478.

Winter, K.G., 1977, "An Outline of the Techniques Available for the Measurement of Skin Friction in Turbulent Boundary Layers," Prog. Aerospace Sci., 18: 1.